Laser Guide Star Wave-Front Sensing in the Extremely Large Telescopes era : Strategies & Detectors

Zibo Ke

Aix*Marseille université
Socialement engagée

NNT/NL : 2021AIXM0001/001ED000

THÈSE DE DOCTORAT

Soutenue à Aix-Marseille Université
le 10 Decembre 2021 par

Zibo KE

Laser Guide Star Wave-Front Sensing

in the Extremely Large Telescopes era : Strategies & Detectors

Discipline
PHYSIQUE ET SCIENCES DE LA MATIERE

Spécialité
Instrumentation
Optique, Photonique et Traitement d'Image

Ecole Doctorale 352

Laboratoire/Partenaires de recherche
Laboratoire d'Astrophysique de Marseille
China Scholarship Council

Composition du jury

Pr. Andres GUESALAGA Pontifica Universidad Catolica, Santiago Chile	Rapporteur
Dr. Maud LANGLOIS Centre de Recherche Astrophyique de Lyon (CRAL)	Rapporteure
Gaetano SIVO Gemini Observatory	Examinateur
Jean-Luc BEUZIT Laboratoire d'Astrophysique de Marseille	Examinateur
Thierry FUSCO ONERA	Directeur de thèse
Benoit NEICHEL Laboratoire d'Astrophysique de Marseille	Encadrant de thèse

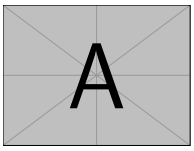
A

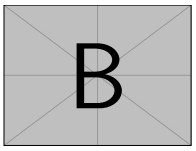
B

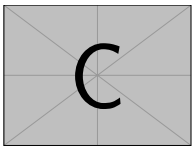
C

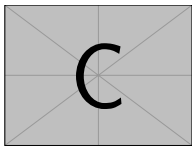
C

Je soussigné, Zibo Ke, déclare par la présente que le travail présenté dans ce manuscrit est mon propre travail, réalisé sous la direction scientifique de Thierry Fusco & Benoit Neichel dans le respect des principes d'honnêteté, d'intégrité et de responsabilité inhérents à la mission de recherche. Les travaux de recherche et la rédaction de ce manuscrit ont été réalisés dans le respect à la fois de la charte nationale de déontologie des métiers de la recherche et de la charte d'Aix-Marseille Université relative à la lutte contre le plagiat.

Ce travail n'a pas été précédemment soumis en France ou à l'étranger dans une version identique ou similaire à un organisme examinateur.

Fait à Marseille le [15/02/2022]

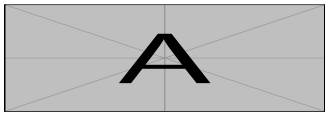

Résumé

L'Europe vient de lancer la construction du plus grand télescope au sol : l'ELT. D'ici la fin de cette décennie, ce géant de 40 m répondra à des questions fondamentales allant de la recherche et la caractérisation des exoplanètes à la formation et l'évolution des premières galaxies de l'univers. L'optique adaptative (AO), en corrigeant en temps réel les aberrations introduites par l'atmosphère, est essentielle pour atteindre les performances ultimes de ce futur géant européen. L'ELT a donc été conçu comme un télescope adaptatif, qui fournira des images avec une résolution angulaire de moins de 10 milli-arsec dans le proche infrarouge. Pour cela, l'ELT est équipé d'un miroir déformable dans son train optique (le 4ème miroir du télescope, alias M4), ainsi que de 8 stations lasers, afin de créer des sources artificielles (Laser Guide Stars ou LGS en Anglais) pour l'analyse du front d'onde. Les étoiles laser sont utilisées en AO sur des télescopes de 8/10m depuis une dizaine d'années maintenant, et les performances sont relativement bien maîtrisées. Cependant, le passage à l'échelle d'un télescope de 40 m représente un défi bien plus important qu'une simple extrapolation des concepts actuels, notamment en raison du problème de l'élongation du spot, qui provient du fait que les étoiles laser ne sont pas des objets ponctuels, mais des sources étendues. En effet, la couche d'atomes de sodium, située à 90km au-dessus du télescope, a une épaisseur comprise entre 10km et 20km. Les étoiles laser résultant de l'excitation de ces atomes de Sodium par la lumière laser propagée depuis le télescope ont donc une forme de "cigare" dans la couche de Sodium. Par effet de perspective, elles apparaissent comme des objets étendus (ellipses) sur le bord opposé de la pupille du télescope. Pour un télescope de 40 m, les taches laser ont une taille comprise entre 1 seconde d'arc pour celles proches du projecteur laser (Laser Launch Telescope - LLT) et une élongation maximale attendue qui peut atteindre jusqu'à 25 secondes d'arc. La difficulté est donc de réaliser une analyse de front d'onde sur des objets très étendus, et dont l'élongation varie dans la pupille. Dans cette thèse, nous explorons le gain apporté par les nouveaux détecteurs CMOS pour faire face à ce problème d'élongation des spots. Les détecteurs CMOS offrent un grand nombre de pixels, ce qui ouvre la possibilité d'obtenir à la fois un bon échantillonnage, et un large champ de vue pour les spots les plus étendus. Dans cette thèse, j'ai d'abord réalisé une caractérisation complète d'un nouveau détecteur CMOS, et montré qu'il était approprié pour construire un LGSWFS pour un ELT. J'ai ensuite construit un premier prototype de LGSWFS, et démontré la chaîne de mesure complète. Ce prototype sert pour les futurs instruments de l'ELT comme HARMONI.

Mots clés : Optique Adaptative, Extremely Large Telescope, Etoile Laser, Détecteurs

Abstract

Europe has just launched the construction of the largest ground-based telescope: the ELT. In operation by 2027, this 40m giant will answer fundamental questions from the search for and characterization of planets to the formation and evolution of the first galaxies of the universe. Adaptive Optics (AO), by correcting real-time aberrations introduced by the atmosphere, is essential to reach the ultimate performance of this future European giant. The ELT has therefore been designed as an adaptive telescope, which will provide images with an angular resolution of less than 10 milli-arsec in the near infrared. For this purpose, the ELT is equipped with a deformable mirror in its optical train (the 4th mirror of the telescope, alias M4), as well as 8 laser stations, to create artificial sources (Laser Guide Stars or LGS) for wavefront analysis. Laser stars have been used in AO on 8/10m telescopes for about ten years now, and the performances are relatively well mastered. However, scaling up to a 40m telescope represents a much bigger challenge than a simple extrapolation of the current concepts, and this in particular because of the "spot elongation" problem.

The spot elongation comes from the fact that the laser stars are not point objects, but extended sources. Indeed, the layer of sodium atoms, located at 90km above the telescope, has a thickness between 10km and 20km. The laser stars resulting from the excitation of these sodium atoms by the laser light propagated from the telescope have thus a "cigar" shape in the sodium layer. By perspective effect, they appear as extended objects (ellipses) on the opposite edge of the telescope pupil. For a 40m telescope, the laser spots have a size between 1arcsecond for those close to the Laser Launch Telescope (LLT) and a maximum expected elongation which can reach up to 25arcseconds. In the case of Shack-Hartmann Wave-Front Sensing, which is the scope of this this work, the difficulty is therefore to perform a wave front analysis on highly extended objects, and whose elongation varies in the pupil.

In this PhD thesis, we explore the gain brought by new CMOS detectors to cope with this spot elongation problem. The CMOS detectors offer a large number of pixels, which open the possibility to get both a good sampling of the best LGS spots and a wide Field-of-View for the most extended spots. However, the CMOS detector comes with other complexities, such as the small physical pixel size, which restrict the potential configurations. In this thesis, we have first performed a full characterisation of a new CMOS detector, and showed that it was appropriate for building a LGSWFS for an ELT. We have then built a first prototype of an LGSWFS, and demonstrated the full measurement chain. This prototype serves for an ELT instrument like HARMONI.

Keywords: Adaptive Optics, Extremely Large Telescope, Laser Guide Stars, Detectors, Wavefront Sensing, Spot elongation.

Remerciements

Seven years ago, when I was in China and going through some tough times of my own, I came across a saying, "All human wisdom is contained in these two words,'Wait and Hope'".I never thought of the profound impact that this sentence had on me, except that I just knew it was written by Alexandre Dumas, "the Count of Monte Cristo", and I had never read it. But these words were so close to my heart that they encouraged me and helped me out of that difficult time, and since then, I have been taking it as my motto, accompanying me through all kinds of setbacks and difficulties.

Before, my bachelor's and master's majors are not related to astronomy and optics, only in the stage of master, I worked on solar telescope instruments for a year and a half , but the observatory telescope and left a deep impression on me, I enjoy the feeling of standing on the observatory, looking at the telescope chasing stars, bathing in the starlight, I've even been thinking the observatory is as sacred a place as a cathedral.Therefore, I am eager to participate in the research of telescope instruments in the doctoral program, even though my professional foundation is weak. Thanks to the funding from CSC (China Scholarship Council) and the support from Benoit Neichel and Thierry Fusco in LAM, I was able to get into the field of adaptive optics that I was looking forward to.

Everything was new when I first came to Europe, the ancient culture, architecture, art, music and so on are all let me fascinated. And Marseille, even though some people have different sounds, but I've never hidden my love for it : forever of sunshine, the blue Mediterranean sea, and enthusiastic Marseille people. More importantly, after coming here and reading "the Count of Monte Cristo", to my surprise, Marseilles was the place that created the words, And that imaginary encouragement, "wait and hope," just appeared in reality, giving me a feeling that I was meant to be here, and it struck me again. Then, looking at château d'If from the vieux port became my habit for three years.

Although I was well prepared to face difficulties in the doctoral project, I did not realize the thorny work until I really started, I had to spend a lot of time to make up for my lack of basic knowledge. The lack of fluent language communication slowed down my learning speed, since the outbreak of the Covid in my second PhD year, the laboratory was once closed, which made the problem more serious and led to the project not progressing fast. This made me confused, and then self-doubt, whether I had really made the right choice. During such a difficult time, I am very grateful to my two supervisors Benoit and Thierry, who helped me find problems, provide suggestions, and solved many basic problems in the project, which restored my confidence. I want to thank Felipe Pedreros, a postdoctoral fellow, for his careful attitude and analysis that helped me improve the quality of my work, although I do not agree with his approach

to some issues. What's more, I still would like to thank "Wait and Hope", which always appears and encourages me to persevere to the end in the difficult times.

Although the whole process was struggling, the process was finally completed. At this moment of finishing the thesis manuscript, I have so many words of thanks to say :

I would like to thank CSC for the funding, without the support of my motherland, I could not fulfill my desire. I would also like to thank Benoit and Thierry for their decision three years ago to allow me to enter my ideal research field, thank you for your meticulous guidance and hard work to help me revise my thesis manuscript. I have benefited a lot from your rigorous academic and working attitude. I would also like to thank LAM and the GRD and PAPYRUS teams. I really enjoy the environment here and thank all the people who have helped me : Vincent Chambouleyron, Romain Fetick, Mathieu Vachey, Raphaël Pourcelot, Nicolas Levraud, Idir Boudjema, Kelly Joaquina, Alexis Lau, Isabelle Racicot, Iva Laginja, Simona Lombardo, Eduard Muslimov, Felipe Pedreros, Pierre Jouve, Olivier Beltramo-Martin, Anne Costille, Elodie Choquet, Jean-François Sauvage, Kacem El Hadi, Kjetil Dohlen.

I would like to thank my family, who have always encouraged and supported me, and have been my strong backing. I would also like to thank my Chinese friends who are also studying in Marseille, Wenjun Liu, Yijun Zhao, Zixi Chen, Qiujuan Shen, Junhao Tu, all of you for giving me an unforgettable pleasures and novel experiences.

I am very fortunate to have spent this unforgettable doctoral period in Marseille, France. However, this does not mean the end. I will start again and continue to strive towards the life journey of constantly understanding myself. And I believe "Attendre et espérer" would be indelible mark in my life.

Table des matières

Table des figures

Liste des tableaux

Introduction

Astronomy is a science where the observations of extremely distant objects are the single source of information. Therefore, over the last hundred years , the size of ground based telescopes has steadily increased to reach diameters of the order of ten meters. This important growth has two main goals, to increase the total flux collected, thus reducing the photon noise that represents the fundamental limit of any observation, and to improve the angular resolution of the observed object. If the first objective is reached - the number of photons collected increases with the square of the telescope diameter - it is unfortunately not the same for the angular resolution. Indeed, the presence of the Earth's atmosphere significantly limits this resolution. The latter never exceeds the theoretical resolution of a telescope of a few tens of centimetres at optical wavelengths, regardless of the telescope diameter considered. In 1953, Babcock proposed a technique called Adaptive Optics [AO] to compensate, in real time, for this effect. To that end, AO technology is based on a deformable mirror which corrects the incoming wave front in real time by using information coming from a Wave Front Sensor [WFS] which measures the turbulent phase. Every measurement/correction step have to be done faster than the typical correlation time of turbulence (in other word every millisecond or so). Over the last twenty years, AO has evolved from a demonstration stage to a technique that is both proven and operational, and almost all large telescopes are equipped with AO.

The next step forward will come from the so-called Extremely Large Telescope (39 m diameter European ELT [E-ELT], 30 m north American Thirty Meters Telescope [TMT], 24 m American and Australian giant Magellan Telescope [GMT]) that should have their first light before the end of the decade (2026 to 2030 depending on the projects). These giants are all relying on AO systems, starting operations from day one. The colossal size of these telescopes and the complexity of the scientific instruments compel us to dramatically change the way AO systems will be designed, integrated, calibrated and operate. Maximizing the astrophysical returns of AO assisted instruments calls for an improvement of the overall system performance combined with a significant gain in sensitivity and robustness. Diffraction limited instruments with access to the whole sky are the key of the ELT success.

Indeed, one of the most exciting promises of this new ELT generation is in trying to understand galaxy formation and evolution. To understand the physical processes taking place in galaxy formation and evolution and to differentiate between intrinsic and environmental effects, the ability to obtain resolved spectroscopy and images across objects is a must. Distant galaxies are marginally resolved in seeing-limited conditions and AO is required. Most of the current extra-galactic AO studies are howe-

ver constrained by the number of targets available to AO correction (the so-called sky coverage), and the need for statistics that requires the observation of many objects across the largest possible field. Those constraints called for the development of a new generation of AO, called Wide Field AO [WFAO]. By using multiple Laser Guide Stars [LGS], WFAO significantly increases the field of the AO corrected images, and the fraction of the sky that can benefit from such correction. Therefore, where the ExAO systems are well suited for observations of exoplanets, the new generation of WFAO is opening the path for extragalactic observations.

Very recently, such capability has been brought to its apogee by coupling the ESO-operated Adaptive-Optics Facility (AOF) with the cutting-edge instrumentation of the MUSE integral-field (3D) spectrograph. Similar instrumental capabilities of the ELTs (e.g., HARMONI, MOSAIC) will revolutionize the extra-galactic field, as we will be able to reproduce the observation of the galaxy structure and kinematics out to distances of tens of millions of light-years. This will certainly modify our understanding of the galaxy mass assembly mechanisms and the Hubble sequence build-up. The use of multi-LGS in astronomy is however a young technology, and the extrapolation of the technique to the ELT size leads to technological barriers regarding Wave-Front Sensing and associated detectors.

To achieve significant sky-coverage, extra-galactic observations assisted by AO require the use of LGS. The artificial reference source is created by shining a laser from the telescope. Light from the beam is absorbed and reemitted by atoms in the upper atmosphere (a sodium layer in the mesosphere) back into the WFS. For LGS AO systems, most of the WFS are Shack-Hartmann WFS [SHWFS]. In this WFS, the optical system is a lenslet array located in a pupil plane, spatially sampling the wavefront. Each lenslet (also called subaperture) is forming an image of the source on the detector. Displacements of the image centroids are proportional to the local wave-front gradient, which provides a linear transformation with respect to the incoming phase. Increasing the number of measurement points across the wavefront (i.e., increasing the number of sub-apertures) allows the measurement of higher spatial frequencies and proportionally reduces the wavefront estimation error. More sub-apertures means dividing the flux into more pieces and consequently the need for more detector pixels.

Due to the vertical extension of the sodium layer (typically between 10 and 20km), the AO guide star is now a 3D-extended object, with a complex shape and temporally evolving with sodium layer dynamical variations. When considering SHWFS, this 3D sodium layer extension creates various elongated spots in each subaperture which can be as large as 20 arcsec for an ELT. Dealing with such a spot elongation using a classical SHWFS requires a tremendously large number of pixels. It calls for very sensitive (almost photon noise limited), very fast (larger than 500 Hz, most likely 1kHz) and extremely large (up to 5 million pixels) detectors.

In this thesis, I worked on the LGS WFS component, focusing on the detection

part. In particular I thoroughly study the performance of a new CMOS detector and I participate to its integration in the first prototype of a LGS-WFS for the ELT Laser Tomographic AO system. Finally I also participate to the development of a dedicated AO system that will be installed on the 1.52m telescope of Observatoire de Haute Provence. One of the goal of this multi-purpose AO system will be to test, on sky, this new CMOS sensor in real operational conditions. After an introduction about Adaptive Optics in Chapter 1 and Laser Guide Star WFS for ELT in Chapter 2, I will present the results of this characterization in the Chapter 3. I then included this camera in an LGS WFS prototype as presented in Chapter 4. I will discuss the impact of the shutter reading mode on the AO performance in 5. Finally I will give, in the Annexe, a status of the Provence Adaptive-optics PYramid RUn System (PAPYRUS) and the I'll present the future plans associated to this developments.

1. Introduction on Adaptive Optics

Sommaire

1.1. Historical Aspects

For more than 400 years, astronomers have been using telescopes to observe the sky and improve the overall understanding of the Universe. However, observations with ground-based telescopes have been suffered from the atmospheric turbulence which induces time variant perturbations (phase delays) on the wavefront coming from the astronomical object. This will lead to a fast jittering and speckle pattern in the scientific instrument focal plane, eventually leading to a strong degradation of the system angular resolution when long exposures are considered. From early on, astronomers built observatories on top of the mountains, to reduce the impact of the atmospheric turbulence on the images. This worked well for small size telescopes, but with the development of larger telescopes nowadays, improving the astronomical

site can not be the only solution for improving the observation performance, and dedicated instrumentation is required.

In 1953, American astronomer Babcock put forward the idea of measuring and compensating the wavefront error in real time to deal with the dynamic disturbances introduced by the atmospheric turbulence (BABCOCK 1953). The idea is to use a photodetector combined with a knife edge test to directly measure a signal proportional to the incoming wavefront, the detected signal is then converted to the charge for an oil film on the surface of the mirror, which can therefor compensate for the input wavefront. The final arrangement of the wavefront sensor and corrector devices in a feedback closed-loop fashion gives the original idea of an Adaptive Optics (AO). However, limited by the technology available at that time, the idea was difficult to implement. Later, with the funding in AO research by the Defense Advanced Research Projects Agency (DARPA), in 1977, the Journal of the Optical Society of America (JOSA) published a number of articles about AO, which indicated that AO became an official research direction.

At first, adaptive optics was not used for astronomical observations, but for military purposes. In 1972, the Itek company developed a Real-Time Atmospheric Compensator (RTAC) system as a feasibility verification study. It used a 21 elements piezoelectric deformation mirror as the corrector and a 32 elements lateral shear interferometer as a sensor to reconstruct the wavefront with an analog circuit. This system was tested in the Roma Air Force Base in 1984 and good results were acquired (HARDY, LEFEBVRE et KOLIOPOULOS 1977). Meanwhile, the Compensated Imaging System (CIS) was developed under the lead of Hardy and the Itek company. This system was implemented in the 1.6m telescope located in America Air force Maui Optical Station (AMOS), and it achieved high resolution imaging aimed at satellite observations (HARDY 1998). In fact, many major AO theories and measurements were developed by the plan of Strategic Defense Initiative (SDI) provided by American president Reagan in 1983. After this mission, Lincoln Laboratory which was the leader among them in technologies published progresses in 1992.

In parallel, Fried worked on the atmospheric turbulence theory and he established the basis about the optical effects of atmosphere (FRIED 1966a), and put forward the major parameters of wavefront correction such as coherence length and isoplanatic angle, which has been the theoretical basis of AO correction. In 1985, due to the limited sky coverage caused by having no enough bright objects within the isoplanatic angle, Foy and Labeyrie introduced the idea of the artificial guide star, which consists in launching a laser from the telescope, to create atmosphere scattering and form a beacon used for Wave-Front sensing (FOY et LABEYRIE 1985). At that time, two methods to produce laser guide stars are presented, the first one using the Rayleigh scattering caused by air molecules at 10 - 20km, and the second one using the resonance scattering from sodium atoms at about 90km (HUMPHREYS, RONALDA et HERRMANN 1992). A first implementation of a Sodium AO system was done with the Short Wavelength Adaptive Technology (SWAT), with 241 elements deformable mirrors, Hartmann wavefront sensor and digital wavefront processor (PRIMMERMAN et FOUCHE 1976). In 1989, Fugate tested the Rayleigh laser guide star system in the 1.5m telescope located

in America air force weapons laboratory starfire optical range (FUGATE, FRIED, AMEER et al. 1991).

After that, the observations slowly moved from military to astronomical targets. The AO requirement of the latter is lower than the former, and astronomy AO also started from infrared wavelengths, it could be operated at smaller coherence length and greenwood frequency. In parallel with US development, in Europe, the COME-ON project was started in 1985 coordinated by P. Léna, F. Merkle, and J.-C. Fontanella. It was based on the existing competences in France and at the European Southern Observatory (ESO), with the aim of demonstrating the performance of AO for astronomy. The consortium in charge of the project was initially made of three French laboratories associated with ESO, COME-ON standing for : CGE, a French company now CILAS (formerly LASERDOT), Observatoire de Paris-Meudon, ESO and ONERA. The purpose of the project was initially to build an AO-prototype system based on the available technologies and test it at an astronomical site, to gather experience for the ESO Very Large Telescope (VLT) program, including multitelescope interferometry with the VLT interferometer (VLTI). The main requirement was to achieve nearly diffraction-limited imaging at the focus of a 4-m class telescope at near IR wavelengths from 2 to 5 m, depending on the seeing conditions (KERN, MERKLE, GAFFARD et al. 1988). The first step was to utilize a 19 elements deformable mirror and Hartmann-Shack wavefront sensor to acquire the AO correction images. The system was successfully developed and obtained the first astronomy AO images in France Haute-Provence Observatory (OHP) in 1989 (MERKLE, ROUSSET, KERN et al. 1990). The next step was to acquire high resolution images at the infrared band by implementing a 52 elements deformable mirror and 32 elements subaperture Hartmann sensor into 3.6m New Technology Telescope (NTT) in 1993. Almost at the same time, Roddier used a curvature sensor and a double sheet deformable mirror to realize the AO correction in 3.6m Canada France Hawaii Telescope (CFHT) (RODDIER 1988).

With the establishing of 8 - 10m telescopes like Keck, VLT, Subaru, Gemini later, AO instrumentation and technology had a large technological development in which the number of wavefront sensing and correction elements increased quickly, as well as fast, lower noise and higher quantum efficiency detectors. However, AO still suffered from the limited field of view (FOV), and small sky coverage. As a result, researchers provided the concepts of Multi-layer Conjugation AO (MCAO), Multi-layer Object AO (MOAO), and Ground Layer AO (GLAO) aimed at increasing both the sky coverage and the field-of-view. For instance, the GLAO system developped for The America Multi Mirror Telescope (MMT) improved the resolution by about twice in the K-band within 2 arcmin FOV. And more recently, the AOF implemented at the VLT improves the resolution at 750nm within 1 arcmin FOV.

Today, the new big challenge for AO comes from the Extremely Large Telescopes, such as the Extremely Large Telescope (ELT)(VERNIN, MUÑOZ-TUÑÓN, SARAZIN et al. 2011), the Thirty Meter Telescope (TMT)(ELLERBROEK, BRITTON, DEKANY et al. 2005), and the Giant Magellan Telescope (GMT)(JOHNS, MCCARTHY, RAYBOULD et al. 2012). All these giants will be equipped and will use AO since the first light. One of the main challenges for running AO on an ELT comes from the Laser Guide Stars, and the

so-called LGS spot elongation, which becomes critical at ELT scales. This PhD thesis deals with this effect and proposes technological solutions to cope with this limitation.

In the next sections, I will introduce the basics about the atmospheric turbulence in Section 1.2 and its impact on the image formation in Section 1.3. Then I will introduce the Adaptive Optics in Section 1.4 and the main sources of limitations in Section 1.5.

1.2. Atmospheric Turbulence

Atmospheric turbulence is an irregular random medium, which is caused by solar heating and wind shear. It often occurs in the surface layer, the body of convective clouds, and in the region of the troposphere. As a result, this irregular movement makes that the atmospheric refractive index profile is not uniform. As the refractive index of the turbulent medium is similar to the surrounding medium, the light does not change its direction of propagation when it passes through the atmospheric turbulence. However, the small differences of refractive index cause a different optical path for the light, therefore after going out of the turbulent medium, the wavefront of a plane wave will no longer be flat, but a random surface, resulting in the jitter, drift, flicker of light intensity, beam expansion etc. of the light. This is the origin of the negative effects on the imaging quality.

1.2.1. The Reynold number

The present theoretical basis for atmospheric turbulence was developed by Kolmogorov, following the local structure turbulence theory of $Reynolds\ number$. The convection currents caused by the solar heating of the earth's surface can be divided into either regular and uniform laminar or turbulent with random subflows. In 1883, Reynold introduced a dimensionless parameter which gives a converting condition between laminar and turbulence. It is defined as the ratio of the kinetic energy to dissipate energy in turbulence, which can be expressed as (KOLMOGOROV 1962) :

$$Re \equiv \frac{kinetic\ \ energy}{dissipated\ \ energy} = \frac{u^3/l}{\nu u^2/l^2} = \frac{ul}{\nu} \tag{1.1}$$

Where u is the characteristic velocity, and l is a characteristic size that is often called *length scale*, and ν is the viscosity coefficient of the fluid motion. When there is a disturbance in the fluid, it acquires a kinetic energy driven by inertial forces, meanwhile this energy is dissipated by viscous forces. Hence, the Reynold number can also be expressed by the ratio of the inertial force to viscous force.

When given the geometry of the fluid, its characteristic size is constant, the viscosity coefficient depends on the properties of the fluid and changes with temperature. For simplifying, the theory assumes that it is also a constant for a given fluid, therefore the Reynold number is proportional to the characteristic velocity u. This means that when the Reynold number is smaller than a critical Re_c, the fluid has a smooth and

clear streamline known as laminar. While the Reynold number is larger than Re_c, the fluid makes irregular and random movements, which is called turbulent. The value of Re_c is set by the geometry of the flow.

1.2.2. statistical descriptions

Ideally, one would like to assume that the physical processes are stationary (i.e., the second-order statistics is not a function of absolute time) so that the analysis can be simplified. However, for many interesting systems, like the atmospheric turbulence including wind speed, temperature, humidity, and pressure is nonstationary and inhomogeneous. The ensemble average of these parameters is not equal to their time average, so we cannot use the time average measurement to approximate the ensemble average. Instead, one should use the statistical descriptions of *structure functions*. For example, the spatial structure functions take the difference between the values of the process at two different location as its variable. That is :

$$D_x(\mathbf{r_1}, \mathbf{r_2}) = \langle [x(\mathbf{r_2}) - x(\mathbf{r_1})]^2 \rangle \tag{1.2}$$

Where $\langle \cdot \rangle$ denotes an average, $\mathbf{r_1}$ and $\mathbf{r_2}$ are two points in space. In practice, the atmospheric parameters change rather smoothly, therefore, although the time average is not able to represent the ensemble average, the ensemble average of the difference can be approximated by the time average of difference.

Furthermore, the atmospheric turbulence is often seen as isotropic, this indicates that the spatial statistics are independent of the orientation. As a result, the structure functions only depend on the scalar of the spatial parameters, $\rho = |\boldsymbol{\rho}| = |\mathbf{r_2} - \mathbf{r_1}|$. Therefore, the equation above can be converted to (KOLMOGOROV 1991) :

$$\begin{aligned} D_x(\rho) &= \left\langle [x(r+\rho) - x(\rho)]^2 \right\rangle \\ &= \left\langle x(r+\rho)x(r+\rho) \right\rangle + \left\langle x(\rho)x(\rho) \right\rangle - 2\left\langle x(\rho)x(r+\rho) \right\rangle \\ &= 2[R_x(0) - R_x(\rho)] \end{aligned} \tag{1.3}$$

Where r is the location of any point, and $R_x(r) = \left\langle x(\rho)x(r+\rho) \right\rangle$ is the correlation function. Equation (1.3) is the mathematical relationship between the correlation function and the structure function.

On the other hand, based on Fourier theory, the spatial statistics description of a generalized stationary random variable can also be expressed as the power spectrum, which can be derived from the correlation function by three-dimensional Fourier transform.

$$\Phi_x(\boldsymbol{\kappa}) = \int_{-\infty}^{\infty} R_x(\boldsymbol{\rho}) exp(2\pi i \boldsymbol{\kappa} \cdot \boldsymbol{\rho})\, d\boldsymbol{\rho} \tag{1.4}$$

where $\boldsymbol{\kappa}$ is the spectrum scale of spatial frequency vector $[m^{-1}]$.

1.2.3. Kolmogorov turbulence model

In 1941, Kolmogorov developed the theory of locally homogeneous isotropic turbulence which is the basis of modern turbulence theory. In this theory, he mainly made three hypotheses : 1. Although the fluid is non-isotropic on the whole, in a given small region, it can be approximated to be isotropic. 2. In the locally homogeneous isotropic region, the fluid movement is set by inertial forces and viscous force. 3. When Re is large, there is a region called the inertial range of length scales in which the inertial forces can be neglected, and the fluid movement is set by viscous forces.

Under these assumptions, Kolmogorov divided a fully developed turbulence into turbulent eddies of different length scales, whose range is $l_0 \leq l \leq L_0$, l_0 is the inner scale used to represent the smallest eddies, and L_0 is the outer scale aimed at the largest eddies. For atmosphere turbulence, the inner scale l_0 is generally millimeter level and the outer scale is dozens of meters. The kinetic energy is transferred between these eddies of different length scales, in the case of large Reynold number, when the disturbance starts to take place, the large eddies split into several small eddies and distribute the energy to them, as the scale length of eddies becomes smaller, so does the Reynold number. As a result, the breaking continues until the Reynold number drops to a certain critical value, which indicates the viscosity of the fluid can prevent the eddies from further splitting into smaller. This process is called the energy cascade. Finally, the kinetic energy is dissipated around due to the viscosity.

Following this analysis, in one dimension, Kolmogorov derived that within the inertial range, the structure function $D_x(\rho)$ should only be decided by the rate of energy transfer per unit mass ϵ, that is the famous 2/3 power law, considering the fluctuation of atmospheric temperature $t = T - \langle T \rangle$, the structure function can be expressed as :

$$D_T(\rho) = C_T^2 \rho^{2/3} \tag{1.5}$$

Where C_T^2 is the temperature structure constant. The statistics of random temperature can also be described by the power spectrum, Tatarski demonstrated the three-dimensional spectrum as (TATARSKI 2016) :

$$\Phi_T(\boldsymbol{\kappa}) = 0.033 C_T^2 k^{-11/3} \tag{1.6}$$

Here k is in the range of $1/L_0 \leq k \leq 1/l_0$ in the spatial domain. As the one-dimensional spectrum is the integral of the three-dimensional spectrum in all directions, the relationship between them is :

$$\Phi_T(k) = 4\pi k^2 \Phi_T(\boldsymbol{\kappa}). \tag{1.7}$$

Therefore, from equation (1.6), the one-dimensional spectrum is :

$$\Phi_T(k) = 0.414 C_T^2 k^{-5/3} \tag{1.8}$$

As the structure constant of refractive index is proportional to that of temperature,

they are related by :

$$C_N(\rho) = 7.5x10^{-7}\frac{P}{T^2}C_T^2 \tag{1.9}$$

Where P is the air pressure expressed in Pascal, and T is the temperature expressed in Kelvins. For the structure function of refractive index, it also follows a 2/3 power law :

$$D_N(\rho) = C_N^2\rho^{2/3} \tag{1.10}$$

Fluctuation of refractive index in atmospheric turbulence is the main reason of the limitations in astronomical imaging, and C_N^2 is an essential parameter in atmospheric optics : its characterization directly affects the design of adaptive optics. C_N^2 is a function of altitude h, the $C_N^2(h)$ profile was originally measured by the scintillation detection of a star to acquire the value with respect to altitude. After that, researchers approximated C_T^2 by measuring the scattering cross section of sound waves and converted it to C_N^2. The phase disturbance caused by refractive index fluctuations in the telescope pupil can be (TATARSKII 1971) :

$$\varphi(\boldsymbol{r}) = k\int_0^\infty n(\boldsymbol{r},h)\,dh \tag{1.11}$$

Here $k = 2\pi/\lambda$ is the wavenumber. By substituting it into equation (1.3), we can obtain the phase correlation function $R_\varphi(\boldsymbol{r})$ and then obtain the phase structure function $D_\varphi(\boldsymbol{r})$expressed by the refractive index structure constant.

$$D_\varphi(r) = 2.91k^2r^{5/3}\int_0^{L_0} C_N^2(h)\,dh \tag{1.12}$$

The parameter r_0 is so-called Fried parameter or atmospheric coherence length defined as :

$$r_0 = \left[0.423k^2(sec\xi)\int_0^{L_0} C_N^2(h)\,dh\right]^{-3/5} \tag{1.13}$$

Where ξ is the angle between the integral path and the zenith direction. The Fried parameter is used to account for the strength of the integrated turbulence on a line of sight. It is given in meters and can be interpreted as an equivalent telescope diameter that would have the same resolution as a telescope of infinite diameter observing through the turbulence.

Finally, the equation (1.12) can be converted to (FRIED 1966a) :

$$D_\varphi(r) = 6.88(\rho/r_0)^{5/3} \tag{1.14}$$

Which provides a simple formulae to compute the phase structure function.

1.3. Optical Effects of atmosphere

The above section introduces the properties of phase fluctuations caused by the refractive index in atmospheric turbulence, and the central Fried parameter r_0. In this section, I discuss the optical effects of the atmosphere, which include the imaging process and the representation of turbulence.

1.3.1. Optical imaging through atmosphere

According to the physical optics, the propagation of light waves in the medium can be described by Helmholz equation :

$$\nabla^2 U + k^2 U = 0 \tag{1.15}$$

Where U is light wave, and k is the wave number. Considering a three-dimensional space in which the light is assumed to propagate along the z direction, and taking $n = n(z)$ as the refractive index in the vertical distance, the light wave can be expressed as :

$$U(x,y,z) = \varphi(x,y,z) exp(-ikz) \tag{1.16}$$

Substituting in equation (1.15), in the near-field condition (Fresnel approximation), we can obtain (FLECK, MORRIS et FEIT 1976) :

$$\frac{\partial^2 \varphi}{\partial^2 x} + \frac{\partial^2 \varphi}{\partial^2 y} - 2ik\frac{\partial \varphi}{\partial z} + 2k^2 \Delta n \varphi = 0 \tag{1.17}$$

Where Δn is the fluctuation of the refractive index. There is no analytical solution to the equation, it is usually computed numerically by Fourier transform which divides the light path into several small segments Δz_n. In each of these small segments, the solution of the light can be obtained from (FEIT et FLECK 1988) :

$$\Phi_n = F\left\{F^{-1}\left[\Phi_{n-1} exp(i\frac{k_x^2 + k_y^2}{4k}\Delta z_n)\right] exp(-ik\Delta n \Delta z_n)\right\} exp(i\frac{k_x^2 + k_y^2}{4k}\Delta z_n) \tag{1.18}$$

Here Φ is the spectrum amplitude corresponding to the light wave amplitude, F and F^{-1} are the Fourier transform and inverse Fourier transform, respectively. In this formula, the first and third parts represent the propagation of the light wave in free space, while the middle part represents the phase disturbance caused by the refractive index fluctuation in the distance of Δz_n. Therefore, the propagation of wave light in the turbulence medium can be considered from two sides, the first is to develop the turbulence into a series of phase screens whose thickness is Δz_n, the propagation in the phase screen is only introducing a certain phase change along the direction of propagation, without changes in the horizontal direction. The second is that when the light is propagated in the phase screen, the effect of turbulence can be neglected, this

is equivalent to the propagation in free space without turbulence.

When the perfect light wave without being affected by atmospheric turbulence is imaged by a telescope system, based on the Fraunhofer diffraction theory, the point spread function (PSF) of the image is diffraction-limited, which can be expressed as :

$$p_0(\boldsymbol{\alpha}) = \frac{\pi D^2}{4\lambda^2}[\frac{2J_1 kD|\boldsymbol{\alpha}|}{kD|\boldsymbol{\alpha}|}]^2 \tag{1.19}$$

Where D is the diameter of telescope, J_1 is the first order Bessel functions, $\boldsymbol{\alpha}$ is the angular coordinates, the full width half maximum is λ/D, which is the angular resolution of an ideal telescope.

Due to the diffraction effect, the image of an astronomical object $o(\boldsymbol{\alpha})$ produced by a telescope is the convolution between $o(\boldsymbol{\alpha})$ and the Airy function :

$$i(\boldsymbol{\alpha}) = \int o(\boldsymbol{\tau})\, p_0(\boldsymbol{\alpha}-\boldsymbol{\tau})\, d\boldsymbol{\tau} \tag{1.20}$$

Here $\boldsymbol{\tau}$ is expressed in angle within the telescope pupil. Equation (1.20) is the so-called imaging equation. When there is no atmospheric turbulence, the telescope system reaches the diffraction limit, the resolution is the highest. In the presence of turbulence, the image of a point source is no longer the ideal Airy disk and the resolution decreases rapidly. The PSF is often used to characterize the quality of the image, we can evaluate the PSF by *Full width at half maximum* (FWHM), as it gets smaller, the resolution of the image becomes higher. At the diffraction limit, the FWHM of the PSF is given by :

$$\text{FWHM}_{dif} = 1.03\frac{\lambda}{D} \tag{1.21}$$

In the presence of turbulence, FWHM of the long-exposure PSF is expressed as :

$$\text{FWHM} = 0.9759\frac{\lambda}{r_0} \tag{1.22}$$

This is the reason that why for a large aperture telescope, i.e., when D is larger than r_0, the resolution is no longer set by the telescope size, but by the atmospheric turbulence.

Making the Fourier transform of equation (1.20), one get the image formation in the spatial frequency domain :

$$I(\boldsymbol{f}) = O(\boldsymbol{f})P(\boldsymbol{f}) \tag{1.23}$$

Here the $\boldsymbol{f}$ is two-dimensional spatial frequency vector in telescope pupil. $P(\boldsymbol{f})$ is the optical transfer function (OTF), which is the Fourier transform of the PSF. The module of the OTF is the modulation transfer function (MTF), when $|\boldsymbol{f}| \geq f_c$ (f_c is the cut-off frequency, and $f_c = D/\lambda$), $|P(\boldsymbol{f})| = 0$, which means with a larger aperture of telescope, the cut-off frequency is larger, and more details of the objects can be acquired. On the

contrary, for imaging through turbulence, the high-frequency information is totally lost.

Since the imaging resolution is decided by atmospheric turbulence r_0 in the case of long-exposures, the OTF should be expressed as the product of atmosphere OTF and telescope OTF (FRIED 1966b) :

$$P_{LE}(\boldsymbol{f}) = P_{tur}(\boldsymbol{f})P_{tel}(\boldsymbol{f}) \tag{1.24}$$

The OTF of the atmospheric turbulence is linked to the statistics of phase fluctuations, that is the phase structure function :

$$P_{LE}(\boldsymbol{f}) = exp[-\frac{1}{2}D_{\varphi}(\lambda \boldsymbol{f})] \tag{1.25}$$

The long-exposure PSF can be acquired by making an inverse Fourier transform of $P_{LE}(\boldsymbol{f})$, and we can also obtain the relationship between FWHM β of the atmosphere PSF and the Fried parameter r_0 :

$$\beta = 0.98\lambda / r_0 \tag{1.26}$$

Where λ is the observing wavelength. The seeing gives the theoretical angular resolution that can be expected when observing through turbulence. The order of magnitude of the seeing is around the arc second in the visible, which implies that we will not be able to discern details smaller than this value.

1.3.2. Modal Representation of Turbulence

Any complex wavefront disturbed by the atmosphere can be represented by a set of orthogonal modes of increasing spatial frequency on a unit circle (NOLL 1976,WANG et SILVA 1980,CUBALCHINI 1979). The most used ones are two-dimensional functions called Zernike polynomials. The low orders of Zernike polynomials correspond to the primary aberrations such as tilt, defocus, astigmatism, etc.. For a wavefront shape in an optical system, $\varphi(\boldsymbol{r})$, its modal representation in Zernike space can be expressed as :

$$\varphi(\boldsymbol{r}) \approx \sum_{k=1}^{M} a_k Z_k(\boldsymbol{r}) \tag{1.27}$$

Here $Z_k(\boldsymbol{r})$ are the Zernike polynomials at kth order, and a_k is the corresponding Zernike coefficient. Fried was the first to use Zernike polynomials to describe the statistical intensity of atmospheric turbulence, then Noll updated for a more suitable description of turbulence. The Zernike polynomial at kth order can be expressed as functions of both azimuthal and radial frequency on a unit circle in polar coordinates :

$$Z_k(\boldsymbol{r}) = \begin{cases} \sqrt{n+1}R_n^m(r)\sqrt{2}cos(m\theta), & \text{if } m \neq 0 \text{ and } k \text{ is even,} \\ \sqrt{n+1}R_n^m(r)\sqrt{2}sin(m\theta), & \text{if } m \neq 0 \text{ and } k \text{ is odd,} \\ \sqrt{n+1}R_n^0(r), & \text{if } m = 0. \end{cases} \tag{1.28}$$

Where n and m are radial order and azimuthal frequency respectively, and (r,θ) are the position vector $\boldsymbol{r}$ in the polar coordinates. Function $R_n^m(r)$ is defined by :

$$R_n^m(r) = \sum_{s=0}^{(n-m)/2} \frac{(-1)^s(n-s)!}{s![(n+m)/2-s]![(n-m)/2-s]!} r^{n-2s} \tag{1.29}$$

in which n and m have the relationship as : $n-|m|$ = odd number.

If we use Zernike polynomials in terms of the first N terms to describe the turbulence, the root mean square(RMS) of its residuals can be expressed as :

$$\Delta_N = \sqrt{\langle \varphi^2(r) \rangle - \sum_{i=1}^{N} \langle |z_i|^2 \rangle} \tag{1.30}$$

When $N > 10$, the RMS of residuals is approximated as :

$$\Delta_N = \sqrt{0.2944 N^{-\sqrt{3}/2} (D/r_0)^{5/3}} \tag{1.31}$$

Where the unit is radian. According to the computation between the normalized wavefront residuals and the number of Zernike modes, the first 10 modes account for about 95% of the atmospheric turbulence. And from equation (1.6), the phase disturbance caused by low frequency in atmospheric turbulence has a larger power spectrum, therefore correcting the low order of Zernike modes can provide the maximum improving of imaging quality.

The Karhunen-Loeve (K-L) modes are also used to replace Zernike modes in some cases. The K-L modes are expressed with respect to the Zernike modes by diagonalization of the Zernike covariance matrix. K-L modes are mainly used when a large number of modes are required (WANG et MARKEY 1978). For low-order correction Zernike polynomials are almost optimum.

1.4. Adaptive Optics System

1.4.1. Wavefront Sensors

The Wave-Front Sensing device is the heart of every AO system. Its goal is to measure the incoming phase perturbations and send this information to the deformable mirror that will correct for it. Ultimately, the Wave-Front Sensor performance drives the final performance of the AO correction and thus the associated astrophysical instrumentation.

The first goal of a wavefront sensor is to convert the wavefront into an intensity that can be detected and measured. Depending on the WFS technology, this intensity can be directly related to the wavefront, or to the wavefront slope (first derivative) or to the second order (second derivative). Because the atmospheric turbulence has a very fast temporal evolution, a WFS has to perform the measurement every millisecond or so, leading to strong constraints in terms of light detection and signal processing. In addition, because the incoming signal can span a wide spatial range, the WFS should accommodate for a large dynamical range. Below are two of the commonly used sensors in adaptive optics.

1.4.1.1. Shack-Hartmann wavefront sensor

Shack-Hartmann wavefront (S-H) sensor is the first sensor used for wavefront detection (NEAL, DANIEL, COPLAND et al. 2002,PRIMOT 2003). As such, it benefits from a mature theory and application. The principle of a S-H wavefront sensor is to divide the wavefront into an array of small wavefront segments by means of microlenses, and to focus each wavefront segment on the focal plane to form an array of spots. The wavefront slope is then obtained by measuring the movements of each spot. To increase the spatial sampling, one needs to increase the number of lenses. However, more subapertures means dividing the flux into more pieces and consequently the need for brighter reference stars and more detector pixels.

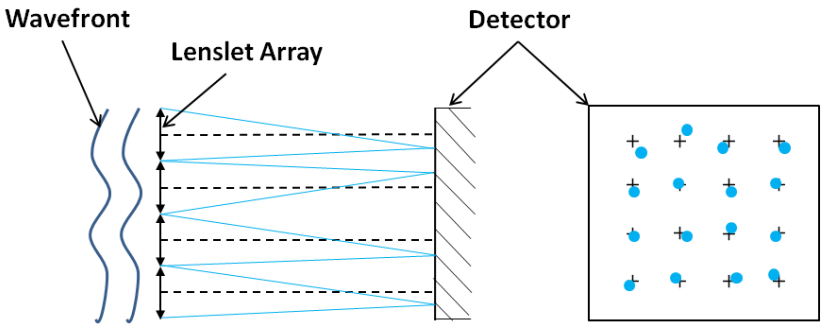

FIGURE 1.1. – Schematic plot of a Shack-Hartmann wavefront sensor (Courtesy : T.Fusco).

From Fig. 1.1, the microlens array is constructed by several small convex lens of the same focal length and aperture. The focal plane of the sensor is conjugated to the plane of the microlens array. When the light passes through the microlens array, it will be segmented into many subapertures, which focal plane images are formed onto the sensor as an array of spots. For an ideal wavefront plane (flat wavefront), the focused spots are located on the optical axis of each lenslet. When the wavefront is distorted by aberrations induced by the atmosphere, the centroid of the spot will be

displaced away from the center. One can therefore compute the wavefront by these spot motions. The displaced centroids (x_c, y_c) are expressed as :

$$\begin{cases} x_c = f_{wfs} s_x = \dfrac{f_{wfs}\lambda}{2\pi A} \iint_A \dfrac{\partial \varphi(\boldsymbol{r})}{\partial x} dxdy + w_x \\ y_c = f_{wfs} s_y = \dfrac{f_{wfs}\lambda}{2\pi A} \iint_A \dfrac{\partial \varphi(\boldsymbol{r})}{\partial y} dxdy + w_y \end{cases} \tag{1.32}$$

Where s_x and s_y (in radians) are the averaged slopes in x and y directions, f_{wfs} is the focal length of the microlens array, A is the subaperture's area, $\frac{\partial \varphi(\boldsymbol{r})}{\partial x}$ and $\frac{\partial \varphi(\boldsymbol{r})}{\partial y}$ denote the angles of arrival, and w_x and w_y are the noise associated to the S-H measurement.

In an actual system, since the detector is not continuous but made of pixels, the integral can be modified to a sum, and the equation is converted to :

$$x_c = \frac{\sum_{i,j} x_{i,j} I_{i,j}}{\sum_{i,j} I_{i,j}}, \; y_c = \frac{\sum_{i,j} y_{i,j} I_{i,j}}{\sum_{i,j} I_{i,j}} \tag{1.33}$$

Here $(x_{i,j}, y_{i,j})$ are the coordinates of the pixel (i, j), and $I_{i,j}$ is the photon flux corresponding to the same pixels. From equation (1.32), the microlens array which has large focal length results in the spot having larger displacements, hence a WFS with a larger sensitivity. However, this comes at the price of linearity, as the Field-of-View per subaperture is not infinite, and usually set by the total number of pixels available to the detector. Hence, for a given and fixed number of pixels and subapertures, the higher sensitivity, the smaller the FoV per subaperture, and the smaller the linearity range. This trade-off is at the heart of the design choices for the LGSWFS of the ELT.

1.4.1.2. Pyramid wavefront sensor

The pyramid wavefront was first proposed in 1996 by Ragazzoni et al (R. RAGAZZONI 1996,R. RAGAZZONI et FARINATO 1999,VÉRINAUD, LOUARN, KORKIAKOSKI et al. 2005). The idea is to divide the light at a focal plane into four beams by focusing it on the vertices of a pyramid, and then to reimage the four corresponding pupils. By computing the intensity differences between these four pupil images, one can get the relationship between the signal and the wavefront. The main advantage of the pyramid sensor comes from its increased sensitivity compared to the S-H. By forming 4 pupil images, a pyramid sensor also requires fewer pixels than a S-H sensor, for a similar number of measured spatial frequencies. However, this gain comes at the cost of a strong nonlinearity, and experimentally, the pyramid sensor requires an extra modulation stage to make it work. This modulation is usually introduced by a Tip-Tilt mirror located in the pupil plane before the pyramid prism.

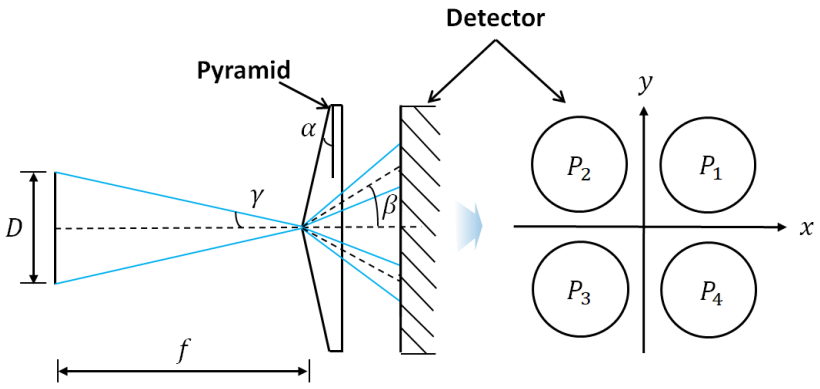

FIGURE 1.2. – Schematic plot of a pyramid wavefront sensor.

The relationship between the wavefront and the intensity of the four images in x and y direction can be expressed as :

$$\begin{cases} \dfrac{\partial\varphi(\boldsymbol{r})}{\partial x} = u_0 \cdot \dfrac{I(P_1)+I(P_4)-I(P_2)-I(P_3)}{I(P_1)+I(P_2)+I(P_3)+I(P_4)} \\ \dfrac{\partial\varphi(\boldsymbol{r})}{\partial y} = u_0 \cdot \dfrac{I(P_1)+I(P_2)-I(P_3)-I(P_4)}{I(P_1)+I(P_2)+I(P_3)+I(P_4)} \end{cases} \tag{1.34}$$

Here u_0 is the largest modulation range. The key of using the pyramid wavefront sensor is to design a certain focal length of the optical system, to avoid overlapping the four images, it has the requirement :

$$F/\sharp > \frac{\sqrt{2}}{2(n-1)\cdot\alpha} \tag{1.35}$$

Where $F/\sharp = f/D$ is the F number of the optical system, and α is the ground angle of the pyramid. And When the pyramid wavefront is working, the modulation can be increased to enlarge the linearity range.

1.4.2. Wavefront Correctors

The wavefront corrector (or Deformable Mirror - DM) is the other important component in an AO system. The corrector is driven by the commands computed from the wavefront sensor and it can actively compensate the wavefront aberrations caused by atmospheric turbulence (MADEC 2012).

There are many kinds of different technologies of DM, which can be made of several segmented mirrors or a whole thin piece of reflective surface. Usually, the actuators are made of piezoelectric or electro-magnetic materials that would move under a given signal. Standard DMs are usually made of three main components. The first is the basement which is made by materials of high stiffness, its function is to support the DM's structure and to be used as a fixed substrate. The second is the actuator, fixed on the basement and linked to the mirror. The third is the thin mirror whose production

materials are optical, glass, silicon, and metal. The actuators convert the voltage to a displacement in the vertical direction and push or pull the mirror . By applying different voltages to different actuator, one can produce complex deformations.

The important parameters for a DM are the stroke (total mechanical motion), linearity and/or hysteresis (are the actuators moving in a reproducible and linear way), the number of actuators (providing the number of degrees of freedom), resolution (minimum size of a step), the time response (how fast an actuator reaches its destination), and the influence function, which is the optical deformation produced for a given signal.

Based on the principle of linear superposition, the correction of a DM can be expressed as the sum of the influence functions for each actuator at different voltages. The typical influence function can be denoted by super-gaussian function as :

$$f_i(x,y) = exp[ln\omega(\sqrt{(x-x_i)^2+(y-y_i)^2}/d)^{\alpha}] \tag{1.36}$$

Where $f_i(x,y)$ is the position of the ith actuator, d is the spacing between adjacent actuators, α is the the gaussian index, ω is the coupling value of actuators, which is the ratio of the deformation δ_2 of the adjacent actuator to the deformation δ_1 of influence function of only one single actuator loaded voltage, $\omega = \delta_2/\delta_1$, is about 5% - 20%. With a larger coupling value, the changing of the surface is more gentle, therefore the coupling value has an important impact on the capacity of wavefront correction of DM.

Finally, and to distribute the stroke budget, AO systems usually decouple the correction between a fast steering Mirror (or tilt mirror), and a DM doing the high order correction.

1.4.3. Wavefront Reconstruction

The objective of the wavefront reconstruction is to restore the overall phase from the measured local slopes.(HARDY 1998)

The reconstruction methods are commonly divided into zonal and modal estimation, the former one consisting in sampling the wavefront by a 2D array of points, while the second use a modal decomposition of the phase (SEIFERT, TIZIANI et OSTEN 2005).

As discussed above, the wavefront can be expressed as a set of basis functions of orthogonal polynomials shown as equation (1.27), the wavefront gradients or slopes measured in x and y directions are :

$$\begin{cases} g^x(x,y) = \dfrac{\partial}{\partial x}\varphi(x,y) \\ g^y(x,y) = \dfrac{\partial}{\partial y}\varphi(x,y) \end{cases} \tag{1.37}$$

In a S-H wavefront sensor, the slope measurements are done over discrete areas, which represent a finite set of slope samples, the slopes at ith actuator (x_i, y_i) can

then be expressed as :

$$\begin{cases} g_i^x = \dfrac{\partial}{\partial x}\varphi_i(x,y) = \displaystyle\sum_{k=1}^{M} a_k \frac{\partial}{\partial x} Z_{ki}(x,y) \\ g_i^y = \dfrac{\partial}{\partial y}\varphi_i(x,y) = \displaystyle\sum_{k=1}^{M} a_k \frac{\partial}{\partial y} Z_{ki}(x,y) \end{cases} \tag{1.38}$$

This equation denotes the relationship between the measured slope g_i and the modal coefficients or command coefficients a_k, it can be written in the form of matrix :

$$\boldsymbol{g} = D\boldsymbol{a} \tag{1.39}$$

Where $\boldsymbol{g}$ is the slopes vector, $\boldsymbol{a}$ is the coefficients vector, and D is the matrix which contains the derivatives of Zernike modes, known as interaction matrix. In the real situation, the objective is to acquire the command coefficient from the slopes measured by the wavefront sensor, therefore this equation is converted to :

$$\begin{aligned} \hat{\boldsymbol{a}} &= B\boldsymbol{g} \\ \text{where} \quad B &= (D^T D)^{-1} D^T \end{aligned} \tag{1.40}$$

Were B is the command matrix which translates the measurements into phases.

Usually, in an AO system, the interaction matrix is calibrated by using an artificial source in a focal plan at the instrument input. By playing the modes or simply by applying push-pull to each of the DM actuators (zonal interaction matrix), we acquire the matrix D. This matrix is then inverted to get the control matrix B. As the interaction matrix may not be easily inverted, one can use a Single Value Decomposition (SVD) to identify the badly seen modes of the system and filter them during the inversion. This allows to avoid noise propagation into the system.

1.4.4. Performance evaluation

There are several indicators to evaluate the performance of an adaptive optics system in a particular direction $\boldsymbol{\alpha}$ of the field of view (Fov), the commonly used indicators are Strehl ratio and residual wavefront error.

(1). The *Wavefront error* (WFE), it's the rms value of the residual phase $\varphi_{res}(\boldsymbol{r},\boldsymbol{\alpha})$ which is acquired after correction in adaptive optics in the direction $\boldsymbol{\alpha}$. The definition can be expressed as :

$$WFE(\boldsymbol{\alpha}) = \sqrt{\langle \frac{1}{A} \iint_A [\varphi_{res}(\boldsymbol{r},\boldsymbol{\alpha})]^2 d\boldsymbol{r} \rangle} \tag{1.41}$$

Where A denotes the telescope pupil area, and $\langle\cdot\rangle$ is the spatial average. The objective of an adaptive optics system is to minimize this residual wavefront error.

(2) The *Strehl ratio* (SR), is defined as the ratio of center intensity of detected image PSF to that of an Airy disk in diffraction-limited images. The SR in the direction $\boldsymbol{\alpha}$ is defined as :

$$SR(\boldsymbol{\alpha}) = \frac{PSF_{\boldsymbol{\alpha}}(0)}{PSF_{Airy}(0)} \tag{1.42}$$

It is sometimes more convenient to compute the SR in the Fourier domain, where it can be expressed by :

$$SR(\boldsymbol{\alpha}) = \frac{\int OTF_{\boldsymbol{\alpha}}(\boldsymbol{f})d\boldsymbol{f}}{\int T_{diff}(\boldsymbol{f})d\boldsymbol{f}} \tag{1.43}$$

Where $OTF_{\boldsymbol{\alpha}}$ stands for the long-exposure OTF in the direction $\boldsymbol{\alpha}$, T_{diff} is the OTF of diffraction-limited image, and $\boldsymbol{f}$ is the spatial frequency vector. Since the diffraction limit is the best quality image that the optical system can obtain, we have $SR \leq 1$. In most cases : $0 \leq SR \leq 1$, and the larger SR, the better the angular resolution of the resulted images.

Finally, when $SR > 20\%$, there is a relationship between the SR and the WFE, according to the Marechal approximation (Ross et Sean 2009) :

$$S_R(\boldsymbol{\alpha}) \approx exp\left\{-[WFE(\boldsymbol{\alpha})]^2\right\} \tag{1.44}$$

Here we can see that maximizing the SR is equivalent to minimizing the WFE.

1.5. Error Sources in Adaptive Optics

1.5.1. Wavefront Sensor Errors

As this thesis focuses on Shack-Hartmann WFS, we restrict the noise analysis to SH-WFS.

The main source of error for a SHWFS comes from the measurement noise when determining the centroids of each of the subaperture spots. These errors are summarized in the table below (Chernyshov, Sterr, Riehle et al. 2005) :

Tableau 1.1. – The errors of center of gravity and their distributions

Classes of errors	Distributions
Signal photon noise	Poisson, $\sigma_p^2 = N_{ph}$
Background photon noise	Poisson, $\sigma_b^2 = N_b$
Readout noise	Gaussian(CCD) or Skew-gaussian(CMOS), σ_r^2
Dark current	Random, minimised by cooling the detector, σ_d^2
Sampling error of spot	Related to the size of the spot and pixel format, σ_{sp}^2

Where N_{ph} and N_b are the number of signal photons and of the background photons acquired by detector.

Photon shot noise in the signal and background is a fundamental property of the quantum nature of light and represents the ultimate limit for a SH-WFS. The Read-Out noise is caused by the charge reading device within the detector and depends on the detector technology. Noise of dark current is produced by thermal electrons in the detector substrate and depends on the detector technology. Finally, the sampling error depends on the optical design of the microlenses and the trade-off between sensitivity and linearity.

These errors have a negative impact on the centroid measurements, which will then propagate into spurious phase reconstruction through the reconstructor. Indeed, the slope vector can then be written as :

$$\boldsymbol{g} = D\boldsymbol{a} + \boldsymbol{n} \tag{1.45}$$

where $\boldsymbol{n}$ is a vector of noise, of the same dimensions as $\boldsymbol{a}$ and it combines all the contributors described above. Then the phase reconstruction provides :

$$\hat{\boldsymbol{a}} = B\boldsymbol{g} + \boldsymbol{n} \tag{1.46}$$

$$\hat{\boldsymbol{a}} = (D^T D)^{-1} D^T \boldsymbol{g} + (D^T D)^{-1} D^T \boldsymbol{n} \tag{1.47}$$

These errors will be analyzed in further details in chapter 3.

1.5.2. Wavefront Fitting Errors

For the wavefront distorted by atmospheric turbulence, the perfect compensation should be made in the full range of spatial frequencies, especially including the extreme high frequencies. However, in real operation, this part of the frequencies are very difficult to be compensated, meanwhile the compensation of them produces a lot of computation and does not improve the system performance very much. Therefore, the fitting error is to characterize how well the wavefront correcting elements can compensate the wavefront caused by atmospheric turbulence. If the wavefront of turbulence is $\varphi_w(\boldsymbol{r})$ and the wavefront of compensation is $\varphi_c(\boldsymbol{r})$, the mean-square fitting error can be expressed as :

$$\sigma^2_{fitting} = \langle [\varphi_w(\boldsymbol{r}) - \varphi_c(\boldsymbol{r})]^2 \rangle \tag{1.48}$$

Where $\boldsymbol{r}$ is the position vector and $\langle \cdot \rangle$ denotes average. This equation can be converted as below when a Kolmogorov spectrum is used to describe a wavefront.

$$\sigma^2_{fitting} = \alpha \left(\frac{d}{r_0} \right)^{\frac{5}{3}} \tag{1.49}$$

Here α is a constant scaling factor which depends on the type of corrector. Since r_0 varies as $\lambda^{6/5}$, the fitting error will decrease with wavelength, which means that the adaptive optics can obtain a better correcting performance at longer wavelength, and

it can also be equipped with less actuators in this case.

1.5.3. Temporal Errors

Wavefront aberrations caused by atmospheric turbulence are changing on temporal scales of the order of a few milliseconds. If the compensation by the adaptive optics system is slower than the turbulence, it produces a temporal error. The temporal error can be defined as the mean-square difference of wavefront aberrations between two moments :

$$\sigma^2_{temporal} = \langle [\varphi_w(\boldsymbol{r}, t) - \varphi_c(\boldsymbol{r}, t + \Delta t)]^2 \rangle \tag{1.50}$$

Where Δt is the delay time. In fact, researchers often utilize $Greenwood\ frequency$ to characterize the temporal error which is related to the structure constant of the refractive index and the wind speed profiles of the atmosphere shown as (GREENWOOD 1977) :

$$f_G = \left[0.102 k^2 sec\xi \int_0^\infty C_N^2(h) v^{5/3}\, dh \right]^{3/5} \tag{1.51}$$

Where ξ is the angle between integral path and the zenith direction and v is the wind speed, for a simple case of a single turbulent layer, the wind speed is a constant, therefore, the equation above can be simplified as :

$$f_G = 0.427 \frac{v}{r_0} \tag{1.52}$$

Defining the control bandwidth of an adaptive optics system by the wavefront sensor exposure and correction by the DM, noted f_S, the temporal error can be expressed as :

$$\sigma^2_{temporal} = \left(\frac{f_G}{f_S} \right)^{5/3} \tag{1.53}$$

1.5.4. Anisoplanatic Errors

The structure of the turbulence is defined vertically above the telescope. If the wavefront sensor points to a direction that is different from the science target, then the volume of turbulence seen by the former will be different than the latter. Within a field that would remain smaller than the isoplanatic angle θ_0, the performance remains good, but degrades rapidly beyond this region. The isoplanatic angle θ_0 is defined as the angle increasing the residual error by $1 rd^2$, and it writes as :(FRIED 1982)

$$\theta_0 = \left[2.941 k^2 (\sec\xi)^{8/3} \int C_N^2(h) h^{5/3}\, dh \right]^{-3/5} \tag{1.54}$$

For a single layer of atmospheric turbulence, the equation above can also be simplified with respect to r_0 :

$$\theta_0 = 0.314(\cos\theta)\frac{r_0}{h} \tag{1.55}$$

And the anisoplanatic error for any off-axis angle θ is finally written :

$$\sigma_\theta^2 = \left(\frac{\theta}{\theta_0}\right)^{5/3} \tag{1.56}$$

The anisoplanatic error scales with the wavelength, such as the isoplanatic angle becomes larger at larger wavelengths.

2. Laser Guide Star Wavefront Sensing in the E-ELT era

Sommaire

2.1. Principle of laser guide stars

2.1.1. Introduction

For classical Adaptive Optics, the measurement of atmospheric aberrations can be done either directly on the object of interest if it is bright enough, or on a star nearby.

The measurements provided by the WFS must be performed at a rate faster than the characteristic time of evolution of the turbulence, that is to say, of the order of a millisecond. Moreover, the quality of the wavefront reconstruction - i.e., the real-time calculation of the shape to be applied to the deformable mirror - is mainly degraded by the photon noise. A good wavefront measurement requires about 100 photons detected per WFS exposure and measurement point. A magnitude 0 star sends us about 10^{10}ph/s/m^2, so only the brightest stars (of magnitude ≤ 11) can be used to measure atmospheric aberrations. In the case of distant galaxies, for example, their low surface brightness makes it necessary to use another reference for the ASO.

On the other hand, the isoplantic angle is relatively small and strongly chromatic. For good quality astronomical sites, the isoplantic angle is of the order of 2 to 5 arcseconds for the visible observations, and 10 to 30 arcseconds for the near infra-red.

By combining the limiting magnitude and the isoplantic angle, we can calculate the area of the sky that could be observed at the diffraction limit of large telescopes. This is called sky coverage, and for the classical AO (SCAO), it does not exceed 1% (HARDY 1998). This is a major limitation for the applications of AO system which only relies on NGS.

In order to improve the sky coverage of the AO system, the U.S. military developed the first technology which consisted of launching a laser into the atmosphere and using the backscattered light for the WFS. This was the starfire optical range (FUGATE, FRIED, AMEER et al. 1991) experiment. This technique of artificially generating bright stars is known as Laser Guide Stars (LGS).

In the early days, the LGS was based on the Rayleigh or Raman backsacttering of nitrogen or oxygen in the atmosphere, simply called Rayleigh LGS. The main advantage was that it was easy to manufacture, and the limited power laser could already produce results. However, the obvious disadvantage comes from the nature of this Rayleigh source : since the launched height of Rayleigh LGS is about 10km, the Rayleigh backscatteing wave is very different from the wave that comes from the reference at the top of the atmosphere. This is known as focus anisoplanatism. Moreover, for Rayleigh LGS, the atmospheric density decreases with altitude, the signal quickly becomes too weak in the upper atmosphere. Hence, pushing Rayleigh laser above 10km was difficult, as it would require a high power laser. In fact, focus anisoplanatism (or cone effect, see section 2.3.2) become the dominant term in the error budget and this LGS method has gradually fallen out of use.

The alternative is to use a sodium laser of 589.19 nm to produce resonant fluorescence from the free sodium atoms at an altitude of 90 - 110 km. This is known as the sodium laser guide star. The LGS produced can potentially be created anywhere in the sky, potentially offering a full sky coverage. However, because the laser light passes through the same atmosphere in uplink and downlink propagation, and due to atmospheric refraction, the actual location of the LGS is unknown. This means that the

image jitter (or tip-tilt) cannot be measured with a LGS (see Section 2.3.1). As a result, we still need one auxiliary NGS to detect these tip/tilt modes. However, considering that the NGS only need to measure the tip/tilt modes, their brightness and distance from the center of the FOV can be significantly relaxed. As an example for one of the first LGS astronomical AO systems built at the Keck Telescope, the requirement for the NGS decreases to 19th magnitude, with a distance from the science target objects as large as 60 arcsec. The sky coverage can then reach up to almost 80 % (WIZINOWICH, LE MIGNANT, BOUCHEZ et al. 2006).

In the next section, I will describe the physics at the origin of the Sodium Laser Guide Stars, and then describe the main errors and limitations induced by doing WFSensing with LGSs.

2.1.2. Generation of sodium laser guide stars

The basic principle of forming a sodium laser guide star is to launch a laser beam tuned to the sodium D-lines to excite the sodium atoms located at 90 - 100km above sea level, which leads to resonant scattering. The D-lines consist of a doublet, with the D_1 line centered at wavelength at 589.7 nm and the D_2 line at 589.1 nm (both wavelengths given in vacuum). The absorption cross section of the D_2 line is about twice than that of the D_1 line, which is why it is the preferred excitation line. More precisely, the D_2 line corresponds to the atomic transition from the $3^2S_{1/2}$ ground state to the $3^2P_{3/2}$ excited state (AGEORGES, NANCY, DAINTY et al. 2013).

In the following, we estimate the laser power required to get a given SNR on the WFS detector. For a laser beam tuned at the center of the D_2 line, a fraction of ξ = 2 - 10 % of photons are absorbed by sodium atoms, leading to optical excitation to the $3^2P_{3/2}$ state. When the excited atoms decay to the $3^2S_{1/2}$ ground state, photons are spontaneously emitted. The natural lifetime of the D_2 line is τ_n = 16 ns, which correspond to a linewidth of $1/(2\pi\tau_n) = 10MHz$ (STECK 2003). At a height of 90 km, the time between two adjacent collisions between the sodium atom and air molecule (mostly molecular nitrogen and oxygen) is about 35 μs (HOLZLÖHNER, RONALD, ROCHESTER et al. 2010), much larger than τ_n, which means that during this period sodium atoms are free to undergo many excitation/emission cycles before they decay via collisions or become transparent to the laser light due to Doppler shift. The mean collision time is is longer at higher altitudes as the number density of molecules decreases. Here we assume that the number of photons emitted by each laser pulse is N, and that the scattered photons by sodium atoms is $N\xi$. The scattering is also assumed to be isotropic. The number of photons ΔN eventually detected at ground with a telescope of collection area $\pi(r_0/2)^2$ can be expressed as :

$$\Delta N = N\xi\frac{r_0^2}{4H^2}, \tag{2.1}$$

where H is the mean altitude (typically the centroid) of the sodium layer, and r_0 is the atmospheric coherent length. Assuming that we are limited by photon noise, the SNR (S) can be computed as $S = \sqrt{\eta \Delta N}$, where η is the the overall efficiency factor, including the optical transmission and quantum efficiency of the detector. Then, the number of photons of each laser pulse can be expressed as :

$$N = \frac{4H^2 S^2}{\eta \xi r_0^2}. \tag{2.2}$$

The energy of a photon is $E = h\nu$, where $h = 6.626$ J·s is the Planck's constant and ν is the photon frequency. The energy per laser pulse is :

$$E_t = Nh\nu = \frac{4H^2 S^2 h\nu}{\eta \xi r_0^2}. \tag{2.3}$$

If we consider a case in which we have good seeing conditions, $r_0 = 20$ cm, the altitude of sodium layer $H = 90$ km, the signal to noise ratio $S = 100$, efficiency factor $\eta = 10\%$, with the sodium wavelength $\lambda = c/\nu = 589.1$ nm, the total energy of each laser pulse should then be $E_t = 0.46J$.

The formulas above assume that the scattered light is isotropic. However, due to optical pumping (AUZINSH, BUDKER et S. ROCHESTER 2010) the forward and backward scattering are stronger than other directions, and as a result, the number of photons or laser power required to achieve a certain SNR is smaller.

After discussing the required energy of the launched laser, another aspect to consider are the shape, size, and length of the LGS for wavefront sensing. Due to the atmospheric turbulence, the uplink laser is broken into smaller spots whose number can be estimated as (HAPPER, MACDONALD, MAX et al. 1994) :

$$M \approx \frac{D}{2r_0}^2, \tag{2.4}$$

where D is the diameter of the laser emitter. Individual speckles are diffraction-limited spots whose diameter d is given by :

$$d = \frac{2H\lambda}{D}. \tag{2.5}$$

And the length of spot in the sodium layer is given by :

$$L = \frac{2H^2\lambda}{D^2} \tag{2.6}$$

2.1.3. Non-linear effects of laser on sodium layer

In the previous section, we have assumed that the photon return scales linearly with the power of the laser. However, some nonlinear effects such as saturation and optical pumping will impact the final photon return.

Thermal motion of atoms in the mesosphere leads to inhomogeneous broadening of the optical transitions. The Doppler broadening can be expressed as

$$\Delta\nu_D = \left(\frac{8\ln 2 k_B T}{m\lambda^2}\right)^{1/2} \tag{2.7}$$

Where k_B is the Boltzmann constant, m is the mass of the sodium atom, and T is the thermodynamic temperature. At the altitude of 90 km, $T = 215K$, and we derive $\Delta\nu_D = 1.190 \times 10^9$ Hz.

Within the Doppler width, a single laser photon can only interact with one velocity group whose linewidth is given by the homogeneous broadening $\Delta\upsilon_n = 10$ MHz. Therefore, the absorption spectrum of sodium atom is the superposition of $\Delta\nu_D/\Delta\upsilon_n = 119$ lines corresponding to different velocity groups. When saturation occurs, the total number of photons emitted can be expressed as :

$$N_S = \frac{\pi d^2}{4\sigma_n}\left(\frac{D}{2r_0}\right)^2, \tag{2.8}$$

where σ_n is peak scattering cross section. From this we can calculate the laser power by :

$$E_S = N_S h\nu = \frac{\pi d^2}{4\sigma_n}\left(\frac{D}{2r_0}\right)^2 h\nu \tag{2.9}$$

If we choose a typical peak scattering cross section of $\sigma_n = 1.1 \times 10^{-9}\ cm^2$, and based on the same parameters as above, the power for which saturation starts is $E_S = 0.17\mu J$. Compared to the power required to get an SNR of 100 computed above, it shows that we will always be saturating some velocity groups. Therefore, the number of photons scattered by sodium atoms is not a linear relation with the laser power.

Pulsed lasers can reach a very strong power in extremely short duration, hence saturation is a major consideration for the design of such laser guide stars. For continuous-wave lasers, as the ones usually used in astronomy, this is however not a major concern.

Another nonlinear effect is the optical pumping in the interaction between sodium atoms and laser. The optical pumping is the process that the sodium atom is excited by the laser and transits from the ground state to the upper state. With the increasing of upper state atoms, the sodium layer is extremely unstable, and these upper state atoms begin to return back to the ground state, releasing a large number of photons, under severe collisions, the sodium atoms produce obvious light amplification. As a result, great changes of the scattering cross section of sodium atoms occur at a given probability.

In fact, the circular polarization improves the scattering efficiency than linear polarization, which has been verified experimentally (JEYS, HEINRICHS, WALL et al. 1992, BUSTOS, HOLZLÖHNER, RONALD et al. 2016), this means the optical pumping can further enhance the brightness of laser guide stars.

2.2. Characteristics of the Sodium Layer

In this section, we summarize some of the main properties of the Sodium Layer. Most of these results are derived from measurements that were done by the (PFROMMER et HICKSON 2014) in Canada, with a three-year campaign employing a high-resolution lidar system installed on a 6-m Large Zenith Telescope (LZT) located near Vancouver, Canada. On the other hand, complementary measurements were done in Cerro Tololo Chile (NEICHEL, D'ORGEVILLE, CALLINGHAM et al. 2013). The data is publicly available.

2.2.1. Seasonal and nightly variations

The sodium abundance displays typical seasonal variations of a factor of 2–4, with the minimum and maximum seasonal abundance occurring in summer and winter, respectively (MOUSSAOUI, CLEMESHA, HOLZLÖHNER et al. 2010). Significant abundance variations on hourly, daily, and yearly time scales have been reported, even on time scales of a few seconds to a few hours (TAKAHASHI, B. CLEMESHA et BATISTA 1995;MILONNI, FUGATE et TELLE 1998; O'SULLIVAN, REDFERN, N. AGEORGES et al. 2000; MICHAILLE, CLIFFORD, DAINTY et al. 2001).

The sodium return (or brightness of the LGS) can change rapidly during a night, and it is expected to reach its lowest average level during summer time, possibly in November/December due to variations in the sodium abundance. As an illustration, Fig. 2.1 extracted from (NEICHEL, D'ORGEVILLE, CALLINGHAM et al. 2013) shows the flux variations during a single night and over several months.

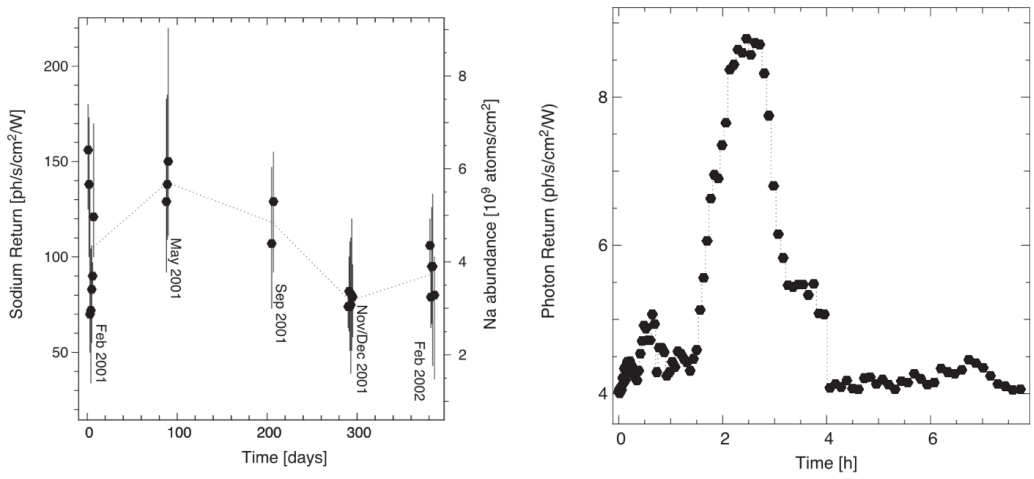

FIGURE 2.1. – Average photon return and sodium abundance measured in 2001 in Cerro Tololo, and example of the night variation of the LGS return measured from the LGSWFS of GeMS.

We also display in Fig. 2.2 a recent statistical study of the return flux measured at AOF (GALACSI) performed by Pierre Haguenauer (ESO). This plot is not normalized for the pointing direction and includes all the GALACSI pointing. As a first remark,

one can clearly see the seasonal variations, with lower returns in summer, and almost twice more returns in winter. It also shows a global trend with less return over the years, which origin is unknown.

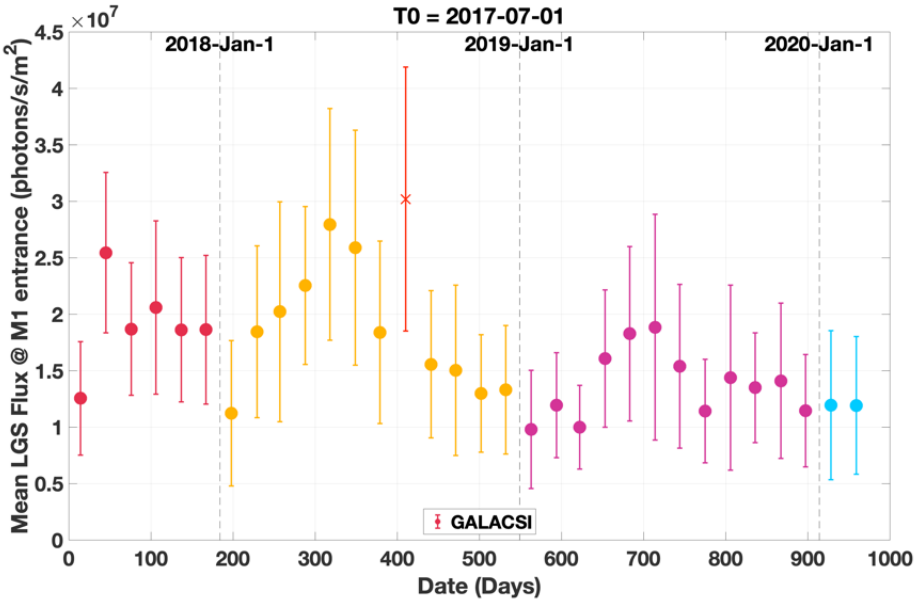

FIGURE 2.2. – Average photon return measured from the AOF/GALACSI system. Courtesy P. Haguenauer.

2.2.2. Sodium return vs. telescope pointing

The photon return varies in a nonlinear way with the zenith angle, which depends on the latitude of the site. Studies performed in (MOUSSAOUI, CLEMESHA, HOLZLÖHNER et al. 2010) and (HOLZLÖHNER, RONALD, ROCHESTER et al. 2010) show non-uniform variations as in Figure Fig. 2.2. This combines the effect of the geomagnetic field, the airmass (i.e., atmospheric absorption), and the distance of the sodium layer. For instance, Fig. 2.3 shows the expected return above Paranal and Mauna Kea.

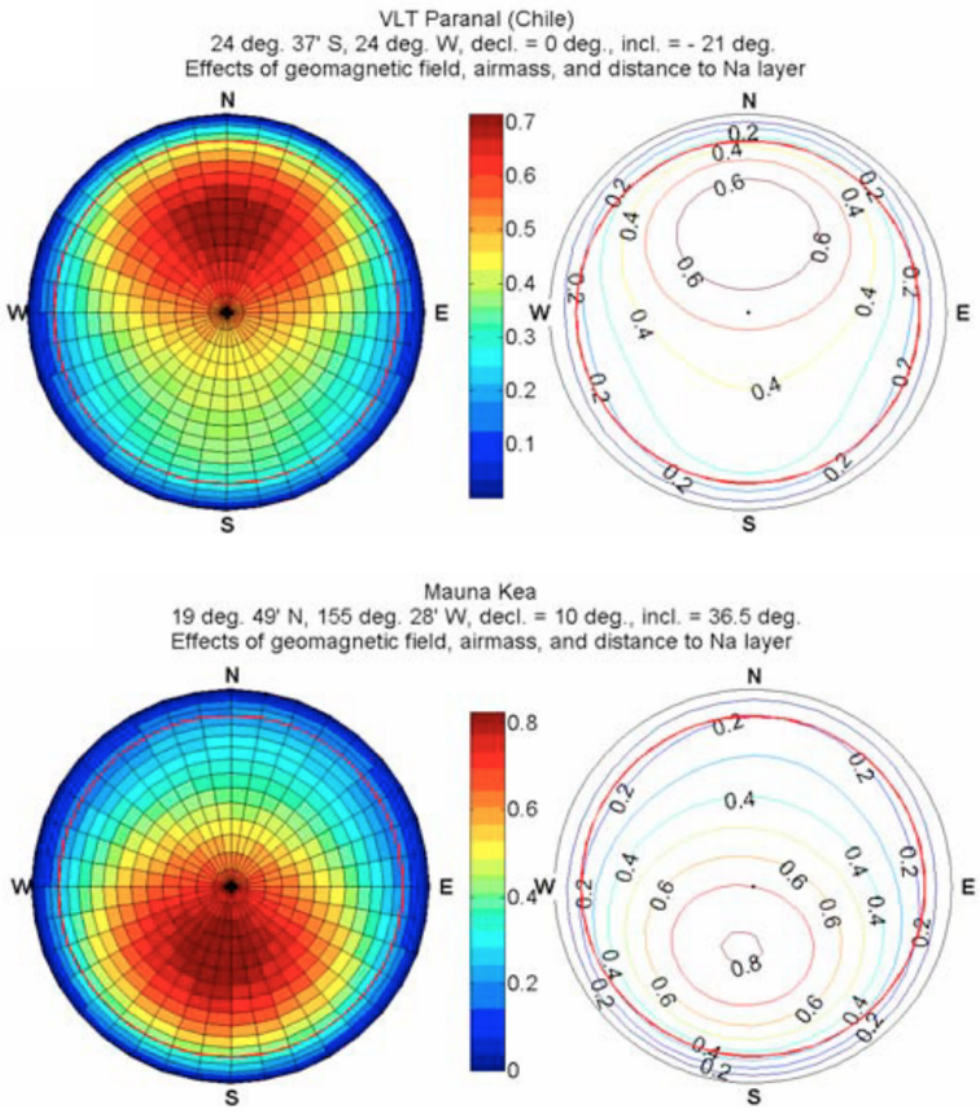

FIGURE 2.3. – Expected photon return across the sky above Paranal and Mauna Kea. Figure from Moussaoui et al.

2.2.3. Sodium altitude and width

As said before, the whole data set of lidar observations made by T. Pfrommer is available upon request. We have then used this data to study the typical variations one can expect to see during a night and over different nights, in terms of sodium altitude and sodium width. First, we show some random profiles in Fig. 2.4. The vertical axis is the altitude, and the horizontal axis is the time evolution over a full night. These profiles show variability of the Na layer along the night, but in these (random) cases, the variations were not very strong.

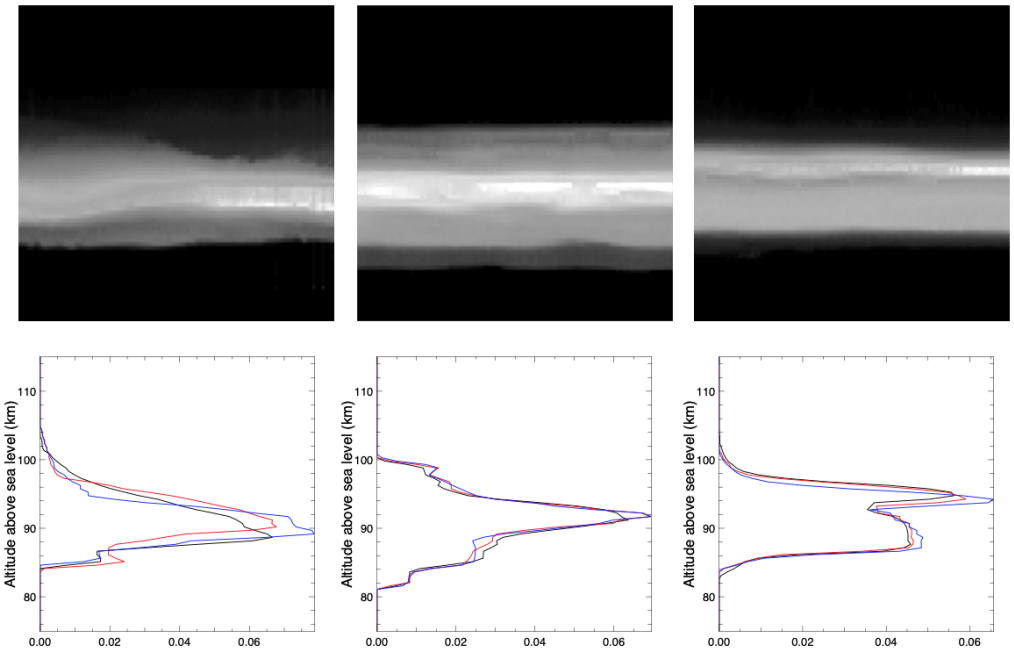

FIGURE 2.4. – Example of Na profiles extracted from the data base provided by T. Pfrommer for 3 random nights. The bottom plot show the temporal variations over the night.

Then we used the whole data set : 109 nights acquired between July 2008 and November 2010, with a vertical resolution of 40m and a temporal resolution as short as 20ms, to look for the statistics of the variations. One example is shown in Fig. 2.5, and the statistical distributions are shown in Fig. 2.6.

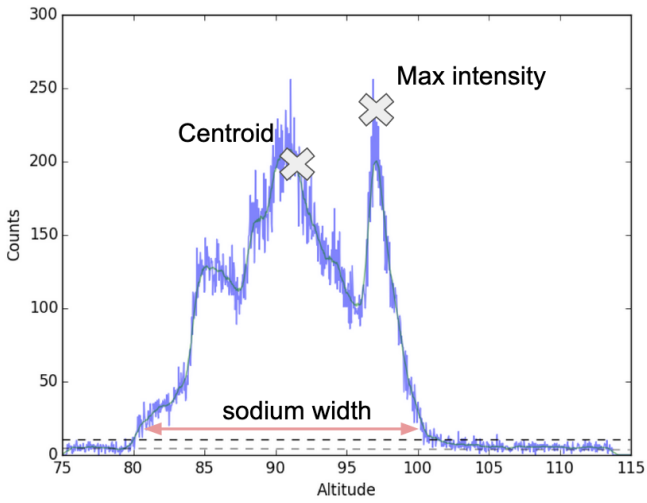

FIGURE 2.5. – Example of a given profile with the definition for the sodium width, centroid altitude and max altitude.

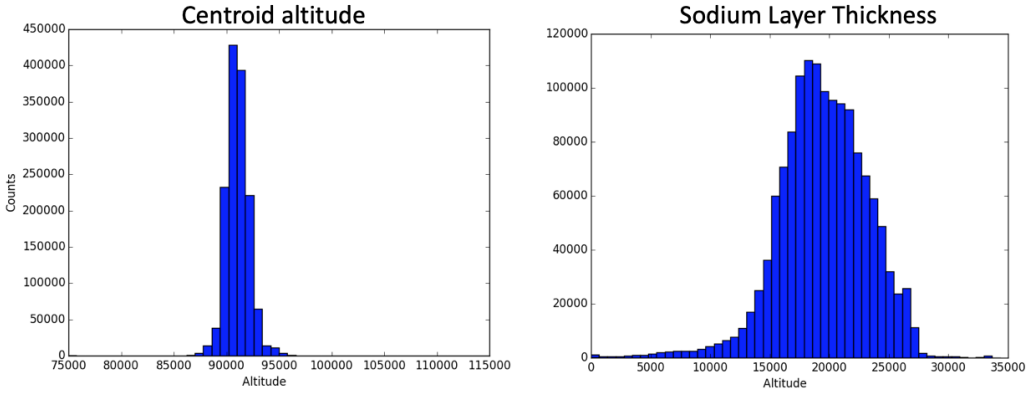

FIGURE 2.6. – Statistics of Sodium profile centroid altitude and width for the whole data Set of T. Pfrommer et al.

From Fig. 2.6 we see that the sodium layer width can be as large as 25km. This will create the so-called spot elongation and associated spot truncation. Considering both the sodium mean height and the sodium layer width, one can also derive the maximal spot elongation to be expected. This is given by Fig. 2.7 and the following formulae :

$$\theta_{elong} = \frac{L\Delta H}{H^2 + H\Delta H} \tag{2.10}$$

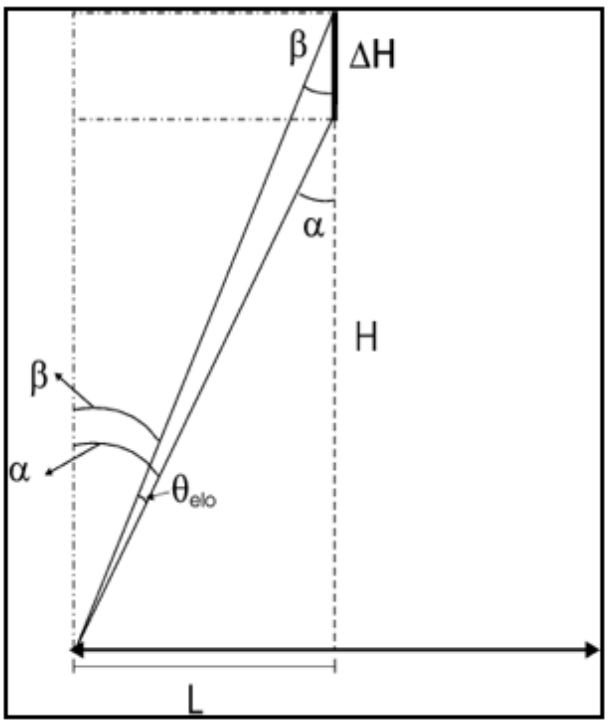

FIGURE 2.7. – Geometry of the LGS elongation.

For a side launch, the most off-axis subaperture is at 21.5 + (37/2) = 40m off-axis. We also have L = 40 m, H = (86 – 25/2) = 73.5 km, ΔH = 25km. The maximal elongation expected at the zenith is therefore 28 arcseconds (!). Note that the elongation scales with the cosine of the Zenith Angle. Hence, for observations at 30 degrees from zenith, the same maximal elongation would be 21 arcsec, and only 14 arcsec at 60 degrees from zenith. For the median conditions (Na width = 19km, Zenith=30degree), the maximum expected elongation will be 16arcsec.

2.3. Limitations of LGS WFS on ELTs

2.3.1. The Tip-tilt determination problem

If we approximate the atmosphere by a single turbulent layer, when the light from a star crosses this turbulent layer, it is deflected. This is the famous Tip-Tilt mode. Assuming that the temporal evolution of the turbulence is slow compared to the light propagation time (from ground to sodium layer to ground), signal emitted by the laser is crossing twice the turbulent layer during its journey. Because the light reemission by sodium resonance scattering is incoherent, the Sodium Laser Guide Star source can be considered fully decorrelated to the incoming laser light. This is true BUT for Tip-tilt. Indeed, the position (on sky) of the Sodium Laser Guide Star is affected by the atmospheric tip-tilt of the turbulent layer during the uplink travel. From this position, the light is reemitted and is affected by the opposite tip-tilt during the down-link travel. The position of the image thus remains fixed for an observer on the ground. It is therefore understood that a source produced from the ground will be insensitive to Tip-Tilt. Thus, the systems based on an analysis of turbulence by laser stars are generally supplemented by an analysis path on a natural guide star to estimate the Tip/Tilt modes.

Fortunately, we have some favorable factors for the determination of tip-tilt in the detection of wavefront error : (1) the isoplanatic angle of low order like tip-tilt is an order of magnitude larger than that of high order. (2) The entire pupil of the telescope can be used to measure the tip-tilt, and as a result, the NGS used for measuring Tip-Tilt only can be significantly fainter than the usual NGS stars in classical AO. (3) The bandwidth of the close loop in terms of tip-tilt compensation is about 1/4 of that of the high order, which can be beneficial for increasing the integration time, hence improving the SNR for faint NGS.

Finally, to further improve the sky coverage, the dual adaptive optics concept was proposed by Rigaut in 1992 (RIGAUT, FRANCOIS, GENDRON et al. 1992). The idea was to use a second LGS and a second AO system to correct the NGS image and open the possibility to work with even fainter NGSs, at the price of increasing the complexity of the AO system.

2.3.2. Cone Effect

The second main limitation of the laser star is the cone effect. The laser is focused at a finite altitude (somewhere in the middle of the sodium layer), hence the wave we receive from the laser source is spherical. Thus, the phase perturbations seen by the ASO are dilated compared to the perturbations coming from an astrophysical object located at infinity (as a first approximation regarding the typical 90 km of sodium layer). When using the dilated aberration measurement to correct the astrophysical object induced aberrations, an error is made. This error is called cone effect or "Focus Anisoplanatism". The larger the diameter of the telescope, the more important the cone effect becomes.

The phase error caused by the cone effect is expressed as :

$$\sigma_{\phi}^2 = k^2 \frac{1}{2\sec\xi} \int C_N^2(h) h^2 (h^{1/3} - 1)\, dh, \tag{2.11}$$

where k is the wave number, H is the altitude of sodium layer, ξ is the zenith angle and $C_N^2(h)$ is the refractive index structure constant in the vertical direction. From the expression above, we can see that the cone effect increases with the increasing of telescope diameter, zenith angle, and r_0, and with the decreasing of wavelength and height of the spot.

In order to simply characterize the phase error of the cone effect, Fried and Belsher introduced the equivalent diameter d_0 of LGS and derived the formula as below :

$$\sigma_{Cone-Effect}^2 = \left(\frac{D}{d_0}\right)^{5/3}, \tag{2.12}$$

where d_0 is the telescope diameter when $\sigma_{\phi}^2 = 1$ rad^2.

For Rayleigh Lasers, produced at 10 km above the telescope, the cone effect quickly becomes the dominant term for large aperture (> 4m) telescopes. For larger aperture telescopes, like 8-10m, Sodium LGS is required to keep the cone effect to a decent level. However, when the diameter of the telescope increases to a certain extent such as 10 - 30 meters, the cone effect of sodium LGS is also significant. To overcome this limitation, multi LGSs are required (see section 2.3.1).

2.3.3. Spot Elongation and Truncation

Due to the finite thickness of the sodium layer, the laser excitation produces a long column of fluorescent atoms with a length between 10 km to 20 km depending on the pointing angle and the vertical density profile of the sodium layer. For an observer located only a few meters off-axis from the laser launch telescope (LLT), the LGS appears as an extended object instead of a point source. This geometrical effect called LGS *spot elongation* becomes dramatic for a 39 m-class telescope with side LLT configuration as the ELT (VERNET-VIARD, DELPLANCKE, HUBIN et al. 1999). For example, a 1 arcsec LGS spot projected at the zenith by a 30 cm diameter laser beam with a 10-20km width sodium layer, which will be seen by the subaperture

of a Shack-Hartmann WFS opposite to the LLT on a 39 m diameter telescope as an elongated spot of about 10–20 arcsec long and about 1 arcsec width (Fig. 2.8).

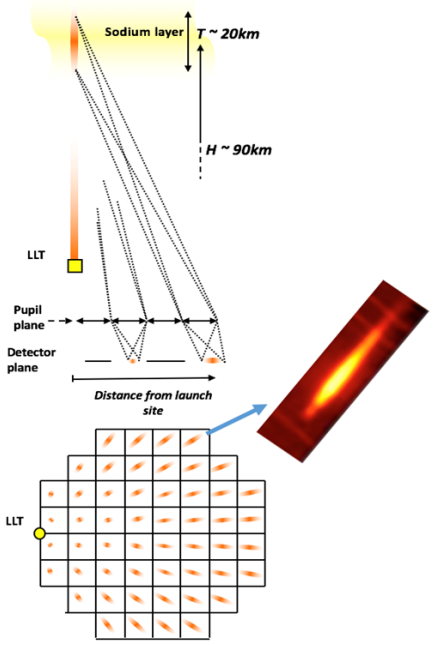

FIGURE 2.8. – Geometry of the LGS wavefront sensing on the ELT showing that with the further distance from launch site, the spots are elongated more severely.

For a Shack-Hartmann WFS, this spot elongation introduces several issues. On the one hand, it reduces the signal-to-noise ratio since the same amount of photons concentrated in a small spot are now distributed on a larger area on the detector, and on the other hand, it increases the wavefront error due to the growing uncertainty in the estimation of the center of gravity (CoG) of an elongated spot (THOMAS, ADKINS, GAVEL et al. 2008). In addition, the spot truncation due to highly elongated spots is not completely imaged on a given subaperture, which leads to a bias in the estimation of the CoG in proportion to the fraction of truncation (CLARE, WEDDELL et LE LOUARN 2020) (Fig. 2.9).

Therefore, the spot elongation and truncation has become the top challenge for LGS wavefront sensing for ELTs, and the prime motivation for this PhD thesis. A non-exhaustive list of solutions are discussed in section 2.3.2 and section 2.4.

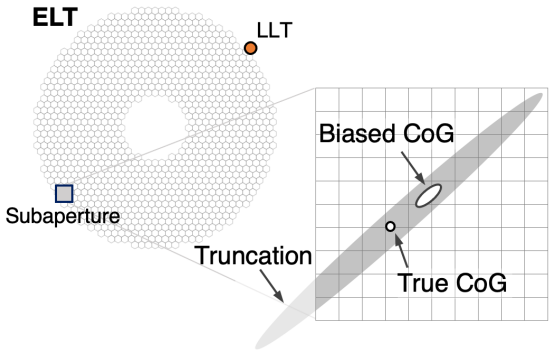

FIGURE 2.9. – Geometry of the LGS wavefront sensing on the ELT showing one LLT in side configuration and the elongated LGS spot projected on a sub-aperture of a Shack-Hartmann WFS. The possible truncation of the spot due to overfilling the field of view of the sub-aperture leads to a bias in the estimation of the center of gravity (CoG) and an error of the measured slope of the local wavefront.

2.4. Approaches to Overcome Current Limitation of LGS

2.4.1. Anisoplanatism limitation : Tomographic reconstruction

Classical AO systems use a single beacon, which limits the correction area to a few arcseconds only due to anisoplanatim. Moreover, when this beacon is a Laser Guide Star, the AO system suffers from focal anisoplanatism or cone effect, which degrades even further the final performance. To compensate for focal anisoplanatism, and potentially open the path for wide field AO for ELTs, the solution is to use several LGSs and perform a tomographic measurement of the turbulent volume above the telescope.

According to the theory introduced in section 1.3, the light propagation in the atmosphere can be considered as the sum of independent phase screens located at different altitudes. This is the foundation of the tomographic reconstruction. Here we briefly introduce the tomographic reconstruction when considering a multi-LGSs system.

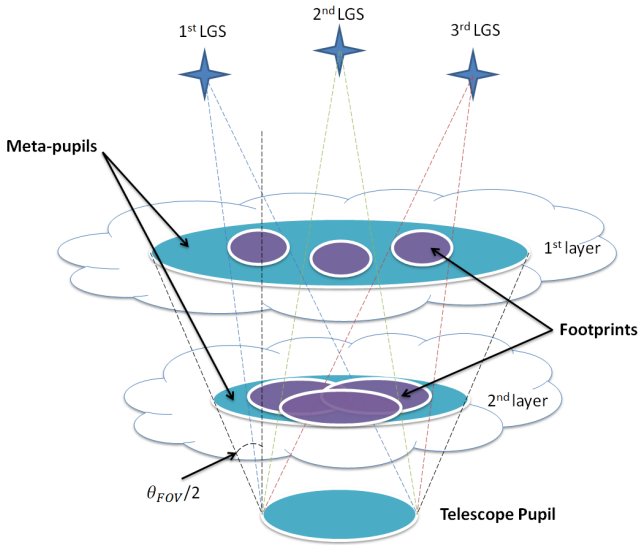

FIGURE 2.10. – Geometric relationship of telescope, LGSs and the layers of atmospheric turbulence. The blue circles denote the meta-pupils and purple circles denote footprints.

Fig. 2.10 shows the geometry of the problem. Each LGS intercepts different turbulent layers with its own cone. The concatenation of all the LGS forms the metapupils. For an altitude h_l, where l corresponds to the l^{th} turbulence layer, and if the LGS constellation covers an angle θ_{FOV}, the diameter of the meta-pupil at altitude h_l is defined by $D + h_l\theta_{FOV}$, where D is the telescope diameter.

If we assume that the telescope pupil is sampled by a $N_0 \times N_0$ grid, in order to keep the same sampling for the meta-pupils, we need $N_l \times N_l$ measurement points, where N_l should be expressed as :

$$N_l = N_0(1 + h_l\theta_{FOV}/D). \tag{2.13}$$

For each layer, the phase grid can be expressed as a column vector $\mathbf{S}_l$, with a number of elements about $\pi N_l^2/4$.

Since the wavefront intercepted by the telescope pupil is the sum of the footprints of each turbulence layer, the phase acquired by the i-th LGS, noted $\mathbf{M}_i$ can be simply written with $\mathbf{S}_l$ as :

$$\mathbf{M}_i = \sum_{l=1}^{L} \mathbf{A}_{il}\mathbf{S}_l, \tag{2.14}$$

where $\mathbf{A}_{il}$ is the projection matrix of i^{th} LGS corresponding to the l^{th} turbulence layer, for the case with G LGSs and L turbulence layers, the above equation can be written as :

$$\begin{pmatrix} \mathbf{M}_1 \\ \mathbf{M}_2 \\ \vdots \\ \mathbf{M}_G \end{pmatrix} = \begin{pmatrix} \mathbf{A}_{11} & \mathbf{A}_{12} & \cdots & \mathbf{A}_{1L} \\ \mathbf{A}_{21} & \mathbf{A}_{22} & \cdots & \mathbf{A}_{2L} \\ \vdots & \vdots & \ddots & \vdots \\ \mathbf{A}_{G1} & \mathbf{A}_{G2} & \cdots & \mathbf{A}_{GL} \end{pmatrix} \begin{pmatrix} \mathbf{S}_1 \\ \mathbf{S}_2 \\ \vdots \\ \mathbf{S}_L \end{pmatrix}. \tag{2.15}$$

Which can also be expressed in matrix form :

$$\mathbf{M} = \mathbf{AS}. \tag{2.16}$$

This equation is similar to the standard SCAO case (1.39), but now the system has $G\pi N_0^2/4$ equations and $\sum_{l=1}^{L} \pi N_l^2/4$ unknowns. This is an ill-conditioned system, and standard inversion may result in large noise amplification. Therefore, it is of common use to call for regularization, as derived for instance by Tikhonov (TIHONOV 1963) as :

$$\begin{aligned} \mathbf{S} &= \min_S \left\{ \|\mathbf{AS} - \mathbf{M}\|^2 + \lambda \|\mathbf{S}\|^2 \right\} \\ &= (\mathbf{A}^T\mathbf{A} + \lambda \mathbf{I})^{-1}\mathbf{A}^T\mathbf{M} \\ &= \mathbf{R}_z\mathbf{M}, \end{aligned} \tag{2.17}$$

where λ is the regularization parameter, and $\mathbf{R}_z = (\mathbf{A}^T\mathbf{A} + \lambda\mathbf{I})^{-1}\mathbf{A}^T$ is the tomographic reconstruction matrix.

As for the classical SCAO case, one can also use a modal representation of the phase instead of the zonal one. The above equations remain similar. The phase screen in telescope pupil and meta-pupils and the footprints can also be expressed by a series of Zernike coefficients. As a result the equation (2.18) can be converted to :

$$\mathbf{b}_g = \sum_{l=1}^{L} \mathbf{T}_{gl}\mathbf{S}_l, \tag{2.18}$$

where $\mathbf{b}_g$ are the Zernike coefficients from the wavefront of the g^{th} LGS, and $\mathbf{T}_{gl}$ is the projection matrix.

The difference between zonal and modal reconstruction is that the former uses grids to construct wavefront but the latter uses Zernike coefficients, as a result, the key of the projection matrix in modal reconstruction is the coordinate transformation from metapupils and the corresponding footprints. According to the locations of LGSs and the turbulence layers, we can calculate the modal projection matrix of a LGS in terms of a layer, and construct them to a entire modal projection matrix T, therefore the equation above can be converted to :

$$\mathbf{b} = \mathbf{Ta}, \tag{2.19}$$

where $\mathbf{b}$ are the Zernike coefficients of the wavefront in all LGSs directions, and $\mathbf{a}$ is that in all turbulence layers. The inversion can also use regularization, and in this case,

$\mathbf{R}_m = (\mathbf{A}^T\mathbf{A} + \lambda\mathbf{K}^T\mathbf{K})^{-1}\mathbf{A}^T$ is the modal tomographic reconstruction matrix. The matrix $\mathbf{K}$ can be computed from the apriori information about turbulence statistics, and in particular take advantage of the Kolmogorov turbulent phase power spectrum.

Being modal or zonal, the multi-LGSs allow to retrieve the instantaneous tomographic 3D information, from which it is then possible to project the reconstructed volume in the direction of interest, and compensate for the cone effect (TATULLI, ERIC et RAMAPRAKASH 2013).

Based on multi-LGSs and tomography, there are several strategies in wide field AO to drive the deformable mirror(s) of the system, depending on the scientific applications.

A first approach is simply to average the signals coming from the WFSs. For atmospheric layers located at high altitude, the measured signal corresponds to decorrelated wavefronts, their average will be zero. For atmospheric layers close to the ground (where turbulence is strongest), the signal is strongly correlated. If we drive a deformable mirror conjugated to the pupil from these averaged measurements, the bulk of the correction is on the layers near the ground. This is called GLAO (for "Ground Layer AO"). The GLAO improves the angular resolution by a factor of 2 or 3 compared to observations limited by turbulence, with fields of several minutes of angle (RABIEN, AGEORGES, BARL et al. 2010). If the size of the field to be corrected decreases, the performance improves until reaching the diffraction limit in the case of a field of the order of θ_0. This is called LTAO, for Laser Tomography AO. The corrected field is limited to a few tens of arcseconds in the near infrared, with a sky coverage of up to 80%. These two techniques associated with the MUSE instrument are implemented at ESO's VLT using an adaptive secondary mirror in the telescope (KOLB, MADEC, ARSENAULT et al. 2017).

In order to increase the size of the corrected field while reaching the diffraction limit, it is necessary to increase the number of deformable mirrors. A first possibility is to use 2 or 3 deformable mirrors in series along the propagation path, with optical conjugation at the altitude of the dominant turbulent layers. The correction is thus performed directly at the source of the disturbances, which provides both an increased correction field compared to the conventional AO and much better performance than in GLAO. This is called Multi-conjugate AO or MCAO. Such a system was commissioned in 2012, at the Gemini-South 8m telescope, it is the GeMS instrument (SIVO, MARIN, RIGAUT et al. 2018,NEICHEL, RIGAUT, VIDAL et al. 2014,RIGAUT et NEICHEL 2018,RIGAUT, NEICHEL, BOCCAS et al. 2014). Another possibility is to use several deformable mirrors, but this time in parallel, each providing a correction for each object of interest within the field defined by the WFFs (CHAPMAN, CONOD, TURRI et al. 2020). This is called Multi-Object AO or MOAO. MOAO allows to reach a good performance in a few points in a much larger field than the MCAO. However, the correction field around each point is limited by anisoplanatism. The demonstration of this concept was made in 2010 with a 4m telescope in the Canary Islands (GENDRON, VIDAL, BRANGIER et al. 2011).

2.4.2. Potential mitigation for spot elongation

There has been several options proposed in the literature to mitigate the spot elongation issue. The proposed solutions include modifications of the laser source itself, an innovative wave-front sensing strategy and advanced centroiding algorithms. Of course, these solutions are not exclusive, and a combination of some is possible. In the following we detail some of these options, but before we describe the impact of spot truncation.

2.4.2.1. Quantifying the impact of spot truncation

The very first thing that we have done was to understand the spatial and temporal content of the aberrations induced by the spot truncation. In order to estimate the impact of truncation, we have done the following simulations :

— First, we create a SH image of the LGS spots. To simplify the modeling and speed-up the simulations, we are not simulating the full diffraction SH. Instead, we only simulate Gaussian spots of 1" FWHM, as expected from the LGS extended object. Those spots are properly sampled with the SH detector (i.e., with pixels of 0.5" or less). Note that we have a double check with full diffractive simulations that this assumption is valid (see below). The bottom-left image of Fig. 2.11 shows one spot.

— The next step is to create elongated spots. An elongated spot can be assumed to be the sum of several incoherent sources, coming from different altitudes (different focus). Within each subaperture, different altitudes correspond to different tilts. The final spots are then done by applying the equivalent tilt within each subaperture and summing all the individual spots together. Each individual spot is weighted by the expected Na intensity profile corresponding to its altitude. This is shown in the images in the bottom of Fig. 2.11, which show how the spots become elongated for a subaperture that would be moving away from the laser launch telescope. In this case, the intensity distribution is shown by the 1D plot on the top-right corner of Fig. 2.11, which itself has been extracted as a single slice from the 2D temporal distribution shown in Fig. 2.11 (top-left). Regarding the Na profiles, we chose 7 profiles, showing a large variety of conditions. Those profiles are shown in Fig. 2.12 We also did tests with simple profiles, like simple or double Gaussians.

— The position of the LLT can be set arbitrarily. As a first test, we set it at one "corner" of the pupil

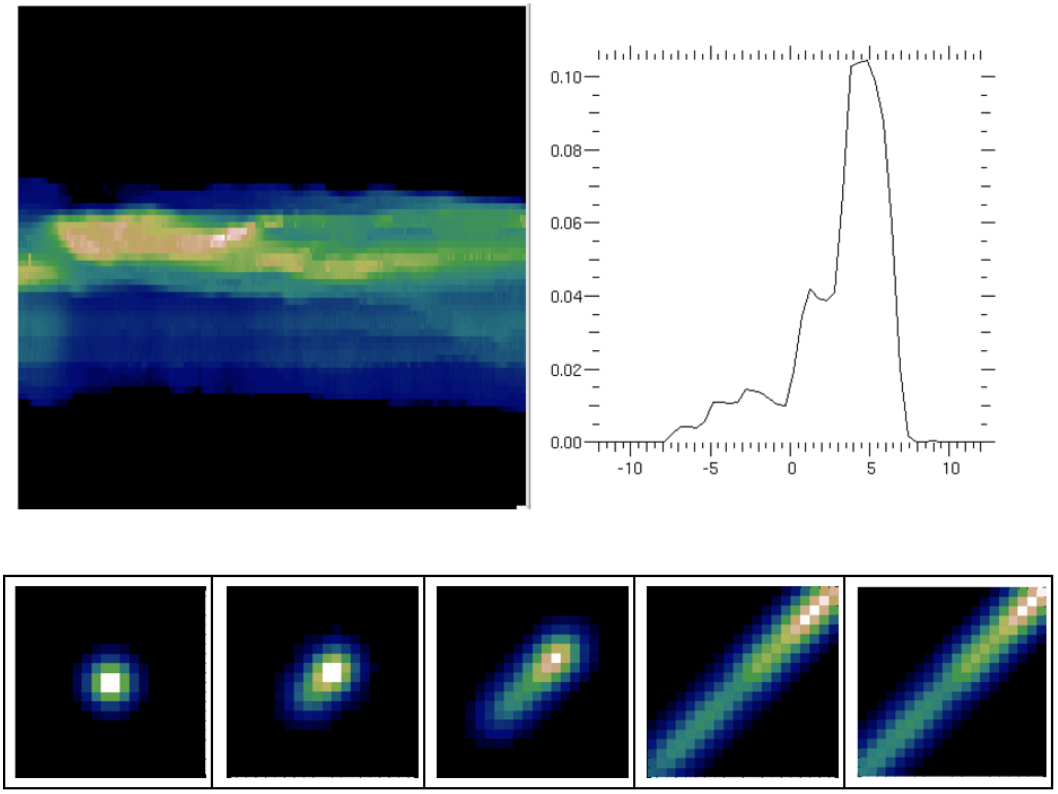

FIGURE 2.11. – Illustration of the process followed to create elongated spots.

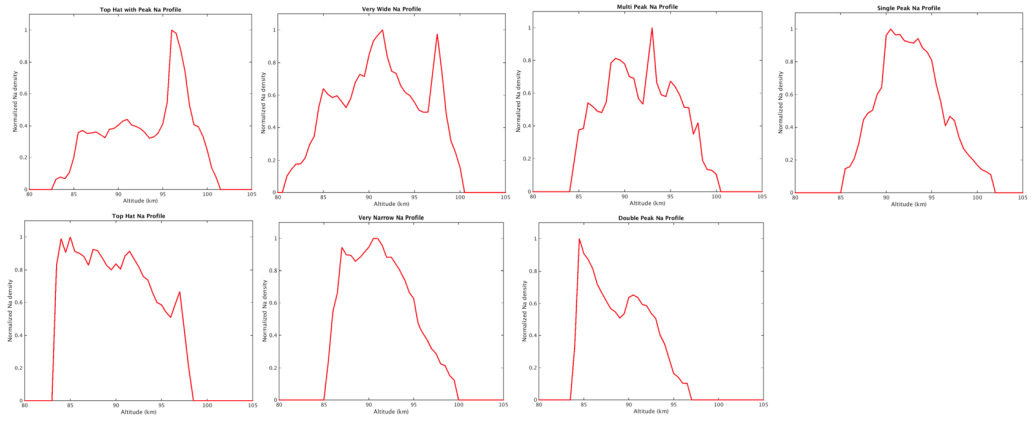

FIGURE 2.12. – Illustration of 7 representative Na profiles. The plots give the intensity distribution above sea level.

The next step is to compute the centroid of those spots and project the centroid maps onto Zernike polynomials. For that we use a simple center of gravity (CoG). As we are working without noise, a simple CoG is sufficient. The projection onto a Zernike basis requires building an interaction matrix. In order to speed up the simulations, we are building this interaction matrix with a simple geometrical model, where we

take the slopes expected as the difference of the phase at the edge of a subaperture. We checked that this step was valid by performing a real diffractive simulation and comparing results between the geometrical model and the diffractive model. We can then reproduce those simulations for each Na profile and for each time step of the profiles. Doing so, we can estimate the aberrations for a single LGSWFS, created by the truncation, and how those aberrations are dynamically evolving. The plot of Fig. 2.13 shows the distribution of the LGS aberrations over the different Zernike, for all the 7 Na profiles considered. The histogram gives the average amplitude of the Zernike coefficient in nm. The error bar shows the 1-sigma variation between the 7 profiles. The blue lines give the maximal value we get for those 7 profiles (peak value). Finally, the red plot shows the cumulative plot, adding the contribution of the Zernike one by one.

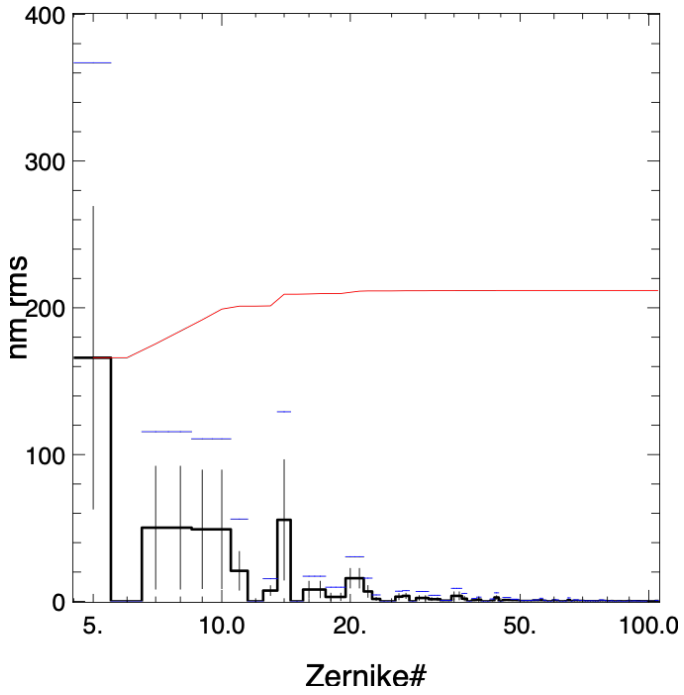

FIGURE 2.13. – Spatial distribution (decomposition on a Zernike polynomial basis) of the aberrations induced by a spot truncation. In that case, the LGS sub-aperture has been set to 10arcsec.

The main conclusion from Fig. 2.13 are that (i) the aberrations induced by the truncation are mostly low order : there is no energy above Zernike 104, and most of the energy is concentrated in the first 36 Zernike and (ii) the absolute amount of aberrations induced can very large, of the order of few hundreds of nanometers in this case. If nothing is done to correct for this effect, this would represent the main offender for the final AO performance. This is then a fundamental error term to be corrected to reach high-performance AO correction.

The next thing we look at is the temporal evolution of these modes. The original

temporal resolution of the Na profiles is very high (some of them are acquired at 20ms). However, the signal to noise ratio is poor for this high temporal resolution data. Hence, we have used a temporal resolution of 10 seconds to improve the SNR. In order to estimate the temporal content at higher temporal resolution, we will simply take the temporal PSD of each Zernike mode and fit it to higher frequencies. This is similar to the approach followed in the papers of (DIOLAITI, SCHREIBER, FOPPIANI et al. 2012) and (SCHREIBER, LIEM, FREIER et al. 2014).

By doing so, we show that the temporal variation of the spurious modes induced by the truncation evolves quickly, on the order of a few tens of seconds. In other words, it will be difficult to calibrate these biases on the line, as the signal evolves quickly.

Finally, the last step we have done was to look at the tomographic propagation of those modes on axis. Indeed, so far the analysis was focused on a single LGSWFS. However, each WFS will see those "equivalent" static aberrations, rotated according to the LLT geometry w.r.t. to the LGS pupil. Those aberrations will then be mixed by the tomographic reconstruction and reprojected on axis by the tomographic reconstruction process. The results are shown in Fig .2.14 for a tomographic system using 6 lasers with a constellation of 34arcsec field of view.

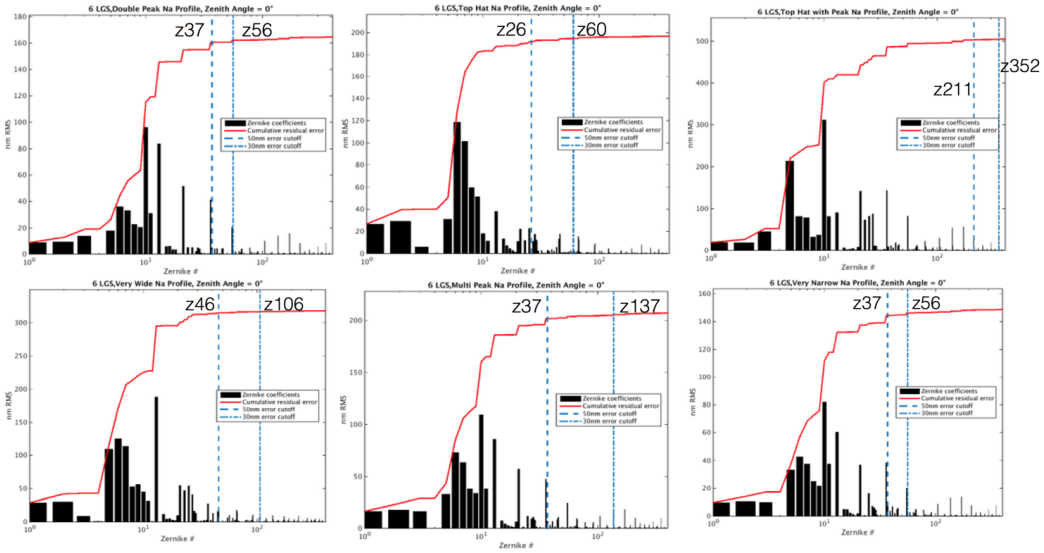

FIGURE 2.14. – Wave-Front Error due to each LGSWFS truncation, projected on-axis by the tomography.

Fig .2.14 confirms that most of the aberrations are relatively low order, or at least lower than a hundred of Zernike polynomials, expected for 2 problematic Na profiles ("Top hat" and "Multi Peak"). Figure 2.14 also shows the amount of Zernike that would need to be measured and cancelled if one would like to reduce the residual truncation error down to 30nm (dash blue line) or 50nm (dash-dot blue line). Finally, Fig .2.15 shows an example of the spurious phase created by the LGS truncation, after the tomographic reconstruction and projected on axis. In this case, we changed the

number of LGS in the tomography from 4 (left) to 12 (right) to illustrate how the static error is averaged and smoothed when many LGS are used.

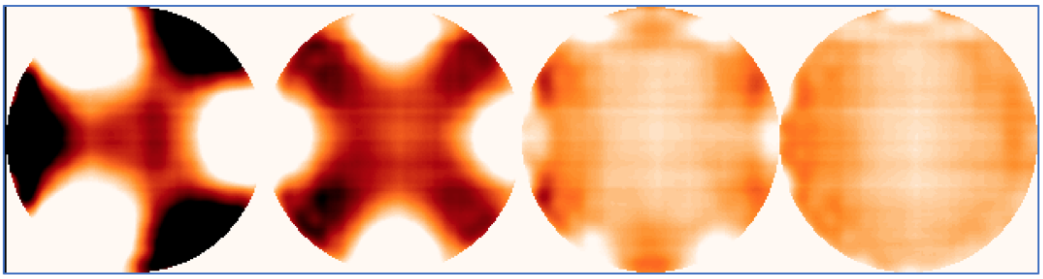

FIGURE 2.15. – Wave-Front Error due to each LGSWFS truncation, projected on-axis by the tomography, for 3, 4, 6 and 12 LGSs.

Because the final wavefront error arrives at from 150nm to 500nm, one important conclusion from Fig .2.14, is that if nothing is done to compensate for the phase biases induced by the LGS spot truncation, the residual eror can reach levels of hundreds of nanometers rms. This is far higher than the total error budget of HARMONI LTAO for instance. It does then represent the major error term and must be mitigated. Different mitigation options are presented in the next sections.

2.4.2.2. Laser range-gated imaging

The first path to reduce LGS spot elongation is to work directly on the LGS source. Indeed, what creates the elongation perspective is the width of the Sodium Layer. Hence, if this layer could be partially illuminated over a smaller width, it would effectively result in a smaller spot elongation. This is the idea behind range-gated laser imaging. In range-gating imaging, it mainly makes use of the Rayleigh LGS, which launchs the laser into the 20km high sky, and the receiving time of the detector is determined according to the emitting time of a laser pulse and the distance of irradiated area, so that the imaging process can be isolated from the background noise and effectively overcome the back scattering.

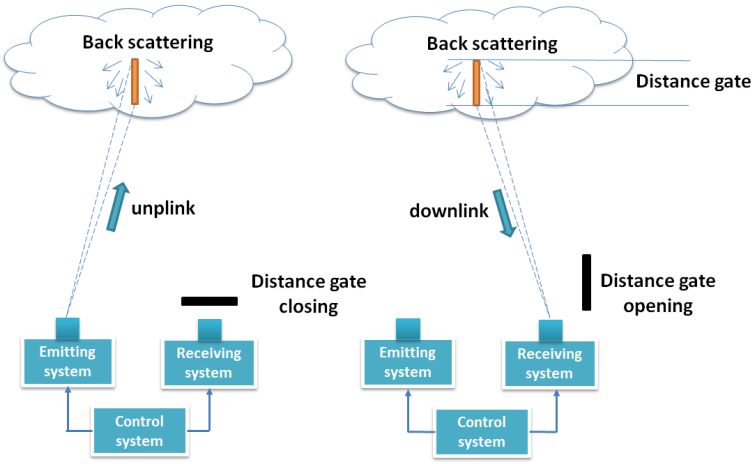

FIGURE 2.16. – The principle of the range-gating imaging, left is the uplink process that distance gate is closed, and right is the downlink process that distance gate is open.

The range-gating imaging system is mainly divided into three parts : a laser pulse emitting system, the time control system, and the receiving system shown in (Fig. 2.16). A pulsed laser emits a laser light that irradiates the sodium layer, and a gated mechanism controls the opening and closing time of the imaging device. The timing is determined precisely so that the WFS will only see a portion of the overall Sodium Layer, eventually reducing the spot elongation. This requires a precise pulsed laser clock synchronization technology, a reasonable optical system, and a high sensitivity detector. Indeed, the main limitation with pulsed laser and gated WFS comes from the very limited return flux obtained, which makes it difficult to deploy for Sodium LGS (BECKERS 1992). It is however required for Rayleigh LGSs.

2.4.2.3. Ingot pupil plane wavefront sensing

Several authors have studied the possibility to use an alternative WFS strategy than the SH for LGSs. One option could be to use a Pyramid WFS on the focal plane mask that could potentially be less constrained by the spot elongation than the SHWFS (QUIRÓS-PACHECO, PINNA, PUGLISI et al. 2013, BLAIN, ESPOSITO, PUGLISI et al. 2015). However, it can be shown that the defocus introduced by the spot elongation at the pyramid tip reduces considerably the pyramid sensitivity, and at the end it becomes equivalent to a gated system, where most of the photons are lost, or just contributing to the noise.

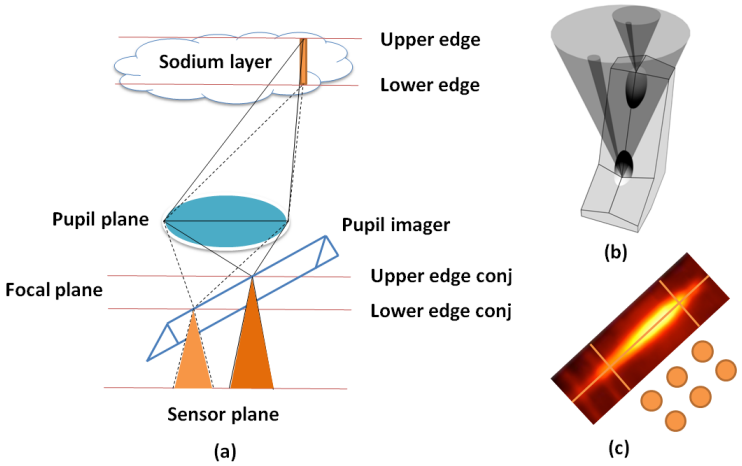

FIGURE 2.17. – (a) The schematic plot of the ingot pupil plane wavefront sensing, (b) The structure of the pupil imager (RAGAZZONI, VIOTTO, PORTALURI et al. 2020), (c) Subdivision of six areas of the elongated spot by pupil imager.

.

In the specific case of a telescope that would use side launching, the extended LGS spot will now be seen at an angle on the LGS focal plane. It is then possible to think of an optical device that will follow this geometry and takes advantage of all the photons produced by the LGS. This is the "ingot" concept proposed by Ragazzoni et al. (RAGAZZONI, PORTALURI, VIOTTO et al. 2018).

The idea of the ingot pupil plane wavefront sensing is to use an "elongated" pyramid located at the LGS focal plane (Fig. 2.17,(b)), following the LGS image geometry, and then subdivide the flux to form a number of pupils. The analysis of the intensity variations in the pupils allows to retrieve the phase information (Fig. 2.17,(c)).

The main difficulty with such a device comes from the fact that the optical filtering element (the stretched pyramid) would have to be adapted to each sodium layer. In other words, if the sodium width changes, then the "stretched" pyramid would have to be changed. This is obviously not a practical option, and the solution proposed by Ragazzoni's team was then only consider one edge of the LGS spot and divide the flux in 3 pupils only (VIOTTO, PORTALURI, ARCIDIACONO et al. 2018). Combined with a zoom optic, the lower edge of the LGS spot can always be imaged on the vertices of this 3 side pyramid, and all the flux of the LGS is collected. Preliminary experimental tests have been done at LAM on the LOOPS bench (FILIPPO, GREGGIO, BERGOMI et al. 2021)

2.4.2.4. Modified Shack-Hartmann

If we come back to the classical Shack-Hartmann WFS, some authors have been proposing a modification of the lenslet array to either minimize / compress the elongated spot, or to do a better utilisation of the available pixels.

The first solution presented here has been proposed by Gendron et al. (GENDRON 2016). It consists in breaking the regular spatial sampling of the pupil done by the Shack-Hartmann, and using a lenslet of different sizes across the pupil, that would have a FoV adapted to the LGS elongation. In other words, for sub-apertures lying nearby the Laser Launch Telescope, the subaperture FoV will be small, and it will increase to accommodate for the spot elongation across the pupil. In practice, it could mean to have sub-apertures of 50cm (when projected on M1) nearby the LLT, but of 2m on the opposite size of the pupil. The phase reconstruction may be more complicated afterwards, but in a tomographic system with multiple LGS, the redundancy of the measurements will make that the part of the pupil poorly sampled by one LGS will be properly sampled by another LGS. The other advantage of this method is that for the spots which are very elongated, the subaperture area is larger, and then even if the flux is spread over many pixels, the signal-to-noise remains good because the number of photons increases with the subaperture area.

Another solution (JAHN, HUGOT, FUSCO et al. 2016) proposed the use of aspheric optics to optically compress the spot images along their elongated direction. Innovative optical approaches can be proposed to significantly reduce the spot elongation before the physical detection by the CCD without any significant loss in flux nor performance. These approaches are based on free form optics and complex amplitude remapping techniques. The option proposed by (JAHN, HUGOT, FUSCO et al. 2016) is to make use of a set of two cylindrical lenses, which the combination allows to keep a unique focal length for the entire array, while providing the right shrinkage.The illustration of such a system is shown in Fig. 2.18.

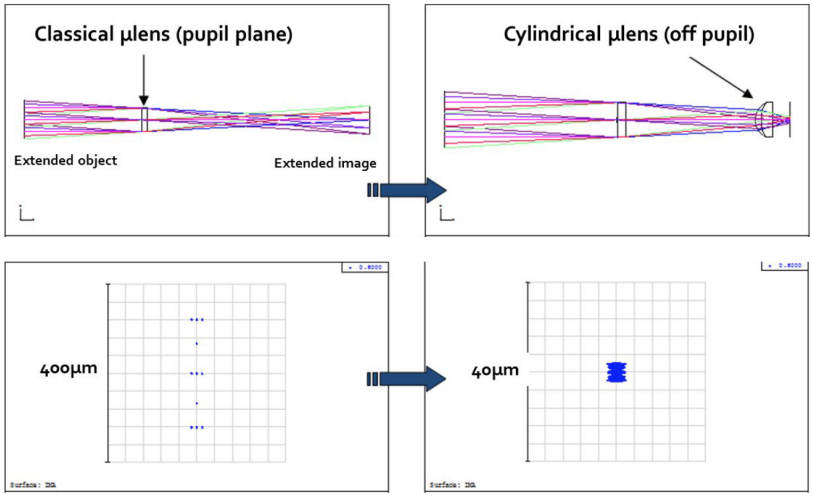

FIGURE 2.18. – Zemax model showing a set of 2 microlenses, one being cylindrical, and allowing for the spot shrinkage along the extended axis. Figure from JAHN, HUGOT, FUSCO et al. 2016.

.

The challenge of this optical solution consists in the actual realization of the cylindrical lenses. This option has never been tested experimentally.

Finally, a third option (- a.k.a. "SPOOF") was proposed to compact the spots over the SH detector and avoid LGS truncation. By using a specially crafted microlens array in which the optical axis of each lens is displaced, one can optimise the packing of the WFS spots to reduce or get rid of spot overlap. Centroids are computed on a nonsquare pixel map assigned to each subaperture. The basic principle is shown in Fig. 2.19.

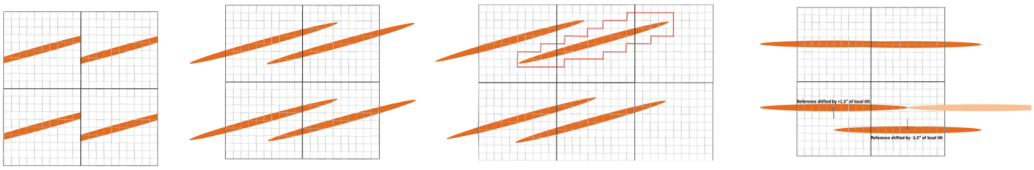

FIGURE 2.19. – Basic principle of "SPOOF", an optimal use of all the SH pixels.

.

The first step is to remove the Field-Stop (FS) which in classical SHWFS is usually set to the subaperture size. By doing this, one allows the elongated spots to spread over the neighbored sub-apertures. The centroiding algorithm should then be defined in the Real-Time Computer to consider the corresponding pixels for each spot. However, as the geometry is fixed and the LGS are not rotating, LGS beams are always at the same position on the LGSWFS. Then, for spots that would have overlap, it will be necessary to shift them. This could be done by adding a Tilt (prism) on the subapertures impacted. This is shown in the last drawing of Fig. 2.19, the spots which are overlapping are shifted. An illustration of how the spot pattern would look like for respectively a side and central launch is shown in Fig. 2.20.

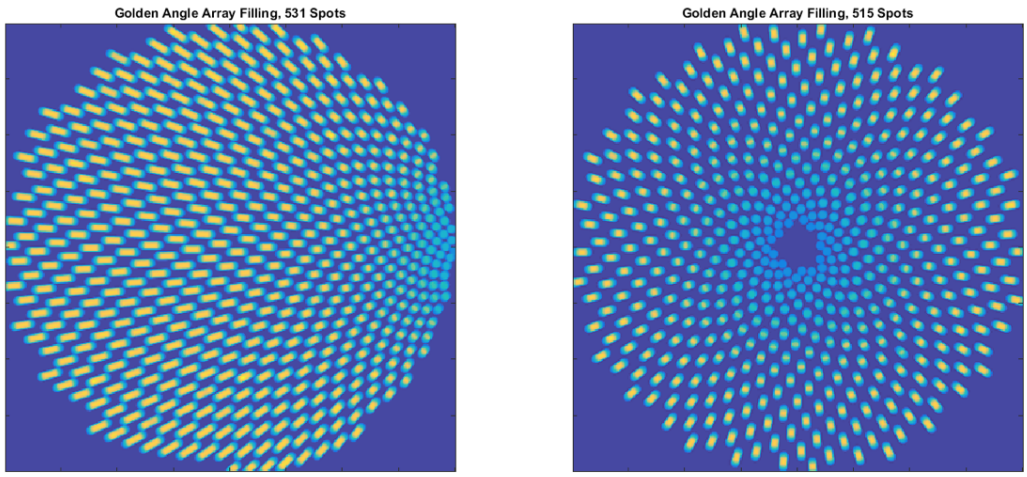

FIGURE 2.20. – Illustration of SPOOF for a side and central LGS launch.

.

The drawback of this solution would first be to have the capability to build such a lenslet array, but also that the overall background light will be increased by the fact that the SH field stop has been removed. This solution has not been tested experimentally yet.

2.4.2.5. Optimized tomographic regularisation

In order to minimize the impact of the truncation, (TALLON, TALLON-BOSC, BÉCHET et al. 2008), proposed the idea to provide a different weight on the measurements according to their elongation. The method consists in weighting the measurements to only reject the ones along the long axis of the elongation (truncated), while keeping those along the small axis (not truncated). For each spot, the small axis would be kept, while the long axis would be rejected if truncated. Thanks to the redundancy of the measurements, and the fact that in a side-launch configuration, the elongated spots of one WFS correspond to the nonelongated spots of another WFS (see Fig. 2.21), the expected impact on performance should be reduced.

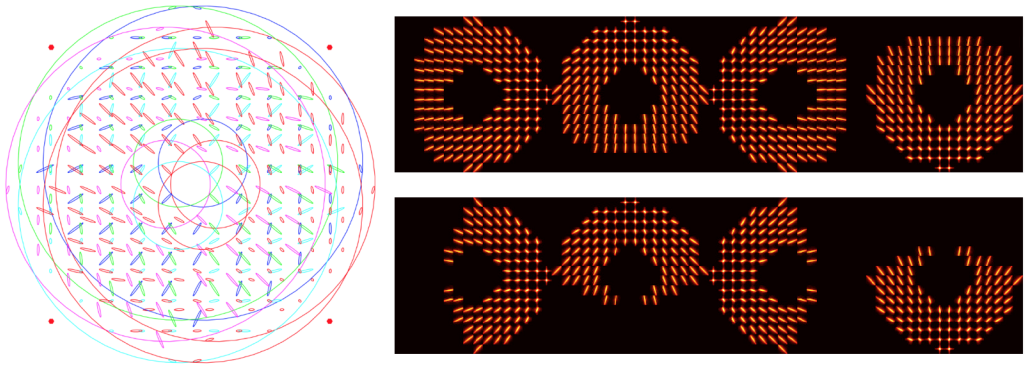

FIGURE 2.21. – Illustration of the measurement redundancy and rejection of biased measurements.

.

2.4.2.6. Sampling vs. FoV trade-off

For a fixed number of pixels associated with a SHWFS, and a fixed number of subapertures, a potential solution to increase the Field-of-View of each subaperture could be to increase the angular size of each pixel. Indeed, usually the SHWFS are designed to have a pixel size providing the Shannon sampling of the spots within each subaperture. For the LGS object, the smaller spot size that one can expect may be around a FWHM of 1arcsec. In this case, the ideal pixel size should be 0.5arcsec. Fixing the pixel size, and if the detector and number of subapertures are fixed, it will automatically fix the FoV per subaperture. Increasing the pixel size can then be an option to increase the subaperture FoV and mitigate LGS truncation. However, working with larger pixels means undersampling the LGS spot, which induces nonlinear effects

(optical gains) in the centroid measurement. An extreme example would be working with quad-cells (2x2 pixels per subaperture), which are known to be very non-linear (VÉRAN et HERRIOT 2000). Basically, when working with undersampled spots, the centroiding will become a function of the LGS spot size. For LGSWFS, and because the spot size changes across the pupil, the nonlinearity will be different for each subaperture, making the wave-front reconstruction very complex. This dependence (known as optical gain for the pyramid WFS) has to be calibrated on line, for example by dithering each LGS with a known signal (DAM 2005). Even though this on-line calibration is feasible, it adds complexity to the AO system, and the centroid gains remain an additional error in the final performance of multi-LGS systems (NEICHEL, RIGAUT, VIDAL et al. 2014).

2.4.2.7. Advanced centroiding strategy

So far, we have been considering a simple centroiding strategy as the Center of Gravity. As shown above, this centroiding will be very sensitive to truncation, and biases in the slopes will be introduced as soon as truncation arises. Another option to mitigate the truncation effect would be to consider advanced centroiding methods that would take into account explicitly the truncation (GRATADOUR, GENDRON et ROUSSET 2010). For instance, correlation or matched filter (BASDEN, BARDOU, CALIA et al. 2017) could potentially help. However, these methods will require a good knowledge of the instantaneuous sodium profile. This latter could be acquired from a parallel smaller telescope monitoring the sodium layer, or directly from multiple Shack-Hartmann images with super resolution algorithms (MELLO et PIPA 2016). In this later paper, the authors show how a high-resolution image of the sodium profile can be extracted from the subimages of the Shack-Hartmann, and then retrofited into the centroiding computation, to eventually mitigate the truncation aspects. A similar work has also been recently presented in this paper (CLARE, WEDDELL et LE LOUARN 2020). Of course, the trade-off will be in the real-time computation complexity, which will be increased significantly for such advanced centroiding methods.

2.5. Motivation of the thesis

The motivation for this thesis was to explore and validate a practical solution for LGSWFS for the ELT when using SHWFS. The thesis is motivated by the development of instruments like HARMONI or MAORY, which will require to implement several LGSWFS. A specific aspect that has motivated this thesis concerns the spot elongation issue, which when we started the work, was still an open problem. It represented one of the major risks for the tomographic AO instruments of the ELT. The goal of the thesis has thus been to study and validate the concept of LGSWFS that would minimize this risk and provide a solid ground for the ELT instruments. In particular, we explored the possibility to use innovative new CMOS detectors allowing for larger formats, and potentially significantly reducing the spot elongation impact on performance.

My research was then to understand the specificity of these detectors, if they could fulfill the need, and demonstrate experimentally that a working design could be found. Chapter 3 focuses on the CMOS detector characterization and Chapter 4 shows the work done to implement this new detector into a full LGSWFS solution. Finally, Chapter 5 adresses numerical simulations about a specific issue related to some CMOS detectors.

3. Characterization of a new CMOS sensor for LGS

Sommaire

3.1. Introduction

As we have described in the previous chapter, one of the main challenges for the ELT AO-assisted instruments will be to deal with the so-called spot elongation when using LGS. For a Shack-Hartmann WFS, the spot elongation introduces several issues. On the one hand, it reduces the signal-to-noise ratio since the same amount of photons concentrated in a small spot are now distributed on a larger area on the detector, and on the other hand, it increases the wavefront error due to the growing uncertainty in the estimation of the center of gravity (CoG) of an elongated spot (THOMAS, ADKINS, GAVEL et al. 2008). In addition, the spot truncation due to highly elongated spots not completely imaged on a given sub-aperture, leads to a bias in the estimation of the CoG in proportion to the fraction of truncation (CLARE, WEDDELL et LE LOUARN 2020) .

The major challenges of LGS wavefront sensing at the ELT scale lie on i) performing a robust wavefront analysis on a single object strongly extended and whose elongation varies across the pupil, and ii) developing a large, fast and low-noise wavefront sensor able to image the full pupil and, at the same time, provide enough sampling for both elongated and non-elongated spots. In this chapter, we investigate the performance of a CMOS sensor intended to be used in a Shack-Hartmann WFS for the ELT.

This chapter is constructed around a publication submitted to JATIS, in the frame of the special issue dedicated to ELT development. The publication has been produced jointly with the Thirty Meter Telescope team (TMT), and it presents results from both the LGSWFS of the ELT and the TMT. The paper has been submitted to JATIS as a "co-first" authorship, between Felipe Pedreros-Bustos and myself. A complementary

analysis about the impact of the acceptance angle on the image formation, and a section about the quantization noise has been added at the end of this chapter.

3.2. JATIS PAPER - CMOS sensor performance for laser guide star wavefront sensing

CMOS sensor performance for laser guide star wavefront sensing

Zibo Ke[a,†], Felipe Pedreros Bustos[a,†], Jenny Atwood[b], Anne Costille[a], Kjetil Dohlen[a], Kacem El Hadi[a], Jean-Luc Gach[a], Glen Herriot[b], Zoltan Hubert[c], Pierre Jouve[a], Patrick Rabou[c], Jean-Pierre Veŕan[b], Lianqi Wang[d], Thierry Fusco[e,a], Benoit Neichel[a]

[a]Aix Marseille Univ, CNRS, CNES, LAM, Marseille, France
[b]NRC-Herzberg Astronomy & Astrophysics, Canada
[c]Univ. Grenoble Alpes, IPAG, CNRS, France
[d]TMT International Observatory LLC
[e]DOTA, ONERA, Université Paris Saclay (COmUE) [Châtillon]

Abstract. The adaptive optics (AO) systems of the future Extremely Large Telescopes (ELT & TMT) will be assisted with laser guide stars (LGS) which will be created in the sodium layer at a height of $\sim$ 90 km above the telescopes. In a Shack-Hartmann wavefront sensor, the long elongation of LGS spots on the sub-pupils far apart from the laser beam axis constraints the design of the wavefront sensor which must be able to fully sample the elongated spots without undersampling the non-elongated spots. To fulfill these requirements, a large CMOS sensor with 1100$\times$1600 pixels and 9 μm pixel pitch could be employed. Here, we report on the characterization of such a sensor in terms of noise and linearity, and we evaluate its performance for wavefront sensing based on the spot centroid variations. We then illustrate how this new detector can be integrated into a full LGSWFS for both the ELT and the TMT.

Keywords: CMOS detector, Wavefront sensing, Extremely Large Telescope, ELT, TMT, Laser Guide Stars.

† co-first authors. Send all correspondence to felipe.pedreros@lam.fr

1 Introduction

The astronomical community has just launched the construction of the largest ground-based telescopes, with the Extremely Large Telescope (ELT) and its primary mirror of 39 m in diameter on one hand, and the Thirty Meter Telescope (TMT) and its 30 m primary mirror on the other hand. These telescopes will answer fundamental questions ranging from the detection and characterization of exoplanets[1] to the formation and evolution of the first galaxies of the universe.[2]

In order to achieve their scientific goals, the TMT and the ELT require the use of adaptive optics (AO) to compensate for the aberrations introduced by atmospheric turbulence in the wavefront of the objects under study.[3] An AO system needs a bright star within the field of view of observation to measure the wavefront distortions using a wavefront sensor (WFS), typically a Shack-Hartmann WFS. These distortions are corrected in real-time by applying a feedback signal into a deformable mirror located in the optical path of the telescope, resulting in a flattened wavefront and therefore a near diffraction-limited image delivered to the science instrument. If a bright natural star is not available, an artificial beacon (laser guide star or LGS) is created by means of optical excitation of a layer of sodium atoms between 85 km and 100 km altitude using one or several lasers launched from the telescope.[4,5] The light emitted from the LGS is then used as a reference for the WFS in the AO system.

Laser excitation of the sodium layer produces a long column of fluorescent atoms whose extension depends on the pointing angle of the telescope and the vertical density profile of the sodium layer. For an observer located only a few meters off-axis the laser launch telescope (LLT), the LGS appears as an elongated object instead of a point source. The LGS spot elongation becomes dramatic for a 39 m-class telescope with side LLT configuration as the ELT.[6] For example, a 1 arcsec

LGS spot projected at zenith by a 30 cm diameter laser beam, will be seen by the sub-aperture of a Shack-Hartmann WFS opposite to the LLT on a 39 m diameter telescope as an elongated spot of about 10–20 arcsec long and about 1 arcsec width. The situation is less dramatic for the TMT, as it uses a central launch scheme, reducing the expected elongation by a factor $\sim$2 compared with the configuration of the ELT.

For a Shack-Hartmann WFS, the spot elongation introduces several issues. On the one hand, it reduces the signal-to-noise ratio since the same amount of photons once concentrated in a small spot are now distributed on a larger area on the detector, and on the other hand, it increases the wavefront error due to the growing uncertainty in the estimation of the center of gravity (CoG) of an elongated spot.[7] In addition, the spot truncation due to highly elongated spots not completely imaged on a given sub-aperture, leads to a bias in the estimation of the CoG in proportion to the fraction of truncation.[8]

Thus, the major challenges of LGS wavefront sensing at the ELT scale lie on i) performing a robust wavefront analysis on a single object strongly extended and whose elongation varies across the pupil, and ii) developing a large, fast and low-noise wavefront sensor able to image the full pupil and, at the same time, provide enough sampling for both elongated and non-elongated spots. While several post-processing mitigation strategies of elongated LGS have been developed,[9–14] we devote this work to the study of a Complementary Metal Oxide Semiconductor (CMOS) sensor intended to be used in a Shack-Hartmann WFS for the ELT and the TMT.

In Sec. 2 we lay out the primary requirements of a LGSWFS for the ELT and give an overview of possible technological solutions. In Sec. 3 we characterize a candidate CMOS sensor for the LGSWFS. In Sec. 4 we provide an analysis of the impact of this type of sensor in wavefront sensing. Finally, in Sec. 6 we assess our results and provide recommendations for the use of a CMOS sensor in the ongoing design of LGSWFS.

2 A detector for LGS wavefront sensing

2.1 Requirements for the Extremely Large Telescope

To ensure a correct measurement of the incident wavefront, the telescope pupil must be spatially sampled with a constant pitch of about 50 cm on the primary mirror. Taking as example the 39 m diameter telescope of the ELT, the Shack-Hartmann wavefront sensor needs to accommodate at least 78$\times$78 sub-pupils.

To correctly sample the smallest LGS spots, the pixel scale of the WFS detector must fulfill the accepted Nyquist sampling criteria of 2 pixels per FWHM. The minimum size of the LGS spot seen by the WFS depends on a number of factors like the laser beam size, telescope altitude, zenith angle, seeing, and thickness of the sodium layer. Statistical analysis of the LGS spot size at Paranal, shows a median angular spot size in the non-elongated direction of 1.5 arcsec FWHM and as low as of 0.95 arcsec FWHM in good atmospheric conditions.[15,16] Taking an LGS spot size of 1.0 arcsec, a pixel scale of 0.5 arcsec/pixel is required to fulfill the Nyquist criteria. Furthermore, if we consider a spot elongation of 16 arcsec on the outermost sub-pupils (this is the case for a $\sim$20 km vertical thickness sodium layer and a pointing angle of 30°), then a total of $\sim$32$\times$32 pixels per sub-pupil are needed to avoid truncation of the spot in the vertical or horizontal direction. To first order, a wavefront sensor with a full size of at least 2496$\times$2496 pixels would be necessary to sample the ELT pupil using 78 sub-pupils across and avoiding truncation of the elongated spot

while keeping the non-elongated direction sampled within the Nyquist criteria. Following a similar approach, the TMT configuration would require a wavefront sensor with 960×960 pixels.

The minimum required photon return flux of an LGS generated with state-of-the-art 20 W lasers is near 4×10^6 photons/s/m^2, therefore the photon flux in a sub-pupil of 50 cm diameter is on the order of 8×10^5 photons/s. Given the nominal integration time of 2 ms (500 Hz) required for AO correction, and provided an estimated optical throughput of 35%, the number of photons per frame on a single sub-aperture of the WFS is ~ 550 photons. The detection signal-to-noise-ratio (SNR) can be expressed as

$$\text{SNR} = \frac{N_P \times \text{QE}}{\sqrt{N_P \times \text{QE} + n_{\text{pix}} \times \text{RON}^2}}, \tag{1}$$

where N_P is the number of photons per sub-aperture per frame, QE is the quantum efficiency of the detector, RON is the root-mean-squared (RMS) read-out noise in electrons/pixel/frame, and n_{pix} is the number of pixels used to sample the LGS spot. Assuming $N_P = 550$ photons, QE $= 0.7$, $n_{\text{pix}} = 4$, and RON $= 3$ e$^-$/pixel/frame, we get an SNR of 19 for the case of a non-elongated spot. Considering an elongated spot covering 16 arcsec, we require $n_{\text{pix}} = 2 \times 32 = 64$ pixels for which we get an SNR of 12. At this point, we approach the read-out-noise-limited regime and, for example, doubling read-out noise (RON $= 6$ e$^-$/pixel/frame) gives an SNR of 7 for the same elongated spot. Therefore, it is critical that the read-out noise of the sensor used for the Shack-Hartmann WFS be as low as possible.

This example shows that an adequate detector for LGS wavefront sensing requires a) a large number of pixels, b) to operate at fast frame rates, and c) to have a very low read-out noise. Such a detector has not yet being developed as it is beyond the current technological capabilities, hence the final design of the wavefront sensor is constrained to the availability of existing detectors that can partially or in full, satisfy the aforementioned requirements.

Different technological strategies have been followed to try to answer this challenge. On the one hand, dedicated custom detector developments have been proposed both for the TMT and the ELT. For the former, the idea was to exploit the specific geometry of the LGS spots, and a radial charge-coupled device (CCD) has been proposed to fit the spot elongations.[17] Indeed, due to the central launch configuration, the spots seen by each of the LGSWFS Shack-Hartmann will be radially oriented. The proposed design implemented sub-apertures of about 4×16 pixels, with a radial geometry adapted to the spot elongation. For the ELT, a custom technological development toward a large 1600×1600 pixels sensor was also attempted,[18] resulting in a 800×800 pixels detector (so-called LISA[19]). In this paper we explore an alternative route offered by CMOS detectors, potentially offering large arrays, with low-noise and high frame-rate.

2.2 CMOS technology for LGS wavefront sensing

CMOS detectors are becoming competitive with respect to traditional CCD for astronomical detection. The construction design of CCDs in which there is only one or few read-out amplifiers for the whole array, increases the overall detector latency as the charge from each pixel are read out sequentially through the amplifiers. In contrast, CMOS technology has one read-out amplifier per pixel allowing massive parallel readout through read-out busses, hence reducing the latency of the sensor array. There are several ways to implement this process across the whole 2D array. Classically, the sensor can be read line-by-line which is known as rolling shutter architecture. This

architecture has the advantage to use only a few transistors per pixel (3 or 4) leading to simpler and lower noise CMOS imagers. However, each line of the array is exposed and read out sequentially so at different instants across the whole array. For objects moving at speeds comparable with the frequency of read-out, the images acquired with a rolling shutter sensor exhibit a distortion artifact called jelly effect. This is a potential disadvantage for wavefront sensing, because of the WFS may not be able to capture the state of the turbulence during one frame without introducing temporal shifts over the pupil spots.

However, in 1997 Fossum[20] introduced a more complex architecture using 5 transistors per pixel giving the ability to take a snapshot of the scene and store it in a memory which is then read out sequentially while the next image is integrated. In this scheme all pixels are read out at different instants, but exposed for the same amount of time, hence eliminating the temporal shifts in the final image. This architecture has the drawback of high read-out noise because of the Johnson–Nyquist reset noise that remains during read out. Later, more complex architectures using 6 transistors[21] or even 8 or 11 transistors architectures[22] permitted to integrate a correlated double sampling circuitry in each pixel that subtract the thermal noise at the expense of a much higher pixel complexity. Usually these imagers use finer lithographic pitch CMOS processes to keep the ratio of detection diode and transistor surface at an acceptable level compared to simpler architectures. The memory zone needs to be metal shielded to avoid collecting light, therefore the pixel fill factor of global shutter devices cannot reach 100% by construction, even if they are back illuminated. To overcome this limitation, micro lenses are integrated in the sensor to concentrate the light falling across the pixel on the detection diode.[23] However, this also brings a reduction in the sensor's sensitivity for oblique angle of incidence. This effect is seldom reported, but it plays an important role in the design of a wavefront sensor.

Recent developments in CMOS technology for astronomical applications[24,25] facilitated the rapid improvement in their performance that narrows or even surpass the gap with CCD. For example, the use of pinned photodiode reduces the dark current significantly,[26] and increasing the conversion gain or the implementation of source-follower transistor structures reduce read-out noise to sub-electron levels.[27] High quantum efficiency is another characteristic relevant for low-light applications, which has been addressed by using back-thinned CMOS sensors.[28] In addition to achieving high performance, another advantages of CMOS detectors is their capability to be operated at room temperature or alternatively with simple water-cooling, without the need of cryocoolers. This feature drastically reduce the complexity of the instrument.

In the following sections, we report on the characterization of a large CMOS sensor and its impact on the performance of laser guide star wavefront sensing.

3 Characterization of a CMOS sensor

3.1 Parameters

The sensor we evaluate is a Sony CMOS detector model IMX425LLJ on board of a C-BLUE One camera.[29] The detector array has 1604 $\times$ 1104 active pixels, each of which with a squared size of 9.0 μm $\times$9.0 μm. The active pixels include an analog-to-digital converter of 8-, 10-, or 12-bits and global shutter read-out. The quantum efficiency reported by the manufacturer is 70% at 590 nm.

In the following we present the characterization of read-out noise, angle of acceptance and cosmetics of the CMOS sensor.

3.2 *Noise characterization*

The main three sources of noise in an optical sensor are the read-out noise, the photon noise, and the fixed pattern noise (FPN). Read-out noise arises from the process of reading the pixel data. Photon noise is due to the quantum fluctuations of the light source and its occurrence is characterized by a Poisson probability distribution. The FPN is caused by spatial inhomogeneities across the sensor array in the analog-to-digital converter (ADC) embedded in each pixel.

In order to characterize the noises of the sensor, the photon transfer curve (PTC) can be obtained. The PTC describes the relationship between the output signal at different flux levels and the corresponding standard deviation of the output signal.[30] We assume that the total noise of the sensor in analog-to-digital units (ADU) is $\sigma_{\text{total}}(\text{ADU})$ and it can expressed as

$$\sigma_{\text{TOTAL}}(\text{ADU}) = [\sigma^2_{\text{RON}}(\text{ADU}) + \sigma^2_{\text{PN}}(\text{ADU}) + \sigma^2_{\text{FPN}}(\text{ADU})]^{1/2}, \tag{2}$$

where $\sigma_{\text{RON}}(\text{ADU})$ is the read-out noise, $\sigma_{\text{PN}}(\text{ADU})$ is the photon noise, and $\sigma_{\text{FPN}}(\text{ADU})$ is the fixed pattern noise.

The total noise can be obtained as the standard deviation of the average flux on a certain region in the sensor after offset subtraction. The photon noise in ADU can be expressed as

$$\sigma_{\text{PN}}(\text{ADU}) = \left[\frac{S(\text{ADU})}{K(e^-/\text{ADU})}\right]^{1/2}, \tag{3}$$

where $S(\text{ADU})$ is the average flux of the frame, and $K(e^-/\text{ADU})$ is the average conversion gain of the pixels.

The fixed pattern noise is stationary and it can be removed by taking the difference of two consecutive frames acquired with the same exposure time.[30] Then, the sum of read-out and photon noises can be expressed as

$$\sigma_{\text{RON+PN}}(\text{ADU}) = \left\{\frac{\sum_{i=1}^{N_{\text{PIX}}}[F1_i(\text{ADU}) - F2_i(\text{ADU})]^2}{2N_{\text{PIX}}}\right\}^{1/2}, \tag{4}$$

where $F1_i(\text{ADU})$ and $F2_i(\text{ADU})$ is the output signal of pixels i of two consecutive frames within a region of N_{PIX} pixels.

After removing the fixed pattern noise, we can estimate the photon noise as

$$\sigma_{\text{PN}}(\text{ADU}) = [\sigma_{\text{RON+PN}}(\text{ADU}) - \sigma_{\text{RON}}(\text{ADU})]^{1/2}. \tag{5}$$

In order to get results in electron unit, we need to obtain the gain of the pixel which can be expressed as

$$K(e^-/\text{ADU}) = \frac{S(\text{ADU})}{\sigma^2_{\text{PN}}(\text{ADU})}. \tag{6}$$

The measurements to characterize the PTC were performed as follows. A fiber-coupled light-emitting-diode (LED) with central wavelength of 595 nm and linewidth of 80 nm was used as a light source. The beam out of the fiber back-illuminated a diffuse white-translucent surface placed in front of the sensor. Black tubing was used between the illuminated surface and the sensor to minimize background light. The acquisition frame rate was set as 481 Hz, the sensor temperature

was 36°C. Although the light source over illuminated the full array, we only evaluated a region of 100×100 pixels in the center of the sensor array to minimize errors due to illumination inhomogeneity. Illumination and frame rate were held constant over the measurements, only varying the exposure time of the array.

The resulting photon transfer curve is shown in Fig. 1 (left). Three regions can be distinguished in the PTC: the read-out noise region at low signal level, the photon-noise region at intermediate signal, and the FPN region at high signal level. Since the read-out noise is the dominant noise source at low signal level, it can obtained in ADU units finding the best-fit horizontal line to the data in the read-out noise region. With increasing signal, the photon noise sets in and follows a linear relationship on the log-log coordinates as shown in yellow squares and with a linear fit. At high levels of signal pixels start to saturate. The full well capacity S_{FW} characterizes the saturation point and it can be calculated by the product between the signal value in ADU at the saturation point and the gain. Then, the estimated read-out noise, full well capacity and gain are $\sigma_{\mathrm{RON}} = 3.44\ \mathrm{e}^-$, $K = 0.28\ \mathrm{e}^-/\mathrm{ADU}$, and $S_{\mathrm{FW}} = 1001\ \mathrm{e}^-$, respectively.

An alternative method consist of acquiring a series of dark frames with short integration time (0.01 ms) and computing the temporal standard deviation of individual pixels. The distribution of noise over the full array is shown as the histogram in Fig. 1 (right). The mean read-out noise is 2.43 e^-, which is consistent with the result obtained from the photon transfer curve. The tail that appears on the distribution is attributed to random telegraph noise (RTN) arising from traps at the thin-layer interface in the source-follower gate region of metal-oxide-semiconductor field-effect transistors (MOSFET) of individuals pixels.[31]

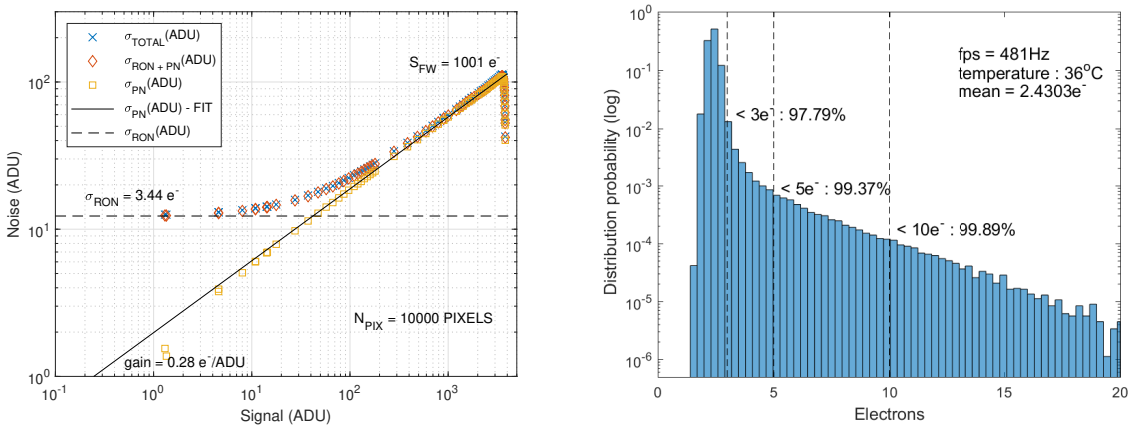

Fig 1 (Left) Measured photon transfer curve of the CMOS detector. (Right) The histogram of read-out noise distribution.

3.3 Angle of acceptance

CMOS sensors have small microlenses at the surface of their pixels that enhance their photon collection efficiency.[23,32] Although the on-axis sensitivity is improved, incident light at oblique angles is focalized off the center of the photosensitive area into light-insensitive structures of the pixel. This leads to a reduction of sensitivity for a light beam with a large angle of incidence. The characterization of the angle of acceptance is critical for the optical design of the wavefront sensor as it allows to choose the appropriate beam f-ratio that minimizes the detection losses.

The measurements setup is described as follows. The output beam from a fiber-coupled LED source (595 nm central wavelenght, 80 nm FWHM linewidth) is collimated with a 100 mm lens to a 23 mm diameter beam. A filter of 10 nm FWHM width centered at 590 nm is used to narrow the spectral width of the source around the sodium emission wavelength. A pupil of 4.2 mm clips the beam that is imaged with a 1:1 lens system into the sensor plane. The sensor is mounted on an micrometric stage that allows on-axis and horizontal rotation. For an initial on-axis position, the sensor is rotated $\pm 26°$ in the horizontal plane. A sequence of 100 frames are obtained for each angular position. The resultant average of the 100 frames is calculated. Only a window of 100×100 pixels centered in the circular footprint of the beam is used for processing. The average of all pixels in the window is taken as the representative intensity of the pixels. Due to the reducing irradiance on the sensor with increasing angle (the beam becomes elliptical on the sensor plane for large incidence angles), a factor of $1/\cos(\gamma)$ is applied to the normalized intensity values, where γ is the tilt angle of the sensor plane. After the full horizontal range in measured, the sensor plane is rotated in the optical axis and a new series of measurements are taken by rotating the sensor in the horizontal plane. Repeating this process, a complete angular sensor response is characterized.

Figure 2 shows the normalized response of the sensor in eight transverse planes. In the same figure, a contour plot representation of the angular response is shown. The response of the sensor is maximal at $0°$ incidence and decreases for larger angles. For each plane, the angular response is symmetric around the normal, but the acceptance angle increases toward the vertical plane. This could be explained by the presence of a rectangular photosensitive area elongated across the vertical axis.

We will show in section 4.3 how the angle of acceptance leads to light losses as a function of the focal ratio of the incident beam on the detector. This will provide valuable information for wavefront sensor designer to choose an appropriate optical configuration.

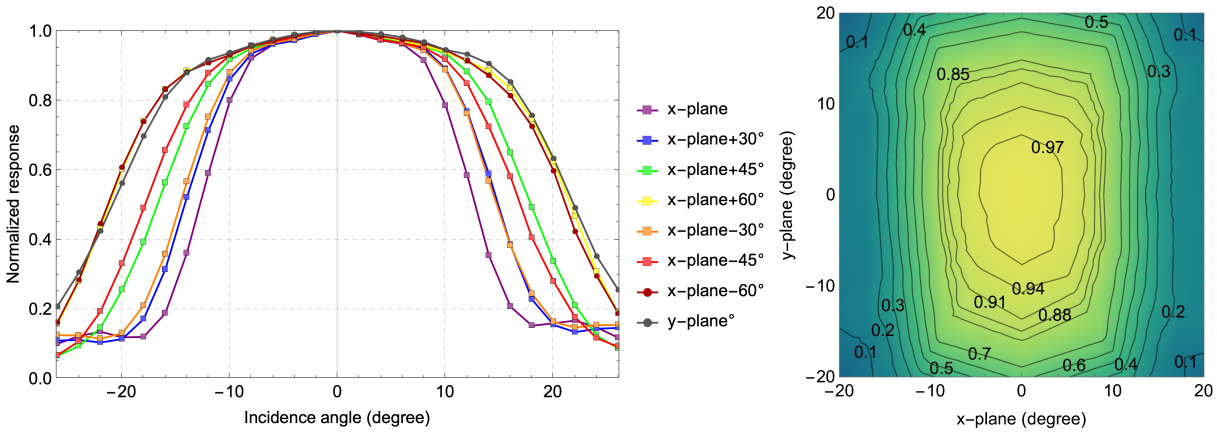

Fig 2 (Left) Normalized pixel angular response of CMOS detector in eight transverse planes (Right) Contour plot of the averaged-normalized angular pixel response.

3.4 Cosmetic

Because the size of the spot on the wavefront sensor is near a single pixel within the subaperture, it is crucial that the sensor array is free of defective elements (also called cosmetic defects). Hot

(bright) or cold (dark) pixels in a subaperture would cause a bias in the centroiding calculation, or a complete loss of the measurement if the defective pixel is located within the LGS spot.[33] Other cosmetic defects may include pixels with temporal instability and non-linear behaviour.

To characterize the presence of defective pixels we take a flat illuminated image with mean intensity at half the full-well-capacity, and we calculate the histogram (Fig. 3). We found no dark nor bright pixels over the entire array, which rules out any loss in performance due to defective elements.

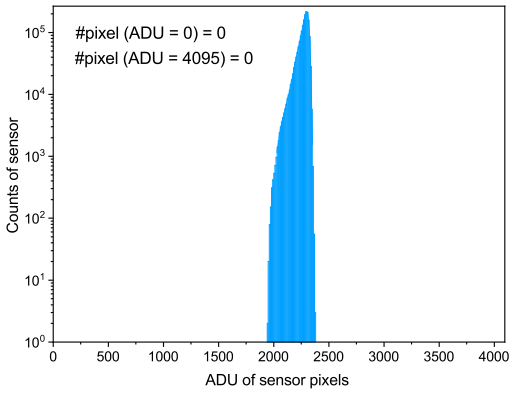

Fig 3 Logarithmic histogram of the flat illuminated image. No dead nor hot pixels are found.

4 Impact on LGS WFS

4.1 Centroiding error

The main sources of noise present in a wavefront sensor are photon noise and read-out noise. These two sources of noise can be expressed as two additive terms in the error of the center-of-gravity (CoG) estimator according to:[34]

$$\sigma^2_{\text{CoG}} = \underbrace{\frac{N_T^2}{8\ln(2)S_e}}_{\text{Photon}} + \underbrace{\left(\frac{\sigma_{\text{RON}}}{S_e}\right)^2 \cdot \left(\frac{N_S^4}{12}\right)}_{\text{Read-out}}, \tag{7}$$

where N_T is the full width at half maximum (FWHM) of the spot on the image, N_S is the pixels number of side length of the sub-aperture, σ_{RON} is the read-out noise, and S_e is the number of photons per sub-aperture and per frame.

Similarly, the weighted CoG (WCoG) can be expressed as:[35]

$$\sigma^2_{\text{WCoG}} = \underbrace{\frac{N_T^2}{8\ln(2)S_e} \cdot \left(\frac{N_T^2 + N_W^2}{2N_T^2 + N_W^2}\right)^2}_{\text{Photon}} + \underbrace{\frac{\pi(N_T^2 + N_W^2)^2}{128(\ln(2))^2} \cdot \left(\frac{\sigma_{\text{RON}}}{S_e}\right)^2}_{\text{Read-out}}, \tag{8}$$

where N_W is the FWHM of a weighted gaussian function.

We compare the theoretical centroiding error using the expressions above versus simulated and measured center-of-gravity errors. Figure 4 shows the CoG and WCoG variance as a function of

the input flux. Dashed lines show the photon-noise and read-out-noise components of the theoretical centroiding variance according to equations 7 and 8. We assumed $\sigma_{\mathrm{RON}} = 3.44\ \mathrm{e}^-$, as measured previously. Read-out noise dominates the centroiding error in the low-flux regime below 6×10^3 (photons/sub-aperture/frame) in the case of CoG estimation and below 1.5×10^3 (photons/sub-aperture/frame) for WCoG. The solid-blue line is the total variance of the CoG estimators. The green and orange squares are simulated centroiding errors. A gaussian spot of $\mathrm{FWHM}_x = 1.4$ pixels and $\mathrm{FWHM}_y = 1.5$ pixels was simulated on a 13×13 pixels sub-aperture. Photon noise was added to the simulated spot, as well as read-out noise following the skewed distribution shown in Fig. 1. The centroids of 200 simulated spots were estimated for each flux level using the CoG and WCoG methods. The simulated data points in the figure show the temporal variance in the x and y direction of the sequence. There is a good agreement between the simulated errors and the theoretical curve. In addition, centroiding measurements were performed by focalizing a spot of $\mathrm{FWHM}_x = 1.4$ pixels and $\mathrm{FWHM}_y = 1.5$ pixels at the center of the sensor. The width was estimated by a gaussian fit on the measured spot. A sequence of 50 frames with 2 ms integration time was obtained for each flux level, and the variance of the CoG sequence was calculated which corresponds to the centroiding error shown in Fig. 4. There is a good agreement between measurements and simulations, and they also show that the WCoG is able to reduce the centroiding error by a factor of ~ 2 within the photon flux regime expected for LGS wavefront sensing.

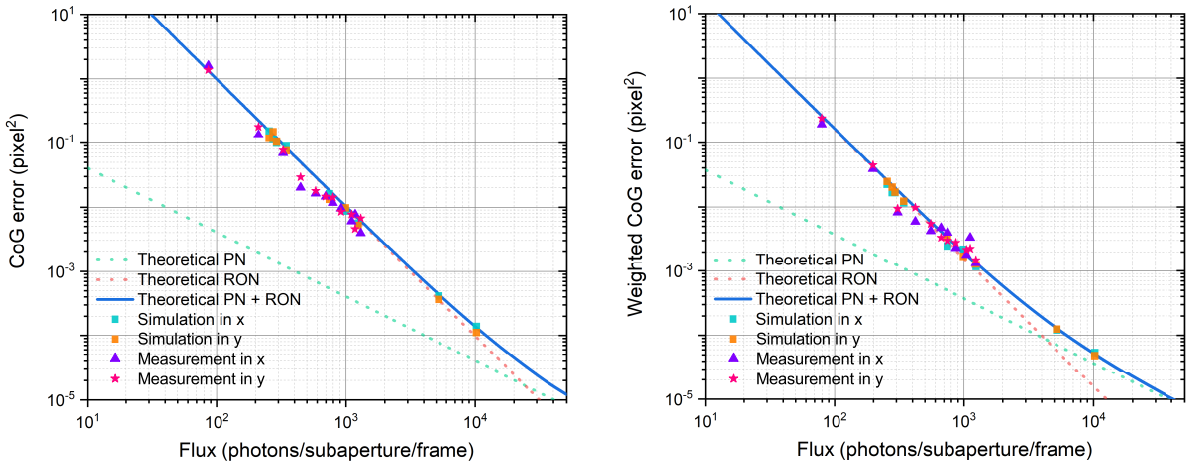

Fig 4 (Left) Comparison of error variance of CoG among real measurements, simulation and theory. (Right) Comparison based on weighted CoG.

The effect of the measured read-out noise distribution in the centroiding is shown in Fig. 5. Here, we compare the resulting centroid error as a function of the photon flux (based on the simulations described above) for a theoretical Gaussian RON distribution and for the measured RON distribution (see inset plot). The additional error introduced by the group of pixels with higher read-out noise is below 0.1 pixel^2 for an incoming flux above 150 (photons/subaperture/frame), showing a negligible impact for typical operating conditions with flux higher than 500 (photons/subaperture/frame).

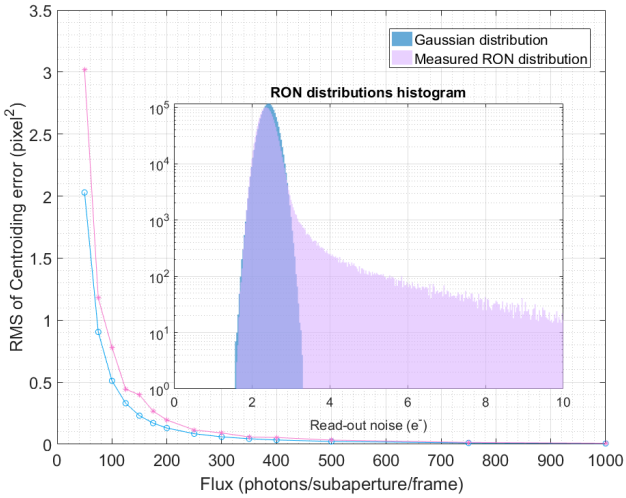

Fig 5 Centroiding error based on a theoretical Gaussian distribution of read-out noise and measured skewed distribution of read-out noise.

4.2 CoG linearity

The spot size relative to the dimensions of the pixels, i.e. the spot sampling frequency (s), can have a significant impact in the linearity of the centroid estimation as the spot size approaches the size of a pixel. Even at the accepted Nyquist sampling criteria of $s = 2$ pixel per FWHM, centroid non-linearities start to build up.[36] Therefore, the selection of the spot sampling frequency in a wavefront sensor is a trade-off between minimum noise (small spot size) and high centroid linearity (large spot size). In this section we study how the centroid varies as a function of the sampling frequency and as a function of the lateral displacement of the spot over the CMOS sensor, and we compare with simulations.

The experimental arrangement consists of a fiber-coupled LED source with a fiber core of 400 μm placed at a distance of 1300 mm from a lens of 24 mm clear aperture and 40 mm focal length that forms an image of the source at the surface of the CMOS sensor located at 40 mm from the lens. In this simple configuration, the magnification of the optical system is $M = 40/1300 = 0.03076$. The theoretical size of the image is 12.3 μm or 1.36 pixels. A lateral displacement of the source is also magnified in proportion to M. In the current setup, the source is laterally shifted with a step of $\delta_S = 40$ μm, corresponding to a spot lateral displacement step of $\delta_I = 1.2$ μm. We displace the spot by 25.2 μm in steps of 1.2 μm over almost 3 pixels. For each step, we acquire 30 consecutive images and calculate the CoG for each frame. The average CoG relative to the initial pixel position and the standard deviation of the CoG are calculated as a function of the pixel position of the spot. In order to understand any possible effects of the acceptance angle in the linearity of the CoG, we repeat the procedure at different tilt angles of the sensor such that the CoG linearity can be evaluated for several angles of incidence.

The CoG at each angle of incidence θ and for a given spot sampling frequency s can be represented as a linear function plus an oscillating term as follows:

$$\mathrm{CoG}_{(\theta,s)}(x) = \underbrace{A\,x + B}_{\text{Linear}} + \underbrace{W_s \sin(2\pi x + \phi_x)}_{\text{Residual}}, \tag{9}$$

where x is the pixel displacement, A and B are parameters of the linear CoG response, W_s is the amplitude of CoG oscillations at a sampling frequency s, and ϕ_x is an arbitrary pixel phase.

Figure 6 shows the calculated CoG relative to the initial pixel position as a function of the pixel displacement for incidence angles between $-20°$ and $+20°$. A linear fit is estimated for each data set. The values of the slopes of the linear component of the CoG (parameter A) for all tilt angles are shown in the inset table in the same figure. The measured linear slope deviate less than 5% with respect to the ideal linear response ($A = 1$), showing a negligible effect on the linearity as a result of the angle of acceptance.

Figure 7 shows the residual of the data shown in Fig. 6, i.e. the difference between the measured CoG's and the linear fit. This corresponds to the residual term of Eq. 9. We show the residuals data obtained at normal incidence and for three spot sizes: 1.08 pixel FWHM, 1.14 pixel FWHM, and 1.36 pixel FWHM. The spot size are estimated using a Gaussian fit and their values correspond to the spot sampling frequency s. For each measurement, a sine function is fit to the data (blue curve) and the result of a simulation is also displayed (red curve). There is a good agreement among simulations, the fit curve, and measurements. The amplitude of the residual CoG, i.e. the degree of non-linearity, is described by the parameter W_s in Eq. 9. The value of W_s for each measurement is shown in the figure. For the most undersampled case ($s = 1.08$ pixel), the degree of non-linearity reaches 4.2% of a pixel and for the least undersampled case ($s = 1.36$ pixel) the degree of non-linearity is reduced to 0.9% of a pixel. These measurements show that the increase in CoG non-linearities in the CMOS sensor under study behave as expected, and that sampling the spot frequency below the Nyquist criteria yield a degree of non-linearities that is relatively small compared to the pixel size.

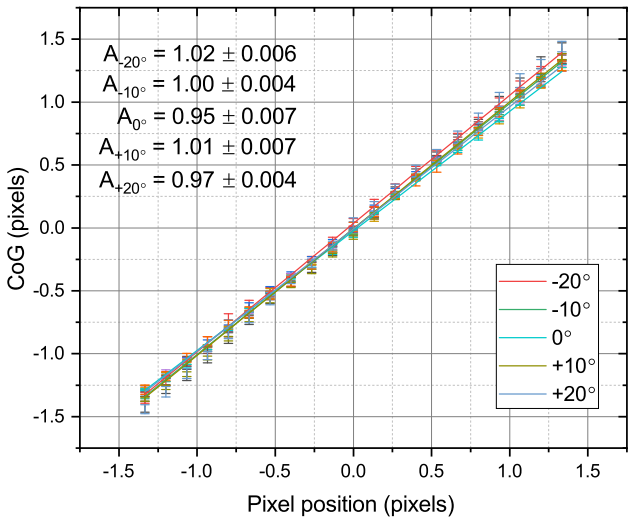

Fig 6 Measured CoG as a function of the pixel displacement with the sensor tilted at five different angles. A linear fit is applied to each data set. The spot sampling frequency was estimated as 1.14 pixels FWHM. The linear slope parameter A for each data set is shown at the top left.

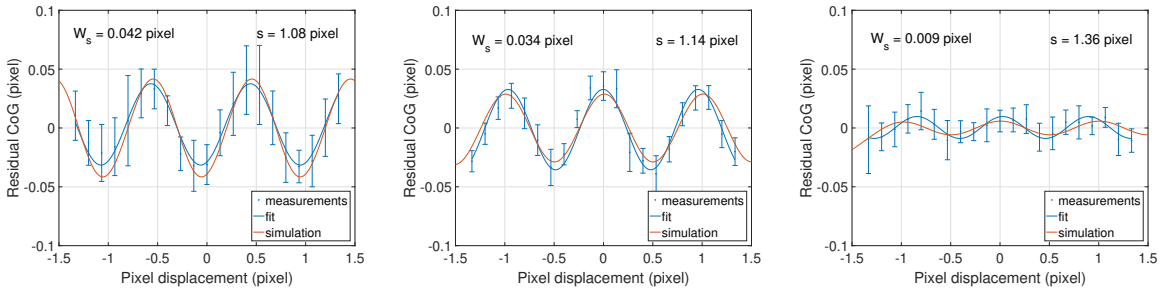

(a) (b) (c)

Fig 7 Residual CoG as a funcion of the pixel displacement compared to a sine fit function and simulations for a spot sampling frequency of (a) 1.08 pixels FWHM, (b) 1.14 pixel FWHM and (c) 1.36 pixel FWHM. All measurements obtained at normal incidence.

4.3 Transmission loss due to angle of acceptance

The angular response characteristic of the CMOS sensor gives rise to a transmission loss through the focalizing element (e.g. lenslet array of the Shack-Hartmann wavefront sensor) as off-axis rays are focalized into the sensor with a slanted angle of incidence.

The photon flux transmission due to the angle of acceptance can be estimated as:

$$\eta_{\text{acc}} = \frac{\int_{-\alpha}^{+\alpha}\int \hat{G}(x,y)dxdy}{H(\alpha)}, \tag{10}$$

where $\hat{G}(x,y)$ is an estimate of the normalized angular response obtained with interpolation of the measured data over the horizontal and vertical angular directions (see Fig. 2), $H(\alpha)$ is a function that describes the lenslet window, and α is the beam detector angle (in degree) given by

$$\alpha = \frac{1}{M}\arctan\left[\left(\frac{\text{FF}+1}{2}\right)\frac{1}{2N_L}\right] \times \frac{180}{\pi}, \tag{11}$$

where N_L is the lenslet nominal side F-number, FF ≤ 1 is the linear fill factor of the lenslet array, and M is the magnification of any optical relay between the lenslet array and the sensor plane. The beam F-number on the detector side is $N_D = 1/(2\ \tan(\alpha))$. For the case of a squared lenslet $H_{\text{squared}}(\alpha) = 4\alpha^2$ and for the case of a circular lenslet $H_{\text{circular}}(\alpha) = \pi\alpha^2$. These expressions assume no loss between the lenslet array and the detector other than the detector angular response. We also assume image telecentricity, i.e. the chief rays are always at normal incidence on the detector, independent of the position of the lenslet over the pupil and of the distance of the object from the center of the field of view.

Assuming FF $= 1$ (no apodization in the lenslet array) and the measured angular response of the CMOS sensor, we estimate the transmission through a Shack-Hartmann wavefront sensor as a function of the detector F-number for the case of a circular and squared lenslet configuration. A reduction in transmission of 4% and 6% occurs at $f/3.0$ for the circular and squared lenslet, respectively. Smaller beam F-ratios lead to a stronger reduction in transmission as the beam is focalized at larger angles. This analysis shows that purely geometric considerations in the design

of a Shack-Hartmann wavefront sensor with a CMOS sensor, result in light losses that should be taken into account to minimize the impact in the overall throughout of the optical system.

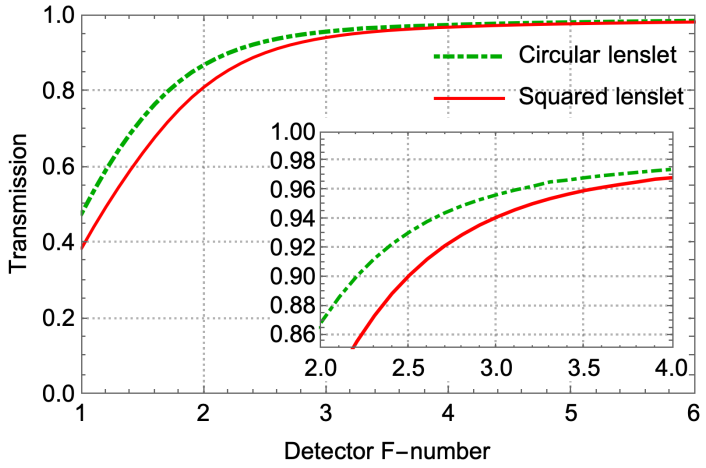

Fig 8 Transmission efficiency due to angle of acceptance of a CMOS sensor as a function of the detector beam F-number.

5 Examples of implementation of a CMOS detector into a LGS WFS

In this section we provide a preliminary design of a full LGS WFS arm for the ELT and the TMT. For the former, we take as an example the Laser Tomography Adaptive Optics (LTAO) system of HARMONI,[37] which will make use of the 6 LGS provided by the ELT. For the latter, we show the implementation for NFIRAOS,[38] the TMT Multi-Conjugate Adaptive Optics (MCAO) system. The goal of this section is not to report on a final design for the these instruments, but rather to show that a practical implementation of the CMOS sensor under study in LGS WFS is feasible.

5.1 HARMONI design

The main parameters of the LGSWFS for HARMONI are summarized in Table 1.

Table 1 Specifications of the HARMONI LGS WFS.

Parameter	Value	Comment
ELT primary mirror diameter	39 m	Size of the pupil
# LGS	6	Side launch provided by 4 launch stations
# Subaperture	68×68	Spatial sampling of 57 cm. Squared lenslets.
# pixels per subaperture	16×16	with at least 15×15 useful pixels
LGSWFS pixel scale	1.1 arcsec/pixel	Required for sampling LGS spots
Subaperture Field of View	16.5 arcsec	Side FoV. Required for minimizing truncation

5.1.1 Optical Relay

Due to the wide field of view (FoV) required for LGS wavefront sensors, the microlens focal length is very short. To avoid assembling a microlens inside the detector chip, it is necessary to design a

relay system to reimage the Shack-Hartmann spots onto the detector. This problem is common with other ELT instruments, and similar conclusions apply to NFIRAOS as well. The implementation of an optical relay between the lenslet and the detector increases the overall size and the number of elements in the WFS, but it also relaxes the complexity of the microlens design. It also allows for a better management of the beam angles and acceptance within the detector.

The primary goal of the optical relay is to compress the pupil size from the lenslet array pupil to the detector size. The pupil diameter on the lenslet array is fixed to be 24 mm, due to other optical constraints. The pupil size on the detector is 9.792 mm, hence the magnification factor is $M = 1/2.45$. In order to provide high optical performance, both in terms of image quality and distortions, a six-lenses design has been proposed as shown in Fig. 9. The overall performance of this relay has been defined such as the distortion shall be less than ± 0.03 sub-aperture with respect to a perfect grid, with a variation of less than ± 0.01 sub-apertures within operating conditions during the instrument lifetime. In terms of optical quality, the relay does not degrade the quality of the spot image when taking onto account the quadratic sum of the contributors to the wavefront error budget. This relay also takes the telecentricity into account, as this is an important factor for coupling light with detector pixels (see Section 5.1.2), and the telecentricity error is less than $\pm 1.5^\circ$ at the detector level. Although the system contains a large number of optical surfaces, the penalty in terms of transmission budget is minor since highly efficient monochromatic AR coatings are available. High performance coatings with less than 0.25% reflectivity are considered here.

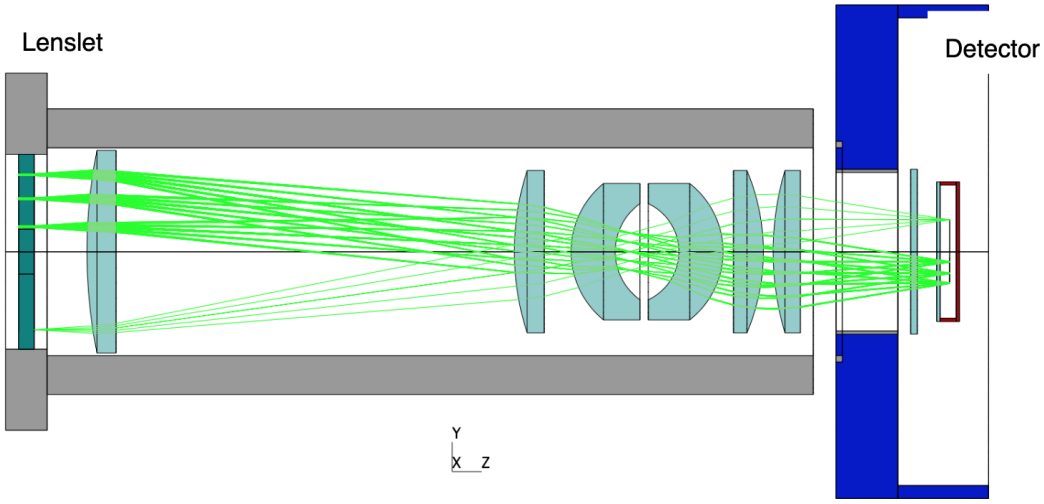

Fig 9 Ray tracing diagram of the lenslet, optical relay and detector. The overall lenght of the relay is about 150 mm.

5.1.2 Lenslet Array

The requirement for LTAO is to have the largest FoV as possible, with at least a squared field stop of 16 arcsec FoV. As described above, one of the challenges imposed by the CMOS detector comes from the acceptance angle. The optical design of the lenslet array must then be carefully though not to loose significant flux at the coupling with the detector. The acceptance angle is linked to the maximum focal ratio that can be accepted by the detector. The focal ratio of the beam onto the

detector plane is determined by specific parameters and the following formula:

$$F = \frac{N \cdot d}{D \cdot \beta}, \tag{12}$$

where N is number of sub-apertures, d is the pixel size, D is the pupil diameter and β is the on-sky pixel scale. For $N = 68$, $d = 9$ μm, $D = 39$ m and $\beta = 1.1$ arcsec/pixel, the detector focal ratio is 2.94. A total of 68 sub-apertures require 1088 pixels, or 16 pixels per sub-aperture. If we consider 1 guard pixel between sub-apertures (for alignment margin purposes), there are 15 useful pixels per sub-aperture, covering a total FoV of 16.5 arcsec. The lateral size of a sub-aperture is then 135 μm and the required focal length of the lenslet is 397 μm. In this optical configuration, the maximum angle of incidence on the edge of the sub-aperture is given by

$$\theta_m = \arctan \frac{d_u}{f_u} = 18.7^\circ, \tag{13}$$

where d_u and f_u are the diameter and the focal length of the lenslet. This angle corresponds to an F-ratio of 1.47. According to the measurement on the CMOS detector, such an angle of incidence would lead to a large loss of light due to the coupling with the pixel.

To decrease the maximum angle of arrival on the detector from LGSS, we propose to use a double microlens concept. Figure 10 shows the ray tracing for a classical microlens array and a double microlens array concept. This concept has the advantages to create a telecentric image, and when in use with an optical relay between the microlens array and the detector, to create a pupil in the relay. In this case, the image is telecentric and then the input angle on the detector is equal to:

$$\theta_m = \arctan \frac{d_u}{2f_u} = 9.35^\circ, \tag{14}$$

corresponding to a F-number equal to 2.94. Hence we are in the acceptable range of angle of acceptance for the detector with a limited impact on LTAO performance. The flux loss, when integrated over the whole subapeture, will be less than 5%. It has then been decided to use a double microlens array for HARMONI.

In summary, the HARMONI design employing a double sided microlens array has several advantages:

- Reduction of the beam angle after the microlens array.
- Creation of a telecentric image.
- Using a thick substrate of 3.5 mm, the focus of the lenslets can be on the backside of the substrate, therefore printing the same lenslet with the same focal length.
- Reduction of the size of the optics inside the relay.
- Reduction of the distortion of the relay optics.

The technical feasibility of such double lenses has been verified with industrial companies, and no issues have been identified. A prototype has been built and tested, showing the conformity of the lenslet built with HARMONI specifications.

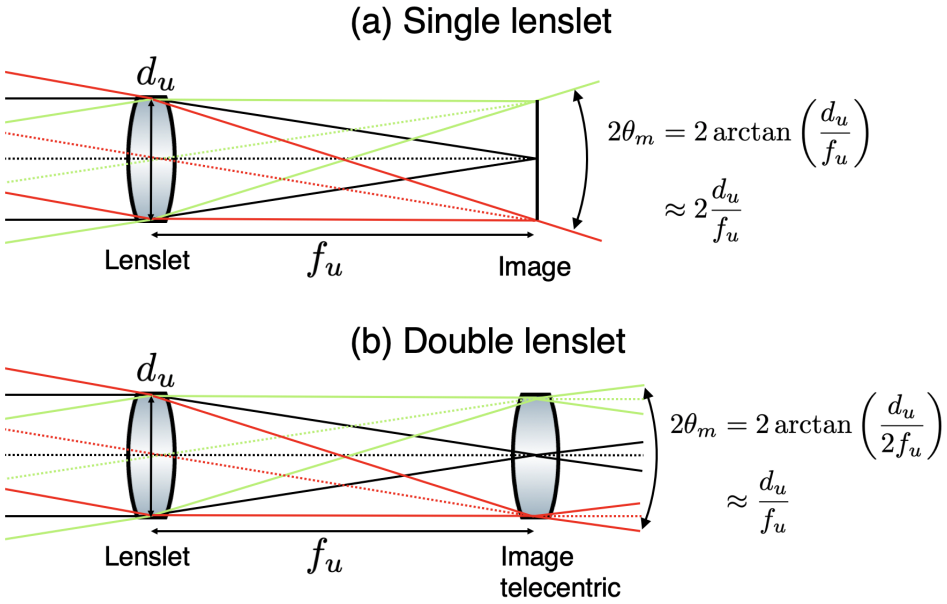

Fig 10 (a) Single lenslet array in front of the detector, and (b) double microlens array concept forming a telecentric image. In the double microlens array concept, the maximum incidence angle is reduced by half in comparison with the single lenslet, and the chief rays are parallel to the optical axis across the full FoV. An optical relay is required to re-image the focal plane on the detector plane.

5.2 TMT NFIRAOS design

For NFIRAOS, the current baseline is:

Table 2 Specifications of the NFIRAOS LGS WFS.

Parameter	Value	Comment
TMT primary mirror diameter	30 m	Size of the entrance pupil
# LGS	6	Central launch provided by a single launch station
# Subaperture	75×75	Spatial sampling of 40 cm
LGS WFS pixel scale	1 arcsec	Required for sampling LGS spots
Subaperture Field of View	11 arcsec	Required for minimizing truncation

5.2.1 Detector configuration

One interesting feature of the CMOS detector is that the read-out architecture can be configured to skip rows. One can therefore decide to only read a region of interest (ROI), the full width of the detector, and the maximum frame rate is increased in proportion to the number of rows skipped. Since TMT has a smaller diameter and will launch its LGSs from behind the secondary mirror, NFIRAOS will see significantly less-elongated spots than HARMONI. The FoV of the NFIRAOS WFS subapertures does not need to be as large and therefore only a portion of the detector can be read. This opens a tradeoff space between the number of sub-apertures, the number of pixels per sub-aperture and the maximum frame rate.

For NFIRAOS, simulations show that a 10 arcsec sub-aperture field of view is sufficient for all simulated sodium profiles with no penalty due to truncation and a pixel scale of 1 arcsec is optimal except for very poor seeing conditions ($r_0 \sim 0.1$ m) where a larger pixel scale could provide better

performance. We add one extra pixel per sub-aperture to accommodate slope offsets. It was also found that slightly over sampling the pupil with 75×75 sub-apertures, compared to the 60×60 deformable mirror (DM), helps to reduce the wavefront reconstruction error, especially in poor seeing conditions or higher signal level cases than our conservative baseline.

The minimal number of pixels required to accommodate the NFIRAOS configuration is 825×825 (11 pixels per sub-aperture over 75 sub-apertures). However, the CMOS camera will read 848×1608 pixels. The extra pixels are allocated among various optomechanical tolerances, as described in the next section.

With this design, the maximum achievable frame rate is slightly over 600 Hz which is still acceptable for the expected LGS signal levels and wind speed.

5.2.2 ROI flexibility and tolerancing

The WFS concept permits loosening or even avoiding various traditionally tight tolerances due to: the flexible readout region; the 23 additional pixels; and an array of 100×100 lenslets.

For example, oversampling the 60×60 DM actuator grid completely removes the strict alignment tolerances to register actuators to lenslet corners, which are usually needed for a Fried geometry. Furthermore, to handle DM pupil illumination shifts at the oversized 100×100 lenslet array, software can select an arbitrary set of lenslets. However, tolerances on magnification of the pupil image remain constrained, because sub-apertures are discretized into 11 pixels. E.g. to read 76×76 sub-apertures would require 11 rows of pixels, too large a fraction of the 23 pixel margin.

The most innovative use of the extra pixels is to handle slope offsets larger than the notional 1 arcsecond budget for non-common path aberration (NCPA) calibration. But that budget applies per sub-aperture. The square regions of pixels for each spot do not have to lie on a square grid. By adding "leap pixels" periodically between sub-apertures (Fig. 11 left), larger dynamic range of offsets can be calibrated, providing they are slowly varying across the pupil, which is the case for low-order aberrations.

One important situation is differential focus among six LGS WFSs. One trombone cannot exactly compensate focus for all LGSs unless they are built and installed perfectly. Differential focus produces a different magnification of the spot pattern among the WFS, and deducts from the slope budget. However we can fix it in software by "stenciling" 11×11 pixels from the image. The stencils are chosen to always keep the slope offset within 0.5 pixel of the center.

Note that to avoid collisions between sub-aperture ROI stencils, we can only add space between them. So for e.g. astigmatism where the calibrated spot pattern is compressed in one axis and expanded orthogonally, the trombone controller calibration would be biased to always expand the pattern.

As shown in the right panel of Fig. 11, clocking of the lenslets versus the detector is handled in software. Note that because the outer active DM actuators are not in a circle, but actually a polygon with flat sides of several actuators in a line, clocking the spot pattern as shown does mean that WFS spots at vertices of the polygon do move outwards by approximately a pixel.

The most difficult constraint remains the profile tolerance (single digits of microns for tilts plus piston) of the detector with respect to the lenslets due to defocussing in fast beams. When NFIRAOS operates at $-30°$C the detector moves $\sim$ 20 μm axially towards the lens mounting interface and the optical relay shrinks in the opposite direction, compared to room temperature.

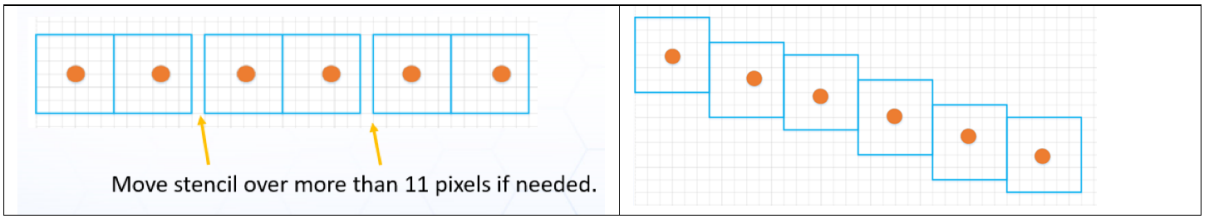

Fig 11 (Left) Leap Pixels for low order NCPA. (Right) Software defined stencils for clocking lenslets versus detector.

We will jointly optimize the athermalization of the relay lens barrel, described below, to account for both.

5.2.3 Optical relay

For NFIRAOS, the pupil diameter on the lenslet array was chosen to be 15.75 mm, leading to a relay with magnification $M = 1/2$. Smaller pupil sizes make the relay shorter and therefore easier to package, but the lenslets become faster, and therefore significantly more challenging and expensive to fabricate. The 15.75 mm pupil diameter was chosen as a reasonable tradeoff.

The proposed relay is shown in Fig. 12. It has six lenses and is actually quite similar to that of HARMONI. The only possibly concerning element is the F2 lens, which exhibits a large curvature that could be costly to fabricate.

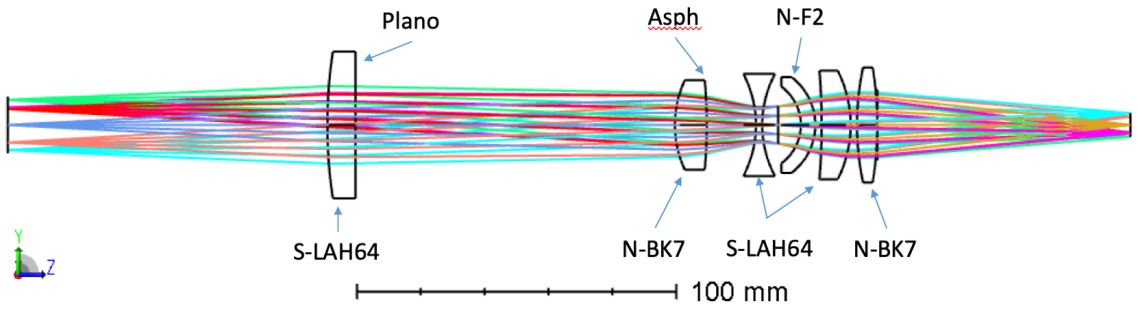

Fig 12 Ray tracing diagram of the lenslet, optical relay and detector. The overall length of the relay is about 380 mm.

This relay design has excellent image quality and distortion over the full field of view. The distortion is $<0.01\%$ and the max RMS wavefront error across the FoV is 0.012˜waves (7 nm) with a variation of 0.005 waves. The design includes one aspheric surface on N-BK7 to help control the wavefront error at the edge of the FOV. The asphere has two terms (4th and 6th order) and ~ 50 μm of departure.

We have modeled the full optical path from the sodium layer, through TMT and NFIRAOS, and through the lenslet and relay to the detector. The images from the top and bottom of the sodium layer are easily resolved in the model. The glasses chosen for this design are all highly transmissive in the visible spectrum, with a bulk absorption of $<1\%$. The overall throughput will therefore depend on the quality of the coatings. As in HARMONI, NFIRAOS plans to use high performance monochromatic dielectric coatings.

5.2.4 *Lenslet array*

For NFIRAOS, we have $N = 75$, $d = 9$ μm, $D = 30$ m, $\beta = 1$ arcsec/pixel, providing a focal ratio of $F = 4.64$ at the detector. The steepest angle of incidence at the edge of the field of view with a conventional lenslet array would be $\theta_m = 12.2°$ resulting in light loss due to the limited acceptance angle of the CMOS pixels. This angle, and therefore the loss, would be further increased because of our proposed scheme to skip pixels in order to use larger slope offsets (section 5.2.2). This motivates the use, like HARMONI, of a double lenslet array, where the second surface acts as a field lens to produce a telecentric image at the detector, thus reducing the steepest angle by half. For the proposed NFIRAOS design, the main parameters of the required lenslet array are 210 μm pitch, a radius of both surfaces of 0.945 mm and thickness of 3 mm. Such a lenslet array is considered well within the capabilities of manufacturers.

6 Conclusion

We have evaluated the performance of a CMOS sensor compatible with the current requirements of wavefront sensor of laser guide stars in the context of extremely large telescopes.

We have shown that the read-out noise around 3 e^- is achievable for a large sensor array. The statistical distribution of read-out noise over the sensor shows a tailed shape which is characteristic of CMOS sensor. The impact of this read-out noise excess is the centroid estimation is negligible for flux above 200 photons/sub-aperture/frame.

The average angular response of the sensor was characterized showing a two-axes symmetry with full width half maximum of 42.6° in the vertical direction and 25.4° in the horizontal direction. The angle of acceptance leads to a light transmission loss depending of the beam aperture on the sensor. We provide the calculated transmission curves for circular and squared lenslet shapes as a reference for wavefront sensor designers using this type of detectors.

The error of center of gravity was employed as a metric to evaluate the performance of the detector to wavefront sensing. We simulated and measured the CoG errors as a function of the photon flux and found a good agreement between theory and experimental results. The centroiding linearity was measured for different spot size and angles of incidence. The rising of non-linearities in the estimation of the CoG is in agreement with our simulations and shows that for a sampling frequency of 1.36 pixel per FWHM (Nyquist undersampled), the degree of non-linearities is only 0.9% of a pixel.

Finally, we show two examples of practical implementations of this detector in LGS wavefront sensors for the ELT and TMT adaptive optics systems. The need of additional relay optics between the microlens array and the detector is common in both cases. In particular, the telecentric double-sided lenslet array in the HARMONI design comes as an innovative solution to minimize the impact of the angle of acceptance in sub-apertures requiring a wide field of view. **[Add here some remarks about the TMT design]**. These two examples show that this type of detector is suitable for LGS wavefront sensing on extremely large telescopes.

Acknowledgments

Z.K. acknowledges financial support from China Scholarship Council. This project received funding from the European Union's Horizon 2020 research and innovation programme under the Marie Sklodowska-Curie grant agreement No 893150. This work also benefited from the support of the

WOLF project ANR-18-CE31-0018 of the French National Research Agency (ANR). This document has been prepared as part of the activities of OPTICON H2020 (2017-2020) Work Package 1 (Calibration and test tools for AO assisted E-ELT instruments). OPTICON is supported by the Horizon 2020 Framework Programme of the European Commission's (Grant number 730890). This work was supported by the Action Spécifique Haute Résolution Angulaire (ASHRA) of CNRS/INSU co-funded by CNES. This work has been partially supported by the LabEx FOCUS ANR-11-LABX-0013

References

1 G. A. Hawker and I. R. Parry, "High-resolution spectroscopy and high contrast imaging with the ELT: looking for O_2 in Proxima b," *Monthly Notices of the Royal Astronomical Society* **484**, 4855–4864 (2019).

2 B. García-Lorenzo, A. Monreal-Ibero, E. Mediavilla, *et al.*, "Black hole-galaxy scaling relation evolution from Z$\sim$2.5: Simulated observations with HARMONI on the ELT," *Frontiers in Astronomy and Space Sciences* **6**, 73 (2019).

3 H. Bonnet, F. Biancat-Marchet, M. Dimmler, *et al.*, "Adaptive optics at the ESO ELT," in *Adaptive Optics Systems VI*, L. M. Close, L. Schreiber, and D. Schmidt, Eds., **10703**, 327 – 335, International Society for Optics and Photonics, SPIE (2018).

4 W. Happer, G. J. MacDonald, C. E. Max, *et al.*, "Atmospheric-turbulence compensation by resonant optical backscattering from the sodium layer in the upper atmosphere," *J. Opt. Soc. Am. A* **11**, 263–276 (1994).

5 C. A. Primmerman, D. V. Murphy, D. A. Page, *et al.*, "Compensation of atmospheric optical distortion using a synthetic beacon," *Nature* **353**, 141–143 (1991).

6 E. Vernet-Viard, F. Delplancke, N. N. Hubin, *et al.*, "LGS Na spot elongation and Rayleigh scattering effects on Shack-Hartmann wavefront sensor performances," in *Adaptive Optics Systems and Technology*, R. K. Tyson and R. Q. Fugate, Eds., **3762**, 8 – 19, International Society for Optics and Photonics, SPIE (1999).

7 S. J. Thomas, S. Adkins, D. Gavel, *et al.*, "Study of optimal wavefront sensing with elongated laser guide stars," *Monthly Notices of the Royal Astronomical Society* **387**, 173–187 (2008).

8 R. M. Clare, S. J. Weddell, and M. Le Louarn, "Mitigation of truncation effects in elongated Shack-Hartmann laser guide star wavefront sensor images," *Applied Optics* **59**, 6431 (2020).

9 L. Schreiber, M. Lombini, I. Foppiani, *et al.*, "An optical solution to the LGS spot elongation problem," in *Adaptive Optics Systems*, N. Hubin, C. E. Max, and P. L. Wizinowich, Eds., *Society of Photo-Optical Instrumentation Engineers (SPIE) Conference Series* **7015**, 70151O (2008).

10 A. G. Basden, L. Bardou, D. Bonaccini Calia, *et al.*, "On-sky demonstration of matched filters for wavefront measurements using ELT-scale elongated laser guide stars," *Monthly Notices of the Royal Astronomical Society* **466**, 5003–5010 (2017).

11 A. Berdja, E. Garcés Santibañez, and C. D. Guzmán, "Experimental results on using artificial neural networks for accurate centroiding in Shack-Hartmann wavefront sensors with elongated spots," in *Adaptive Optics Systems V*, E. Marchetti, L. M. Close, and J.-P. Véran, Eds., *Society of Photo-Optical Instrumentation Engineers (SPIE) Conference Series* **9909**, 99093Y (2016).

12 C. Béchet, M. Tallon, I. Tallon-Bosc, *et al.*, "Optimal reconstruction for closed-loop ground-layer adaptive optics with elongated spots," *J. Opt. Soc. Am. A* **27**, A1–A8 (2010).
13 E. N. Ribak and R. Ragazzoni, "Reduction of laser spot elongation in adaptive optics," *Optics Letters* **29**, 1351–1353 (2004).
14 L. Gilles and B. Ellerbroek, "Shack-Hartmann wavefront sensing with elongated sodium laser beacons: centroiding versus matched filtering," *Applied Optics* **45**, 6568–6576 (2006).
15 S. Oberti, J. Kolb, P.-Y. Madec, *et al.*, "The AO in AOF," in *Adaptive Optics Systems VI*, L. M. Close, L. Schreiber, and D. Schmidt, Eds., *Society of Photo-Optical Instrumentation Engineers (SPIE) Conference Series* **10703**, 107031G (2018).
16 W. Hackenberg, D. Bonaccini Calia, B. Buzzoni, *et al.*, "ESO 4LGSF: Integration in the VLT, Commissioning and on-sky results," in *Adaptive Optics Systems VI*, *Society of Photo-Optical Instrumentation Engineers (SPIE) Conference Series* **9909** (2016).
17 J. E. Beletic, J. W. Beletic, and P. Amico, "Scientific Detectors for Astronomy 2005," *Astrophysics and Space Science Library* **336** (2006).
18 M. Downing, M. Casali, G. Finger, *et al.*, "AO WFS detector developments at ESO to prepare for the E-ELT," in *Adaptive Optics Systems V*, E. Marchetti, L. M. Close, and J.-P. Véran, Eds., *Society of Photo-Optical Instrumentation Engineers (SPIE) Conference Series* **9909**, 990914 (2016).
19 M. Downing, P. Amico, M. Brinkmann, *et al.*, "Update on development of WFS cameras at ESO for the ELT," in *Adaptive Optics Systems VI*, L. M. Close, L. Schreiber, and D. Schmidt, Eds., *Society of Photo-Optical Instrumentation Engineers (SPIE) Conference Series* **10703**, 107031W (2018).
20 E. R. Fossum, "Active pixel sensor array with electronic shuttering," *US patent 6,486,503* (1997).
21 K. Yasutomi, S. Itoh, S. Kawahito, *et al.*, "Two-stage charge transfer pixel using pinned diodes for low-noise global shutter imaging," in *International Image Sensor Society Workshop*, (2009).
22 T. Inoue, S. Takeuchi, and S. Kawahito, "CMOS active pixel image sensor with in-pixel CDS for high-speed cameras," in *Sensors and Camera Systems for Scientific, Industrial, and Digital Photography Applications V*, N. Sampat, R. J. Motta, and M. M. Blouke, Eds., **5301**, 250 – 257, International Society for Optics and Photonics, SPIE (2004).
23 R. Zhang and L. Lai, "Optical design of microlens array for CMOS image sensors," in *8th International Symposium on Advanced Optical Manufacturing and Testing Technologies: Design, Manufacturing, and Testing of Micro- and Nano-Optical Devices and Systems; and Smart Structures and Materials*, X. Luo, T. Ye, T. Xin, *et al.*, Eds., **9685**, 1 – 7, International Society for Optics and Photonics, SPIE (2016).
24 M. Downing, J. Kolb, D. Baade, *et al.*, "Backside-illuminated, high-QE, 3e- RoN, fast 700fps, 1760x1680 pixels CMOS imager for AO with highly parallel readout," in *High Energy, Optical, and Infrared Detectors for Astronomy V*, A. D. Holland and J. W. Beletic, Eds., *Society of Photo-Optical Instrumentation Engineers (SPIE) Conference Series* **8453**, 84530C (2012).
25 M. Downing, J. Kolb, B. Dierickx, *et al.*, "LGSD/NGSD: high speed visible CMOS imagers for E-ELT adaptive optics," in *High Energy, Optical, and Infrared Detectors for Astronomy VII*, A. D. Holland and J. Beletic, Eds., **9915**, 401 – 408, International Society for Optics and Photonics, SPIE (2016).

26 E. R. Fossum and D. B. Hondongwa, "A review of the pinned photodiode for ccd and cmos image sensors," *IEEE Journal of the Electron Devices Society* **2**(3), 33–43 (2014).

27 M. Guidash, J. Ma, T. Vogelsang, *et al.*, "Reduction of cmos image sensor read noise to enable photon counting," *Sensors* **16**(4) (2016).

28 P. Jerram, D. Burt, N. Guyatt, *et al.*, "Back-thinned CMOS sensor optimization," in *Optical Components and Materials VII*, S. Jiang, M. J. F. Digonnet, J. W. Glesener, *et al.*, Eds., **7598**, 298 – 309, International Society for Optics and Photonics, SPIE (2010).

29 J.-L. Gach, D. Boutolleau, C. Brun, *et al.*, "C-BLUE One: a new CMOS camera dedicated for laser guide star wavefront sensing on ELTs," in *Adaptive Optics Systems VII*, L. Schreiber, D. Schmidt, and E. Vernet, Eds., **11448**, International Society for Optics and Photonics, SPIE (2020).

30 J. R. Janesick, *Photon Transfer*, vol. PM170, SPIE press (2007).

31 X. Wang, P. R. Rao, A. Mierop, *et al.*, "Random telegraph signal in cmos image sensor pixels," in *2006 International Electron Devices Meeting*, 1–4 (2006).

32 P. W. R. Connolly, X. Ren, A. McCarthy, *et al.*, "High concentration factor diffractive microlenses integrated with cmos single-photon avalanche diode detector arrays for fill-factor improvement," *Appl. Opt.* **59**, 4488–4498 (2020).

33 S. Gousset, C. Petit, V. Michau, *et al.*, "Modeling of high-precision wavefront sensing with new generation of cmt avalanche photodiode infrared detectors," *Appl. Opt.* **54**, 10163–10176 (2015).

34 N. Muller, *Analyse de front d'onde sur étoiles laser pour les extremely large telescopes*. PhD thesis, Université Paris Diderot (2011). Thèse de doctorat dirigée par Rousset, Gérard et Michau, Vincent Astronomie et astrophysique Paris 7 2011.

35 M. Nicolle, T. Fusco, G. Rousset, *et al.*, "Improvement of shack–hartmann wave-front sensor measurement for extreme adaptive optics," *Opt. Lett.* **29**, 2743–2745 (2004).

36 J. G. Robertson, "Detector Sampling of Optical/IR Spectra: How Many Pixels per FWHM?," *Publications of the Astronomical Society of Australia* **34**, e035 (2017).

37 N. A. Thatte, I. Bryson, F. Clarke, *et al.*, "HARMONI: first light spectroscopy for the ELT: instrument final design and quantitative performance predictions," in *Ground-based and Airborne Instrumentation for Astronomy VIII*, C. J. Evans, J. J. Bryant, and K. Motohara, Eds., **11447**, 415 – 425, International Society for Optics and Photonics, SPIE (2020).

38 J. Crane, G. Herriot, D. Andersen, *et al.*, "NFIRAOS adaptive optics for the Thirty Meter Telescope," in *Adaptive Optics Systems VI*, L. M. Close, L. Schreiber, and D. Schmidt, Eds., **10703**, 1094 – 1106, International Society for Optics and Photonics, SPIE (2018).

3.2.1. Mirolens impact : Fourier analysis

CMOS sensors have small microlenses at the surface of their pixels that enhance their photon collection efficiency. Although the on-axis sensitivity is improved, the incident light at oblique angles is focalized off the center of the photosensitive area into light-insensitive structures of the pixel. This leads to a reduction of sensitivity for a light beam with a large angle of incidence. In the JATIS paper, we have shown that a potential way to reduce the negative effect of this light coupling issue is to implement a telecentric optical relay between the lenslet and the detector. This would allow to minimize the light loss and ensure a transmission larger than 94-95% for this specific aspect. In practice, the light loss is not uniform across the pupil, but it takes the shape and apodization function, reducing the transmission at the edges of each subaperture. This is illustrated by Figure 2 of the JATIS paper, and this figure will be duplicated above each subaperture. Apart from the flux reduction, the impact of this apodization function will be two-fold. On the one hand, it will slightly modify the diffraction pattern of each sub-aperture. On the other hand, it will introduce an extra aliasing term.
Indeed, the subaperture response will not be a rectangular function anymore, but the product of this rectangular shape with the apodization function, which can be approximated by a super-gaussian function, such as :

$$\begin{aligned} f(x,y) &= \exp\left(-\left(\frac{(x-x_0)^2}{2\sigma_X^2}\right)^{P_X} - \left(\frac{(y-y_0)^2}{2\sigma_Y^2}\right)^{P_Y}\right) \\ &= \exp\left(-\left(\frac{(x-x_0)^2}{2\sigma_X^2}\right)^{P_X}\right) \cdot \exp\left(-\left(\frac{(y-y_0)^2}{2\sigma_Y^2}\right)^{P_Y}\right) = f_x(x) \cdot f_y(y) \end{aligned} \tag{3.1}$$

Where x and y are spatial coordinates, centered around x_0 and y_0, σ_X and σ_Y are the standard deviation in two axes, P_X and P_Y are the factors of Gaussian shape.

For a standard microlens array, the microlens aperture is square, and its side length is a and b respectively. Considering the finite size of the microlens, its transmittance is :

$$t_s = t_l(x,y) \cdot rect\left(\frac{x}{a}\right) \cdot rect\left(\frac{y}{b}\right), \tag{3.2}$$

where $rect$ denotes the rectangular function.

In the case of the CMOS with a given acceptance angle, this rectangular function is multiplied by Gaussian (or super-gaussian) functions and can be expressed as :

$$t_s = t_l(x,y) \cdot f_x\left(\frac{x}{a}\right) \cdot f_y\left(\frac{y}{b}\right), \tag{3.3}$$

where f_x and f_y are the subaperture response functions in two directions.

As mentioned above, this new transmission will have an impact on the diffraction pattern, and potentially on the aliasing propagated by the sensor. For the first aspect, the impact is negligible, as for any LGSWFS, the final spot size is limited by the laser size, which is usually 5 times larger than the diffraction. Indeed, the diffraction at 589nm for a subaperture of 50cm, gives a spot size of about 0.25arcsec, while the typical LGS size is larger than 1arcsec. The second effect, extra-aliasing, is however interesting to look at.

To understand the Shack-Hartmann aliasing term, it is interesting to use the Fourier space. Starting from the direct space, one can write the SH measurement along one axis as :

$$s_x = \left[\left[\frac{\partial \phi(r)}{\partial x} \right] \star \Pi(\frac{r}{d}) \right] \Omega(\frac{r}{d}) \Pi(\frac{r}{D}) + n_x \tag{3.4}$$

Where the phase $\phi(r)$ is averaged over the subaperture. In this equation, d is the the subaperture size and D is the telescope size. The convolution product with the gate of size d symbolizes the spatial average over a subaperture. The product of the Dirac comb of step d represents the sampling of the phase by the subaperture array. The multiplication by the size gate D corresponds to the cutout due to the telescope. n is the detector noise in x direction. Then going to the Fourier space, the SH measurement simply writes as :

$$\tilde{s}_x = \left[2j\pi f_x \boldsymbol{sinc}(\pi d f_x) \boldsymbol{sinc}(\pi d f_y) \tilde{\phi}(f) \right] \star \left[d^2 \Omega(f_x d) \right] + n_x \tag{3.5}$$

In direct space, we only measure a sampled version of the derivative of the phase due to the finite number of subpupils. A first consequence of this spatial sampling is that a SH is only sensitive to frequencies below its cutoff frequency defined by $f_c = 1/2d$.
The second consequence of sampling is the periodization of the spectrum of the measured signal in the Fourier space with a frequency $f_{ech} = 1/d$. Since the turbulent spectrum has an infinite extension, when measuring a frequency f one is not only sensitive to the value of the spectrum measured for this frequency, but also to the value of the spectrum measured for a high folded frequency (f_{ech} - f). From a mathematical point of view, the aliasing is translated by the convolution product which appears in Eq. 3.5 and which causes the repetition of the measurements on a regularly spaced grid.

Now, if the subaperture transmission is modified because of the apodization caused by the angle of acceptance, it can simply be accounted for in the equation by adding the function $f(x, y)$ such as :

$$s_x = \left[\left[\frac{\partial \phi(r)}{\partial x} \right] \star (\Pi(\frac{r}{d}) f(x, y)) \right] \Omega(\frac{r}{d}) \Pi(\frac{r}{D}) + n_x \tag{3.6}$$

And then, going again to the Fourier space, we find :

$$\tilde{s}_x = \left[2j\pi f_x \boldsymbol{sinc}(\pi d f_x)\boldsymbol{sinc}(\pi d f_y)\tilde{\phi}(f) \star FT(f(x,y))\right] \star \left[d^2\Omega(f_x d)\right] + n_x \qquad (3.7)$$

We then understand that the aliasing term will be impacted as the convolution is affected. This is illustrated first by Fig. 3.1 which shows the SH response in the presence of square subapertures (black plot), and in the case of an apodized subaperture (red plot). The dashed lines show the signal repetition due to the aliasing. A simple way to understand that the aliasing will be increased is to see that the overlap between the black and dashed black curve is smaller than the ones for the red (apodized) subapertures.

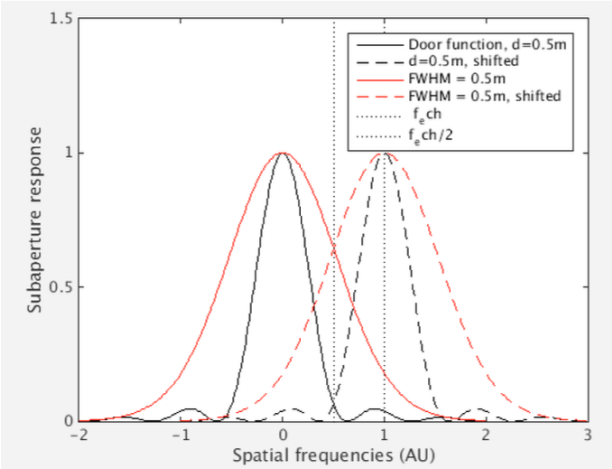

FIGURE 3.1. – Illustration of the increase of aliasing due to an apodization of the subaperture transmission. The black plots show the Fourier spatial filtering caused by a square sub-aperture, the red one is for an apodized subaperture. The apodization allows the transmission of more frequencies, however the overal with the signal repetition is higher, which means more aliasing.

As a next step, we have simulated the AO performance for different sizes of apodization. This is illustrated in Fig. 3.2. It shows that the performance indeed decreases when the apodization function starts to be larger than a loss of transmission of about 0.8 at the edge of the subaperture. This is an important input to be taken into account when doing the overall design of the LGSWFS, and as explained in the JATIS paper, we will usually be in a more favorable configuration.

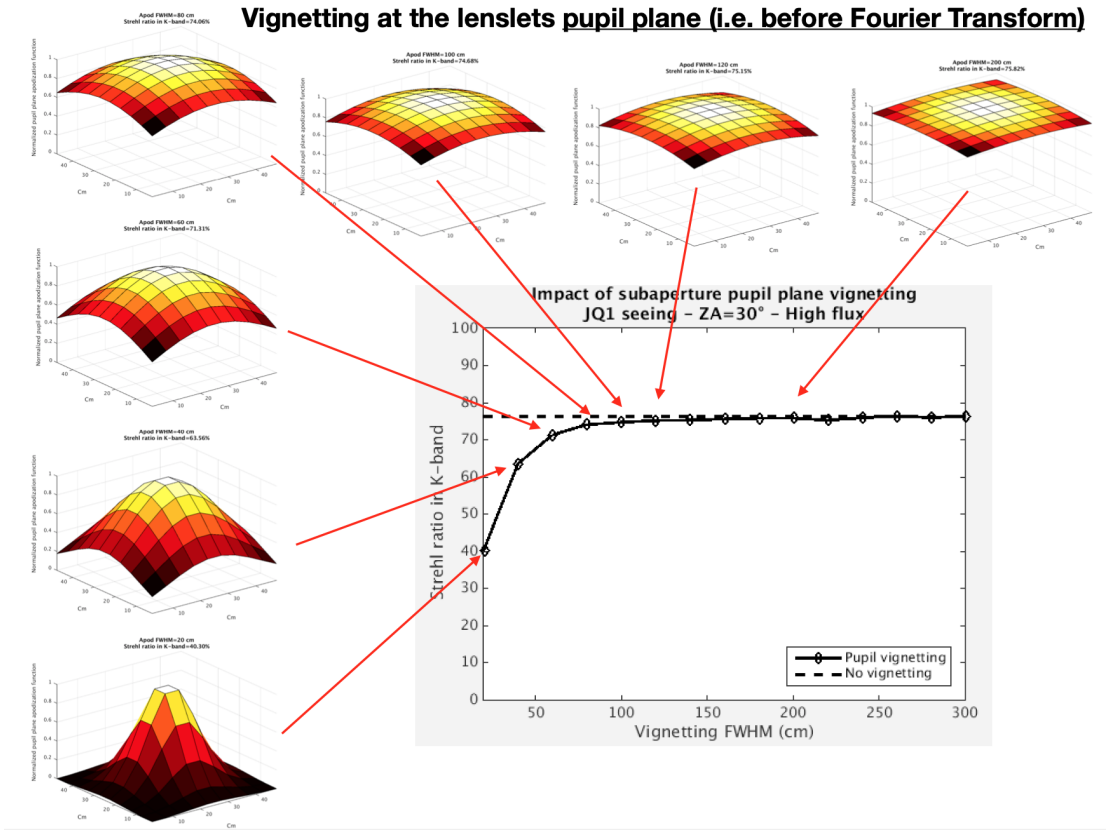

FIGURE 3.2. – Impact of sub-aperture apodization on the AO performance. In this plot both the flux loss and the aliasing are accounted for.

Finally, as the plot of Fig. 3.2 was accounting for both the flux losses and aliasing, in Fig. 3.3 we isolated the two contributions and showed the theoretical expected performance loss due to the extra aliasing only. This is computed based on the Fourier expression, and it shows a agreement with the full end-to-end simulation, and thus concludes the analysis for this extra-aliasing term.

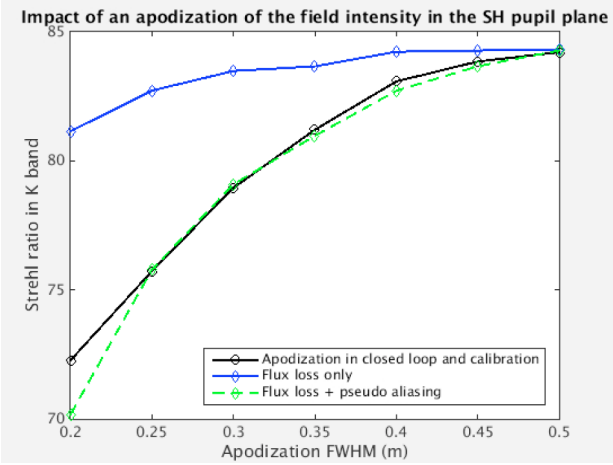

FIGURE 3.3. – Fit of the performance loss with a function taking into account the extra-aliasing due to the apodization.

3.2.2. Quantization noise

We briefly discuss the impact of the conversion resolution of the sensor's ADC on the centroiding performance. Because of the low-flux regime of operation and the elongation effect on the outer sub-apertures, the LGS wavefront sensor is prone to quantization errors due to rounding of the input signal to the digital output. The noise added to the signal can be approximated by (WIDROW et KOLLAR 2008) :

$$\sigma_q^2 = q^2/12, \tag{3.8}$$

where q is the quantization step. As the quantizing level increases, i.e., the quantizing step decreases, the centroid error induced by the quantization noise diminishes.

We perform a simulation of the LGS spot within a sub-aperture of 13×13 pixels as a function of the spot elongation, for two flux levels of 500 and 2000 photons/sub-aperture/frame. The spots are modeled as Gaussian with a width in the nonelongated direction of 1.5 arcsec. The conversion gain was set such that the peak ADU level at a flux of 2000 (photons/sub-aperture/frame) corresponds to 90% the full well capacity measured in the CMOS sensor. Photon and read-out noise following the measured distribution are added to the simulated spots, which are then quantized into 8- and 12-bits images. Sample images for high and low flux at three different elongation levels are shown in Fig. 3.4. The CoG of a sequence of 1000 frames is calculated as well as the temporal standard deviation of the sequence. The variations of the CoG for each case are shown in Fig. 3.5. Results show that a small resolution leads to larger CoG errors.

This result shows that 12-bit resolution is preferable over 8-bit resolution to maintain the CoG error low in sub-apertures affected by strong spot elongation.

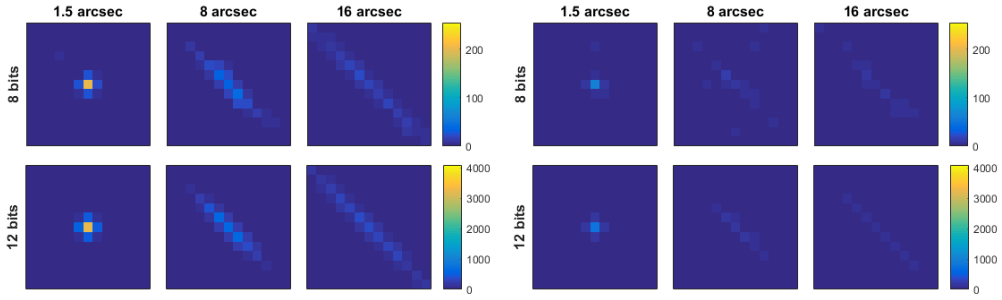

FIGURE 3.4. – Simulated quantized images assuming measured noise characteristics of the CMOS sensor, for a flux of 2000 (photons/sub-aperture/frame) (left) and 500 (photons/sub-aperture/frame) (right).

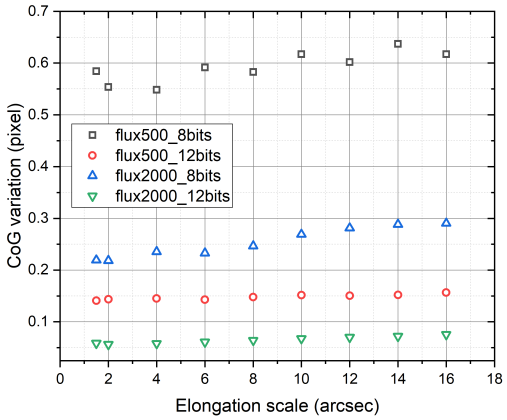

FIGURE 3.5. – CoG variations as a function of spot elongation for high- and low-flux images, and for 8 and 12 bits quantization.

3.3. Conclusion

In this chapter we have presented the work done to perform a full characterization of a CMOS detector that could potentially be used for the LGSWFS of the ELTs. The work done in this chapter has led to a publication in the special issue of the JATIS journal, dedicated to the ELT instruments.

We have shown that this CMOS detector could be an ideal candidate for LGSWFS for ELTs, by combining large numbers of pixels (1100x1600), a decent read-out noise (less than 3 e^-) and a quasi-perfect cosmetic with no bad or dead pixels. We have also shown that the pixel RON was following a skewed distribution, but the impact of this tail was negligible on the centroiding error.
One specificity of the CMOS detector is to only allow for a limited angle of acceptance.

The average angular response of the sensor was characterized showing a two-axis symmetry with a full width half maximum of 42.6 in the vertical direction and 25.4 in the horizontal direction. This effect causes light loss when coupled to a SH lenslet array, as well as a potentially an extra aliasing error. In the JATIS paper, and the development following, we have shown that this impact can be kept to a reasonable level, by minimizing the transmission loss to <5% and getting a negligible extra-aliasing term.

Finally, the JATIS paper shows the first two examples of practical implementations of this detector in LGS wavefront sensors for the ELT and TMT adaptive optics systems. These two examples show that this type of detector is perfectly suitable for LGS wavefront sensing on extremely large telescopes.

The next chapter will now focus on the development of a first full-scale LGSWFS prototype for the ELT.

4. Laser guide star system Detector Module Prototype

Sommaire

4.1. Introduction of HARMONI

HARMONI is a High Angular Resolution Monolithic Optical and Near-infrared Integral field spectrograph which equips with adaptive optics for the Extremely Large Telescope (ELT), providing a core spectroscopy of ELT at first light. As one of the two first-light instruments funded by the European ELT, it will be expected as a workhorse instrument that deals with a range of different scientific cases : including solar system science cases, intermediate mass black holes, nearby galaxies, Gamma-Ray bursts and cosmology. By virtue of AO to obtain scales close to the diffraction limit, HARMONI can utilize the sensitivity gains of the ELT to make significant gains in sensitivity and spatial resolution, which will dramatically change the landscape of visible and near-infrared astronomical observations. HARMONI will be highly complementary and synergistic to Atacama Large Millimeter/submillimeter Array (ALMA) and James

Webb Space Telescope (JWST), it will have similar angular resolution with ALMA and comparable sensitivity with JWST. The first light of HARMONI is planned for 2027.

Tableau 4.1. – Spatial resolution and Field of View (FoV) of HARMONI

Scale(mas)	FoV	Comments
60 ×30	$9.1'' \times 6.2''$	Non-AO or visible observations
20 ×20	$3.0'' \times 4.1''$	Optimal sensitivity (faint targets)
10 ×10	$1.5'' \times 2.1''$	Best combination of sensitivity and spatial resolution
4 ×4	$0.6'' \times 0.8''$	Highest spatial resolution (diffraction limited)

HARMONI is designed to cover a large spectral range from visible to near-infrared range ($0.46\mu m \sim 2.4\ \mu m$), and provide a spectral resolution of R ($=\lambda/\Delta\lambda$) 3,300 to 17,300 and an angular resolution of 60 to 4 mas shown as the table upon. It has a FoV of 152×,214 spatial pixels, and 4000 spectral bands per spatial pixel. The different spatial scales correspond to different instrument configurations aimed at a wide range of scientific goals. For example, the coarsest scale of 30×60 mas is for the seeing limited observation at visible bands without AO system, and the finest scale of 4×4 mas can acquire a diffraction limited observation whose FoV is $0.6'' \times 0.8''$ at near-infrared channels equipped with AO system. HARMONI has two kinds of adaptive optics modes or non-AO (NEICHEL, FUSCO, SAUVAGE et al. 2016), the first is a classic single conjugate AO system (SCAO) operated with a natural guide star whose lowest magnitude is 16, the compensation field of SCAO is 15 arsec with 1% sky coverage, which is suited for galatic center or densely populated fields. And the second one is a large laser tomography AO system assisted by laser guide stars (LTAO), it has a field of 2 arcmin, and the lowest magnitude of NGS is 19, therefore LTAO can provide a wider sky coverage of about 50% ~ 90% over the whole sky.
The performance requirements for HARMONI are summarized by Fig 4.1.

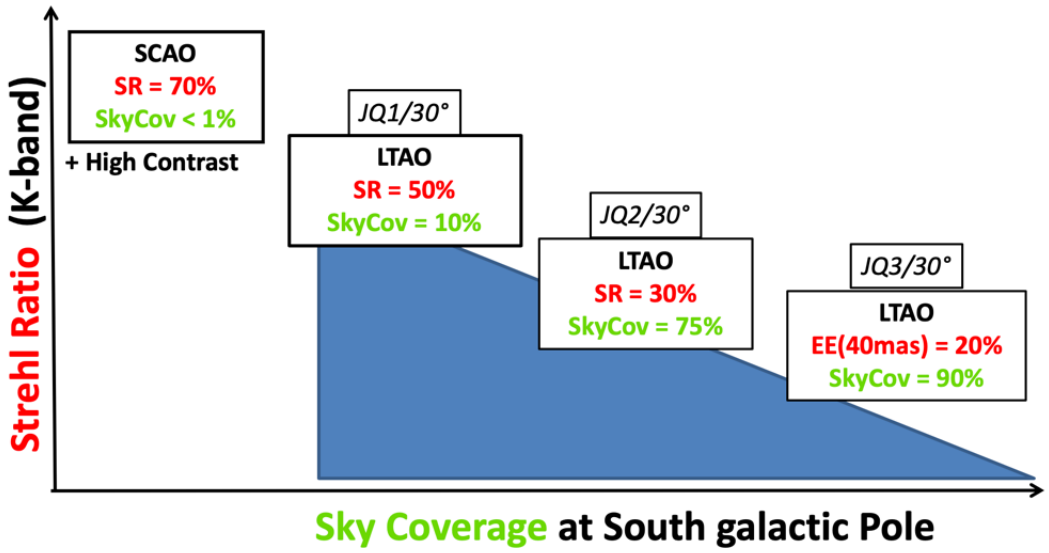

FIGURE 4.1. – Expected performance of HARMONI, from the High performance / low sky coverage provided by the SCAO module, to the good performance / wide sky coverage provided by the LTAO module.

The performance defined above can be divided between a jitter budget on the one hand, and a High-Order budget on the other hand, this latter including all the remaining modes. This separation is convenient for the system design, as these two budgets impact two different subsystems of HARMONI, respectively, the Low-Order WFS working with NGS, and the High-Order WFS working with LGSs. For what matters in this thesis, we will focus on the High-Order LGS part.
As such, the error budget of HARMONI has been defined as :

— Peak Performance - Best conditions : 50% SR over 10% of the sky for the best (IQ20) seeing conditions. This can be reached with a total error budget of 291nm, which could be distributed into 260nm for the High-Order terms (SR=57% @ 2.2 microns) and 130nm for Jitter control (equivalent to 2mas jitter)
— Good Performance - median conditions : 30% SR over 75% of the sky for the median (IQ50) seeing conditions. This can be reached with a total error budget of 385nm, which could be distributed into 285nm for the High-Order terms (SR=51% @ 2.2 microns) and 260nm for Jitter control (equivalent to 4mas jitter)
— Good Performance - worst conditions : EE(40mas) = 20% over the whole sky, for the worst (IQ75) seeing conditions. This can be reached with an error budget which could be distributed into 340nm for the High-Order terms (SR=39% @ 2.2 microns ; EE(40mas)=40% @ 2.2 microns), and 15mas total jitter

The high-order error budget can be further decomposed into several terms (see Table 4.2), including the LGS measurement limitations as studied in this thesis. The detailed error budget is defined by :

Tableau 4.2. – HARMONI High-Order error budget

Error Term	Peak Performance Best conditions	Good performance Median conditions	Good performance worst conditions
M4 Fitting	70	92	105
Aliasing	40	50	60
Pupil Fragmentation	70	80	125
Tomography + noise	185	195	230
LGS Spot truncation	40	40	40
Temporal	40	85	100
Tomography Model Error	50	50	50
NCPA	70	70	70
Telescope Field aberrations	50	50	50
Other terms	80	90	120
Total	260	285	340

A brief description of the different terms is provided below.

Fitting Error The turbulence fitting error depends on the actuator geometry of the Deformable Mirror, which in the case of the ELT is M4. We have checked with simulations and analytical models that the M4 geometry provides a fitting error consistent with an hexagonal distribution of the actuators. This is illustrated in Fig 4.2. This reduces the fitting error compared to a Cartesian distribution. Indeed, for a Cartesian geometry, the overall fitting error is defined by :

$$\sigma^2_{fitting} = 0.232 \left(\frac{d}{r_0}\right)^{5/3} \tag{4.1}$$

Where, d is the DM pitch and r_0 is the fried parameter at the observing wavelength. For an hexagonal distribution, the fitting error is expressed by :

$$\sigma^2_{fitting} = 0.200 \left(\frac{d}{r_0}\right)^{5/3} \tag{4.2}$$

with d equivalent pitch. The numerical computation of the fitting error is given in Table 4.3.

Tableau 4.3. – Fitting Error computation for different DM geometry

Seeing (r0)	0.48 (21cm)	0.65 (15.5cm)	0.85 (12cm)	1.2 (8cm)
Fitting error for Real M4 (4760 actuators)	66nm	85nm	105nm	139nm
Fitting error for pure hexagonal DM (4689 actuators)	68nm	88nm	110nm	146nm
Fitting error for pure cartesian DM (4072 actuators)	75nm	97nm	121nm	162nm

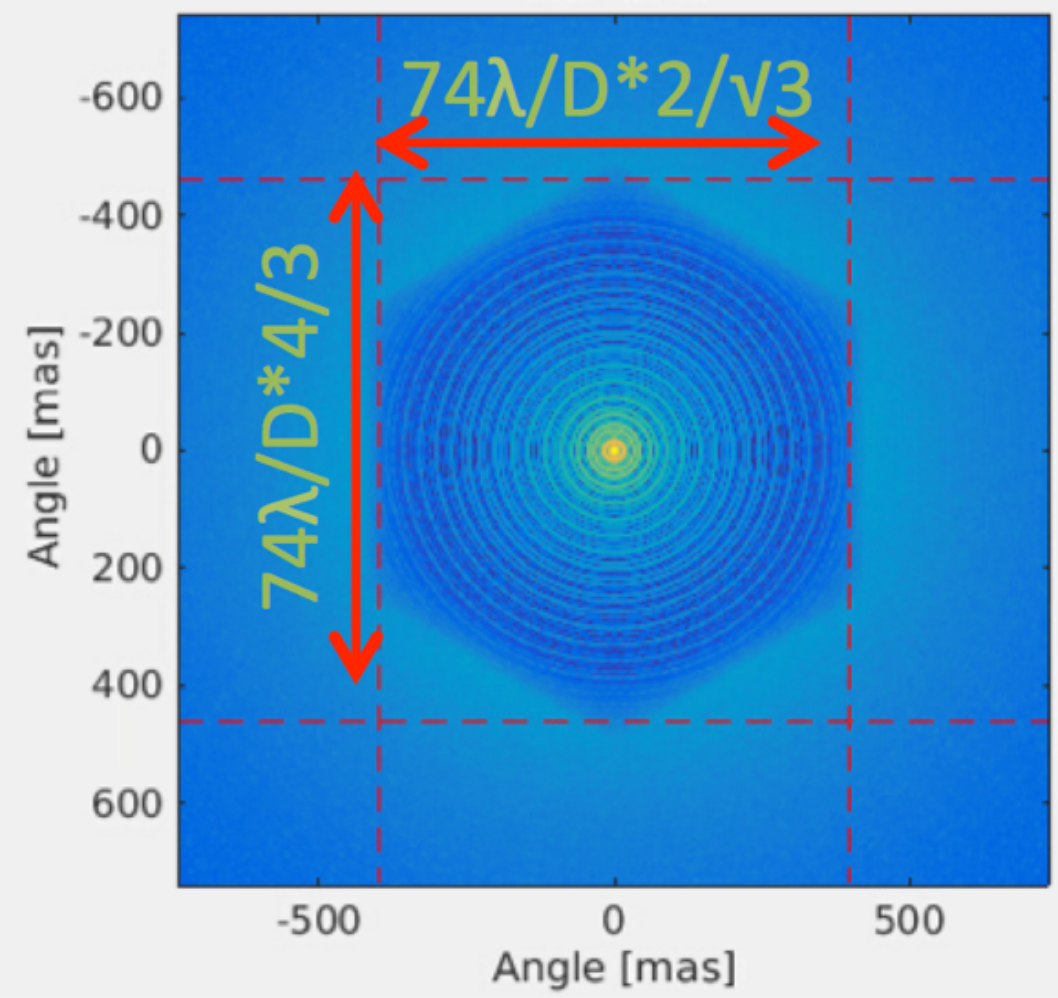

FIGURE 4.2. – Illustration of the fitting error in an hexagonal geometry configuration.

Aliasing Aliasing effects are due to the unmeasured high spatial frequencies seen by the SH-WFS. The aliasing error is directly linked to the fitting error and in the specific case of a SH-WFS (or any other slope sensor) it is roughly equal to 35% (in variance) of this fitting error. Nevertheless, aliasing is nothing but an additional error term in the

measurement process. Therefore, it will be propagated through the reconstruction process (and thus it will depend on the type of phase reconstructor considered). In particular, the tomographic process, with its unseen or badly seen modes, will lead to some over amplification of the aliasing noise and thus to a degraded performance. As an example, it goes from 88 nm rms for the classical AO case up to 108 nm rms for an LTAO case. It is however possible to explicitly take the aliasing into account in the tomographic reconstructor, and therefore use the statistical properties of this noise to attenuate its effect. For instance, a classical MMSE reconstructor accounts for prior knowledge of both Cn2 profile and system noise to optimally deal with noise propagation and perform phase extrapolation using its statistical knowledge. Since aliasing can be seen as an additional noise on the WFS data (although this noise is correlated with the signal itself), it is therefore possible to extend the "traditional" MMSE reconstructor to include this particular error item. For a standard SCAO system and a standard reconstruction, we have :

$$\sigma^2_{alias} = 0.125 \left(\frac{d}{r_0} \right)^{5/3} \tag{4.3}$$

And by doing an explicit MMSE reconstruction, this term can be reduced to (CORREIA et TEIXEIRA 2014) :

$$\sigma^2_{alias} = 0.07 \left(\frac{d}{r_0} \right)^{5/3} \tag{4.4}$$

Pupil Fragmentation Because of the shadow of the telescope spiders on the LGSWFS projected pupils, some unwanted modes may appear on the reconstructed wavefront. These modes are mostly differential pistons between the 6 segments, and are called "petalling" or "pupil fragmentation". It is important to understand that these modes are not related to the so-called "Low Wind Effect", which by nature is a different effect. Where the pupil fragmentation comes from an AO control issue, with the introduction by the AO loop of unwanted modes, the LWE has its origin in a real phase distortion introduced by different temperatures within the dome and the telescope structure. In other words, we want to prevent the first one to appear, while we will want to compensate for the second one. For LTAO, pupil fragmentation is taken care of by tomographic control and the regularization. It does not completely discard the effect, as some differential piston modes exist in the atmosphere, but it avoids to diverge.

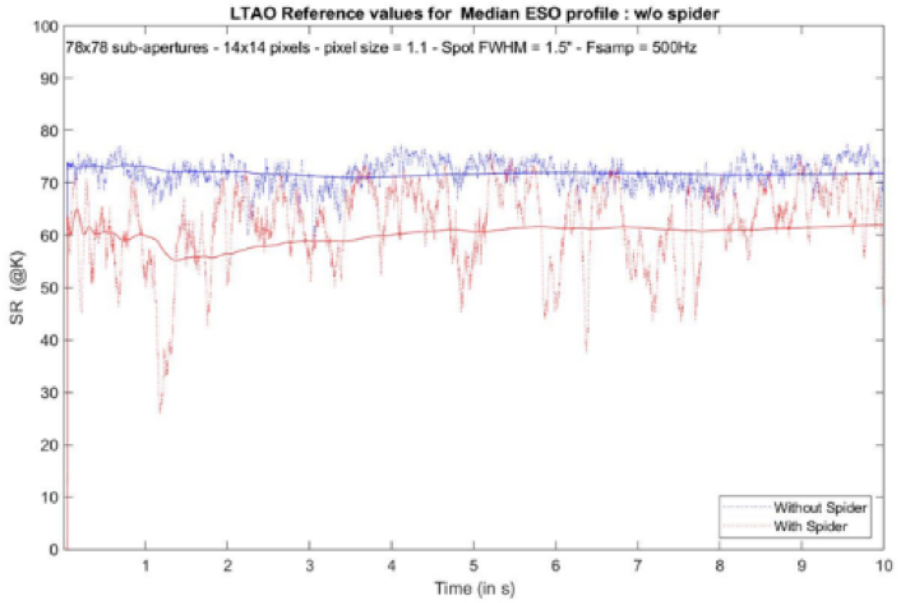

FIGURE 4.3. – LTAO performance over time for an ELT pupil without (blue) and with (red) the telescope spiders. Performance is more unstable in presence of spiders because of the so-called petalling (differential piston between the 6 pupil pies).

Typical expected performance in the presence of spiders is shown in Fig. 4.3.

Tomography + noise It can be shown that it exists an optimal angle when the LGS light cones exactly synthetize the NGS cylinder. This optimal constellation occurs when the LGS are launched parallel to the telescope truss, or following the telescope "rim ray". One can compute that if the lasers are launched following this constellation strategy, for a 39m telescope and a sodium layer located at 90km above the telescope, the optimal constellation is ~40 arcsec radius.

— Note that if the constellation is smaller than this angle, the performance drops as some of the turbulence on the outer edges of the pupil is not seen (see the left picture of Figure 4.4). On the other hand, if the constellation is larger than this angle, the performance decreases as the tomography becomes more sensitive to model errors (second picture in Figure 4.4). This drop in performance is however less steep than when the constellation is too small and depends on the Cn2 profile.

— Note also that when the zenith angle increases, and as the relative distance to the sodium layer increases, this optimal angle decreases (see the third and fourth pictures in Figure 4.4). To a first order, the angle scales with the cosine of the zenith angle

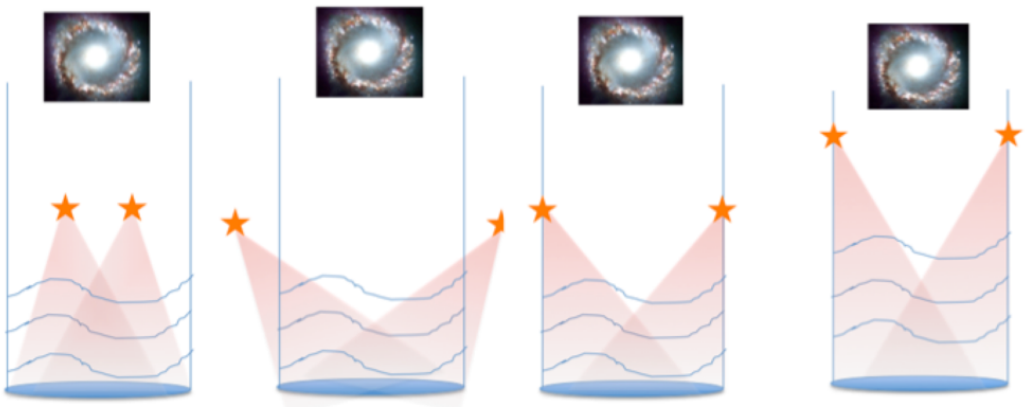

FIGURE 4.4. – Illustration of the optimal constellation configuration

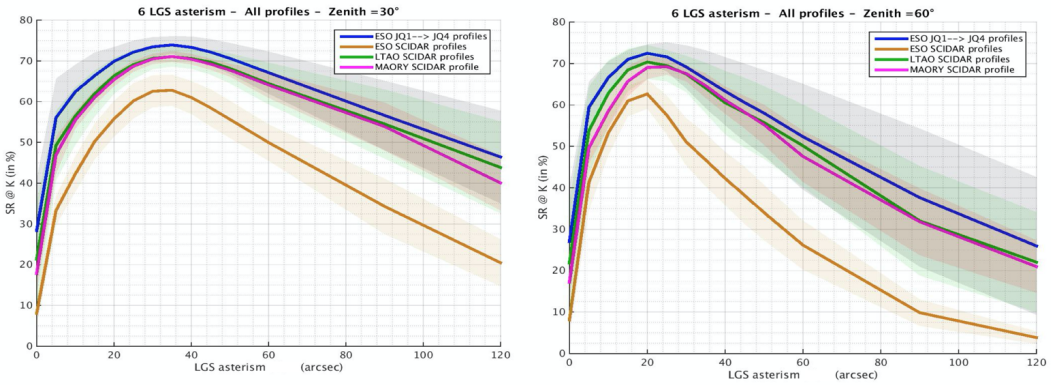

FIGURE 4.5. – HARMONI LTAO performance for different LGS constellations, different elevations and different atmospheric profiles.

The LTAO performance for different LGS constellations and different elevations is shown in Fig. 4.5. The LGS constellation is kept fixed with a radius of 34arcsec.

LGS spot truncation The LGS spot elongation is at the heart of this thesis problematic. As described in the previous chapter, the LGS spot elongation is a challenge for the ELT, since the expected LGS spot shape can go up to 20arcsec. If not treated properly, the impact on performance can be pretty severe, inducing several hundreds of nanometers of wavefront error. We have also shown in the previous chapter that this error evolved quickly and will be difficult to calibrate out. This error then must be minimized at the source as much as possible. This implies having the wider FoV per subaperture as possible, while keeping a decent sampling (pixel scale) not to jeopardize the measurements on the best spots. The detector choice is further discussed in Section 4.2.1. However, even though we demonstrated that large, low-noise CMOS detectors are suitable for LGSWFS, the final number of pixels remains too small to accommodate wider elongations. The strategy used for HARMONI-LTAO is then to mitigate the residual truncation error by using a weighted tomographic reconstruction,

as described in Michel TALLON, Isabelle TALLON-BOSC, Clémentine BÉCHET et al. 2010. Combining both the CMOS large detector, and the optimized reconstruction strategy, the truncation error can be minimized even for the worst conditions, when working close to Zenith, and for the widest Sodium profiles. The performance estimation is shown in Fig. 4.6. The detector choice and parameter optimization are discussed below in Section 4.2.1.

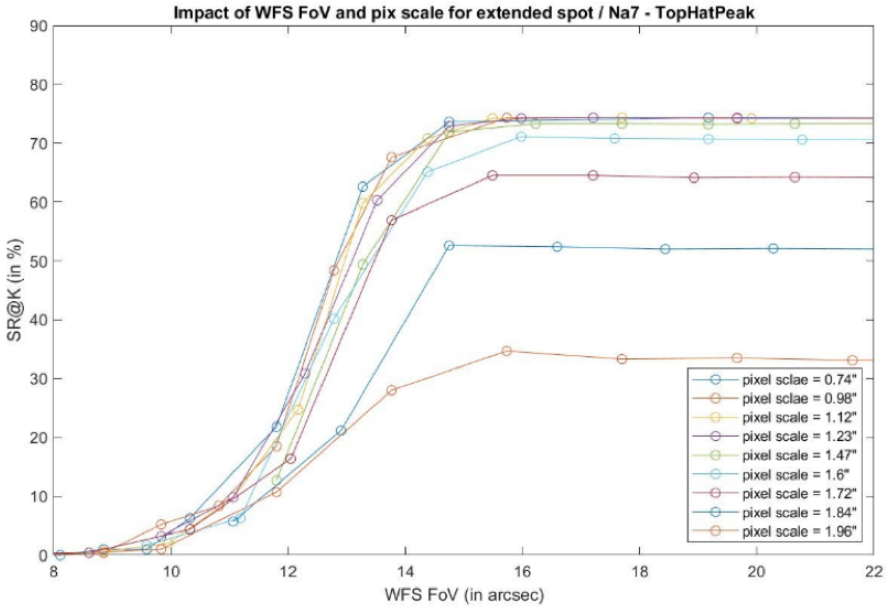

FIGURE 4.6. – HARMONI LTAO performance for different LGS constellations, different elevations and different atmospheric profiles.

Temporal The temporal error is estimated for high flux and the results only account for AO loop delays. For the first level of description, only 4 parameters have to be considered :

— The integration time (Ti)
— The read out time (T_{RO}) which includes the detector read out time and all the possible RTC computation done before the arrival of the last detector pixel
— The pure delay (τ) includes the last computations to be done by the RTC after the last pixel read and transferred by the detector
— Tp is the propagation time through the telescope RTC up to the M5 and M4 motions themselves

Those 4 parameters are summarized in Fig 4.7.

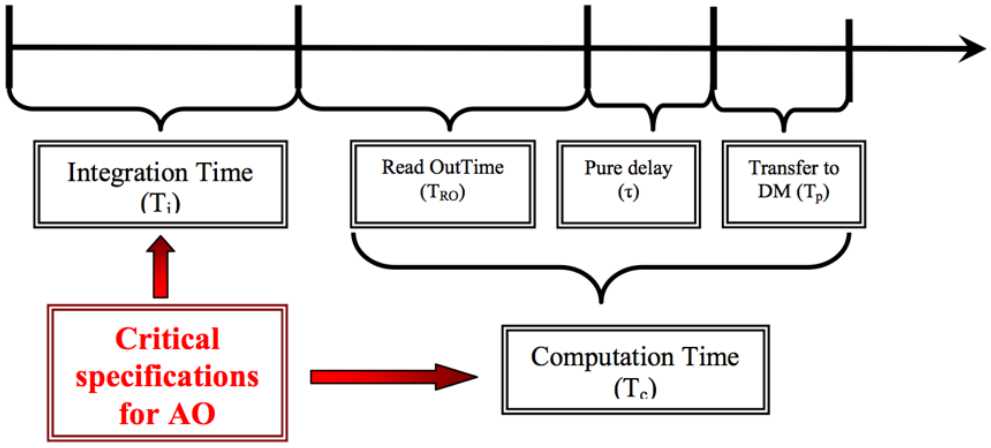

FIGURE 4.7. – Loop delay block diagram.

For an integration time of 2ms (500Hz), and an extra delay of 2ms, and for a wind seep value of 12.5m/s, the nominal value for the temporal error in the best seeing conditions is ~40nm.

Tomography model error The tomographic model error comes from the fact that the "a piori" model used in the tomographic reconstruction may be different from the actual conditions. In particular, this is true for the number and altitudes of the turbulent layers (NEICHEL, FUSCO et CONAN 2009). This has been evaluated by HARMONI, by using a large database (10000) of turbulence profiles measured at Paranal. This statistical analysis is very informative and provides the inputs required for (i) the number of atmospheric layers that must be reconstructed in the tomographic process and (ii) the update rate at which the tomographic reconstructor must be updated. Below is a graph extracted from (FARLEY, OSBORN, Tim MORRIS et al. 2020 FARLEY, OSBORN, MORRIS et al. 2019) which shows the required number of layers that must be reconstructed, if one does not want to increase the tomographic error by more than 10% (left), 20% (middle) and 40% (right), vs. the LGS constellation diameter (this is for 6LGS). The HARMONI LTAO constellation is 1.13arcmin diameter. The two colors show two different approaches to compress the atmospheric layers, blue is the standard « equivalent layers » (FUSCO, CONAN, MICHAU et al. 1999), while orange is an optimal compression scheme recently proposed by the Linz group (SAXENHUBER, AUZINGER, LOUARN et al. 2017). Solid lines are for the median profile cases, and shaded regions for 90% of the cases. Form Fig. 4.8, we conclude that if we do not want to increase the tomographic error by more than 10%, the LTAO RTC shall reconstruct 10 layers. Note that 10 layers is the maximum number of reconstructed layers and in many cases (at least more than 50% of the time), less than 7 layers only will be enough.

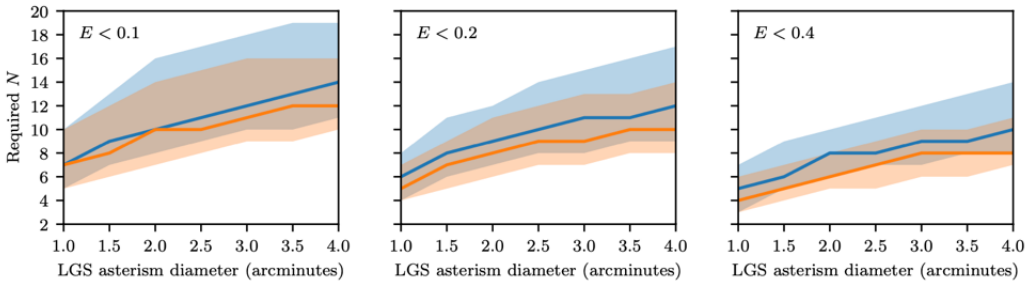

FIGURE 4.8. – Impact of the number of layers used in the tomographic reconstruction as a model error.

NCPA NCPA are coming from different sources, especially in HARMONI where the distance between the WFSs and the science instrument can be large. The main NCPAs will be introduced between the LGSWFS and the science path. As such, the first optical elements introducing NCPAs are the LGS dichroic and the LGSWFS path. In the case of the LGSWFS, NCPA will be induced by the optics, but also by the alignment between the lenslet array and the WFS detector. The opto-mechanical design is such that the lenslet to detector assembly is fixed, but the LGSWFS optics moves because of the LGS zoom, and the beam will move on the LGS dichroic due to rotation. The lenslet to detector mis-alignment is absorbed as "reference slope" that will move the LGS spot positions out of the center of the subpupil, and eventually leads to a reduced available FoV. As the subpupil FoV is a critical parameter for truncation, we require the LGSWFS to have a total field distortion < +/-0.5pixels. In other words, the total FoV of the subaperture should not be reduced by more than 1 pixel. This budget mostly includes tilt and rotation that will be minimized during the alignment. It also includes higher-order distortion due to the lenslet, that must be kept as low as possible in design. For the LGS optics and LGS dichroic, and because these NCPAs will be moving during operation, the goal will be to minimize as much as possible the "moving" NCPAs, and potentially avoid LUTs. From the error budget point of view, a residual NCPA of 50nm post calibration is allocated. Ideally, it should be the residual if one uses a single set of NCPA compensation for all configurations, or at least for a set of configurations spanned during an observation.

Telescope field aberrations For an object conjugated at infinity, the telescope off-axis aberrations are extremely small, less than 10nm for a 2 arcminute field. For an object non-conjugated to infinity, e.g., a LGS, the field aberrations are higher and may reach hundreds of nanometers. On top of those static aberrations, the telescope introduces quasi-static aberrations due to the 5 mirrors design. The expected aberrations are an additional telescope allocation for quasi-static wavefront errors of 200nm rms, pointing excluded and field aberration of less than 100nm / arcmin, field distortions excluded. To a first order, we assume that the 6 LGS being at 30arcsec off-axis will have to deal with 50nm of these aberrations. Differential aberrations between the 6 LGSWFS will be mis-interpreted by the tomographic process and will lead to a tomographic

reconstruction error. This is the 50nm allocated here.

Other terms Other terms include mis-registration (a misalignment between the WFS and the DM actuators that would occur during operation and that would not have been considered during a calibration step), chromatism (the difference between the wavefront sensor effective wavelength and the imaging wavelength), telescope vibrations which can be dealt with by the tip-tilt mirror and dome seeing .

4.2. Trade-Off study for the LGSWFS of HARMONI

As described above, HARMONI will use the signal from 6 LGSs, to be sampled by 6 LGSWFS, to provide LTAO correction for the on-sky science beam. The error terms that we are looking at in this section concerns the trade-off of the LGSWFS design, and the detector choice, in particular, for HARMONI.

4.2.1. LGSWFS parameters

The main free parameters that must be explored for the LGSWFS design are summarized in Table 4.4.

Tableau 4.4. – LGSWFS main parameters

Parameter	Proposed range	Comments	Priority
Number of subapertures	from 64^2 to 78^2	See Section 4.2.3	Medium
Field of View	At least 16arcsec	See Section 4.2.4	High
Pixel Scale	Lower than 1.15arcsec	See Section 4.2.2	High

There is obviously a trade-off between these parameters, and the technological constraints will come from the detectors. Especially, the main limitation will come from the available number of pixels. Therefore, to understand the potential trade-off, we describe a bit further the impact of these parameters on the HARMONI performance.

4.2.2. pixel scale

As described in Chapter 3, the sampling impacts the LGSWFS linearity. As soon as one considers a sampling lower than Shannon (2 pixels per FWHM), an optical gain will appear. For the LGS, this optical gain (conversion between CoG in pixel and CoG in arcsec) will be different for X and Y, and different for each subaperture. This gain changes with seeing and monitoring, it requires complex calibration procedures. The extreme examples are WFS working with quadcells, and it has been shown that in this case it could represent an important performance limiting factor (SIVO, MARIN,

RIGAUT et al. 2018). For HARMONI, it has been decided to provide, as much as possible, a proper sampling of the LGS spots, at least being able to have 1 pixel / FWHM.

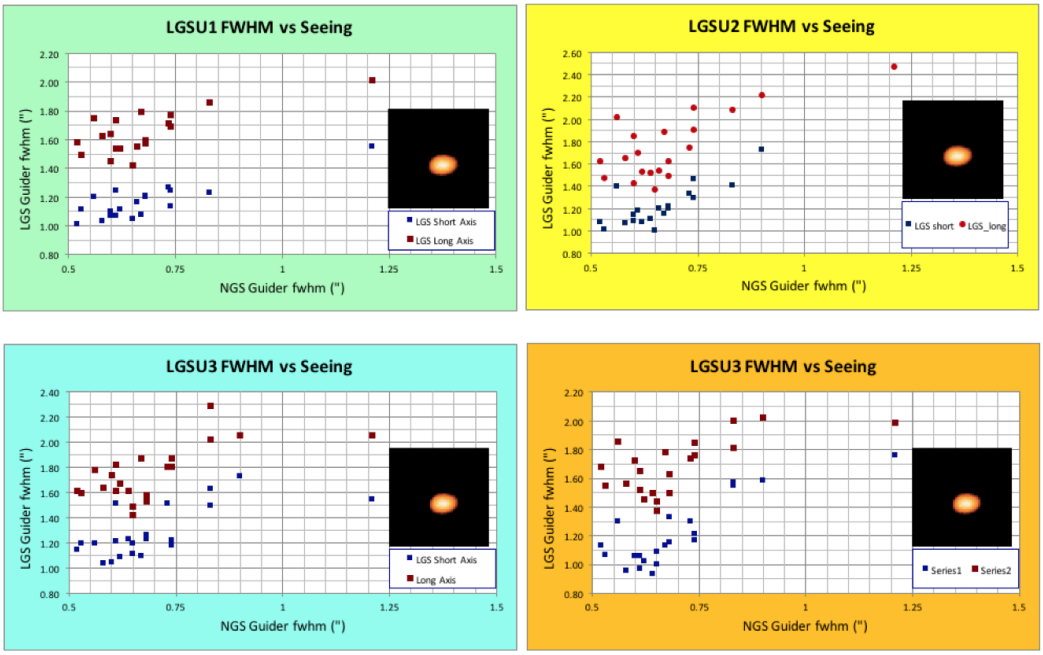

FIGURE 4.9. – Short exposure FWHM of LGS spot vs. seeing, measured by VLT-UT4 guider. Courtesy : P. Haguenauer

The statistics of the expected LGS FWHM spots, as a measure by the VLT AOF system are shown in Fig. 4.9 (courtesy : P. Haguenauer). It shows that for good seeing conditions, the short-axis LGS spots can go down to ~1 arcsec. Median FWHM is around ~1.2 arcsec. In order to avoid the difficult WFS nonlinearities, and optical gains, the pixel scale is then a critical parameter that must be kept as small as possible, and ideally smaller than 1.15arcsec.

4.2.3. Number of sub-apertures

The number of sub-apertures defines the wavefront sampling. For classical AO systems, the number of sub-apertures usually matches the DM sampling. For the ELT, the DM is M4, and we have seen that it provides an equivalent sampling of about 80x80. The number of sub-apertures shall then logically be around this number. Note that it may be interesting to even increase this number to reduce the aliasing, if enough LGS flux / subaperture is available. For HARMONI, we will use a different strategy, and we will take the full benefit of the redundancy between the 6 LGSWFS to numerically increase the ultimate WFS sampling frequency. This concept is known as super-resolution, and it has recently been introduced for AO (Oberti et al., 2021, submitted). The idea is quite simple, and it consists in shifting and/or rotating the WFS one from each other, to obtain a non-redundant grid sampling wavefront. This

concept is illustrated with a simple 4 LGS case by Fig. 4.10. For the four WFSs on the left, the WFS sampling grid is aligned with the pupil in the same way for the 4 LGSs. The four grids are perfectly superimposed. For the four WFSs on the right, we have rotated the WFS grid to be aligned with the LGS elongation and minimize the spot truncation. However, now the WFSs grids are not perfectly superimposed anymore, and the phase sampling is illustrated by Fig. 4.11.

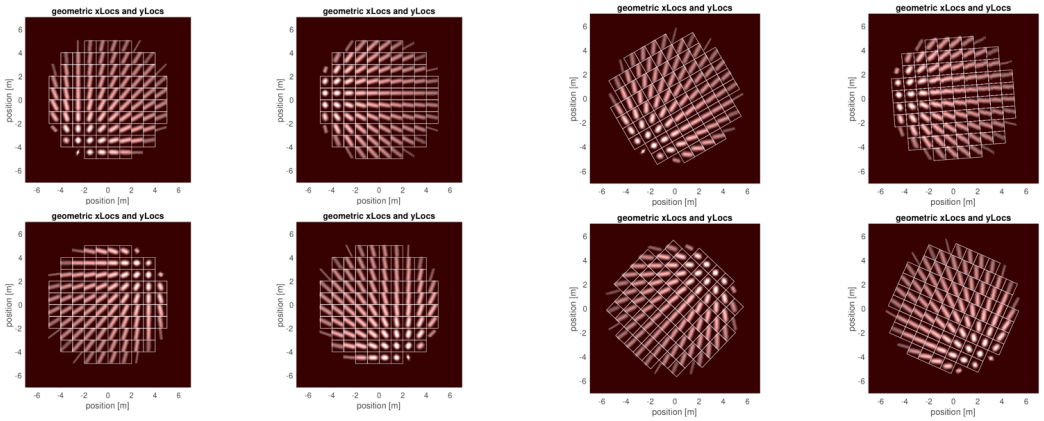

FIGURE 4.10. – Illustration of the super resolution concept for a simple 4 LGS case. Courtesy : C. Correia.

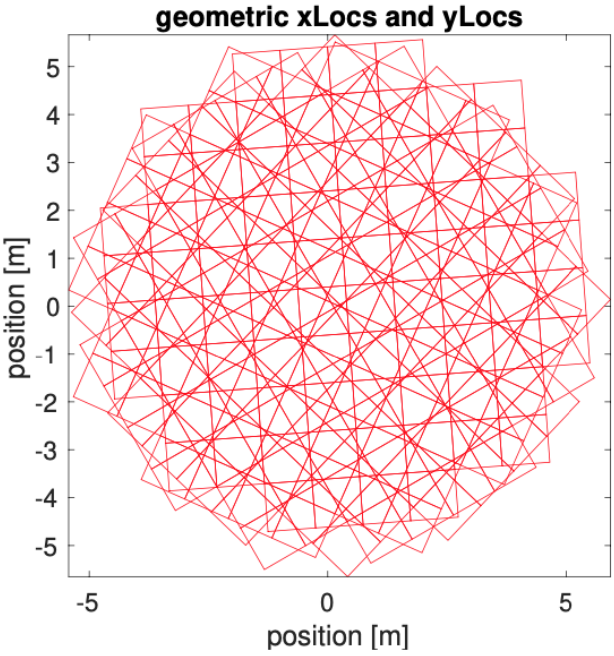

FIGURE 4.11. – Superposition of the four WFS grids for the case when the WFS are rotated to be aligned with the LGS spot elongation. Courtesy : C. Correia.

From Fig. 4.11, we understand that if the 4 WFSs see the same wavefront (as it

is the case for the ground layer for instance), the effective phase sampling can be increased compared to the native sampling of each WFS. With four WFSs, we can basically measure the spatial frequencies four times higher. This implies that the phase reconstruction is done on a larger number of modes than the one usually set from the number of subapertures of a single WFS. Note that in tomography, the super-resolution naturally arises for layers in altitude, where the WFS grids are shifted. Rotating the WFSs allows to reproduce this effect for the ground layer (which is generally the most energetic layer), and at the same time, it allows to minimize even further truncation by aligning the LGS elongation with the subaperture corners. The other implication is that one can potentially reduce the number of subapertures of the WFS and break the dogma where the number of subapertures has to be equivalent to the number of DM actuators. Reducing the number of subapertures has two big advantages for HARMONI. First, it will allow to increase the flux per subaperture, but most importantly, it will also help in the truncation impact, as for a given number of pixels, less subaperture means more pixels per subaperture. The HARMONI LTAO performance has been computed for different WFS sampling and is reported in Fig. 4.6. We see that the WFS sampling can potentially be reduced to ~60x60 before impacting the LTAO performance. To keep some margins, the range considered for HARMONI is from 64^2 to 78^2.

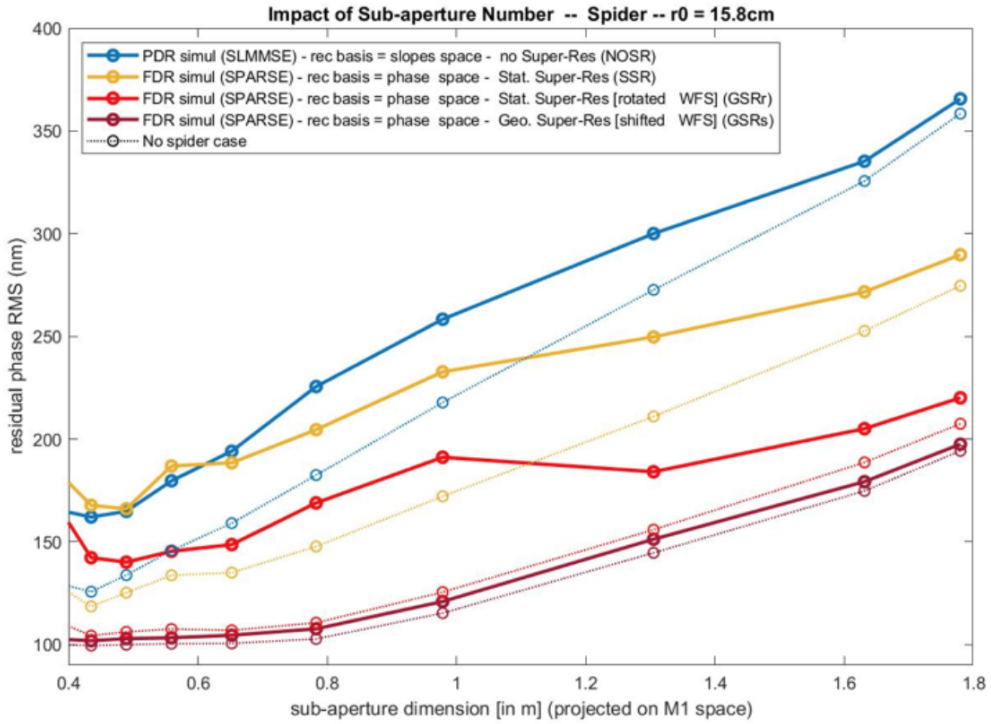

FIGURE 4.12. – Impact of the number of sub-apertures on the LTAO performance. Courtesy : T. Fusco.

4.2.4. subaperture FoV

The final parameter impacting the performance is the famous spot truncation. As described above, HARMONI will make use of an optimized reconstructor to minimize the truncation impact, but this may not be enough for the largest spots. As such, aiming for a large FoV per subaperture remains a priority. The performance of the HARMONI-LTAO for one of the worst sodium profiles and different FoV is provided by Fig. 4.13.

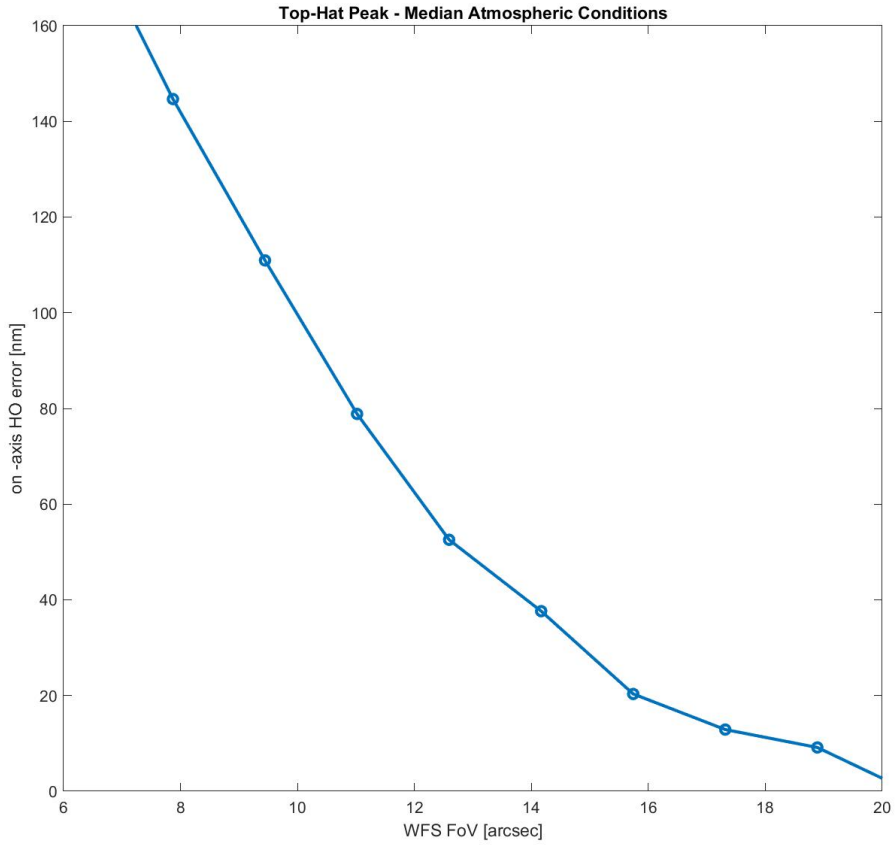

FIGURE 4.13. – Impact of the subaperture FoV on the LTAO performance. Courtesy : T. Fusco.

For this configuration, we see that a FoV of at least 15 to 16arcsec is mandatory to reduce the spot truncation error. For HARMONI, the decision is to have a FoV larger than 16arcsec per subperture.

4.2.5. detector trade-off

The system trade-off described above can be translated into detector requirements. This is summarized in Table 4.5, where we have reported the HARMONI requirements

and the characteristics of 2 potential detectors : the LVSM detector provided by ESO and the C-Blue camera from First Light company characterized in chapter 3.

Tableau 4.5. – LGSS detector specifications, LVSM and C-BLUE detector comparison

Specifications	HARMONI Requirements	LVSM detector	C-Blue detector
Dimension (pixels)	2000×2000	800×800	1608×1136
Pixel size (μm)	10 - 40	24	9
Reading mode	global shutter	rolling shutter	global shutter
Number of bits	12 bits	9 bits	8 or 12 bits
QE @ 589nm	> 95%	> 85%	73%
Fill factor	100%	100%	100%
Readout noise	$< 3e^-$	$\sim 3.1e^-$	$2.77 \pm 0.0773e^-$
Frame rate	100 Hz - 500 Hz goal is 1000 Hz	700 Hz	480 or 660 Hz selectable
Cosmetics	Less than 1 bad pixel on each 10x10 pixels	< 0.1%	0 dead pixels 545 hot pixels
Angle of acceptance	$\pm 10 - 20^\circ$	$\pm 30^\circ$	$\pm 20^\circ$

Of course, there are no ideal solutions, but based on the detectors available described in Table 4.5, we can draw potential implementations, as summarized by Table 4.6. In this table, we define first the number of subapertures and the number of pixels per subaperture. For this later, we also consider the practical implementation, which will certainly require to have guard pixels. We then allocate 1 pixel per subaperture as guard pixels, or in other words, we assume that the edges of the subaperture will not be good enough to be properly exploited for wavefront sensing. This is reported as "used pixels" in table 4.6. Based on the number of subapertures and the number of pixels, we derive the total number of required pixels and the potential detector. The last step is to look at the pixel scale and subaperture FoV. For that, we set the subaperture FoV to be equal to 16arcsec, as we have shown above that this configuration should minimize the truncation error, and we derive the pixel scale from this.

Tableau 4.6. – Potential implementations of LGSWFS for HARMONI

Parameters	Case1	Case2	Case3	Case4
subaps	64^2	68^2	78^2	64^2
pixels	17^2	16^2	14^2	12^2
used pixels	16^2	15^2	13^2	12^2
Total pixels	1088^2	1088^2	1092^2	768^2
Detector	C-BLUE	C-BLUE	C-BLUE	LVSM
plate scale ("/pix)	1	1.07	1.23	1.3
FoV (")	16	16	16	16

The results from 4.6 show that the LVSM detector, even if working with a limited number of subapertures and no guard pixels, will not be suitable to provide the right pixel scale. This would mean the implementation of a dedicated centroiding gain tracking calibration, which we would like to avoid. The C-BLUE camera, with a larger number of pixels provides more margins in the final choice. For instance the "Case2" solution fullfills all our requirements and will be selected as the baseline for HARMONI LGSWFS.

4.2.6. Discussion on Acceptance Angle

As explained in the previous chapter, one of the limitations of the CMOS detector (implemented in the C-BLUE camera) comes from the pixel acceptance angle, which can potentially lead to optical constraints. As we just discussed above, the baseline implementation for the HARMONI LGSWFS has been selected to be "Case2". In this section, we explore what means in terms of light-pixel coupling due to the acceptance angle. Indeed, the angular pixel size and the number of subapertures will have a direct impact on the required f-ratio of the microlenses. And depending on this f-ratio, the coupling of the light to the pixels will be different.

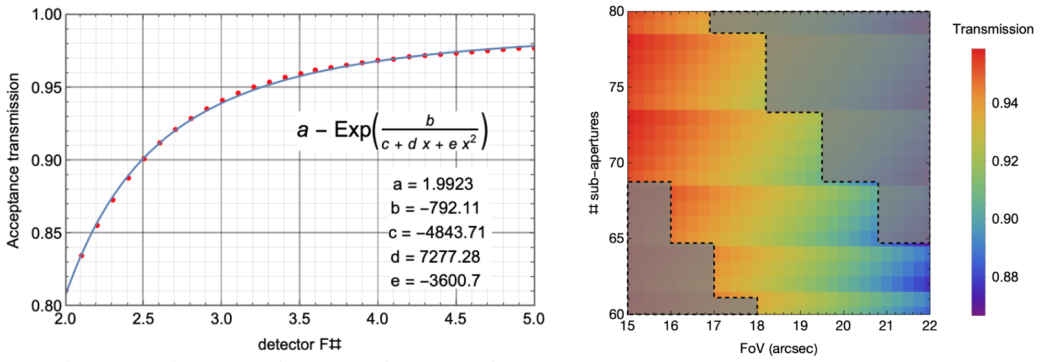

FIGURE 4.14. – Left : Pixel acceptance transmission for different f-ratio. When the incoming beam is more open (smaller f-ratio), the coupling with the pixel decreases, and the overall transmission is reduced. F-ratio around 3 or higher should be preffered. Right : Acceptance transmission for different configuration of number of subaperture and total FoV. Courtesy : F. Pedreros.

From Fig. 4.14, one can see that some specific optical configurations will provide a better transmission than others. If we want to reduce the impact of the transmission acceptance, faster beams, and hence smaller pixel scales are better. From this correspondence between the number of subapertures, the field of view and the acceptance transmission, we can derive the specific transmission loss for the 3 cases proposed above. It gives a transmission of 0.93, 0.935, and 0.95 respectively. We see here that the transmission loss is indeed kept to a small and reasonable value, which confirms the

baseline choice for HARMONI. Now that we have specified the main parameters for LGSWFS of HARMONI, we will see in the next section the practical implementation.

4.3. Description of the Laser guide star system and the Laser Detector Module

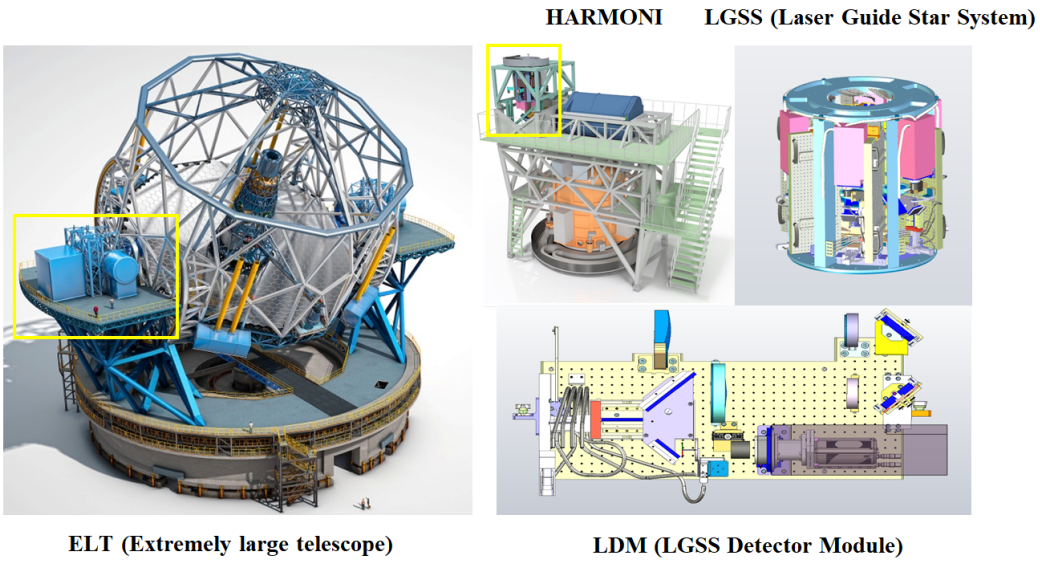

FIGURE 4.15. – The construction of HARMONI in ELT.

The HARMONI LGS-System is more than just a Shack-Hartmann. In fact, it includes a trombone that will serve to accommodate the focus of the LGSWFS and follow the LGS range when the telescope pointing changes altitude. It also includes a pupil stabilisation mirror, located in the focal plane, to stabilize the pupil position on the lenslet array. Note that the jitter control is not done at the LGSWFS level, but directly from the telescope Laser Lunch Telescope. The LGS pointing control is also done at the telescope LLT level. Fig. 4.15 shows the location of the LGSS in HARMONI : a dichroic extracts the 589nm light at the entrance of the instrument and folds it into the LGSS. Then 6 similar optical benches are mounted vertically, with 6 lenses located nearby the LGS focus to physically separate the 6 LGS beams. The whole assembly is mounted on a rotator to follow the telescope pupil while the telescope is tracking. The LGS are fixed with respect to the telescope, which in effect means that they will rotate around the science field during an observation. As everything is symmetrical, and because the science field is small, there is no variation of performance due to this rotation. Once the beams are separated, corrected for focus and pupil position, each LGS pupil is imaged at the entrance of the Laser Detector Module. The LGSS detector module is made of :

— A microlens array, at the location of the WFS bench pupil, conjugated to ELT pupil whose size is 24.36mm,
— An optical relay that conjugates the microlens array to the detector array of the camera,
— A C-Blue camera to image the LGS spots.

One of the specificities of this design is the optical relay between the microlenses and the detector. Indeed, usual SH-WFS designs have the microlenses directly in front of the detector. However, in the case of the ELT, the need for a relay arises for both types of detector options (LVSM or C-BLUE). For the LVSM detector, and even though the pixels are 24microns wide, the LISA camera implementation is such that the front window is too far from the detector. There is no possibility to have the microlens focal length long enough to accommodate for this distance, unless a very small (<40x40) number of subapertures is chosne. In the case of the C-BLUE, the optical relay is required because the pixels are smaller (9microns), and the pupil needs to be optically compressed to fit into the detector. The implementation of an optical relay between the lenslet and the detector may sound complicated, on the other hand, it allows for :

— Microlens feasibility : the lenses would be very small and very fast without a relay, at the limit of feasibility,
— Acceptance angle : to minimize the loss of transmission due to the pixel acceptance, the microlense design will be made by double microlenses. Double microlens arrays allow for a telecentric image, dividing the angle of incidence by a factor 2. This is illustrated by (Fig.4.16,right).

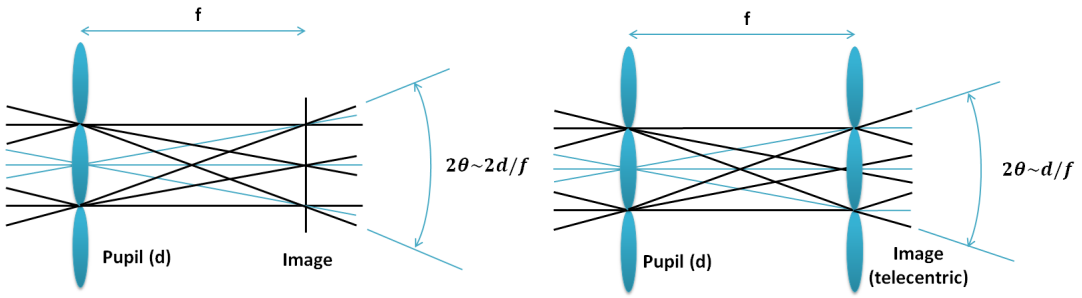

FIGURE 4.16. – (Left) : classical micro-lens array in front of a detector. (Right) : double micro-lens array concept with telecentric image.

4.4. Prototyping a Laser Detector Module

We have made a prototype Laser Detector Module to validate the concept and perform the first WFSensing tests. First, the prototype included a source, an optical relay + lenset, and a prototype C-BLUE camera. The detector tests have been presented in the previous chapter. As this development was made in parallel with the HARMONI system study, the lenslet array and optical relay are not the same one as the design choice selected for HARMONI, but close enough to be representative. We also used

a simplified mechanical interface for the relay, which was easier to implement. The associated parameters of the relay and lenslet are summarized in Table 4.8.

Tableau 4.7. – The associated parameters of the optical relay and micro-lens

Optical relay		Micro-lens	
Pixel scale	1.16”/pixel	Focal distance	2.5mm
Number of pixel per sub-aperture	13×13	Useful number of lenslet	80×80
Magnification	2.47	F number	8.645
FoV per subaperture	15.08”	Optimal pupil size	24.36mm

Then we upgraded the prototype and the bench to include a real C-BLUE camera from First Light Imaging, and to include a Spatial Light Modular in the pupil plane before the LDM, to produce phase aberrations. This whole bench is shown in Fig. 4.17.

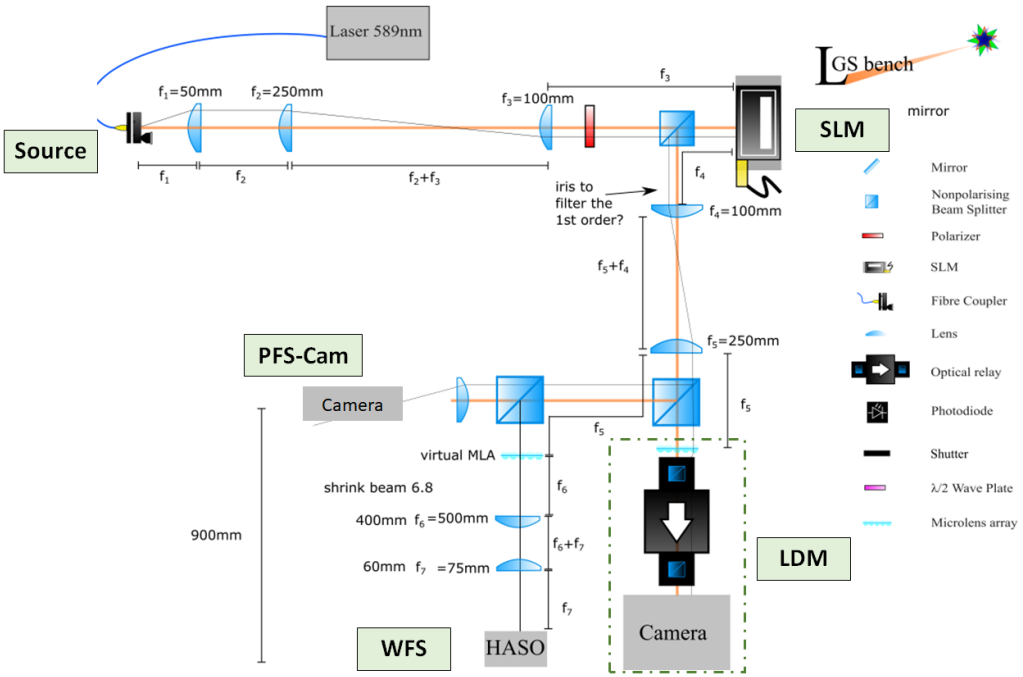

FIGURE 4.17. – LGS bench.

In the following section we report the work done on the characterization of the individual components, and the first results obtained with the whole bench

4.4.1. Lenslet Array

Double-sided lenslet arrays are noncommon in adaptive optics and tests on the manufacturing and performance of the lenslet array were necessary to identify any

issues we could meet during the manufacturing and development of the final ones for HARMONI. In 2019, we manufactured a prototype of the double-sided lenslet array. A set of 5 lenslet arrays has been ordered to Aμs, received and tested. The requirements are summarized in the table below.

Tableau 4.8. – The parameters of the micro-lens

Material	Fused silica (n=1.46 @ 589.3 nm, 20C)
Substrate characteristics and dimensions	Shape : Circular. Dimensions : 30 mm diameter
Lenslet arrays alignment	aligned to within 10 μm (goal 2 μm)
Lenslet shape	Square side for each lenslet on both sides with spherical convex surface
Number of lenslets	86 lenslets on the diameter on each side of the substrate
Useful circular aperture	24.94 mm diameter
Lenslet pitch	1st array pitch : 0.290 ± 0.005 mm
Lenslet central thickness	3.5 ± 0.1mm
Lenslet curvature radius	1st array Rc : 1.1 ± 0.04 mm 2nd array Rc : 1.1 ± 0.04 mm
Lenslet Surface Figure Error	1st array : <20 nm RMS with curvature removed 2nd array : < 20 nm RMS with curvature removed
Lenslet RMS roughness	1st array : < 5 nm RMS 2nd array : < 5 nm RMS
Lenslet filling factor	> 97% the ratio of the clear aperture of one individual lenslet to the total available space
Alignment on the substrate	± 0.05 mm with respect to substrate center
Coating on both surfaces	AR at 589.3 nm required on both sides
Cleanliness and cosmetic requirements	Component visibly clean at delivery
Surface defects	no more than < 10% of the surface of any lenslet

Several companies have been contacted to manufacture the double-sided lenslet array. The main interesting ones were :

— AMUS, that can manufacture a lenslet array with a minimal thickness of 3.5mm but for a price around 15 keuros
— Jenoptik, that was able to manufacture the lenslet for a essential price (>60 keuros), no limitation in term of thickness
— IOF, that was able to manufacture the lenslet for an important price (>25 keuros), no limitation in term of thickness

After analysis of the offer and the budget available at LAM for this development, we have chosen to work with AMUS and to manufacture 5 lenslet arrays : 4 with an AR coating on both sides (R<0.5% at 589.3nm) and one uncoated. Fig. 4.18 shows the lenslet ordered and received.

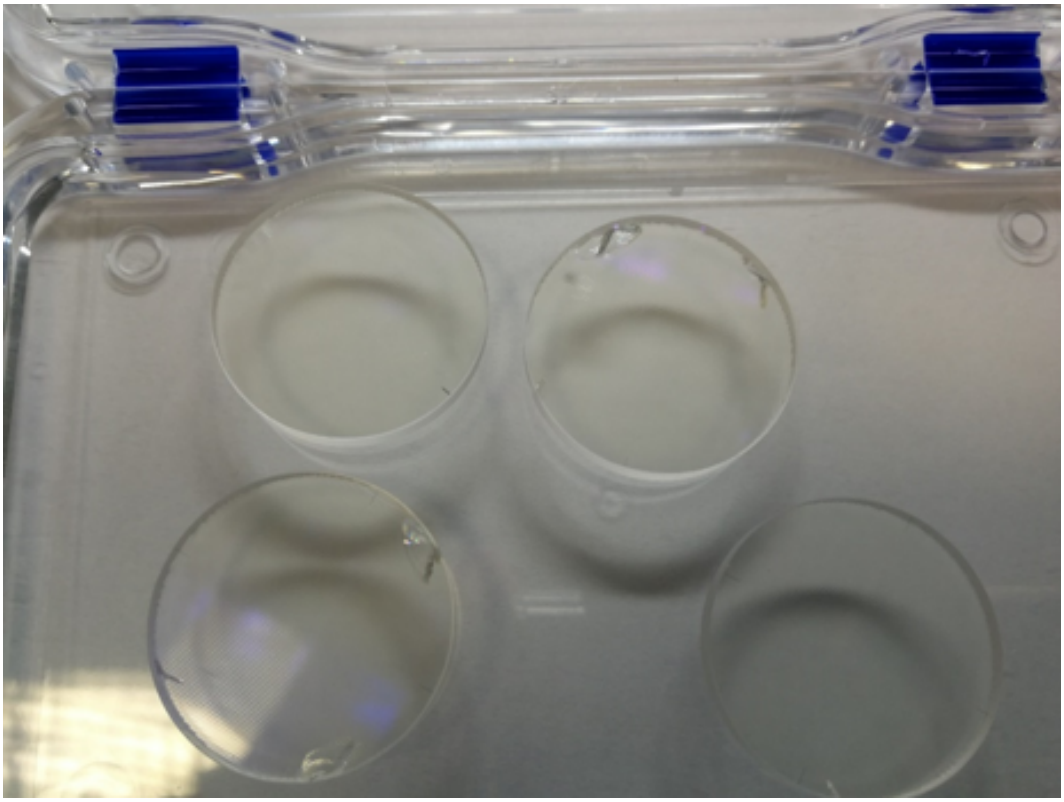

FIGURE 4.18. – Picture of the 4 coated microlens array.

The tests that we performed with the Microlense Array (MLA) were :
— Radius of curvature done with the Wyko and still micrometer
— Roughness measurements
— Image quality : Shape of the image at the focal point with collimated source and microscope camera.

Fig. 4.18 shows the microlense surface center with and without coating observed with the interferential microscope Wyko. We noticed a regular pattern, a defect at the center of each microlens, on both sides of the MLA. The affected area is 30-50μm diameter and the height of the defect is few nm. It could be caused by the photolithographic step of the µlenses machining, the smoothing of the µlenses surface done by a heating treatment, or the cleaning process : maybe the position of the components during the drying leads to drops staying at the summit of the µlenses. Further tests were done to understand the impact of this defect on the image quality. For that, the small bench shown in Fig. 4.19 has been developed. The test bench is composed by a fibered source at 635nm. A 2" diameter lens makes a collimated beam. This beam is checked by a shear plate. This beam illuminates the microlens array. A microscope objective makes an image of µlenses on the detector.

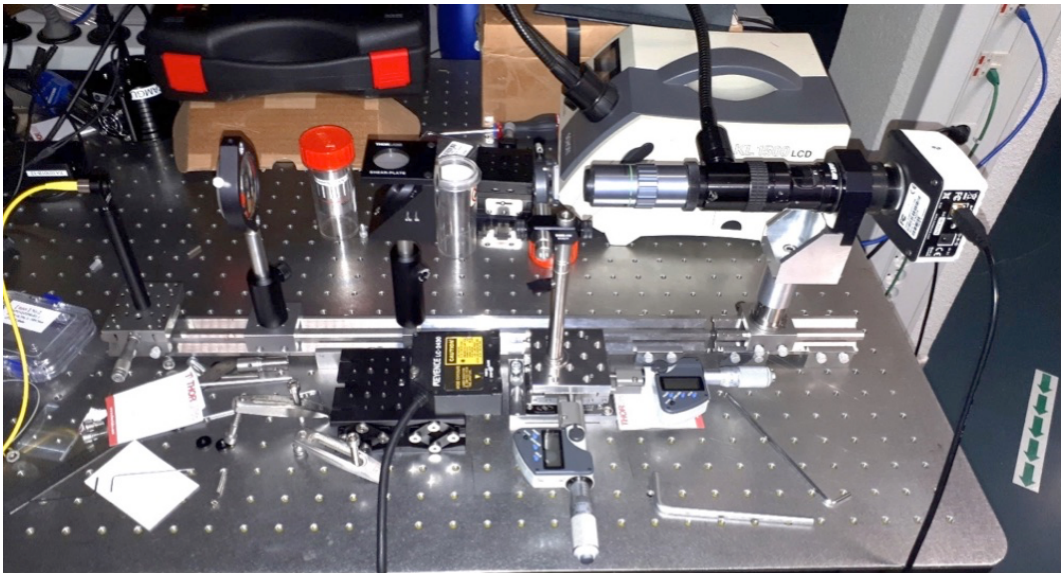

FIGURE 4.19. – Picture of the test bench. The source is on the left side and microscope camera on right side

An alignment of the test bench is done with the following steps : (1) adjust the position of the collimated lens with the source object to make a collimated beam, (2) check the collimation of the beam with the shear plate, (3) insert the µlens array, (4) put in place the microscope with the camera, (5) adjust the microscope with the µlens array to make an image of the 2nd microlens array. When the ring located on top of the µlens is the focus, we considered that the microscope images the 2nd microlens array. Images obtained are shown in Fig. 4.20. The effect of the ring is clearly visible when the microscope is focused on the lenslet surface, however, the image quality is not impacted, and the lenslet PSF are limited by the diffraction. The effect when out of focus must translate to diffusion / background. This will be corrected when ordering the final MLA for HARMONI.

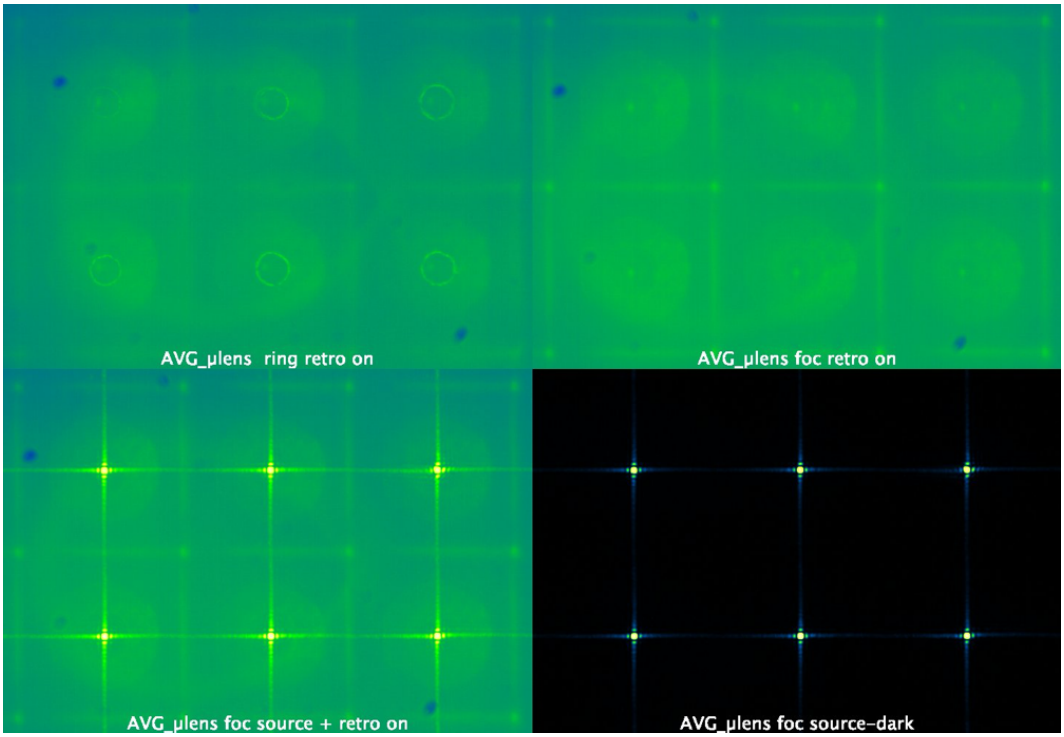

FIGURE 4.20. – Lenslets images, with/without backlight and ring/best image focus. Top-Left : focus 0 μm (ring), retro light on. Top-Right : focus 216 μm, retro light on. Bottom-Left : focus 216 μm, retro light on, source on. Bottom-Right : focus 216 μm, source on. Source intensity level saturates central peak on detector, in order to highlight diffraction pattern

The other test that was done was to analyse the telecentricity error across the lenslet FoV. Results are shown in Fig. 4.21.

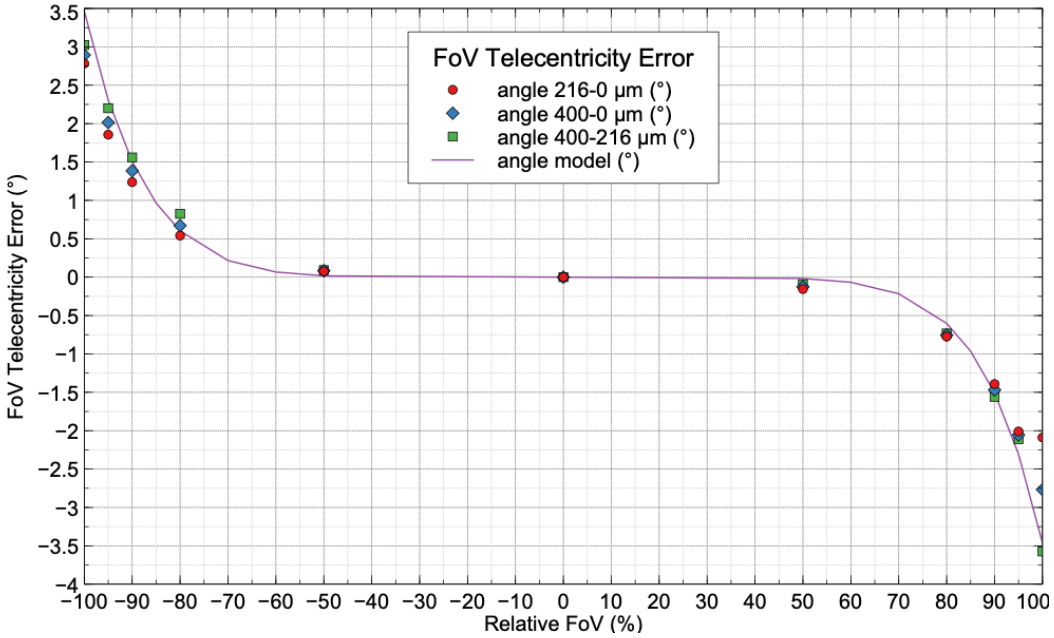

FIGURE 4.21. – Lenslets images, with/without backlight and ring/best image focus. Top-Left : focus 0 μm (ring), retro light on. Top-Right : focus 216 μm, retro light on. Bottom-Left : focus 216 μm, retro light on, source on. Bottom-Right : focus 216 μm, source on. Source intensity level saturates central peak on detector, in order to highlight diffraction pattern

For FOV > 15arcsec (95% of lenslet full FoV 15.75arcsec), telecentricity error is > ±2°, which means that for a relay magnification of about 1 :2.5, the beam incidence angle on detector is > ± 5°. In addition, due to the inversion of curvature induced by the transition zone, the beam aperture (already ± 8.5° on detector) is increased (beam elongation when out of focus). This is not compatible with the detector acceptance angle and will probably result in the edge of field darkening. This point has been feedback to the company, and the specifications will be updated for the final MLA for HARMONI, to optimize the useful FoV of the MLA. This first MLA prototype has then been very useful to identify the key parameters and to confirm the component feasibility. Even if not perfect, this MLA is good enough to be implemented in the LDM prototype.

4.4.2. Optical Relay design and alignement

The optical relay has been designed by Eduard Muslimov, from a preliminary design made by Patrick Rabou (IPAG). It consists of 6 custom lenses, providing a magnification of 2.47. The design is shown in Fig. 4.22.

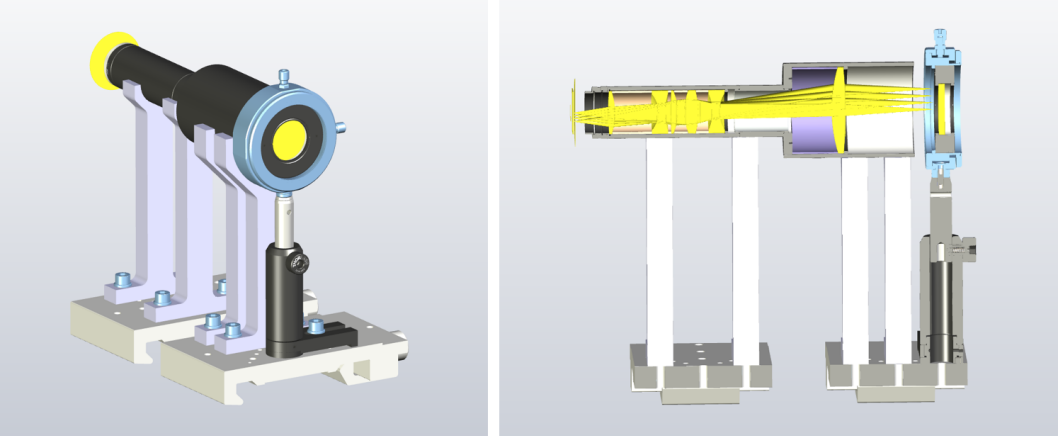

FIGURE 4.22. – Design of the optical relay

Once the relay has been mounted and a first alignment was done, we measured the magnification with 2 methods : by measuring the distance between 2 spots when the lenslet array is inserted in the relay, and simply by measuring the image of a known target. This is illustrated in Fig. 4.23. We measured an averaged distance between spots of 12.78 pixels, which corresponds to a magnification of 2.52. This is not exactly the expected theoretical value, but close. This first analysis also revealed strong spot distortion at the edges of the pupil, which was later identified as a mis-alignment of the lenses within the relay and corrected.

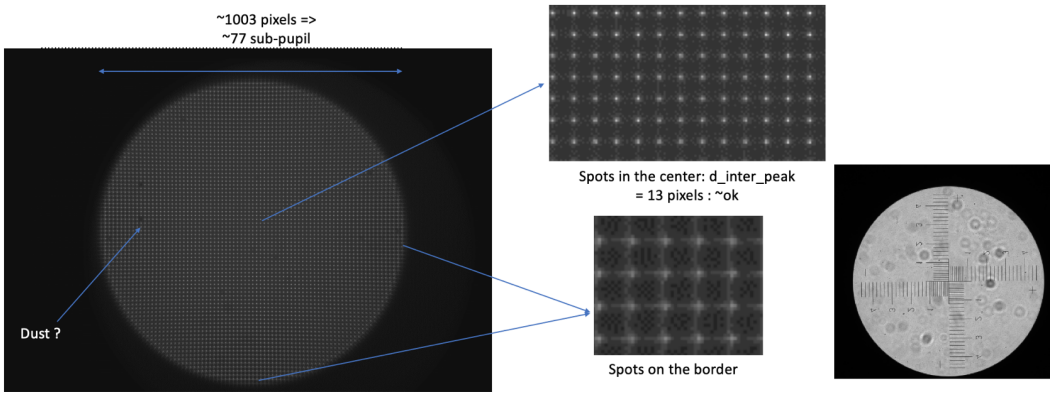

FIGURE 4.23. – Measurement of the relay magnification, with both the lenslet and a target.

The next step was to optimize the relay alignment in to minimize the spot ellipticity and distortions. For that, we can adjust the position of the first set of lenses and acquire the spot images. The spot detection, centre of gravity and FWHM measurement were done automatically with a software developed in Matlab. Fig. 4.24 shows the relay and the lenses adjusted to optimize the image quality. Fig. 4.25 shows the results after optimization for the distribution of spot FWHM across the pupil.

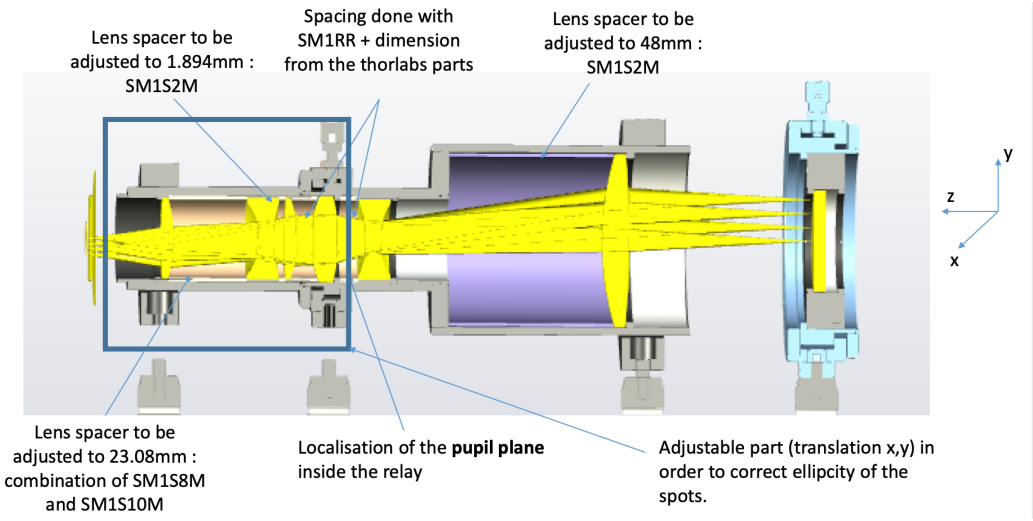

FIGURE 4.24. – Optimization of the relay alignment.

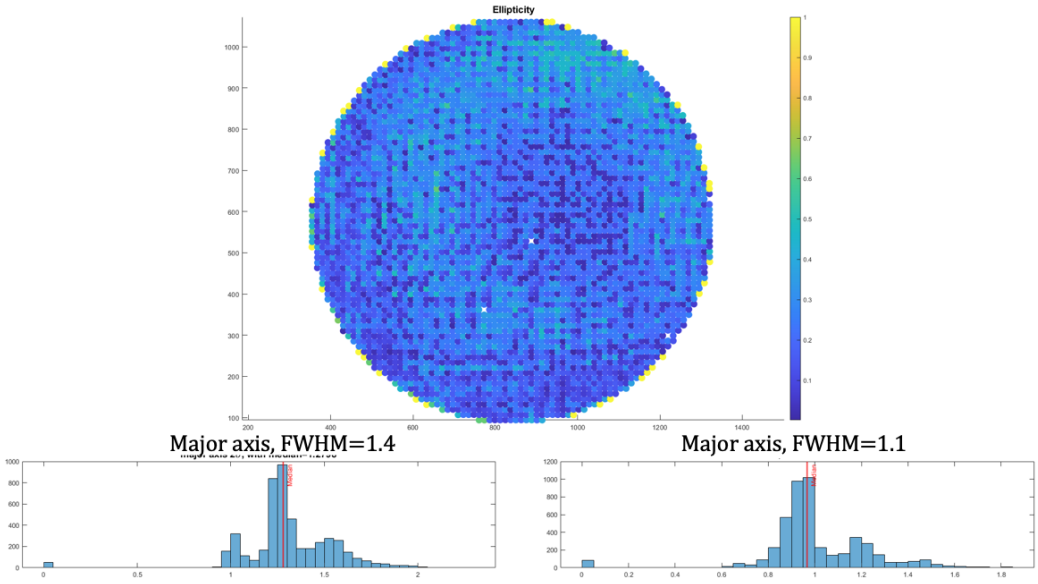

FIGURE 4.25. – Distribution of the spot FWHM across the pupil. The median FWHM is between 1.1 and 1.4 pixels which is in accordance with the optical prescription.

Finally, in Fig. 4.26 we plot the distance between the Center of Gravity measured on each spot, and the center of the subaperture. This gives the NCPA of the system. After optimization of the relay alignment, the slopes measured are between 0.2 and 0.8pixels. Again, this is not perfect, but good enough to work with the LDM prototype and continue the LGSWFS validation.

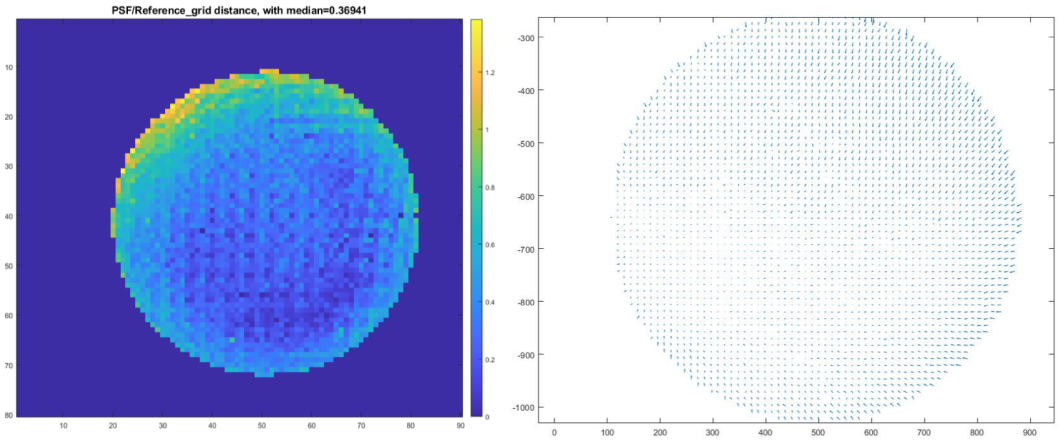

FIGURE 4.26. – Distance between each spot and the subaperture center, after optimization of the optical relay alignment. This corresponds to the LDM internal aberrations and lenslet distortion. In a real system, it would be absorbed as reference slopes, and NCPA. For our prototype, we demonstrated that the reference slopes are as small as 0.5pixels in average. This will be even further optimized for the final HARMONI WFS.

4.4.3. Measurements of C-BLUE reflectivity

In the first version of the LDM prototype, we worked with the simplest implementation of a Sony detector. In 2020, once the C-BLUE camera was commercialized by FLI, we bought one of the first cameras and installed it in our prototype bench. The C-BLUE camera comes with a window in front of the camera, that in our version was not treated for anti-reflections. We implemented a simple experimental setup to characterize the reflectivity due to this window. This is shown by Fig. 4.27, where we indeed see 2 reflections, due to the camera and detector window. By using a powermeter, we could even quantify the amount of reflected light and confirm that it was consistent with the 2 standards (no specific anti-reflection coatings) windows shown as Fig. 4.28. If the glass has no anti-reflection coating, we can assume that the reflectivity of each interface is 4%, then the two spots acquired by the sensor are $r_{11} = r_1 \times 0.96^4 = 0.85 \times r_1$ and $r_9 + r_{10} = 2 \times r_1 \times 0.04^2 \times 0.96^4 = 0.0028 \times r_1$, therefore the ghost spot is 0.28 % of the incoming ray, this should be kept in mind, so a new version of the C-BLUE camera will implement optimized windows to minimize these reflections.

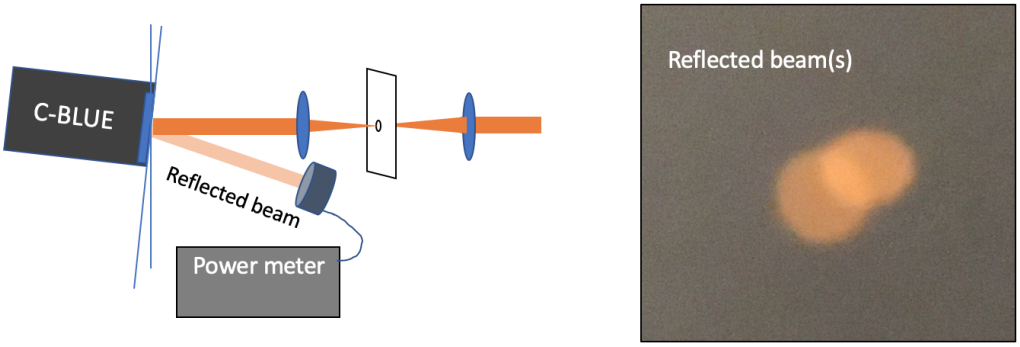

FIGURE 4.27. – C-BLUE window reflectivity characterization.

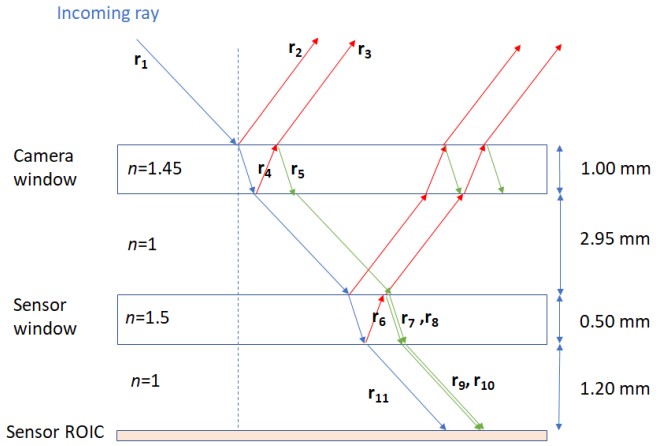

FIGURE 4.28. – Schematic plot of C-BLUE window reflectivity.

4.5. First results with the Laser Detector Module prototype

Now that we have characterized each individual component (lenslet, relay, camera), and demonstrated that they were conforming with the specifications, we continued the work by upgrading the bench with a Spatial Light Modulator to generate aberrations. The goal of this step will be to demonstrate that the proposed design can indeed work as an LGSWFS, and as such validate the HARMONI design. The goals for this bench are :

— Reproduce the ELT environment and the M4 features with the SLM. Indeed, the SLM provides an exquisite phase sampling of more than 1000x1000 points, which will be used to emulate M4 influence functions. We can implement between 10 and 12 SLM pixels per M4 actuator, allowing for an accurate phase generation.

— Measure the interaction matrix with the fake M4, and validate the numerical models for the WFS.

— Optimize the interaction matrix acquisition procedure. Validate the strategy for HARMONI on-sky. Demonstrate both zonal and modal interaction matrix construction.
— Close AO loop (with a single WFS) on turbulence.
— Demonstrate the concept of super-resolution, with multiple acquisition of shifted phases introduced by the SLM
— Study the impact of the spider shadow on phase measurement and reconstruction.
— Test and validate calibration methods for pupil registration and control. In this case, we can shift the phase introduced by the SLM and demonstrate that our algorithms are able to detect and compensate the mis-registration.
— As a potential upgrade of the bench : implement elongated sources, and anchor the numerical simulations of truncation with real bench data.

4.5.1. Implementation of the LDM prototype into a laser bench

The proposed bench implementation is described by Fig. 4.17. It includes a source, in our case we use a laser source at 589nm. In this version of the design, the source will be diffraction limited. An upgrade of the source to be able to reproduce elongated sources will be considered in a later stage. The source is then imaged on a pupil plane where we introduce an SLM. The SLM (shown in Fig. 4.29) is from Meadowlark Optics. The main characteristics of this SLM are the following :

— 1920 x 1152 liquid crystal « pixels », 9.2microns
— 8 bits grayscale coding for 256 phase
— AR coated 488-800 nm, < 1 %
— High-speed version, up to 800 fps
— water cooling

We chose this SLM because it is the only model which can potentially run as fast as 800Hz. Standard SLMs are usually set with a refresh rate of about 60Hz, so this model is very interesting for this fast feature. Indeed, it can potentially be used in the AO loop to generate turbulence at high-speed, and used to emulate the M4 correction too.

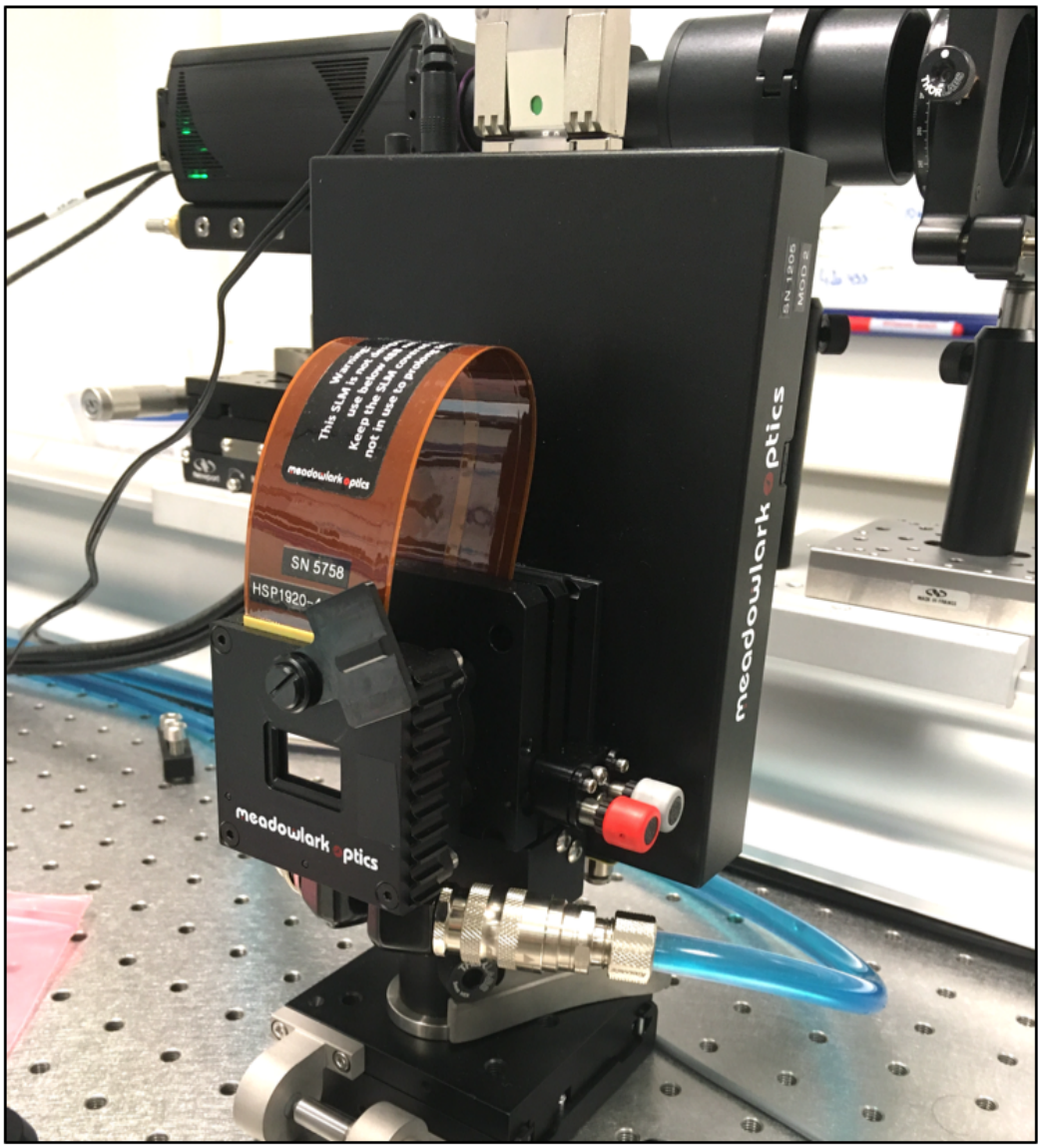

FIGURE 4.29. – .

The SLM was first tested and characterized in stand-alone, with the bench described by Fig. 4.30. This step was necessary to calibrate the SLM output and later properly control the phase generation.

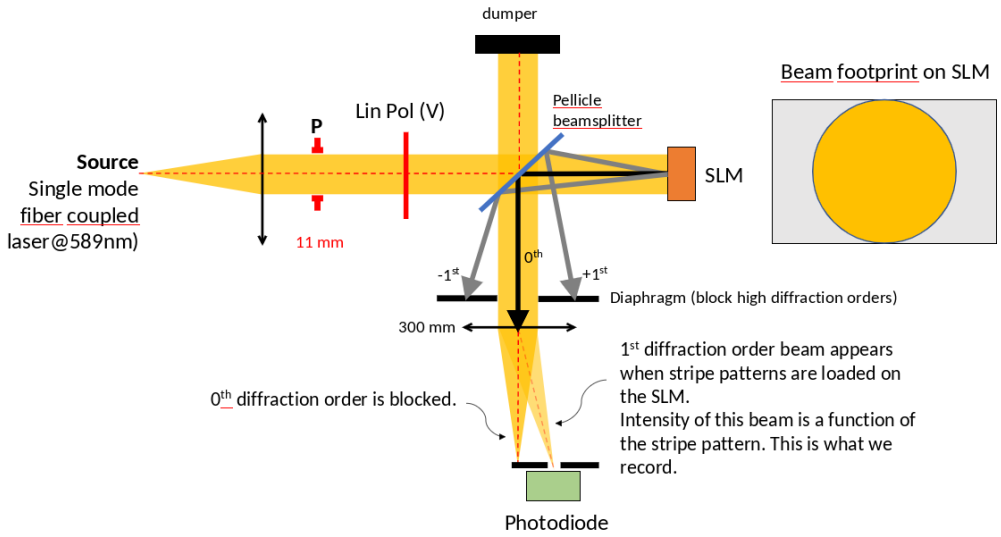

FIGURE 4.30. – SLM stand-alone bench for characterization.

Figure 4.31 shows 2 PSFs generated with the source and the SLM, when no turbulence is introduced on the left, and with some turbulence on the right.

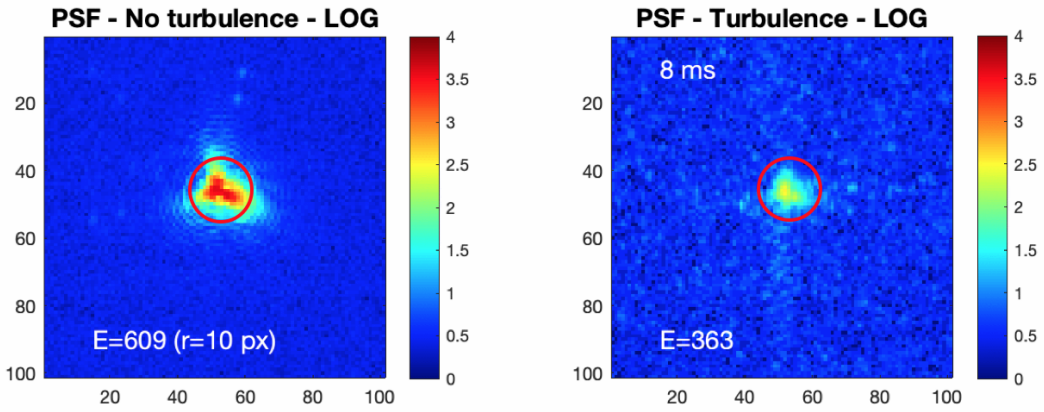

FIGURE 4.31. – PSFs obtained with the stand-alone SLM bench, with and without turbulence. PSF are short-exposure PSFs.

We also characterized the temporal behavior of the SLM. For that, we injected phase patterns on the SLM, sequentially, and we measured with an oscilloscope raising time. Results are shown in 4.32.

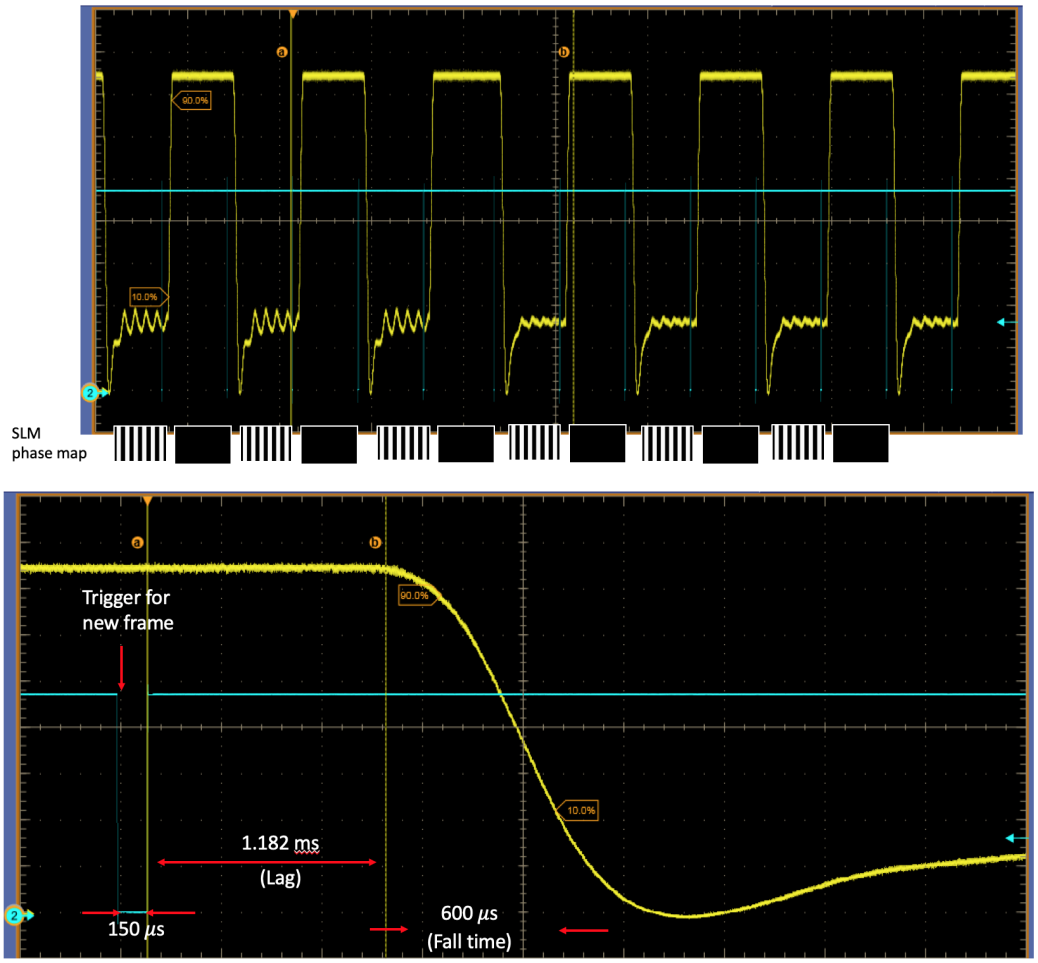

FIGURE 4.32. – Tests of SLM temporal behavior.

4.5.2. Interaction Matrix

The first measurements of an interaction matrix were done at the end of my thesis. In Fig. 4.33 we show 2 examples when introducing a Focus and and Astigmatism on the SLM.

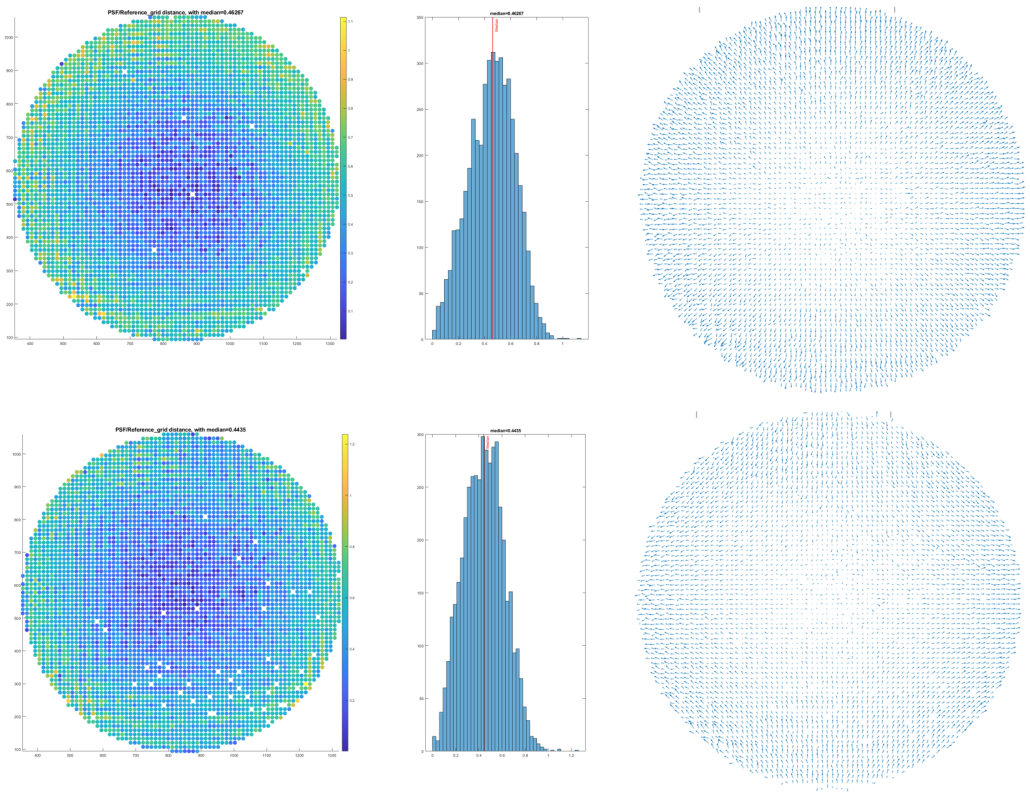

FIGURE 4.33. – LGS Slopes measurement for 2 modes (Focus and Astigmatism) introduced by the SLM.

The next step will be to build a full interaction matrix and eventually close the AO loop in the lab. This will finalize the validation of the design of the LGSWFS for HARMONI.

4.6. Perspective

The full LDM bench, including the SLM will be used to test and validate several concepts of the HARMONI design. In particular, this bench will be used for :

— Test and validate the LGSWFS linearity (finalise the pixel scale choice)
— Check noise propagation from the interaction matrix and the performance under different flux implementation
— Reproduce the exact M4 actuator geometry with the SLM, and validate the numerical interaction matrices used in the simulations
— Validate the concept of super-resolution, by shifting temporally the phases printed on the SLM
— Demonstrate and optimize calibration algorithm such as the mis-registration identification, pupil tracking
— Test the introduction of slope offsets for NCPA compensation

— Test and validate algorithm for under-illuminated segments, or missing segments
— Check impact of phasing error on M4
— Test tomographic algorithm, by implementing a temporal acquisition of several phase screens
— Optimize the acquisition and other templates.

All this work will continue in the next months, and the experimental work that I started will serve as a foundation for this.

5. Detector Shutter Impact on Adaptive Optics

Sommaire

5.1. Introduction

In this section, we analyse another aspect that would bring potential risk for the system's performance, which is the read-out scheme of the detector.

In current mainstream CMOS detectors, two read-out modes exist. These modes are namely the rolling shutter and global shutter, respectively. The differences between these two modes mainly come from the pixel technology and the way they can be read-out. In a global shutter scheme, as shown in (Fig.5.1,(a)), a single read exit (red square) which is used for the whole array. The full frame is integrated simultaneously, and then the data is extracted line-by-line through this read exit. This implies some latency due to the data transfer, the so-called "read-out" time. For a Rolling Shutter (Fig.5.1,(b)), pixels on each line correspond to one read exit. This allows the data to be read out line by line : the pixels of each line can be integrated directly without waiting for previous lines. This read-out mode is known as rolling shutter. Compared with the Global Shutter, the Rolling Shutter decreases the read speed. However, when observing a moving target, it also brings distortion to the image because the last pixel

is read almost one full frame late with respect to the first pixel. This is illustrated in (Fig.5.2).

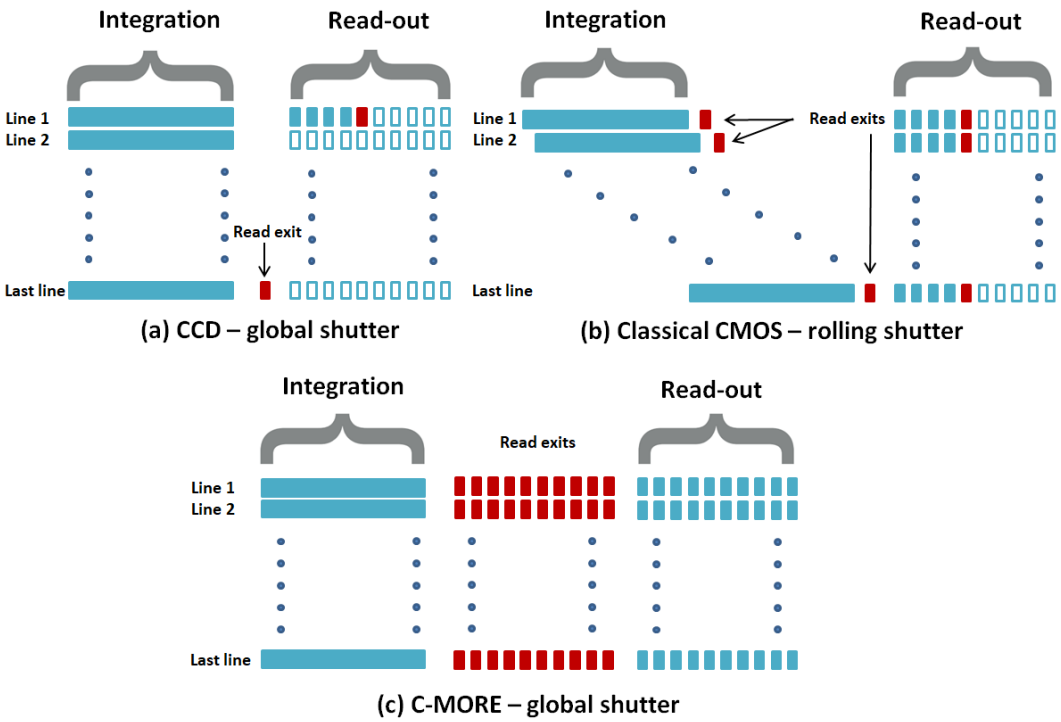

FIGURE 5.1. – The read-out modes of CCD, classical CMOS and C-MORE. (a) shows the process of CCD, the blue bars correspond to each line in one frame, the red square denotes the read exit (amplifier/ADC) and the pixel is reading out, the blue squares are the pixels whose data has been read out, and the white squares are the ones that are not read out. (b) illustrates the process of classical CMOS with rolling shutter, each line has one read exit, therefore the data is read out line by line vertically or horizontally (according to the arrangement of read exits). (c) shows the process of CMOS with global shutter, each pixel has one read exit, the frame can be integrated and read out simultaneously.

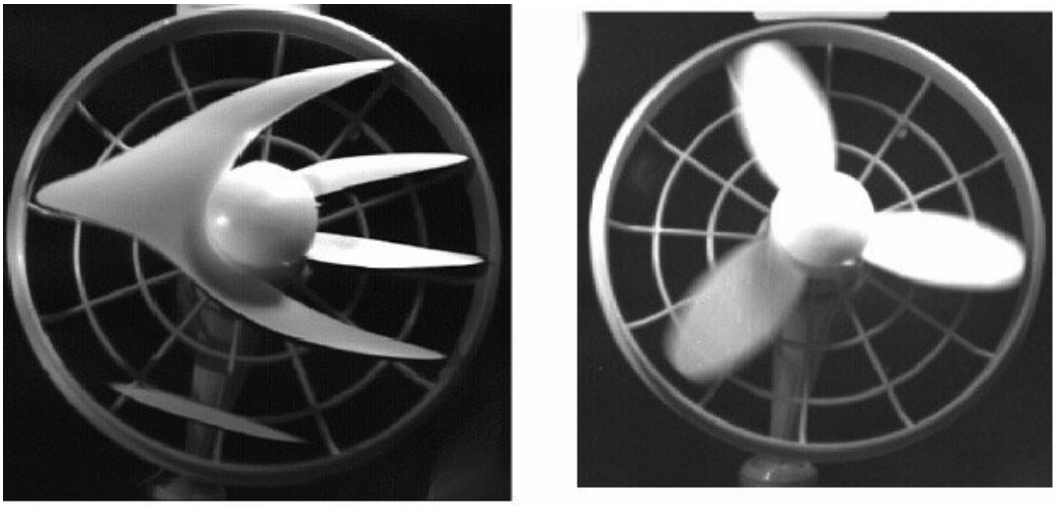

FIGURE 5.2. – Illustration of the potential impact of a Rolling Shutter read-out (a) when observing a moving target. Because pixels are not integrating simultaneously, but continuously, it creates distortions in the images when compared to the standard Global Shutter read-out scheme (b). Credits : Fayçal Saffih - Foveated Sampling Architectures for CMOS Image Sensors

For adaptive optics, a rolling shutter means that pixels across the pupil are read at different timings. In effect, it may mean that the turbulence would have evolved between the beginning of the pupil sampling and the end. This would cause an extra error in the phase reconstruction, and it can be interpreted as an extra-aliasing error. For instance, if we assume the tilt only, if this tilt signal evolves during the reading of the pupil, part of it will be interpreted as a focus, or other higher-order modes (in fact, it is a sort of anti-aliasing, where low order induces higher-order modes). This would not be the case with a global shutter. This mode confusion can be dramatic for the AO loop, but also for specific tasks such as the identification and control of vibrations within the system. A vibration within a global shutter system can be simply identified through a power spectrum analysis of WFS slope data, be it tip/tilt, or a reconstructed higher-order mode. For a rolling shutter device, tip-tilt vibrations at rates below the frame rate of the camera will introduce a bias in the WFS measurements that appear as a slope gradient between adjacent rows of sub-apertures (assuming each subaperture is only a few rows of pixels and the device is rolled row-by-row). Vibration identification for fast higher-order modes would be far more challenging as accurately reconstructing modes from a single row of rolling sub-apertures is difficult. The signal of a given high order oscillation becomes a function of its oscillation frequency. As the frequency of oscillation decreases, the signal approaches that of the global shutter, however this implies that the sensitivity of the WFS to higher temporal-frequency aberrations will decrease, and these may be incorrectly identified as other wavefront modes. To account for this, the AO control system will need to reconstruct the tempo-

ral fingerprint for every mode of interest across the full range of potential frequencies. This implies a large additional computational load on the soft real time computer (RTC) solely for vibration identification. Subsequent temporal control within the hard RTC may also require modification to properly correct for aberrations.

Another issue with the rolling shutter arises when one would need to synchronize different cameras together. This is the case for tomographic reconstruction, where it is crucial that the several WFSs see the same part of the pupil at the same time, in order to be able to properly perform the tomographic reconstruction. If using Rolling Shutter detectors, it means that the several WFSs will have to be all aligned identically with the pupil, which can impose severe opto-mechanical constraints on the system. Moreover, and taking the example of the ELT, it could be interesting to rotate each WFSs to be aligned with LGS elongation, in order to minimize the truncation impact. The Rolling shutter, by imposing to have all the 6 WFSs aligned would not allow for such a configuration.

One way to mitigate the Rolling Shutter effect would be to have a "rolling DM" (DIRNBERGER, RIGAUT, MINOWA et al. 2018), where we send the commands to DM on partial parts of the pupil. This would actually also improve the overall bandwidth of the system. However, the generalization of this approach to tomographic system is not straightforward, and more critically, the DM technology does not necessarily accept rolling commands. As an illustrative case : M4 - the ELT DM - does not accept such rolling commands. In fact, the rolling shutter approach, when not used with a rolling DM, would actually add some delays to the loop.

Based on the discussion above, the shutter impact has to be analyzed and this chapter makes a qualitative and quantitative analysis of the shutter impact in the AO performance.

5.2. Simulating the shutter impact

The process to simulate the shutter impact is described below. First we create phase screens, either single Zernike modes or the full turbulence, that will be temporally evolving in-front of the WFS. The temporal aspects are important, as compared to classical AO simulation, it is necessary to temporally over-sample the wavefront evolution. Indeed, where the usual AO simulations assume that the wavefront is static, or averaged during the exposure of the WFS, it is important to properly simulate the temporal evolution for estimating the Rolling Shutter impact.

5.2.1. Simulation scheme

The overall process is described by (Fig. 5.3). It can be summarized by the following steps :

— Create N sub-frames of aberrations (single Zernike, or full turbulence) to be measured by the WFS. The temporal sampling of this phase screen must be scaled such as it corresponds to at least 2 consecutive RS reads. In other words, if we assume a detector reading each line in a RS scheme, and a turbulence evolving parallel (or perpendicular to) the pixel lines, one should create as many phase screens as there are detector lines to emulate a single WFS exposure. If we assume the WFS sampling frequency (FPS) to f_f, and a detector made by n lines read one after the other, then the phase screen evolution must be sampled over a frequency of $n \times f_f$
— For each of these phase screens, we create the corresponding spot images.
— An equivalent Global Shutter WFS spot frame is then created by simply averaging the n sub-frames corresponding to a single WFS exposure.
— The Rolling Shutter equivalent image is produced by taking the first line of the first sub-frame, then the second line of the second sub-frame and so on. This is illustrated by Fig. 5.4.
— Finally, we chose a reference with which we will be comparing the performance. For that, we chose to use the WFS spot images created by the middle sub-frame. We call this image the reference image.
— From the 3 WFS spot images described above, we perform the corresponding phase reconstruction based on a modal interaction matrix.
— The performance is finally estimated by computing the difference between the GS reconstructed phase and the reference phase, and on the other hand, the difference between the RS reconstructed phase and the reference phase

More precisely, the process to compute the equivalent RS frame can be expressed as :

$$PSF^i_{RS}(x, y_k) = PSF^i_k(x, y_k). \tag{5.1}$$

Where $PSF^i_{RS}(x, y_k)$ denotes the k^{th} $(1 \leq k \leq n)$ line of the i^{th} full-frame, and $PSF^i_k(x, y_k)$ denotes the k^{th} line of the k^{th} sub-frame in the i^{th} full-frame. Since there are n sub-frames in the i^{th} sampling time (the i^{th} full-frame), and each sub-frame has n lines the RS PSF in the i^{th} full-frame is expressed as :

$$PSF^i_{RS}(x, y) = PSF^i_{RS}(x, y_k), (1 \leq k \leq n). \tag{5.2}$$

For the GS operation, the construction of PSF is the time average of all the sub-frames in a full-frame, which can simply be expressed as :

$$PSF^i_{GS}(x, y) = \frac{\sum_{k=1}^{n} PSF^i_k(x, y)}{n}, \tag{5.3}$$

where $PSF^i_{GS}(x, y)$ is the GS PSF. In order to compute the difference between GS and RS phases, we define the reference frame as :

$$PSF^i_{Ref}(x, y) = PSF^i_{n/2}(x, y), \tag{5.4}$$

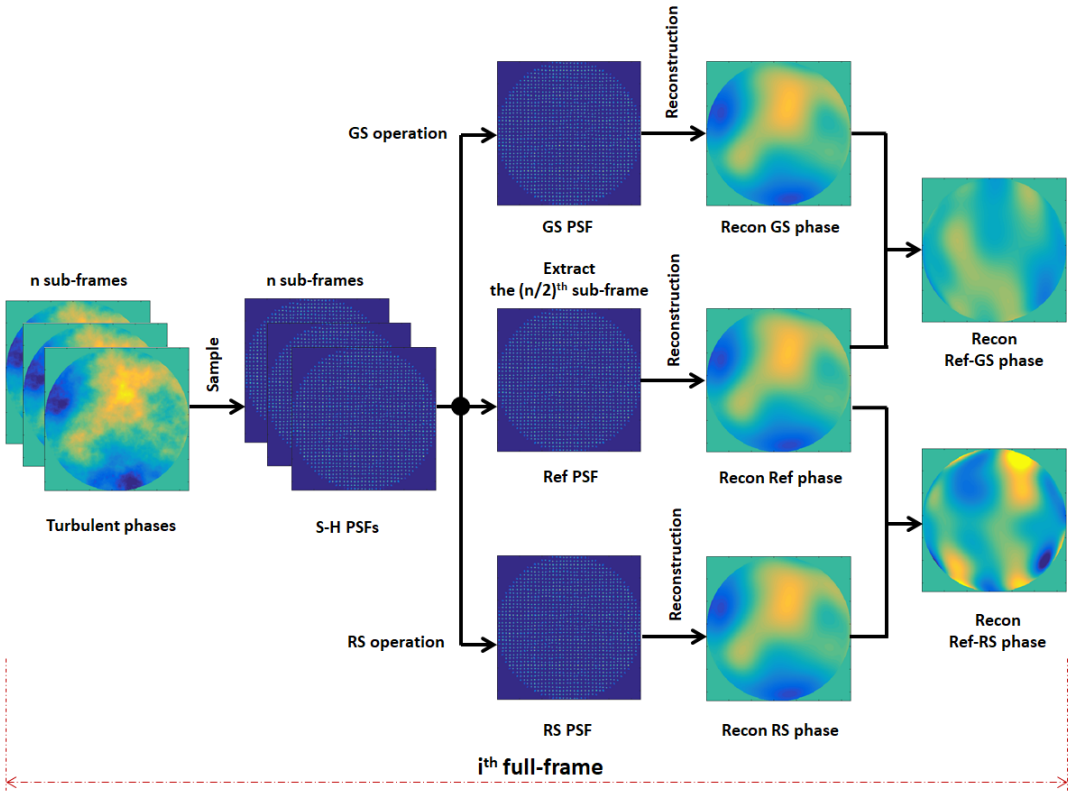

FIGURE 5.3. – The reconstruction process of GS and RS phases. When the turbulence phases are sampled by Shack-Hartmann WFS (S-H WFS), these S-H PSFs will be divided into three ways to produce Ref PSF, GS PSF and RS PSF respectively. After the reconstruction, the Ref- GS and Ref-RS phases are formed by calculating the difference between Ref phase and GS phase, and the difference between Ref phase and RS phase.

And as explained above, the final error is estimated by computing the error in terms of the reconstructed wavefront, by :

$$\begin{cases} \varphi^i_{GS-Ref}(x,y) = \varphi^i_{GS}(x,y) - \varphi^i_{Ref}(x,y) \\ \varphi^i_{RS-Ref}(x,y) = \varphi^i_{RS}(x,y) - \varphi^i_{Ref}(x,y) \end{cases} \tag{5.5}$$

5.2.2. Illustrating the rolling shutter mode confusion

This section qualitatively analyzes the effect caused by the shutter impact in wavefront sensing. For that, we first start by a simple case considering a single Zernike mode. In particular, we look at how a tilt mode would be seen in the presence of a Rolling Shutter scheme. Later, we evaluate the impact for a full turbulence seen by the WFS.

It is first necessary to choose the simulation parameters. Here, and for the sake of

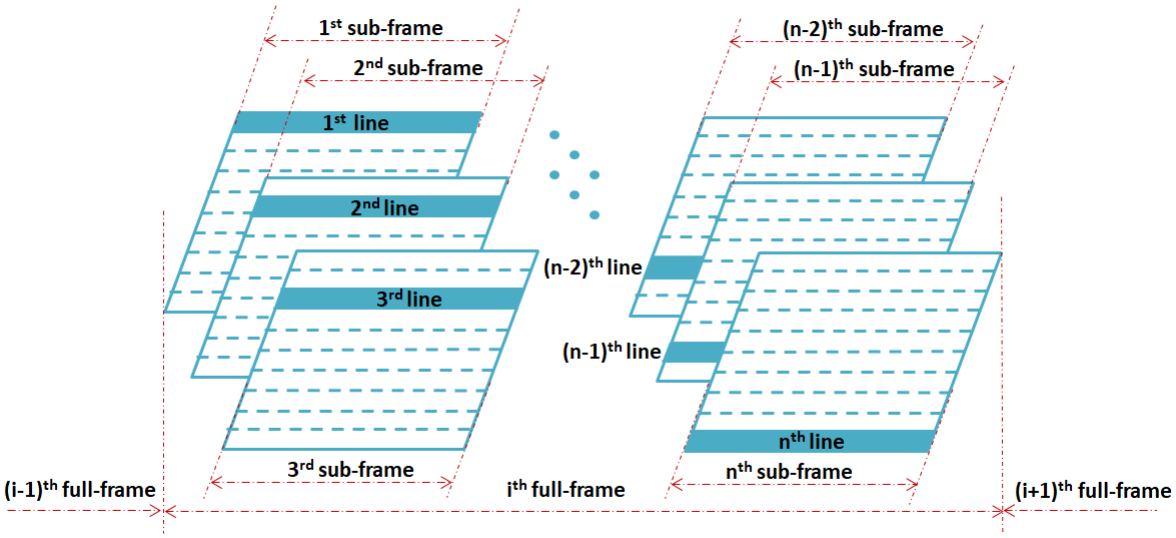

FIGURE 5.4. – The schematic plot of the construction of RS PSF. Each full-frame consists of n sub-frames, and each sub-frame consists of n lines divided by dash lines.

illustration, we chose : telescope diameter D = 8m, fried parameter r_0 = 25cm, sub-aperture number $n_s \times n_s$ = 20x20 , pixel number per sub-aperture $n_p \times n_p$ = 16x16, sampling frequency of each full-frame f_f = 500Hz, and a phase reconstruction done for 50 Zernike modes.

For the rolling shutter simulation, and as explained above, we are creating a total of 320 sub-frames, corresponding to the 20x20 subaperture times 16pixels per subaperture. The GS full-frame is computed by averaging all the sub-frames. The Ref frame is chosen at the middle of sub-frames (equation 5.4), here it is the 160^{th} sub-frame.

Results for a single Tilt mode are shown in Fig. 5.5. The comparison between the original tilt phase, reconstructed Ref, GS and RS phases is shown in (a), while (b) shows the residual between the reference tilt, the tilt reconstructed with the Rolling Shutter or Global shutter. For this specific example, we see that the Global Shutter case provides a perfect reconstruction, while the effect of the rolling shutter is to convert part of the tilt energy into higher orders. More precisely, inset (d) shows how the original tilt is projected onto higher orders due to the Rolling Shutter read-out scheme. This can be seen as a sort of anti-aliasing effect, where low order will be interpreted as higher order. This will create an extra-error in the final error budget of the AO instrument. From the quick analysis done here, we show that a significant fraction of this signal (~40%) would be aliased onto higher order, which can potentially impact the final AO performance.

For an LGS system, the Tip-Tilt modes are usually filtered out, as their are not correlated with the atmospheric Tip-Tilt signal. This means that there are basically running in "open-loop", and the analysis done here is perfectly valid. It also means that the

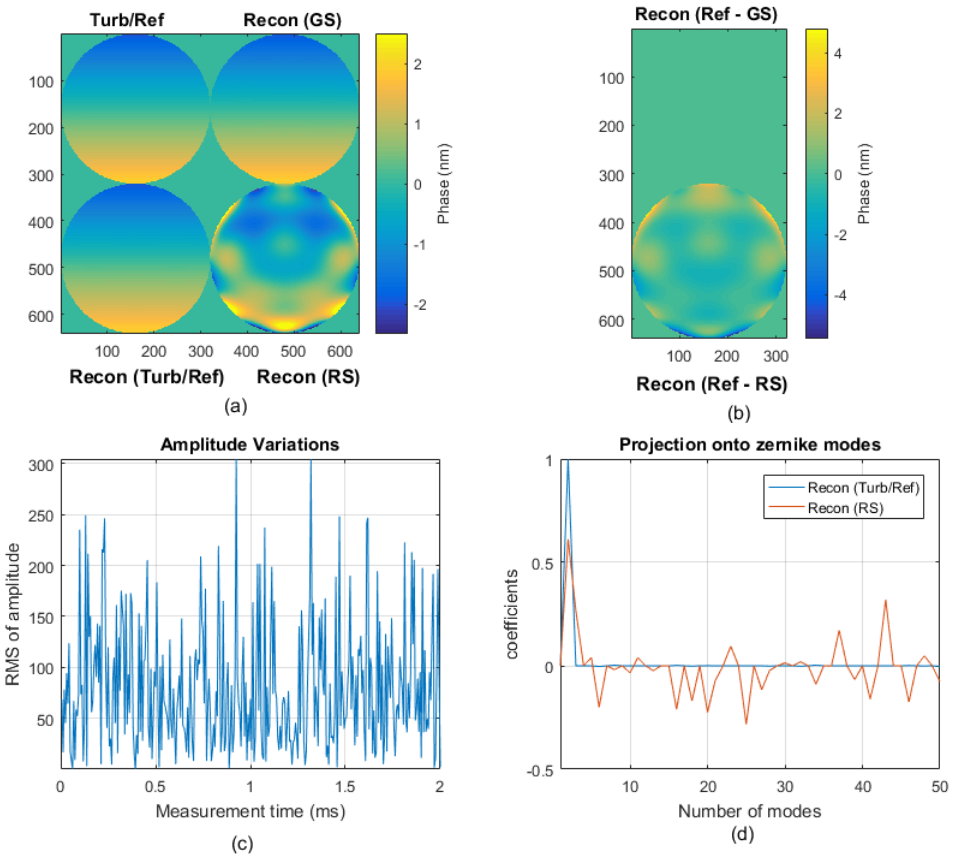

FIGURE 5.5. – Simulation results for a tilt phase. (a) is the original tilt phase, reconstructed Ref, GS and RS phases. (b) is the reconstructed phases of the difference between Ref and GS (Ref - GS) and that between Ref and RS (Ref - GS). (c) is the random amplitude variations. (d) is the coefficients of reconstructed Ref and RS phases projected onto zernike modes.

residual residual jitter seen by an LGSWFS can be large. For instance, the Gemini GeMS instrument is reporting ~100mas rms of residual jitter (NEICHEL, RIGAUT, VIDAL et al. 2014). This jitter can be converted into wavefront error by :

$$\sigma_{tilt} = 1.21 D \sigma_{jitter} \tag{5.6}$$

Where σ_{jitter} is given in mas, D is the telescope diameter and σ_{tilt} is in nanometers rms. For an 8m telescope, the mode confusing induced just by the tilt would then be around 200nm RMS of wavefront error. And for an ELT, the error scales by a factor 5 and reaches up to 1micron. Of course, the exact quantification of this extra error depends on the specific system configuration, but to a first order we can easily conclude that this error only is clearly a show stopper for using a RS for LGSWFS AO system.

In Fig. 5.6 we generalized the analysis to a WFS measuring the full turbulence. In this case, we assume a single phase screen, and the reconstruction is made over 50 Zernikes. In Fig. 5.6, inset (a) shows the turbulence and the reconstructed phase screens for, respectively, the GS, the RS and the Reference case. With 50 modes reconstructed, the initial phase is smoothed, and visually the 3 reconstructed phase screens look quite similar. Inset (c) shows the corresponding decomposition into Zernike modes, which again looks similar between the 3 cases. In insets (b) and (d), we show the residual error when comparing the reconstructed wavefront between GS, RS and subtracting the reference. The errors introduced by the RS are now more prominent. In particular, we see that the residual error does contain a lot of tip, but also higher order. The corresponding decomposition of the error into Zernike modes is shown in (d). As for the tilt only, one can see that the residual error is increased in the presence of RS, when compared to the GS. In the next section, we will investigate more quantitatively the impact of the Rolling Shutter on the AO performance.

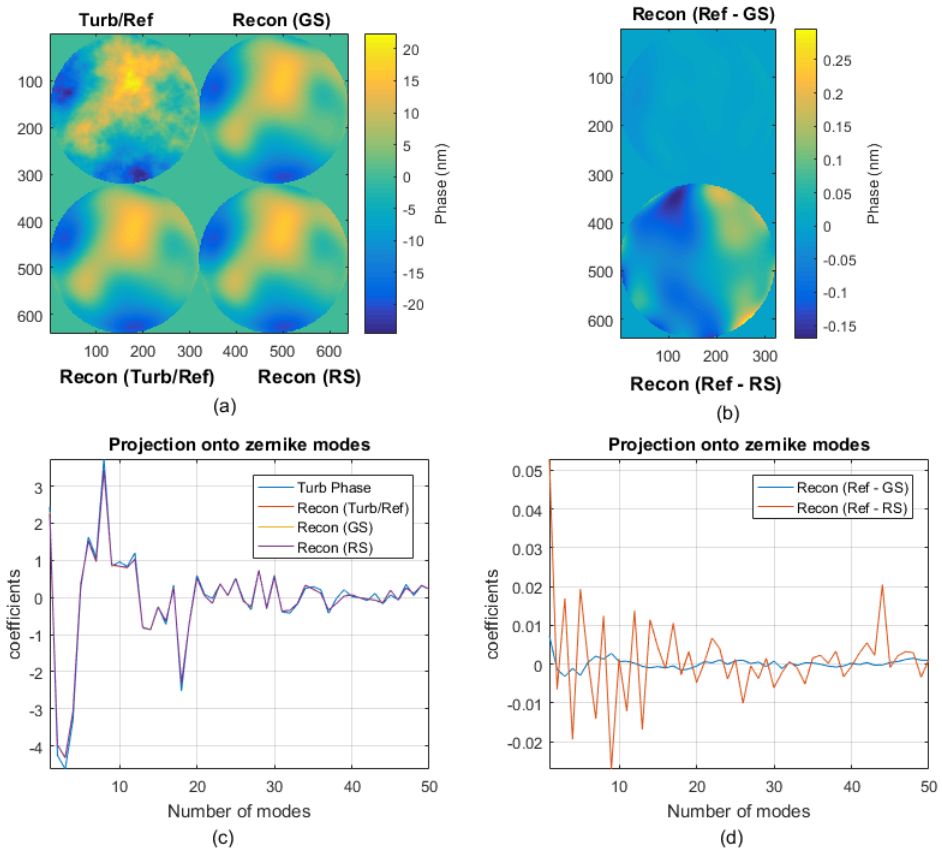

FIGURE 5.6. – Simulation with a real atmospheric phase screen. (a) is the original turbulence phase, reconstructed Ref, GS and RS phases. (b) is the reconstructed phases of the difference between Ref and GS (Ref - GS) and between Ref and RS (Ref - RS) . (c) is the the Zernike coefficients of the original turbulence and reconstructed Ref, GS and RS phase . (d) is the coefficients of reconstructed Ref - GS and Ref - RS phase projected onto zernike modes.

5.3. Application for an Open-loop AO system

The previous section qualitatively introduces the mode confusing effect caused by the rolling shutter. In this section, we try to quantify further the effect, first by assuming an Open-Loop phase reconstruction. For that, a moving phase screen is shown to the WFS, and we compare the phases reconstructed in a RS or GS scheme. We first look at the error propagation at the level of the centroids (Section 5.3.1) and then at the level of the reconstructed phase and the associated Strehl Ratio (5.3.2). Finally, section 5.3.3 investigates the sensitivity of the RS mode confusion error for different system and atmospheric parameters.

5.3.1. Center of Gravity variations

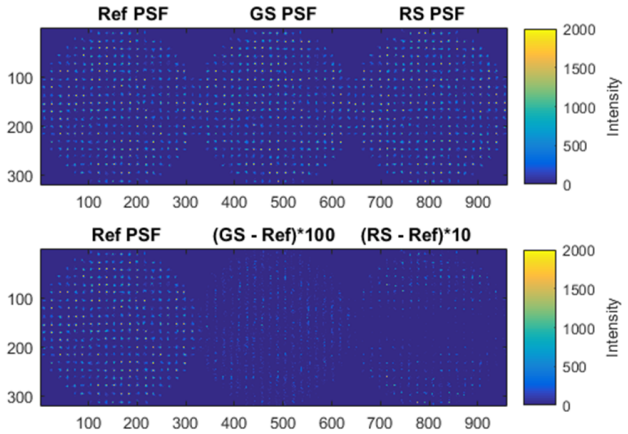

FIGURE 5.7. – (Top) : PSF for the reference case, the GS case and the RS case. (Bottom) : PSF for the reference case and PSF for the GS - Ref case (error are x100) and PSF for RS - case (error are x10). A 20 m/s wind speed and 0° wind direction is considered here.

First, and based on the same simulation parameters as the previous section, Fig. 5.7 shows the SH spots obtained for the reference, the GS and RS respectively. The second row of Fig. 5.7 shows the error in the SH spots when the reference image is subtracted. The intensity of the difference is a factor 10 higher in the RS scheme than in the GS case. In this case, the wind direction is along the Y-axis, and we clearly see a pattern in the centroiding error along this axis. The error is minimal around the center of the pupil because the reference frame is chosen to be the one corresponding to the middle of the temporally oversampled frames. Then the error grows toward the edge of the pupil, as the signal reconstructed for the RS is temporally more and more different from the reference. For the GS, the error is much more uniform across the pupil, as the spots are built as the average of the temporal evolution. So this is already an interesting effect, in the sense that the RS error is not only larger than the GS one, but it also creates patterns within the pupil, which could be problematic for some applications.

As a next step, we focus on a single subaperture, and we look into more details at the CoG error, when computed over the x and y axes. This is shown by Fig. 5.8 for the x axis, which is aligned with the wind direction, and in Fig. 5.9 which is perpendicular to the wind axis. The subaperture chosen here corresponds to the one close to a corner (a=15,b=15), but the results for other sub-apertures are very similar. Fig. 5.8 and Fig. 5.9 shows the CoG evolution with time (left) and the associated error for a RS or GS readout scheme. As previously discussed, the centroiding error is amplified by the RS scheme, and we also highlight here that the errors get bigger when aligned with the wind direction, as the temporal evolution would be larger in this direction. In this

case, and for a wind speed of 20m/s, the centroiding error induced by the RS can be as big as a few pixels.

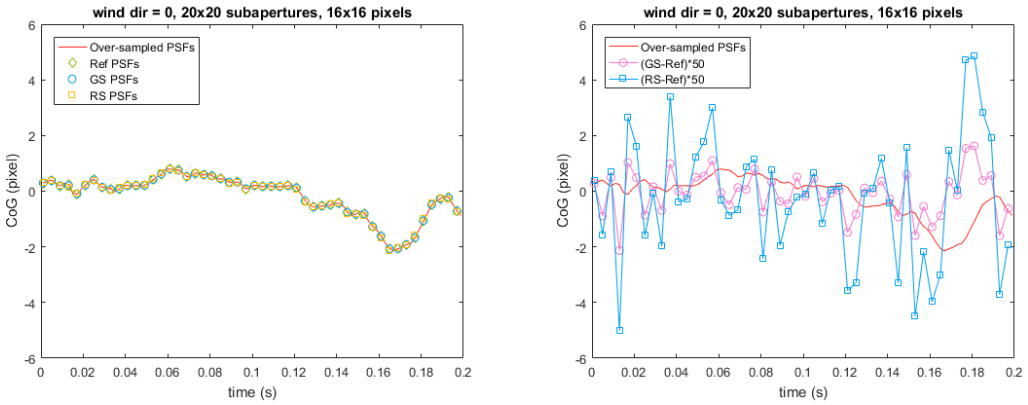

FIGURE 5.8. – (Left) CoG for the Oversampled, Ref, GS and RS cases. (Right) CoG ×50 for GS - Ref and RS - Ref PSFs. The x CoG measurement of the sub-aperture labelled (a=15,b=15) is plotted here. A 20 m/s wind speed and 0° wind direction is considered here.

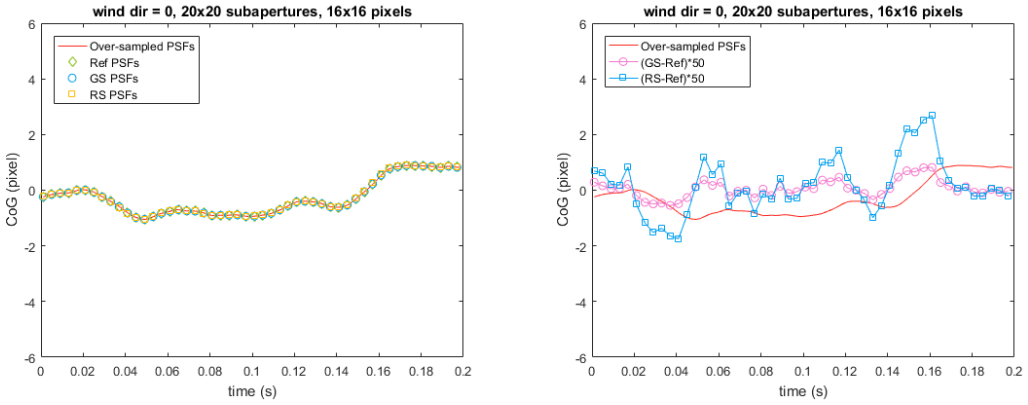

FIGURE 5.9. – (Left) CoG for the Oversampled, Ref, GS and RS cases. (Right) CoG ×50 for GS - Ref and RS - Ref PSFs. The y CoG measurement of the sub-aperture labelled (a=15,b=15) is plotted. A 20 m/s wind speed and 0° wind direction is considered here.

In the following, we will look at the impact of the wind direction and speed on the centroiding error. For that we define two criteria. The first one will be a 2D map of the CoG errors, for both x and y, when averaged over several frames. These error maps are built according to :

$$\begin{cases} err_{CoG^i_{RS\_x}(a,b)} = \sqrt{\frac{1}{N}\sum_{i=1}^{N}[CoG^i_{RS\_x}(a,b) - CoG^i_{Ref\_x}(a,b)]^2} \\ err_{CoG^i_{RS\_y}(a,b)} = \sqrt{\frac{1}{N}\sum_{i=1}^{N}[CoG^i_{RS\_y}(a,b) - CoG^i_{Ref\_y}(a,b)]^2}, \end{cases} \tag{5.7}$$

where CoG_{RS} and CoG_{Ref} are the center of gravity, (a,b) is the sub-aperture number, and N is the number of full-frames.

The second metric we look at is then simply the average error over the pupil, to get the total centroiding error. This is defined by :

$$\begin{cases} \overline{err}_{CoG_{RS\_x}} = \frac{1}{N_{sub}}\sum_{a=1}\sum_{b=1} err_{CoG_{RS\_x}(a,b)} \\ \overline{err}_{CoG_{RS\_y}} = \frac{1}{N_{sub}}\sum_{a=1}\sum_{b=1} err_{CoG_{RS\_y}(a,b)}, \end{cases} \tag{5.8}$$

where N_{sub} is the number of valid sub-apertures.

The 3 following figures, Fig. 5.10, Fig. 5.11 and Fig. 5.12 show these metrics for a wind direction of respectively 0°, 45° and 90°, and different wind speeds from 0m/s to 50m/s. For each figure, the left part shows the 2D map of the errors for the Global shutter (top row) and the Rolling shutter (bottom row), for x-centroiding (left column) and y-centroiding (right column). The plot on the right shows the error integrated over the pupil for the x and y-axis, but for different wind speeds.

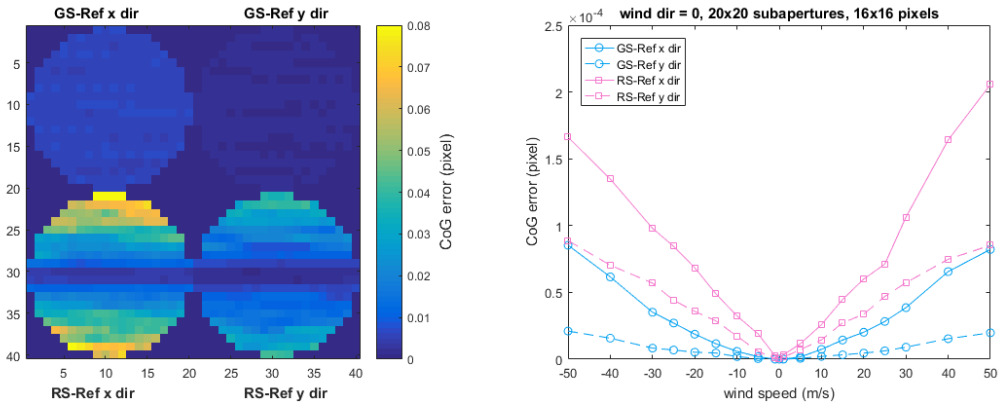

FIGURE 5.10. – (Left) CoG error of each sub-aperture for 100 sampled full-frames under 20 m/s wind speed. (Right) The average CoG error of all the sub-apertures for 100 sampled full-frames under different wind speeds. 0° wind direction is considered here.

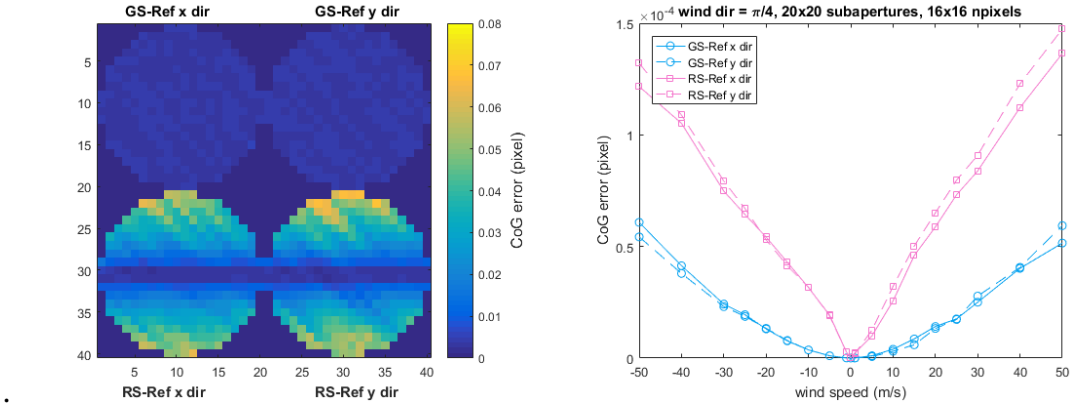

FIGURE 5.11. – (Left) CoG error of each sub-aperture for 100 sampled full-frames under 20 m/s wind speed. (Right) The average CoG error of all the sub-apertures for 100 sampled full-frames under different wind speeds. 45° wind direction is considered here.

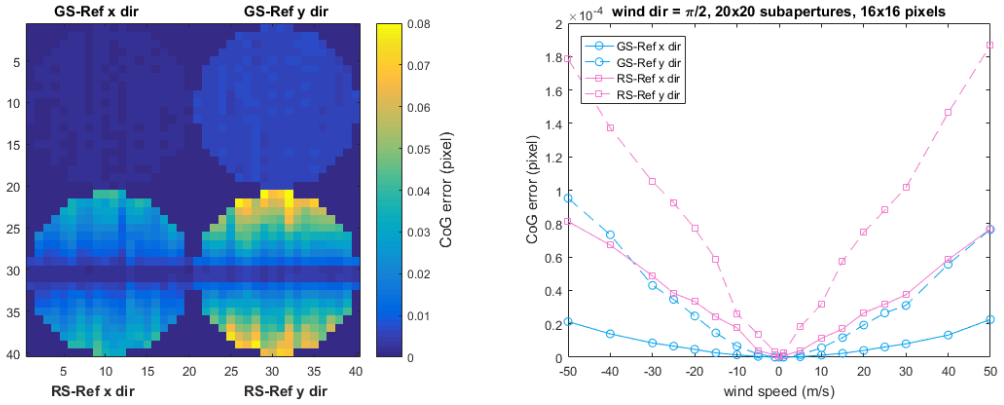

FIGURE 5.12. – (Left) CoG error of each sub-aperture for 100 sampled full-frames under 20 m/s wind speed. (Right) The average CoG error of all the sub-apertures for 100 sampled full-frames under different wind speeds. 90° wind direction is considered here.

As described above, we retrieve in Fig. 5.10, Fig. 5.11 and Fig. 5.12 the specific error shape across the pupil induced by the RS scheme. Again, the overall "v-shape" is caused by the definition chosen for the reference frame to be at the middle of the temporally oversampled frames. If one would have chosen the reference frame as the first frame for instance, then the error would have been growing across the pupil, and eventually ended up to be twice larger. In any case, it is important to understand that the RS will introduce anisotropic errors across the pupil, which is not the case for the GS scheme.
The amplitude of the error will change with the wind direction. When the wind is aligned with the x-axis, the error is larger than this direction, as shown in Fig. 5.10. For

a wind at 45°, the error will be of the same amplitude between the 2 axes, as shown in Fig. 5.11. And logically, in Fig. 5.12 the error is larger along the y-axis, as the wind is blowing along this direction.
Finally, and again as expected, the right parts of Figures 5.10, 5.11 and 5.12 show that the overall error increases with the wind speeds. As the RS error is related to a temporal evolution, the fastest the wind, the larger the error. In a typical 20 m/s wind speed, the RS errors are about 3 - 7 times larger than the GS errors.

5.3.2. Phase errors and Strehl ratio

After looking into the centroid variations, the next step is to analyze the reconstructed phases and the impact on the Strehl ratio.

An example of the reconstructed phase is shown in Fig. 5.13. The top row shows the reconstructed phase screen from the reference frame, GS and RS respectively. The bottom row shows the error for the GS and RS.

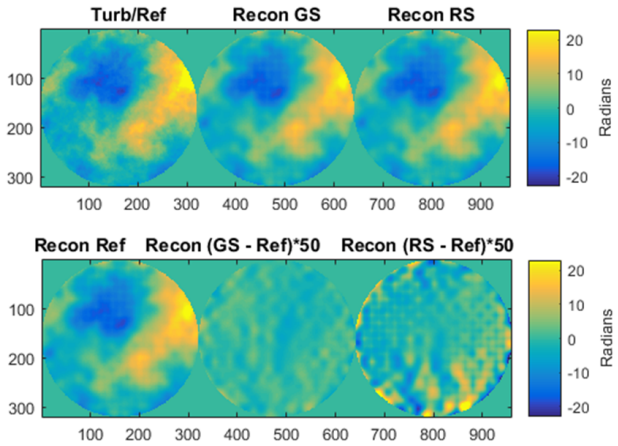

FIGURE 5.13. – (Top) : reconstructed phases for the reference case, the GS case and the RS case. (Bottom) : reconstructed phases for the reference case and phases for the GS - Ref case (error are x50) and phases for RS - Ref case (error are x50). A 20 m/s wind speed and 0° wind direction is considered here.

As previously said, Fig. 5.13 shows that the RS introduces a mode confusion, which ends up in fake high order. This is clearly seen especially at the edge of the pupil. And again, where the GS error will be uniform, the RS error will be localized in some area of the pupil toward the edge.

As for the centroids, we then compute the phase error over several frames as :

$$\begin{cases} \overline{err}_{\varphi_{GS-Ref}} = \dfrac{1}{N}\sum_{i=1}^{N} err_{\varphi^i_{GS-Ref}} \\ \overline{err}_{\varphi_{RS-Ref}} = \dfrac{1}{N}\sum_{i=1}^{N} err_{\varphi^i_{RS-Ref}}, \end{cases} \tag{5.9}$$

where N is the number of full-frames or iterations. The phase error is given in nanometers. And finally, one can compute the equivalent Strehl Ratio loss due to this specific error, by using :

$$\begin{cases} SR_{GS-Ref} = exp(-\overline{err}^2_{\varphi_{GS-Ref}}) \\ SR_{RS-Ref} = exp(-\overline{err}^2_{\varphi_{RS-Ref}}). \end{cases} \tag{5.10}$$

Results are given in Fig. 5.13 and Fig. 5.15. For the chosen configuration here, we see that the effect of the RS is about a few tens of nanometers for typical wind speeds, which corresponds to a few points of SR. Of course, these results will change with the system configuration, and especially impacted by the number of subapertures and the number of pixels per subaperture (see next section). A few tens of nanometers may not be critical for the overall budget of some AO systems, but yet it could be significantly reduced if using a GS technology instead of the RS one. We also emphasize that the RS error is not uniform across the pupil, which can be problematic for some specific applications, like High-Contrast. Finally, in a case of multiple-WFS will remain the issue of the proper synchronisation between all the cameras, in order to perform tomography. This last point has not been studied in this thesis, but remains an important question mark for the potential use of the RS-technology for tomographic AO systems.

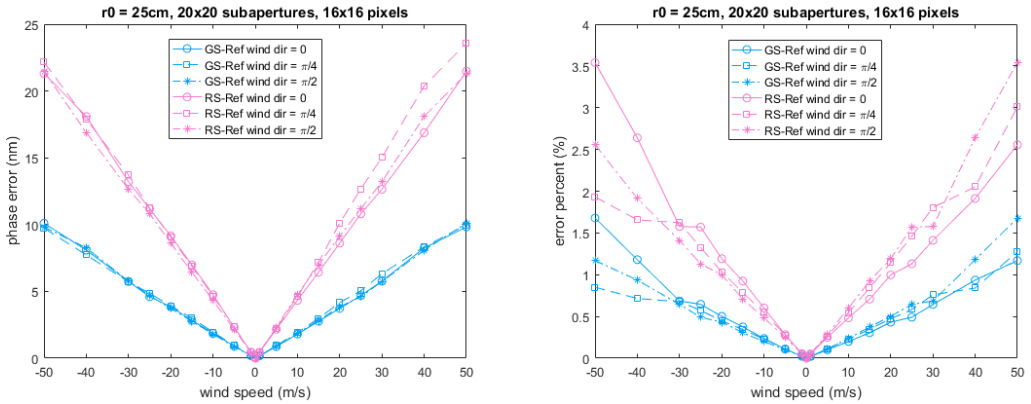

FIGURE 5.14. – (Left) : The phase errors of GS-Ref and RS-Ref cases under different wind speeds and directions. (Bottom) : The error percent of GS - Ref and RS - Ref phases under different wind speeds and directions.

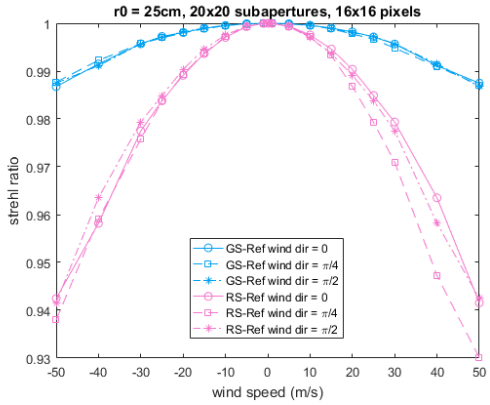

FIGURE 5.15. – The strehl ratio of GS-Ref and RS-Ref phases under different wind speeds and directions.

5.3.3. Rolling Shutter error evolution vs. system parameters

In this section, we study the evolution of the RS error for different system configurations. Basically, we looked at the impact of the pupil sampling (called pupil grids in the plot) and the number of pixels per subaperture (called wfs-pixels). The first parameter corresponds to the number of points used in the simulation to sample the phase per subaperture, while the second corresponds to the number of pixels on the detector per sub-aperture. The phase sampling is really related to simulation, and the idea here is to understand what should be the minimum number one should use not to add extra numerical errors. This is important in the frame of ELT simulations, as all the arrays become very large. Hence, keeping the size of the phase screen to a reasonable number is important.
The other parameters of the simulation are kept fixed and similar as the previous simulation : the telescope diameter D is 10m, sub-aperture number $n_s \times n_s = 20 \times 20$, therefore the dimension of each subaperture is 0.5m.

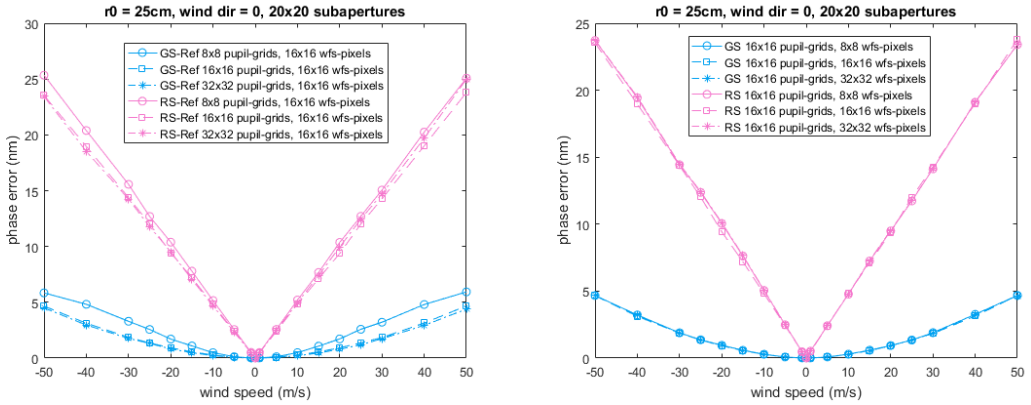

FIGURE 5.16. – (Left) The phase error by changing the number of grids for sampling the pupil and fixing the number of pixels for sampling the focused spot on detector. (Right) The phase error by changing the number of pixels for sampling the focused spot on detector and fixing the number of grids for sampling the pupil.

The left plot in Fig. 5.16 shows the phase error with wind speed by changing the number of grids for sampling the pupil from 8×8 to 32×32 and fixing the WFS pixels as 16×16. What this plot shows is that when using 8×8 pixels to sample the pupil per subaperture, then an extra numerical error appears. This error is not real (purely numerical), and will not exist in a real system where the pupil is sampled over an infinite number of points. And this error as soon as more pixels are used to sample the pupil. This tells us that a minimum of 16×16 pixels per-subaperture to sample the pupil is required, but it is not necessary to use grids like 32×32 that would make the computation time much longer.
In the right plot in Fig. 5.16 we then look at the impact of the number of pixels per-subaperture. In here, we always assume the same overall sampling time to be 500Hz. So even if more pixels are used per subaperture, it means that in a RS scheme they will be read faster, and at the end the total error remains the same. To increase the RS error, one would need to reduce the frame rate (which is equivalent to increasing the wind speed, as shown in these plots).

In conclusion, in this section, we have shown that, in a pure Open-Loop configuration, the RS scheme introduces errors non-uniform across the pupil, and almost an order of magnitude larger than the GS scheme. The next step for this work would be to extend the simulations to ELT scale, and tomographic systems. This has not been done in this thesis, but would be important to get a definitive conclusion about the risk associated with such a read-out scheme for ELT-AO systems. In the next section we will remain in a 10meter class configuration, but we will now look at a full close loop configuration.

5.4. Application to Close Loop AO systems

5.4.1. Simulation process

This section introduces the simulation developed to reproduce a close loop AO system, in the presence of a WFS equipped with a RS detector. The overall process is described by Fig. 5.13.

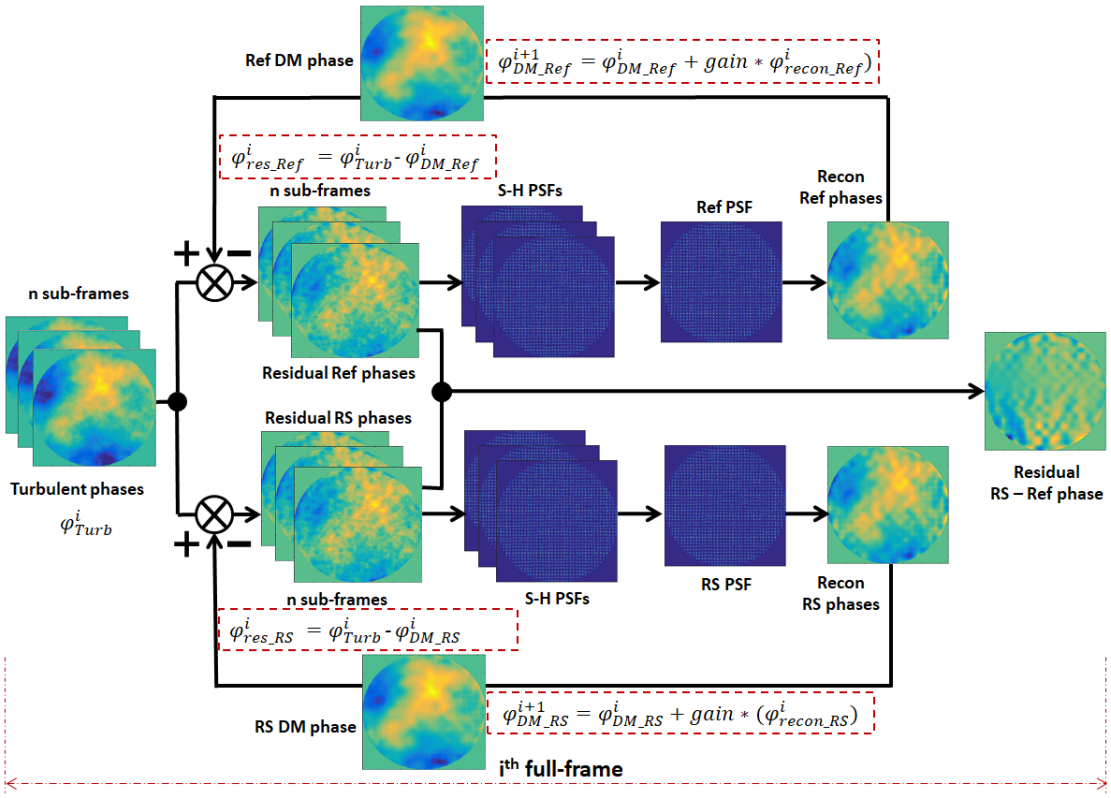

FIGURE 5.17. – The close loop process of rolling shutter in an iteration, the same as the global shutter.

As previously, the turbulent phase has to be temporally oversampled first, so that the RS equivalent frames can be built. From these oversampled SH-spot frames, we build the global RS frame, from which we do the phase reconstruction. This phase is then sent to the DM and replicated as many times as required to have a similar temporal sampling as the turbulence. The correction is then done on each oversampled turbulent frame and reinjected into the SH-WFS. The close loop equation can be written as :

$$\begin{cases} \varphi^{i+1}_{DM\_GS} = \varphi^{i}_{DM\_GS} + gain \times \varphi^{i}_{recon\_GS} \\ \varphi^{i+1}_{DM\_RS} = \varphi^{i}_{DM\_RS} + gain \times \varphi^{i}_{recon\_RS} \end{cases} \tag{5.11}$$

The residual phases are obtained according to :

$$\begin{cases} \varphi^{i}_{res\_RS,k} = \varphi^{i}_{Turb,k} - \varphi^{i+2}_{DM\_GS,k} \\ \varphi^{i}_{res\_RS,k} = \varphi^{i}_{Turb,k} - \varphi^{i+2}_{DM\_RS,k}, \end{cases} \tag{5.12}$$

where i is the label of full-frame or iteration, and $k(1 \leq k \leq n)$ is the label of sub-frames in each iteration.

We compute the phase error as :

$$\begin{cases} err_{\varphi^{i}_{GS-Ref}} = \sqrt{\frac{1}{N_{sub}} \sum_{a=1} \sum_{b=1} [\varphi^{i}_{res\_GS}(a,b) - \varphi^{i}_{res\_Ref}(a,b)]^2}, \\ err_{\varphi^{i}_{RS-Ref}} = \sqrt{\frac{1}{N_{sub}} \sum_{a=1} \sum_{b=1} [\varphi^{i}_{res\_RS}(a,b) - \varphi^{i}_{res\_Ref}(a,b)]^2}, \end{cases} \tag{5.13}$$

where a and b are the labels of the sub-apertures, and N_{sub} is the number of valid sub-apertures. And finally, we can compute the Strehl ratio by :

$$\begin{cases} SR^{i}_{GS-Ref} = exp(-err^2_{\varphi^{i}_{GS-Ref}}) \\ SR^{i}_{RS-Ref} = exp(-err^2_{\varphi^{i}_{RS-Ref}}) \end{cases} \tag{5.14}$$

In the following, we consider the same parameters as for the open loop analysis and choose a typical case under 0° wind direction, 0.5 system gain, and 20m/s wind speed. The phase error is computed over 100 iterations.
Results are shown in Fig. 5.18 and Fig. 5.19. For Fig. 5.18 the left plot shows the total residual phase error for the reference, the GS, and the RS case. When the loop closes, the residual error decreases to a stable state for all the 3 cases. The performance is relatively similar between the 3 cases, and here certainly dominated by the fitting error. In the right part of Fig. 5.18 we show the error when subtracting the quadratically the reference case. This should provide the error due to the shutter mode. As seen for the OL case, the RS adds extra errors or the order of tens of nanometers. This decreases the SR by a few points, as shown in Fig. 5.19.

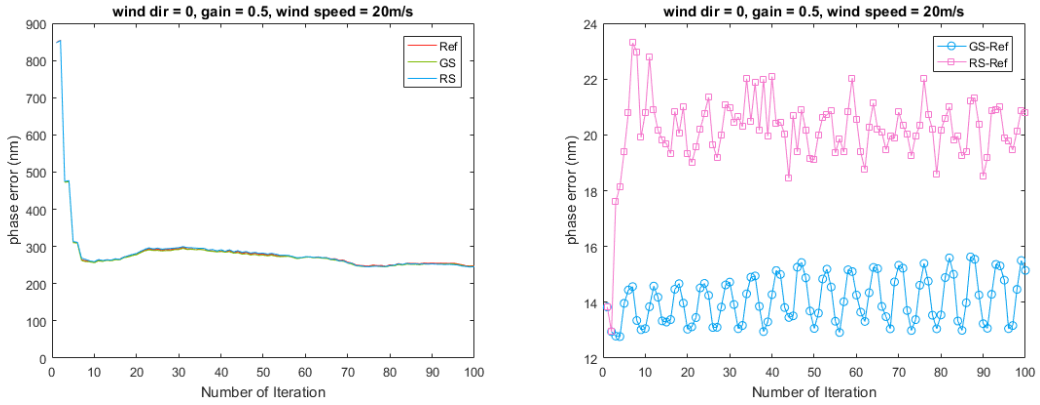

FIGURE 5.18. – (Left) : The phase errors of the Ref, GS and RS case. (Bottom) : The phase errors of GS - Ref and RS - Ref phases. A single wind direction, gain and wind speed is considered here

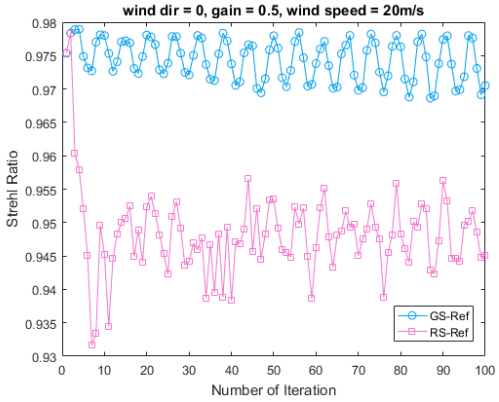

FIGURE 5.19. – The strehl ratio of GS-Ref and RS-Ref phases, a single wind speed 20m/s system gain 0.5 and 0° wind direction is considered here.

5.4.2. Residual phase errors vs. wind speed

Based on the previous analysis under a single wind speed, system gain and wind direction, this section considers the phase error with multiple wind speeds from 1m/s to 50m/s. The system gain is fixed to 0.5.
Results are shown in Fig. 5.20. As expected, the higher the wind speed, the higher the final error. This is true both for the total error, as the overall temporal error increases in the error budget, but also for the relative error between GS and RS. In other words, the RS error increases more than the GS when the wind speed increases. The RS is more sensitive to the temporal aspects than the GS. This is illustrated by the bottom-right plot of Fig. 5.20.

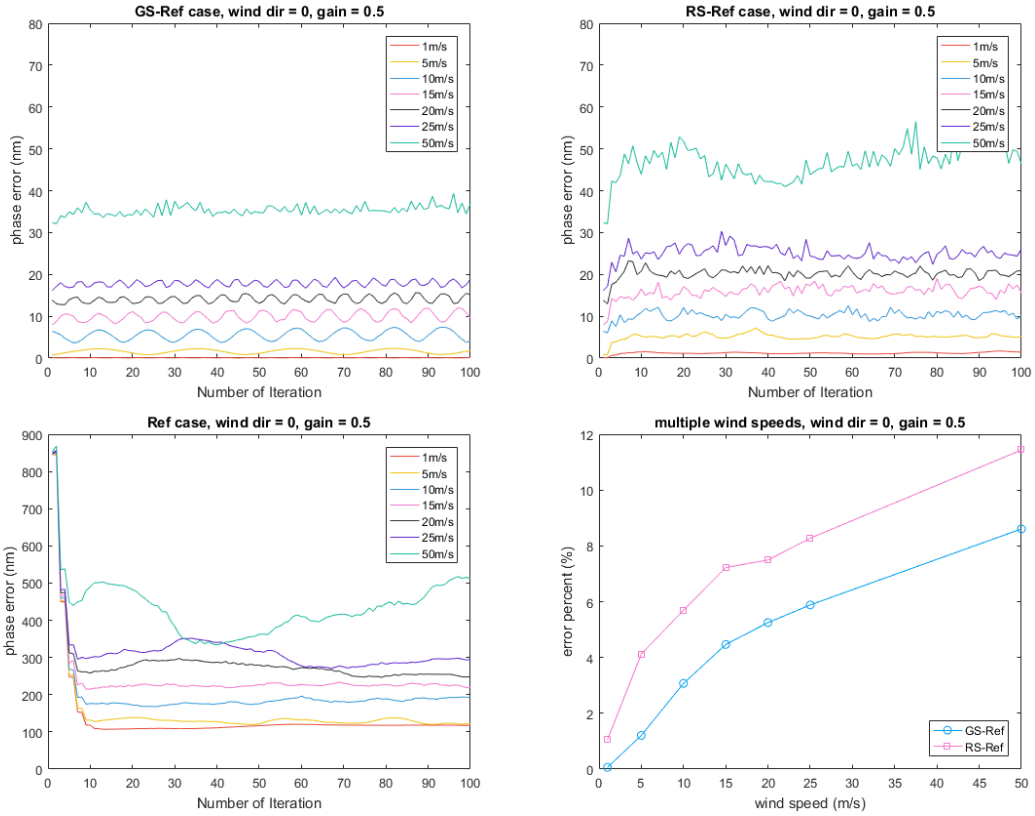

FIGURE 5.20. – (Up left) : The residual phase errors with wind speeds for GS-Ref case. (Up right) : The residual phase errors with wind speeds for RS-Ref case. (Bottom left) : The residual phase errors with wind speeds for Ref case. (Bottom right) : the error percent with wind speeds for GS-Ref and RS-Ref cases, wind direction is 0°, and the system gain is 0.5.

5.4.3. Residual phase errors vs. system gain

In a close loop system, the temporal aspects are driven by the close-loop gain. So far we have kept this gain fixed at 0.5. In this section, we explore the impact of the gain on the overall performance and on the relative performance between GS and RS. Results are shown in Fig. 5.21. First, if we look at the bottom-left plot of Fig. 5.21 we see that the overall performance can be improved by pushing the gain. This reduces the overall temporal error, which is significant in this case of a wind speed of 20m/s. Above the gain of 0.7 the loop becomes unstable, as expected from the control theory. From the (up-left) and (up -right) plots of Fig. 5.21, we can see that the gain does not make a dramatic change in the GS case but increases the RS error. As a result, in the (bottom-right) plot, the higher gains bring larger differences between GS-Ref and RS-Ref cases. The RS cases are more sensitive to how the temporal aspect of the loop will be optimized and will certainly require more care for designing the control laws.

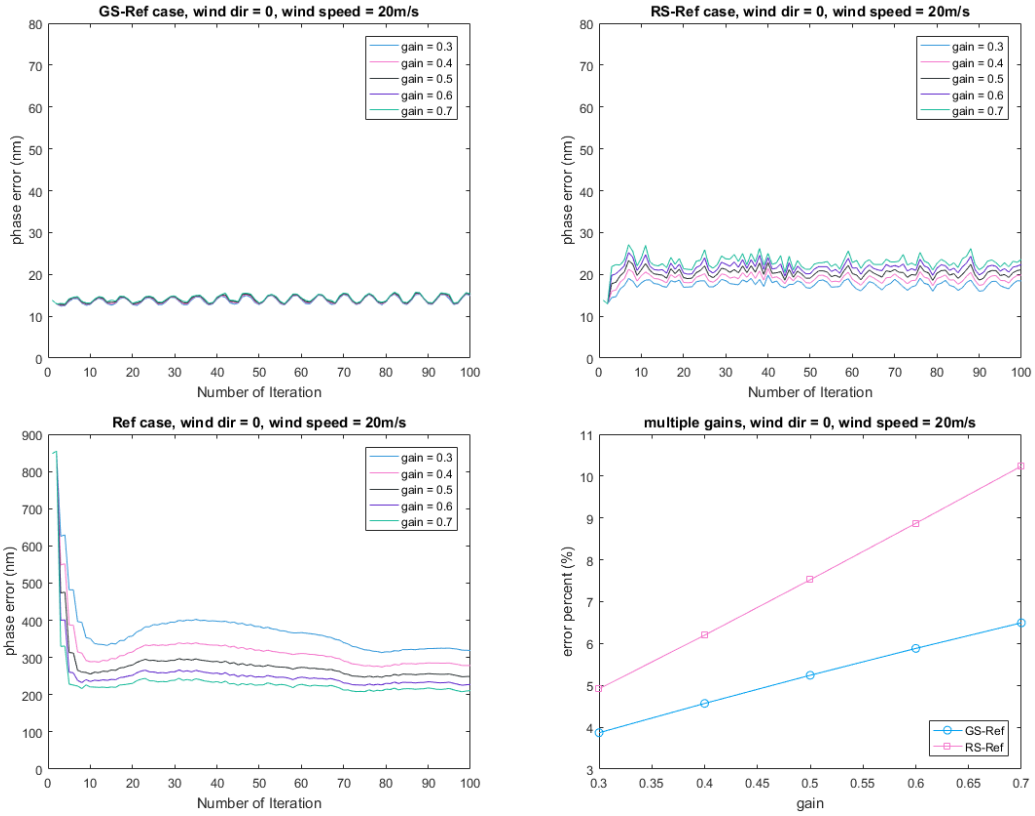

FIGURE 5.21. – (Up left) : The residual phase errors with gains for GS-Ref case. (Up right) : The residual phase errors with gains for RS-Ref case. (Bottom left) : The residual phase errors with gains for Ref case. (Bottom right) : the error percent with gains for GS-Ref and RS-Ref cases, wind direction is 0°, and the wind speed is 20m/s.

One aspect which has not been considered in this thesis is the use of an advanced control law, and this could be compatible, or not, with a RS scheme. Indeed, we show here that the RS scheme is already more sensitive to the gain tuning in a simple case of a classical integrator. How the RS scheme could be coupled with a Kalman controller, a vibration rejection controller or a predictive controller remains to be studied.

5.4.4. Residual phase errors vs. wind direction

In the open loop analysis, we have seen that although the CoG error changes with different wind direction, the phase error basically remains the same. In here we confirm this behavior in the close loop scheme. For that, we look at the impact of different wind directions on the final performance, for a fixed gain of g=0.5. This is shown in Fig. 5.21. We can see that the different wind directions would make some variations on the reference phase errors, but for the GS-Ref case, the error always remains the same. However, it brings some fluctuations for the RS-Ref case in (up -right) plot. This highlights again that overall, the RS scheme will be more sensitive to variations in the

inputs, such as wind speed or direction. A RS would require more care for reaching an optimized performance.

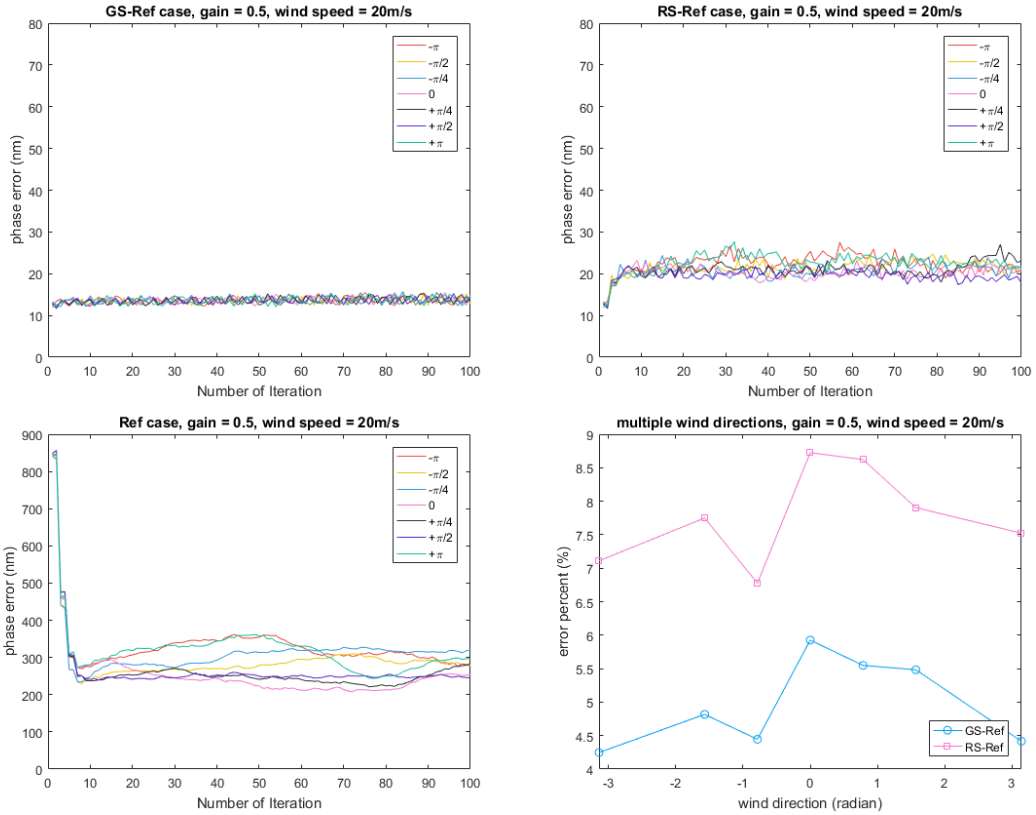

FIGURE 5.22. – (Up left) : The residual phase errors with wind directions for GS-Ref case. (Up right) : The residual phase errors with wind directions for RS-Ref case. (Bottom left) : The residual phase errors with wind directions for Ref case. (Bottom right) : the error percent with wind directions for GS-Ref and RS-Ref cases, system gain is 0.5, and the wind speed is 20m/s.

5.5. Conclusion

In conclusion, for this section about the impact of a Rolling Shutter scheme, we have shown that :

— The Rolling shutter implies mode confusion in the phase reconstruction process, turning low-order into higher order.

— This modal confusion can introduce errors on the order of 20% to 40% of the input signal.

— For an LGS AO system, the residual jitter seen by each LGSWFS is usually large (around 100mas) as this mode is filtered from the main control loop. As a matter of fact, the mode confusion induced by the jitter on the LGSWFS leads to residual

errors of several hundreds of nanometers on higher order modes, which, if nothing is done, is clearly a show stopper for using RS detectors.
— Overall, the RS scheme is much more sensitive to the optimization of the loop gain and to the wind characteristics than a standard GS scheme. The extension of RS to the advanced control law remains to be studied.
— The integration of a RS scheme into a full tomographic system, where the synchronisation of several cameras is crucial for the 3D phase reconstruction remains a risk.
— For a typical AO system, the performance gain provided by the faster read-out of a RS is lost and superseded by the mode confusion effect.
— Today, as Global Shutter detectors are providing better performance as rolling shutters, the use and need of RS detectors for AO is questionable.

6. Conclusion

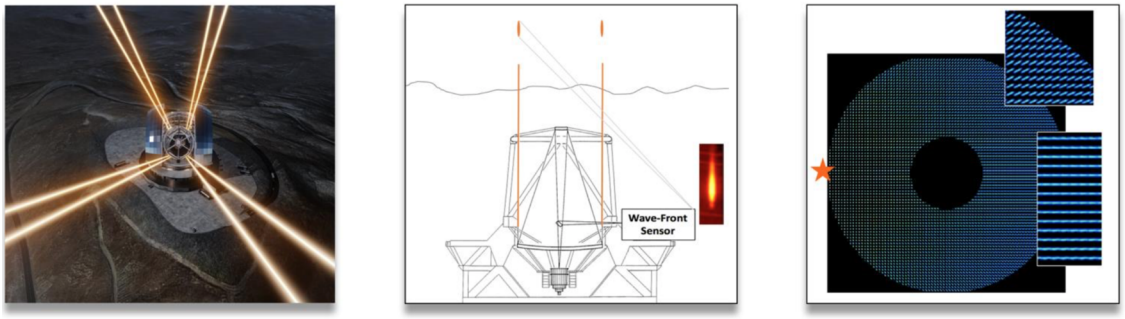

FIGURE 6.1. – Summary of the PhD : from the ELT, to the spot elongation and down to the Shack-Hartmann WFS.

Summary

The frame of this PhD work was about the development of instrumentation for large ground-based, optical and near-infrared telescopes. Ground based astronomy has made tremendous progress in the past tens of years, and the state of the art of large optical telescopes reaches ~10meter diameters. Larger telescopes mean increasing the light collecting power and a better sensitivity to fainter targets. Larger telescopes also potentially open the path for higher angular resolution, and eventually the ability to detect finer details on the astronomical objects under study. Toward these objectives, one of the key technological breakthroughs done in the past decades was the introduction of Adaptive Optics (AO) for astronomical observations. At the cross of optics, electronics, atmospheric science, control theory, computer science, and mathematics, AO is a technique that aims at compensating quickly varying optical aberrations to restore the ultimate angular resolution limit of an optical system. It uses a combination of wave-front sensors to analyze the light wave aberrations, and deformable mirrors to compensate them. For astronomical telescopes, AO allows to overcome the natural "seeing" frontier : the blurring of images imposed by atmospheric turbulence and limiting the angular resolution of ground-based telescopes to that achievable by a 10 to 50cm telescope, an order of magnitude below the diffraction limit of large 8-m class telescopes which are the current standard.

Adaptive Optics opens a new, wide and unique range of astronomical studies that were not possible before. Most of the current AO systems, however, require a bright and/or close reference source, and as such are well-suited for observations of relatively bright compact objects. For instance, in the past 20-years, AO observations have

brought major discoveries in the study of the massive black hole at the center of our galaxy or the first images of exo-planets, but only a handful number of major extra-galactic studies in cosmological fields, as they are usually lacking of bright enough reference stars.

A new generation of AO systems, a.k.a. Wide Field AO (WFAO), is addressing this limitation by significantly increasing the field of view of the AO-corrected images, and/or the fraction of the sky that can benefit from such correction. For that, WFAO uses artificial guide stars, using lasers tuned at 589nm on the atomic sodium D2 line, which excite sodium atoms located in the mesosphere around 100km altitude. These "Laser Guide Stars" [LGS] could be created at arbitrary locations in the sky, thus solving partially the problem of scarcity of suitable guide stars. Nowadays, all major ground-based telescopes are equipped with such lasers. The second pillar of WFAO system is the atmospheric tomography. Indeed, because the atmospheric turbulence is not concentrated within a single layer but spread in a volume -typically the first 10km above sea level- the light coming from different directions will not see the same perturbations. As a matter of fact, this reduces the corrected Field Of View. To overcome this limitation, WFAO uses several LGSs, paving the science field, to perform a full tomographic reconstruction of the 3D perturbations. From this information it is then possible to optimize the performance for the science application.

Today (2021), WFAO starts to be in routine operation in some observatories around the world (LBT, VLT, Keck, Gemini). Very recently, such capability has been brought to its apogee by coupling the ESO-operated Adaptive-Optics Facility (AOF) with the cutting-edge instrumentation of the MUSE integral-field (3D) spectrograph. And the WFAO landscape is growing rapidly. For instance, the Keck Telescope has been funded for the start-up of a multi-LGS wide-field AO (LTAO) system. The Gemini telescope has also just announced funding for the development of a new MCAO system for its telescope in Hawaii, and the Subaru is embarking on the adventure of a secondary adaptive mirror. On the European side, ESO is funding a high performance MCAO system, to offer the diffraction limit of the VLT in the visible wavelength range, over a field of several tens of arcseconds, and for an almost complete sky coverage. This last instrument, called MAVIS, should allow to offer an alternative to the HST for the access to high angular resolution images in the visible, and to cover a parameter space complementary to the ELTs or JWST, which work in the near infra-red. Thus, the global landscape clearly shows a trend towards the generalization of WFAO to telescopes of the 8-10m class.

Within a decade, the world will see a new generation of telescopes with diameters up to 40m, called the Extremely Large Telescopes [ELTs]. The light collection power and unique angular resolution of the ELTs equipped with AO will revolutionize astronomical observations. To provide a single example, the ELTs will allow to reproduce the observation of the galaxies' structure and internal motions of the first galaxies formed in the Universe, where we are limited today to the most massive or closer

galaxies. The scientific potential of the ELTs relies on challenging new AO concepts, integrated inside the telescope itself, and providing high-resolution images to all the instrumentation downstream.

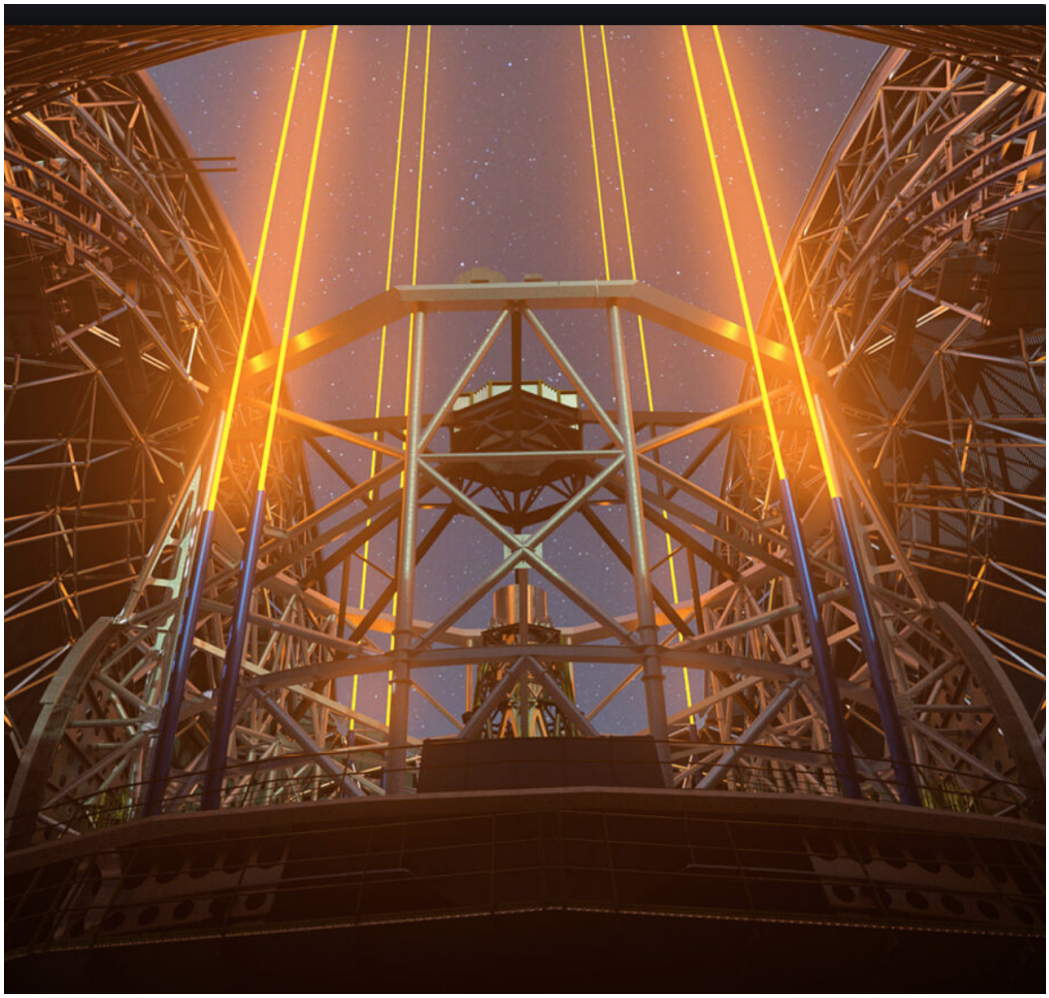

FIGURE 6.2. – Artist view of the future ELT with the Laser Guide Stars

Considering the success and reliability of the 10m-class telescope AO, one could think that the task will be easy on the ELT, and that a simple scaling will be enough. Unfortunately, this is not the case, as the ELT brings its own set of conceptual, technological, and programmatic challenges. One example of the paradigm shift concerns the interface between the telescope and its instruments. While until now the boundary between control and responsibility for the wavefront was clearly defined between the telescope and its AO (the telescope was in charge of Active Optics, the AO instruments), the ELT sees a shared control between the telescope and the instruments. The Deformable Mirror is integrated in the telescope, and it is used by both the telescope and the instruments. Another example, which has motivated the development of this PhD, concerns the wave-front sensing associated with Laser Guide Stars, and in particular

the so-called spot elongation problem.

The spot elongation comes from the fact that the laser stars are not point objects, but extended sources. Indeed, the layer of sodium atoms, located at 90km above the telescope, has a thickness between 10km and 20km. The laser stars resulting from the excitation of these sodium atoms by the laser light propagated from the telescope have thus a "cigar" shape in the sodium layer. By perspective effect, they appear as extended objects (ellipses) on the opposite edge of the telescope pupil. For a 39m telescope, the laser spots have a size between 1arcsecond for those close to the Laser Launch Telescope (LLT) and a maximum expected elongation which can reach up to 25arcseconds. The difficulty is therefore to perform a wave front analysis on highly extended objects, and whose elongation varies in the pupil. At the beginning of my PhD, several solutions were envisioned to solve this challenge, but none were actually demonstrated and validated. The goal of my PhD was then to study different options to cope with LGS elongation for the ELT-scale AO instruments, propose solutions, and eventually validate through an experimental bench the robustness of the proposed solution.

In chapter 2 of this thesis, I described the principle of the Laser Guide Stars, showed the main limitations related to this technology, and explained the spot elongation issue. By analyzing sodium data acquired in Canada, I could quantify the potential impact of the spot truncation on the AO performance. This analysis was done both spatially, by determining the wave-front biases induced by truncation, and temporally, by quantifying the speed at which these biases were evolving. I then proposed an exhaustive description of potential solutions, showing the pros and cons for each of them.

In Chapter 3, I further developed one of the solutions envisioned to cope with the LGS spot elongation limitation : the deployment of a new large format CMOS detector. This new detector was made available at the beginning of my PhD, and I had to understand if it would be suitable for the purpose of LGS Wave-Front Sensing for an ELT. Based on the requirements defined in Chapter2, I analyzed the performance of this new CMOS detector. For that, I developed both a full simulation tool and an experimental bench used to characterize the detector. The main properties that I looked at where the read-out noise, and how it would affect the wavefront sensing. Indeed, even though the CMOS test detector showed very good RON performance, with a measured median below 3e-, it also showed a tail toward larger noises. By means of simulations and experimental measurements, we demonstrated that this tail had barely no impact on the accuracy of spot centroiding, hence on WFSensing. Another important parameter of this CMOS detector came from the "angle of acceptance", and how this would affect the WFSening. This angle of acceptance comes from small lenses implemented in front of each of the detector pixels. These lenses are used to increase the detector throughput, but they impose some limitations on the maximum angle of the beams that can be coupled to the detector. We have shown that if one can

propose a telecentric optical design, then this effect can be reduced to a transmission issue only, which can be kept to a minimal impact, even for a LGSWFS requiring a large Field Of View. All these results have been presented in a publication for a special issue of JATIS, in a paper titled "CMOS sensor performance for laser guide star wavefront sensing". This paper has been prepared jointly with teams working for the ELT (for HARMONI and MAORY) and for the TMT (NFIRAOS). It basically demonstrated that this new detector is perfectly suited for building a performing and reliable LGSWFS for these future giant telescopes. This is an important result, as it validates the design of these key components for the ELT and for the TMT.

Further to the results presented in the paper, I then carried an analysis to understand the impact of the acceptance angle on the spot shape, and potentially on the aliasing. Indeed, we show that the acceptance angle is equivalent to an apodization of the pupil around each lenslet. In this case, the spot diffraction will be modify, but this only has a small impact as the final spot image is dominated by the LGS size. However, this apodization induces an equivalent extra-aliasing, which can be simulated from a Fourier analysis. The impact of this extra-aliasing remains small and does not change the conclusion about the suitability of the CMOS detector for building efficient LGSWFS for ELTs.

In chapter 4, I show how this specific detector could have been integrated into a full-scale ELT LGSWFS. We took the HARMONI instrument as a baseline for the requirements for building a prototype LGSWFS. We first recalled the HARMONI error budget and the potential trade-off required to define the associated LGSWFS. This work was done based on full End-to-End simulations of the full HARMONI case. From these requirements, I have participated in the design and development of a full-scale LGSWFS prototype. This included the definition and characterization of the lenslet array, an optical relay required to re-image the pupil onto the detector, and the characterization of a commercial camera implementing the CMOS detector studied in Chapter 3. This Laser Detector Module (LDM) has then been integrated into an AO bench, using a Spatial Light Modulator to mimic the atmospheric turbulence and the ELT M4 deformable mirror. This work finishes with the first measurement of an interaction matrix for the full-scale LGSWFS prototype.

In Chapter 5, I focused the work on a specific aspect of some of the CMOS detectors, namely the "Rolling Shutter" reading of the pixel array. For adaptive optics, a rolling shutter means that pixels across the pupil are read at different timings. In effect, it may mean that the turbulence would have evolved between the beginning of the pupil sampling and the end. By means of simulations, I looked at the potential impact on the performance of such an effect, and how it would compare to the standard "Global Shutter" approach. I used the integrated OOMAO simulation tool that I modified to take this specific effect into account. I obtained results for classical AO systems, working both in open-loop and close-loop, and I showed that the impact of the RS on performance is on the order of tens of nanometers. This for turbulence only, and the

RS still presents unknowns when integrated into a full AO loop.

Chapter 6 presents the work that goes beyond the first frame of this PhD, but for which I also devoted part of my time : the PAPYRUS project. PAPYRUS is a student-led project at LAM, with the goal of developing a pyramid-based AO system to be installed at the 1.52m telescope of Observatoire Haute Provence. The project started in 2019, after my first PhD year. The idea appeared after a visit to the OHP site, and from the finding that most of the critical components (pyramid-glass, OCAM2, 17x17 ALPAO DM) were available at LAM. PAPYRUS has then been organized as a project, with a design, AIT and on-sky validation phases. The project gathers almost 20 students, each bringing his own expertise. I have been involved in the simulation, error budget, DM and WFS characterization. The project passed a "Design Review" in March 2021, and integration started soon after. At the time of writing these lines, the project is close to be completed at LAM, and should hopefully see the first light in the next months or so. From my perspective, it was a very rich and instructive experience to have the possibility to participate in the whole chain of development of an AO system.

Perspectives
The work developed in this PhD opens several perspectives in the field of wavefront sensing for Extremely Large Telescopes. First, from the technology development point of view, we can mention three axes : (i) the finalization of the evaluation of the impact of the Rolling Shutter for tomographic AO systems, (ii) the continuation of the full-scale tests with the LGSWFS prototype, and (iii) the development of a full ELT simulator based on the Laser bench developed for the LGSWFS tests.

Regarding the Rolling-Shutter aspect, the first study presented in this PhD has shown a potential negative impact on the performance, but we restricted ourselves to a simple classical AO case. The generalization of the simulation toward multiple-LGS, tomographic AO systems would allow to conclude definitely on the potential usage of RS for AO. In particular, two aspects seem relevant to be pushed : (i) the impact of mis-synchronisation between several LGSWFS and (ii) the mode confusion induced by low-order modes usually filtered from the LGS measurements such as the Tip-Tilt and the Focus. Because these modes may present a large amplitude (not controlled, they almost remain open-loop in the LGS direction), the RS mode confusion may be a show stopper for the AO performance. As of interest too would be to understand how to implement the advanced controller in the presence of a RS detector. Note that this problematic is not directly relevant for HARMONI or NFIRAOS, as their detector baseline will implement a Global Shutter scheme. However, it will be relevant for MAORY, for which the baseline is to use the ESO-developed LISA camera, implementing a RS.

Regarding the continuation of the LGSWFS prototype, at the end of this PhD we reached a state where the system was ready to start AO tests. In particular, we have seen that the Spatial Light Modulator (SLM) used in the pupil plane offers a wide flexibility in terms of potential AO tests. By coupling the SLM with the LGSWFS pro-

totype, and even though only 1 channel over six is implemented, one could already look into specific aspects such as the noise propagation of the sensor, its sensitivity to differential flux level, the optimization of the detector gains across the pupil and the measurement linearity. After that, the SLM could be used to mimic the same geometry as the ELT M4, in terms of Influence Functions and actuator spatial distribution. This would allow to perform many AO tests, such as the demonstration of mis-registration and pupil registration monitoring algorithm, the building of the real interaction matrix, the impact of missing segments, or the impact of wide telescope spiders on the wavefront reconstruction. All these tests will allow the team to gain confidence in the design, develop and validate the appropriate algorithms, and eventually detect and solve potential issues. This work will be carried out in the next months / years and will use my experimental work as a foundation.

Still regarding the LGSWFS prototype, one upgrade that could be implemented is to introduce an elongated source at the entrance of the bench. In its current version, only a 2D source is used, which does not allow yet to experimentally reproduce the LGS spot elongation. One option that has been studied at the Durham University, in the frame of their DRAGON bench (REEVE, MYERS, MORRIS et al. 2014) was to use a Rodhamine cell that would absorb and emit light exactly as sodium would do. An illustration of such a cell with four LGS is shown in Fig. 7.3. Such a source would allow to validate the impact of spot truncation as studied in Chapter 2 of this manuscript. It would allow to anchor the numerical models developed with experimental results, and later explore more configurations from simulations.

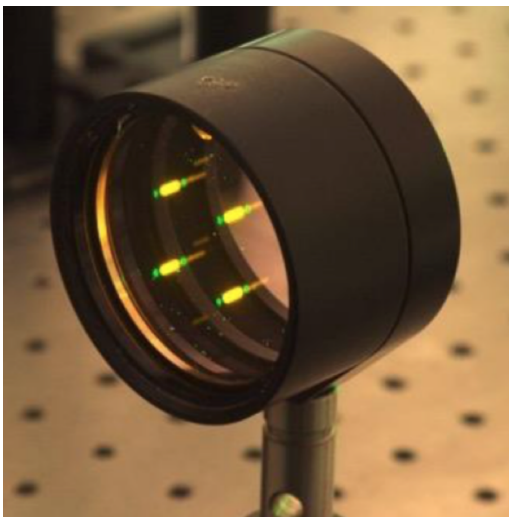

FIGURE 6.3. – Picture of an elongated LGS constellation produced with a Rodhamine cell. Courtesy Durham Univesrity.

As a longer term development, the source and SLM bench developed here will serve as a piece of an ELT simulator for testing the HARMONI LTAO system, when it will

be integrated in the lab at LAM. The concept, shown in Figure 7.4, will use 6 SLMs and 6 laser sources, one per each of the HARMONI LGSWFS. A numerical simulation will compute the phase screens to be printed on the SLM. These phase screens will the results of the atmospheric propagation in the 6 LGS directions, to which we could add any telescope effects (field aberrations, co-phasing error, petalling, ...) and subtract the M4 correction, using the exact M4 geometry. Theses SLM phases are then illuminated by 6 laser sources, and the light sent to the actual HARMONI hardware with 6 LGSWFS. The measurements from these 6 LGSWFS can then be used by the Real-Time-Computer to get the tomographic reconstruction and the projection of the correction phase on-axis. The loop is then closed in the simulation, by propagating again the turbulence and subtracting the newly computed M4 shape. The loop could even be closed in almost real-time thanks to the fast SLM characterized in Section 4.5.1 of this manuscript.

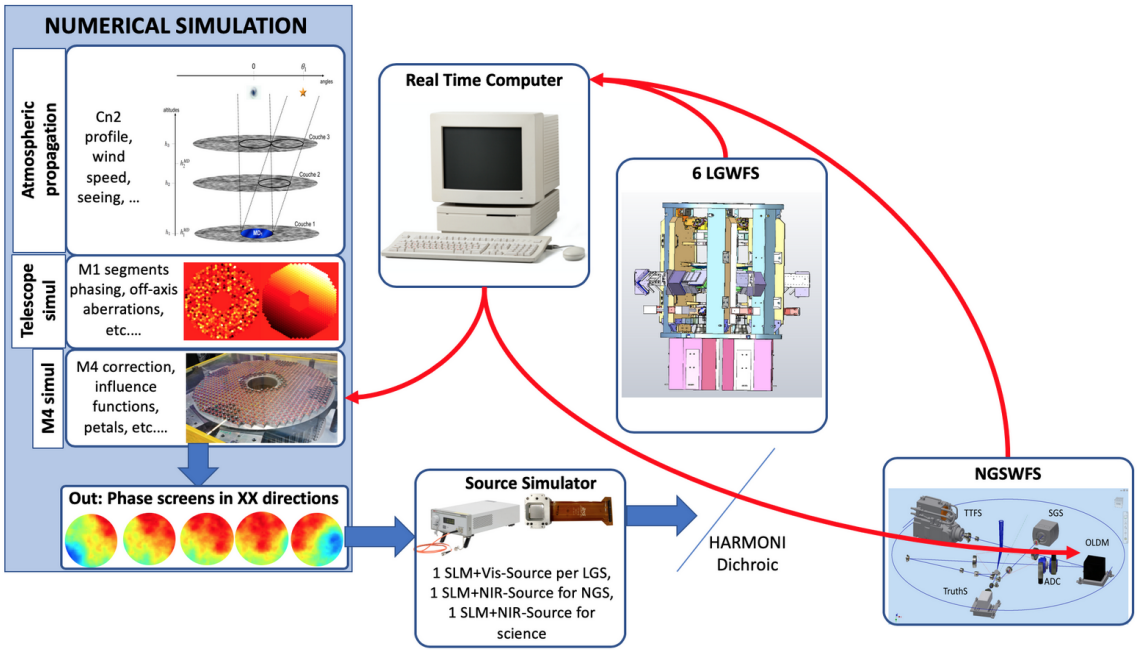

FIGURE 6.4. – Concept for an ELT simulator, based on using 6 SLMs and Laser Source, to feed the HARMONI LTAO system when integrated at LAM.

Finally, another path to test the LGSWFS prototype would be to couple it with the PAPYRUS bench. We have looked at the PAPYRUS design and shown that an extra WFS path could be added in parallel to the pyramid path. In the case of PAPYRUS, we would not be able to look at laser sources, but it would be interesting to have both a high-order pyramid and Shack-Hartmann running side by side, on-sky.

From the conceptual point of view, this PhD thesis was focused on the study and optimization of a Shack-Hartmann WFS. It would be very interesting to explore alternative WFS solutions, especially the ones inherited from the Fourier WFS (for which

the pyramid is one of the realizations). Toward this path, in Chapter 2 we have mentioned the Ingot WFS, as an adaptation of the pyramid for elongated sources. Based on the work currently developed at LAM toward optimizing Fourier WFS for given applications, there is certainly an avenue to pursue this work for elongated sources. This work has been started by a master student in the frame of collaboration with the University Catolica of Santiago, and could potentially open for a new PhD work.

Concluding remarks

To conclude this manuscript, it was important to recall the specific context in which this PhD has been developed, in the middle of the Covid-19 pandemic. A large part of my PhD work was related to experiments, while the access to the labs were strongly restricted. Even though it is difficult to quantify the impact of these restrictions on the final work, it is clear that everything was slowed down.

7. Résumé en Français

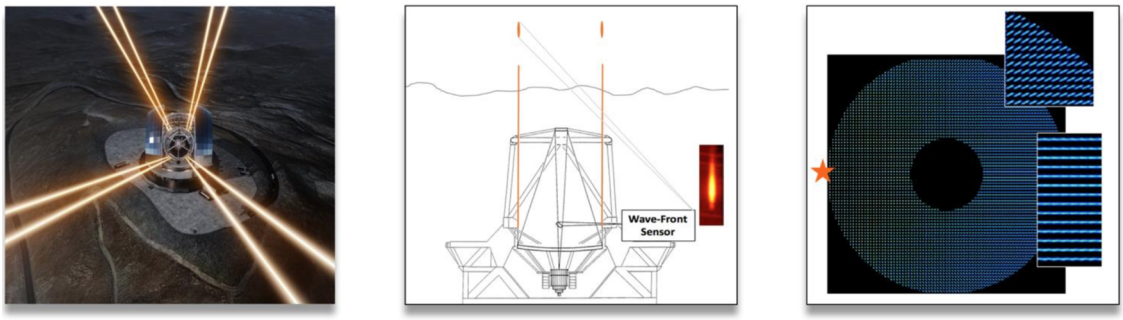

FIGURE 7.1. – A gauche l'ELT, avec ses 8 étoiles laser, au centre, une illustration de l'élongation de spot et à droite une simulation de l'analyseur de surface d'onde Shack-Hartmann.

Sommaire

Le cadre de ce travail de doctorat porte sur le développement de l'instrumentation pour les grandes télescopes au sol, optique et proche infrarouge. L'astronomie au sol a progressé énormément depuis une dizaines d'années et l'état de l'art des grands télescopes optiques atteint 10 mètres de diamètres. Augmenter la taille des télescope signifie augmenter le pouvoir collecteur de la lumière et donc une meilleure sensibilité pour les cibles faibles. Augmenter la taille des télescope offre également la possibilité d'atteindre une résolution angulaire plus élevée et, éventuellement, la capacité de détecter des détails plus fins sur les objets astronomiques à l'étude. Pour atteindre ces objectifs, l'une des percées technologiques clés réalisées au cours des dernières décennies est l'introduction de l'optique adaptative (OA) pour les observations astronomiques. À la croisé de l'optique, l'électronique, la science atmosphérique, la théorie de contrôle, linformatique et les mathématiques, l'OA est une technique qui vise à compenser rapidement des aberrations optiques a fins de restaurer la limite de résolution angulaire ultime d'un système optique. l'OA utilise une combinaison d'analyseur de surface d'onde, pour mesurer les aberrations qui affecten londe lumineuse et des miroirs déformables pour les compenser. Pour les télescopes astronomiques, l'OA permet de surmonter le flou d'image imposé par la turbulence atmosphérique. Celle-ci limitant la résolution angulaire d'un télescope au sol à celle réalisable par un télescope de 10 à 50 cm, un ordre de grandeur inférieur à la limite de diffraction des grands télescopes de classe 8 m qui sont la norme actuelle.

La plupart des systèmes d'OA actuels nécessitent une source de référence brillante et / ou proche angulairement. De fait, l'OA dite classique convient bien aux observations d'objets compacts relativement brillants. Par exemple, au cours des 20 dernières années, les observations d'OA ont apporté des découvertes majeures dans l'étude du trou noir massif au centre de notre galaxie ou des premières images d'exoplanètes, mais seulement un nombre réduit d'études extra-galactiques majeures. Ceci est du au fait que les champs cosmologiques manquent généralement d'étoiles de référence suffisamment lumineuses.

Une nouvelle génération de systèmes OA, dites OA grand champ (WFAO en Anglais) permet de s'affranchir de cette limitation en augmentant de manière significative le champ de vue des images corrigées et / ou la fraction du ciel pouvant bénéficier de cette correction. Pour cela, les système de WFAO utilisent des étoiles guides artificielles. Celles-ci sont générées par des lasers emettant à 589 nm, sur la longueur d'onde d'absoprtion du Sodium (raie D2), ce qui excite les atomes de sodium situés dans la mésosphère. Ces "étoiles laser" (LGS en Anglais) peuvent alors être créées à des endroits arbitraires dans le ciel, résolvant ainsi partiellement le problème de la rareté des étoiles guides. De nos jours, tous les grands télescopes au sol sont équipés de tels lasers. Le deuxième pilier des des systèmes WFAO est la tomographie atmosphérique. En effet, étant donné que la turbulence atmosphérique n'est pas concentrée dans une seule couche mais distribuée dans un volume, la lumière provenant de différentes directions ne verra pas les mêmes perturbations. En fait, cela réduit le champ de correction. Pour surmonter cette limitation, les systèmes de WFAO utilisent plusieurs LGS, afin de fournir un pavage du champ scientifique, qui sera utilisé pour effectuer une reconstruction tomographique complète des perturbations 3D. À partir de ces informations, il est alors possible d'optimiser les performances dans la direction scientifique souhaitée.

Aujourd'hui (2021), les systèmes de WFAO commencent à être en opération régulière dans un certains nombre d'observatoires mondiaux (LBT, VLT, Keck, Gemini). Et le paysage WFAO se développe rapidement. Par exemple, le télescope Keck a été financé pour le démarrage d'un système (LTAO). Gemini vient d'annoncer un financement pour le développement d'un nouveau système MCAO pour son télescope à Hawaii et la Subaru s'engage dans l'aventure d'un miroir adaptatif secondaire. Côté européen, l'ESO finance un système de MCAO à haute performance, afin d'offrir la limite de diffraction du VLT dans la gamme de longueurs d'onde visibles, sur un champ de plusieurs dizaines d'arcsecondes et pour une couverture de ciel presque complète. Ce dernier instrument, MAVIS, devrait fournir une alternative au HST dans le visible et couvrir un espace de paramètre complémentaire à l'ELT ou à JWST, qui fonctionnent dans l'infrarouge. Ainsi, le paysage mondial montre clairement une tendance vers la généralisation des système WFAO sur les télescopes de la classe de 8-10m.

D'ici la fin de cette décennie, le monde verra une nouvelle génération de télescopes avec des diamètres allant jusqu'à 40 m, appelé les télescopes extrêmement grand (ou

ELT en Anglais). Le pouvoir collecteur et la résolution angulaire unique des ELT équipé d'AO révolutionneront les observations astronomiques. Le potentiel scientifique des ELT repose sur de nouveaux concepts d'OA, intégrés à l'intérieur du télescope lui-même et qui devront fournir des images à haute résolution à toute l'instrumentation en aval.

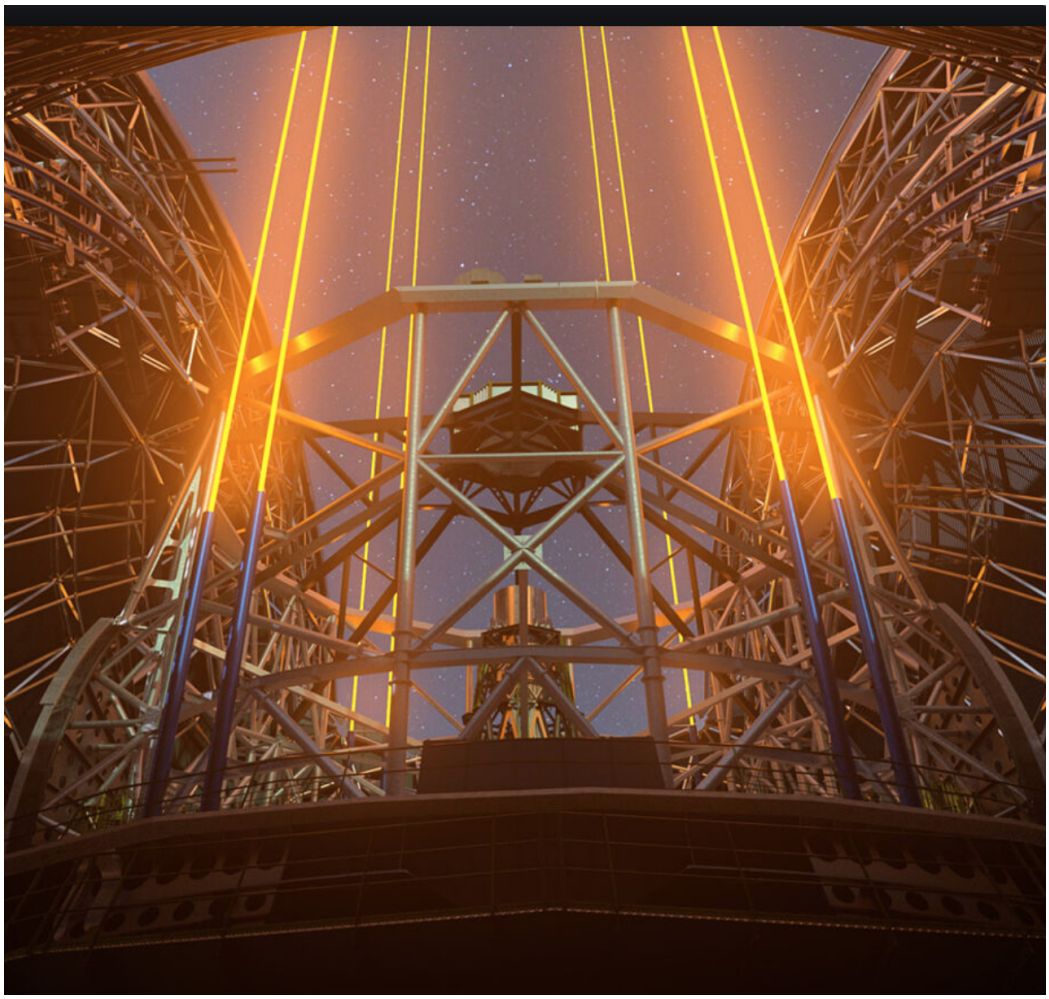

FIGURE 7.2. – Vue d'artiste du futur Elt avec ses étoiles laser.

Compte tenu du succès et de la fiabilité des systèmes d'OA actuellement en opération sur les télescope de classe 10m, on pourrait penser que la tâche sera facile sur l'ELT et qu'une simple mise à l'échelle sera suffisante. Malheureusement, ce n'est pas le cas, car l'ELT apporte son ensemble de défis conceptuels, technologiques et programmatiques. Un exemple du changement de paradigme concerne les interfaces entre le télescope et ses instruments. Jusqu'à présent, la frontière entre le contrôle et la responsabilité du front d'onde était clairement définie entre le télescope et son AO (le télescope était chargé de l'optique active, les instruments de l'AO). Mais l'ELT est dôté d'un contrôle partagé entre le télescope et les instruments. Le miroir déformable est

intégré dans le télescope et il est utilisé à la fois par le télescope et les instruments. Un autre exemple, qui a motivé le développement de ce doctorat, concerne la détection de front d'onde associée aux étoiles laser, et en particulier le problème dit de l'élongation de spot.

L'élongation des spots LGS provient du fait que les etoiles laser ne sont pas des objets ponctuels, mais des sources étendues. En effet, la couche d'atomes de sodium, située à environ 90 km au-dessus du télescope, a une épaisseur comprise entre 10 km et 20 km. Les étoiles laser résultant de l'excitation de ces atomes de sodium par la lumière laser propagée du télescope ont donc une forme "cigare" dans la couche de sodium. Par effet de perspective, ils apparaissent comme des objets étendus (ellipses) sur le bord opposé de la pupille du télescope. Pour un télescope de 39 m, les taches laser ont une taille comprise entre 1 arcseconde pour celles proches du projecteur laser et une allongement au maximum attendu pouvant atteindre 25 arcsecondes. La difficulté est donc d'effectuer une analyse de surface d'onde sur des objets hautement étendus et dont l'élongation varie dans la pupille. Au début de mon doctorat, plusieurs solutions étaient envisagées pour résoudre ce défi, mais aucunes n'était réellement ni démontrée, ni validée. L'objectif de mon doctorat était alors d'étudier différentes options pour faire face à l'allongement des LGS pour les instruments AO de l'ELT, proposer des solutions et éventuellement valider à travers un banc expérimental la robustesse des solutions proposées.

Au chapitre 2 de cette thèse, je décris le principe des étoiles laser, et je montre les principales limitations liées à cette technologie. En analysant les données de sodium acquises par des experiences de LIDAR, je quantifies l'impact potentiel de la troncature spatiale sur la performance de l'AO. Cette analyse a été effectuée à la fois spatialement, en déterminant les biais induits par troncature et temporellement, en quantifiant la vitesse à laquelle ces biais évoluent. J'ai ensuite proposé une description exhaustive des solutions potentielles, montrant les avantages et les inconvénients pour chacunes d'elles.

Au chapitre 3, j'ai développé l'une des solutions envisagées pour faire face à la limitation de l'élongation LGS : le déploiement d'un nouveau détecteur CMOS de grand format. Ce nouveau détecteur a été mis à ma disposition au début de mon doctorat, et je devais comprendre s'il conviendrait à des fins d'analyseurs de surface d'onde LGS pour un ELT. Sur la base des exigences définies au chapitre 2, j'ai analysé les performances de ce nouveau détecteur CMOS. Pour cela, j'ai développé à la fois un outil de simulation complet et un banc expérimental utilisé pour caractériser le détecteur. Les principales propriétés que j'ai examinées sont le bruit de lecture et la manière dont cela affecterait la mesure de front d'onde. En effet, même si le détecteur CMOS a de très bonnes performances de RON, avec en particulier une médiane mesurée en dessous de 3 e^-, il a également montré une queue de la distribution de bruit vers des valeurs plus importantes. Au moyen de simulations et de mesures expérimentales, j'ai démontré que cette queue n'avait pas d'impact sur l'exactitude de la mesure de front

d'inde. Un autre paramètre important de ce détecteur CMOS est venu de l'« angle d'acceptance » et de la manière dont cela affecterait le détection de front d'onde. Cet angle d'acceptance provient de micro-lentilles mis en œuvre devant chacun des pixels du détecteur. Ces micro-lentilles sont utilisés pour augmenter la transmission du détecteur, mais elles imposent certaines limitations sur l'angle maximal des faisceaux pouvant être couplés au détecteur. Nous avons montré que si l'on peut proposer un design optique de LGSWFS télécentrique, cet effet à un impact minimal, même pour un LGSWFS nécessitant un grand champ de vue important. Tous ces résultats ont été présentés dans une publication pour un numéro spécial de Jatis, dans un article intitulé "Performances du capteur CMOS pour la détection des ondes de guidage au laser". Cet article a été préparé conjointement avec des équipes travaillant pour l'ELT (pour HARMONI et MAORY) et pour le TMT (NFIRAOS). Il a essentiellement démontré que ce nouveau détecteur convient parfaitement à la construction d'un LGSWFS performant et fiable pour ces futurs télescopes géants. Il s'agit d'un résultat important, car il valide la conception de ces composants clés pour l'ELT et pour le TMT.

Suite aux résultats présentés dans cet article, j'ai ensuite effectué une analyse pour comprendre l'impact de l'angle d'acceptance sur la forme de la PSF et potentiellement sur l'aliasing. En effet, je montre que l'angle d'acceptance équivaut à une apodisation de la pupille autour de chaque micro-lentilles. Dans ce cas, la diffraction est modifiée, mais cela n'a qu'un faible impact sur la performance finale. Cette apodisation induit aussi un effet d'extra-aliasing équivalent, qui peut être simulé à partir d'une analyse de Fourier. L'impact de cette extra-aliasing reste petit et ne change pas la conclusion sur l'adéquation du détecteur CMOS pour construire un LGSWFS efficace pour les ELTs.

Au chapitre 4 de cette thèse, je montre comment ce détecteur spécifique pourrait être intégré dans un LGSWFS pour l'ELT. Nous avons pris l'instrument HARMONI comme une base de référence pour la construction d'un prototype LGSWFS. Nous avons d'abord rappelé le budget d'erreur HARMONI et le compromis requis pour définir les LGSWFS associés. Ce travail a été fait grâce à des simulations complètes de la performance d'HARMONI. À partir de ces "requirements", j'ai participé à la conception et au développement d'un prototype de LGSWFS à grande échelle. Cela comprenait la définition et la caractérisation de la matrice de microlentilles, un relais optique requis pour ré-imager la pupille sur le détecteur et la caractérisation d'une caméra commerciale mettant en œuvre le détecteur CMOS étudié au chapitre 3. Ce module de détecteur (LDM) a alors été intégré dans un banc AO, à l'aide d'un modulateur spatial de lumière (SLM en Anglais) pour imiter la turbulence atmosphérique et le miroir déformable ELT M4. Ce travail se termine avec la première mesure d'une matrice d'interaction pour le prototype LGSWFS de HARMONI.

Au chapitre 5, j'ai concentré mon travail sur un aspect spécifique de certains des détecteurs, à savoir la lecture de « rolling shutter » de la matrice de pixels. Pour l'optique adaptative, un rolling shutter signifie que les pixels à travers la pupille sont lus à

différents timings. En effet, cela peut signifier que la turbulence aurait évolué entre le début de l'échantillonnage de la pupille et la fin. Grâce à des simulations, j'ai examiné l'impact potentiel sur la performance d'un tel effet et comment il se comparerait à l'approche standard dites "global shutter". J'ai utilisé l'outil de simulation OOMAO que j'ai modifié pour prendre en compte cet effet spécifique. J'ai obtenu des résultats pour les systèmes d'AO classiques, travaillant à la fois en boucle ouverte et en boucle proche, et j'ai montré que l'impact du Rolling Shutter sur la performance est de l'ordre de quelques dizaines de nanomètres. Je conclus que le Rolling Shutter présente un risque à determiner lorsqu'il est intégré à une boucle d'OA complète.

Dans l'annexe de cette thèse, je présente enfin un travail qui dépasse la problèmatique de ce doctorat, mais pour lequel j'ai également consacré une partie de mon temps : le projet PAPYRUS. PAPYRUS est un projet dirigé par les étudiants du LAM, dans le but de développer un système d'OA basé sur la pyramide et installé sur le télescope de 1,52 m de l'observatoire de Haute Provence. Le projet a commencé en 2019, et l'idée est apparue après une visite du site. PAPYRUS s'appuie sur des composants déjà disponibles au LAM tels que la pyramide en verre, une caméra rapide OCAM et un mirroir déformable 17x17. Papyrus a ensuite été organisé en tant que projet, avec des phases de validation de conception, d'AIT et de validation sur le ciel. Le projet regroupe près de 20 étudiants, chacun apportant sa propre expertise. Pour ma part, j'ai participé à la simulation, au budget d'erreur, à la caractérisation DM et WFS. Le projet a validé son design en en mars 2021 et l'intégration a débuté peu après. Au moment de la rédaction de ces lignes, le projet est proche d'être achevé au LAM et devrait espérer voir la première lumière dans les prochains mois. De mon point de vue, c'était une expérience très riche et instructive d'avoir la possibilité de participer à toute la chaîne de développement d'un système d'OA.

Perspectives

Les travaux développés dans ce doctorat ouvrent plusieurs perspectives dans le domaine de l'analyse de surface d'onde pour les télescopes extrêmement grands. Premièrement, du point de vue de la technologie, nous pouvons mentionner trois axes : (i) la finalisation de l'évaluation de l'impact du Rolling Shutter pour les systèmes AO tomographiques (ii) la poursuite des tests à grande échelle avec le prototype de LGSWFS, et (iii) le développement d'un simulateur complet d'ELT basé sur le banc laser développé pour les tests LGSWFS.

En ce qui concerne les aspects rolling-shutter, la première étude présentée dans ce doctorat a montré un impact négatif potentiel sur la performance, mais nous nous sommes limités à un cas simple d'OA classique. La généralisation de la simulation avec plusieurs LGS, des systèmes d'OA tomographiques permettrait de conclure définitivement sur l'utilisation potentielle du RS en OA. En particulier, deux aspects semblent pertinents à pousser : (i) l'impact d'une mauvaise synchronisation entre les plusieurs LGSWFS et (ii) La confusion modale induite par les bas ordres généralement

filtrés des mesures LGS tels que le Tip-Tilt et le focus. Étant donné que ces modes peuvent présenter une grande amplitude (non contrôlée, ils restent presque en boucle ouverte), la confusion modale induite par le RS peut être "show stopper" pour la performance finale. Aussi, il serait également nécessaire de comprendre comment mettre en œuvre un contrôleur avancé en présence d'un détecteur RS.

En ce qui concerne la poursuite du prototype LGSWFS, à la fin de ma thèse, nous avons atteint un état où le système était prêt à démarrer les tests d'OA. En particulier, nous avons vu que le SLM utilisé dans le plan de pupille offrait une grande flexibilité en termes de tests potentiels. En couplant le SLM avec le prototype LGSWFS, on pourrait déjà examiner des aspects spécifiques tels que la propagation de bruit du capteur, sa sensibilité à différents flux, l'optimisation des gains du détecteur à travers la pupille et la linéarité de la mesure. Après cela, le SLM pourrait être utilisé pour imiter la même géométrie que le M4 de l'ELT, en termes de fonctions d'ingluence et de distribution spatiale des actionneurs. Cela permettrait d'effectuer de nombreux tests d'OA, tels que la démonstration d'algorithme de calibration, la mesure de la matrice d'interaction, l'impact des segments manquants ou l'impact des araignées du télescope sur la reconstruction de front d'onde. Tous ces tests permettront à l'équipe de gagner en expertise dans la design, de développer et de valider les algorithmes appropriés et de détecter et de résoudre des problèmes potentiels. Ces activités seront menés dans les prochains mois / ans et utiliseront mon travail expérimental comme fondation.

En ce qui concerne le prototype LGSWFS, une mise à niveau pouvant être mise en œuvre consiste à introduire une source allongée à l'entrée du banc. Dans sa version actuelle, seule une source 2D est utilisée, ce qui ne permet pas encore de reproduire de manière expérimentale l'allongement des LGS. Une option qui a été étudiée à l'Université de Durham, dans le cadre de leur banc de "dragon" consistait à utiliser une cellule de Rodhamine, qui absorberait et émettrait la lumière exactement comme le ferait le sodium. Une illustration d'une telle cellule avec quatre LGS est illustrée à la Fig. 7.3. Une telle source permettrait de valider l'impact de la troncature ponctuelle telle qu'étudiée au chapitre 2 de ce manuscrit. Cela permettrait d'ancrer les modèles numériques développés avec des résultats expérimentaux, puis d'explorez plus tard plus de configurations à partir des simulations.

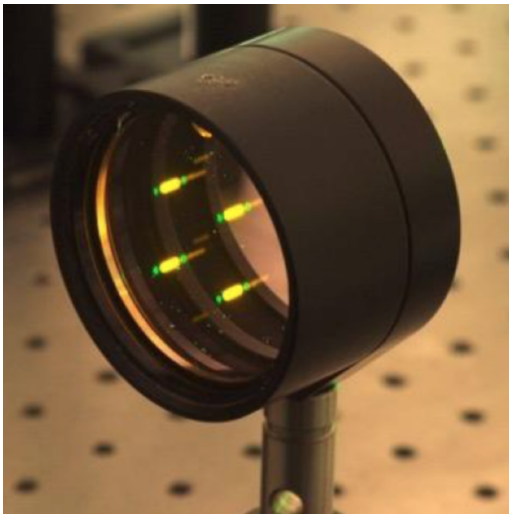

FIGURE 7.3. – Image d'une constellation LGS allongée produite avec une cellule Rodhamine. Source Université Durham.

En tant que développement à long terme, le banc de test développé ici servira de brique pour un simulateur ELT, pour tester le système HARMONI, lorsqu'il sera intégré au LAM. Le concept, illustré à la figure 7.4, utilisera 6 SLMs et 6 sources laser, une par chacun des LGSWFS. Une simulation numérique calculera les écrans de phase à imprimer sur les SLMs. Ces écrans de phase seront les résultats de la propagation atmosphérique dans les 6 directions LGS, auxquels nous pourrons ajouter des effets de télescope (aberrations de champ, erreur de co-phasage, pétallin, ...) et la correction du M4, Les SLM sont ensuite éclairés par 6 sources laser et la lumière envoyée aux vrais LGSWFS d'Harmoni. Les mesures de ces 6 LGSWFS peuvent ensuite être utilisées par l'ordinateur temps réel pour obtenir la reconstruction tomographique et la projection de la phase de correction sur l'axe. La boucle est ensuite fermée en simulation, en propagant à nouveau la turbulence et en soustrayant la forme de M4 nouvellement calculée. La boucle pourrait même être fermée quasi en temps réel grâce au SLM rapide caractérisé à la section 4.5.1 de ce manuscrit.

Enfin, une autre option pour tester le prototype LGSWFS serait de le coupler avec le banc PAPYRUS. Nous avons examiné le design de PAPYRUS et nous montrons qu'un WFS supplémentaire pourrait être ajouté en parallèle de la pyramide. Dans le cas de Papyrus, nous ne pourrions pas envisager de regarder des sources laser, mais il serait intéressant d'avoir à la fois une pyramide de haut ordre et une shack-hartmann à côté à côte, sur le ciel.

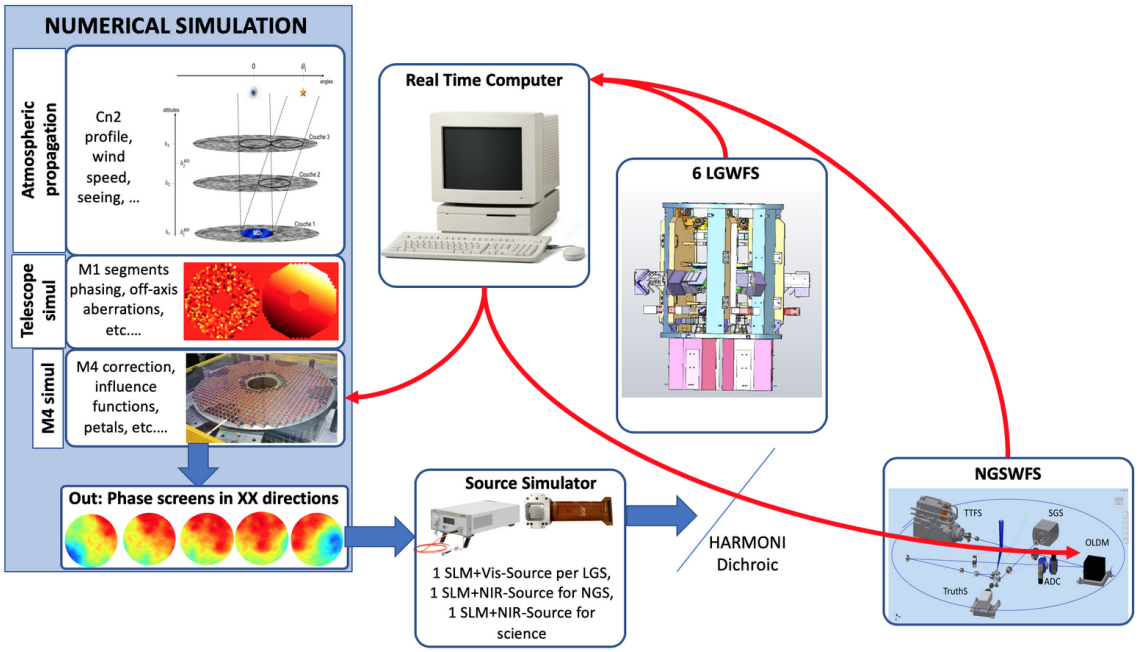

FIGURE 7.4. – Concept pour un simulateur ELT, basé sur l'utilisation de 6 SLMs et une source laser, pour alimenter le système LTAO d'HARMONI lorsqu'il sera intégré à LAM.

Du point de vue conceptuel, cette thèse a été axée sur l'étude et l'optimisation d'un Shack-Hartmann WFS. Il serait très intéressant d'explorer des solutions alternatives en terms de WFS, en particulier des WFSs hérités de la pyramide. DAns cette voie, au chapitre 2, nous avons mentionné le Ingot WFS, comme une adaptation de la pyramide pour des sources allongées. Sur la base des travaux actuellement développés à LAM vers l'optimisation des WFSs, il existe certainement une voie à suivre pour poursuivre ce travail pour des sources allongées. Ce travail a été lancé par un étudiant dans le cadre d'une collaboration avec l'université de Santiago et pourrait potentiellement s'ouvrir pour un nouveau travail de doctorat.

Concluding remarks

Pour conclure ce manuscrit, il était important de rappeler le contexte spécifique dans lequel ce doctorat a été développé, au milieu de la pandémie Covid-19. Une grande partie de mon travail de doctorat était liée à des expériences, tandis que l'accès aux laboratoires était fortement restreint. Même s'il est difficile de quantifier l'impact de ces restrictions sur le travail final, il est clair que tout était ralenti.

Bibliographie

[Age+13] AGEORGES, NANCY, DAINTY et al. *Laser guide star adaptive optics for astronomy*. T. 551. Springer Science & Business Media, 2013 (cf. p. 44).

[ABR10] Marcis AUZINSH, Dmitry BUDKER et Simon ROCHESTER. *Optically polarized atoms : understanding light-atom interactions*. Oxford University Press, 2010 (cf. p. 45).

[Bab53] Horace W BABCOCK. « The possibility of compensating astronomical seeing ». In : *Publications of the Astronomical Society of the Pacific* 65.386 (1953), p. 229-236 (cf. p. 23).

[Bas+17] BASDEN, BARDOU, Bonaccini CALIA et al. « On-sky demonstration of matched filters for wavefront measurements using ELT-scale elongated laser guide stars ». In : *Monthly Notices of the Royal Astronomical Society* 466.4 (2017), p. 5003-5010 (cf. p. 69).

[Bec92] Jacques M BECKERS. « Overcoming perspective elongation effects in laser-guide-star-aided adaptive optics ». In : *Applied optics* 31.31 (1992), p. 6592-6594 (cf. p. 64).

[Bla+15] Celia BLAIN, Simone ESPOSITO, Alfio PUGLISI et al. « Use of laser guide star with pyramid wavefront sensor ». In : *Adaptive Optics for Extremely Large Telescopes 4–Conference Proceedings*. T. 1. 1. 2015 (cf. p. 64).

[Bus+16] BUSTOS, HOLZLÖHNER, RONALD et al. « Sodium vapor cell laser guide star experiments for continuous wave model validation ». In : *Adaptive Optics Systems V*. T. 9909. International Society for Optics et Photonics. 2016, 99095P (cf. p. 46).

[Cha+21] CHAMBOULEYRON, FAUVARQUE, SAUVAGE et al. « The focal-plane assisted pyramid wavefront sensor : enabling frame-by-frame optical gains tracking ». In : *arXiv preprint arXiv :2103.02297* (2021) (cf. p. 191).

[Cha+20] CHAPMAN, CONOD, TURRI et al. « The multi-object adaptive optics system for the Gemini infra-red multi-object spectrograph ». In : *Adaptive Optics Systems VII*. T. 11448. International Society for Optics et Photonics. 2020, p. 1144872 (cf. p. 58).

[Che+05] CHERNYSHOV, STERR, RIEHLE et al. « Calibration of a Shack–Hartmann sensor for absolute measurements of wavefronts ». In : *Applied optics* 44.30 (2005), p. 6419-6425 (cf. p. 38).

[CWL20] Richard M CLARE, Stephen J WEDDELL et Miska LE LOUARN. « Mitigation of truncation effects in elongated Shack–Hartmann laser guide star wavefront sensor images ». In : *Applied Optics* 59.22 (2020), p. 6431-6442 (cf. p. 54, 69, 71).

[CT14] CORREIA et TEIXEIRA. « Anti-aliasing Wiener filtering for wave-front reconstruction in the spatial-frequency domain for high-order astronomical adaptive-optics systems ». In : *JOSA A* 31.12 (2014), p. 2763-2774 (cf. p. 107).

[Cub79] Ronald CUBALCHINI. « Modal wave-front estimation from phase derivative measurements ». In : *JOSA* 69.7 (1979), p. 972-977 (cf. p. 31).

[Dam05] van DAM. « Measuring the centroid gain of a Shack–Hartmann quad-cell wavefront sensor by using slope discrepancy ». In : *JOSA A* 22.8 (2005), p. 1509-1514 (cf. p. 69).

[Dio+12] DIOLAITI, SCHREIBER, FOPPIANI et al. « Dual-channel multiple natural guide star wavefront sensor for the E-ELT multiconjugate adaptive optics module ». In : *Adaptive Optics Systems III*. T. 8447. International Society for Optics et Photonics. 2012, 84471K (cf. p. 62).

[Dir+18] DIRNBERGER, RIGAUT, MINOWA et al. « Rolling shutter detector data flow strategies to push the limits of AO performance ». In : *Adaptive Optics Systems VI*. T. 10703. International Society for Optics et Photonics. 2018, 107034O (cf. p. 141).

[Ell+05] ELLERBROEK, BRITTON, DEKANY et al. « Adaptive optics for the thirty meter telescope ». In : *Astronomical Adaptive Optics Systems and Applications II*. T. 5903. International Society for Optics et Photonics. 2005, p. 590304 (cf. p. 24).

[Far+19] OJD FARLEY, James OSBORN, T MORRIS et al. « Identifying optical turbulence profiles for realistic tomographic error in adaptive optics ». In : *Monthly Notices of the Royal Astronomical Society* 488.1 (2019), p. 213-221 (cf. p. 111).

[Far+20] OJD FARLEY, James OSBORN, Tim MORRIS et al. « Limitations imposed by optical turbulence profile structure and evolution on tomographic reconstruction for the ELT ». In : *Monthly Notices of the Royal Astronomical Society* 494.2 (2020), p. 2773-2784 (cf. p. 111).

[Fau+17] FAUVARQUE, NEICHEL, FUSCO et al. « General formalism for Fourier-based wave front sensing : application to the pyramid wave front sensors ». In : *Journal of Astronomical Telescopes, Instruments, and Systems* 3.1 (2017), p. 019001 (cf. p. 191).

[Fau+19] Olivier FAUVARQUE, Pierre JANIN-POTIRON, Carlos CORREIA et al. « Kernel formalism applied to Fourier-based wave-front sensing in presence of residual phases ». In : *JOSA A* 36.7 (2019), p. 1241-1251 (cf. p. 191).

[FF88] FEIT et FLECK. « Beam nonparaxiality, filament formation, and beam breakup in the self-focusing of optical beams ». In : *JOSA B* 5.3 (1988), p. 633-640 (cf. p. 29).

[Fét+20] R JL FÉTICK, LM MUGNIER, Thierry FUSCO et al. « Blind deconvolution in astronomy with adaptive optics : the parametric marginal approach ». In : *Monthly Notices of the Royal Astronomical Society* 496.4 (2020), p. 4209-4220 (cf. p. 191).

[Fil+21] Di FILIPPO, GREGGIO, BERGOMI et al. « Ingot wavefront sensor : from the optical design to a preliminary laboratory test ». In : *arXiv preprint arXiv :2101.07742* (2021) (cf. p. 65).

[FMF76] FLECK, MORRIS et FEIT. « Time-dependent propagation of high energy laser beams through the atmosphere ». In : *Applied physics* 10.2 (1976), p. 129-160 (cf. p. 29).

[FL85] R FOY et A LABEYRIE. « Feasibility of adaptive telescope with laser probe ». In : *Astronomy and Astrophysics* 152 (1985), p. L29-L31 (cf. p. 23).

[Fri66a] David L FRIED. « Limiting resolution looking down through the atmosphere ». In : *JOSA* 56.10 (1966), p. 1380-1384 (cf. p. 23, 28).

[Fri66b] David L FRIED. « Optical resolution through a randomly inhomogeneous medium for very long and very short exposures ». In : *JOSA* 56.10 (1966), p. 1372-1379 (cf. p. 31).

[Fri82] David L FRIED. « Anisoplanatism in adaptive optics ». In : *JOSA* 72.1 (1982), p. 52-61 (cf. p. 40).

[Fug+91] Robert Q FUGATE, David L FRIED, Guillermo A AMEER et al. « Measurement of atmospheric wavefront distortion using scattered light from a laser guide-star ». In : *Nature* 353.6340 (1991), p. 144-146 (cf. p. 24, 43).

[Fus+99] FUSCO, CONAN, MICHAU et al. « Phase estimation for large field of view : application to multiconjugate adaptive optics ». In : *Propagation and Imaging through the Atmosphere III*. T. 3763. International Society for Optics et Photonics. 1999, p. 125-133 (cf. p. 111).

[Gen16] GENDRON. « Optical solutions for accommodating ELT LGS wave-front sensing to small format detectors ». In : *Adaptive Optics Systems V*. T. 9909. International Society for Optics et Photonics. 2016, 99095Z (cf. p. 66).

[Gen+11] GENDRON, VIDAL, BRANGIER et al. « MOAO first on-sky demonstration with CANARY ». In : *Astronomy & Astrophysics* 529 (2011), p. L2 (cf. p. 58).

[GGR10] GRATADOUR, GENDRON et ROUSSET. « Intrinsic limitations of Shack–Hartmann wavefront sensing on an extended laser guide source ». In : *JOSA A* 27.11 (2010), A171-A181 (cf. p. 69).

[Gre77] Darryl P GREENWOOD. « Bandwidth specification for adaptive optics systems ». In : *JOSA* 67.3 (1977), p. 390-393 (cf. p. 40).

[Hap+94] W HAPPER, GJ MACDONALD, CE MAX et al. « Atmospheric-turbulence compensation by resonant optical backscattering from the sodium layer in the upper atmosphere ». In : *JOSA A* 11.1 (1994), p. 263-276 (cf. p. 45).

[Har98] John W HARDY. *Adaptive optics for astronomical telescopes*. T. 16. Oxford University Press on Demand, 1998 (cf. p. 23, 36, 43).

[HLK77] John W HARDY, J E_ LEFEBVRE et CL KOLIOPOULOS. « Real-time atmospheric compensation ». In : *JOSA* 67.3 (1977), p. 360-369 (cf. p. 23).

[Hol+10] HOLZLÖHNER, RONALD, ROCHESTER et al. « Optimization of cw sodium laser guide star efficiency ». In : *Astronomy & Astrophysics* 510 (2010), A20 (cf. p. 44, 48).

[HRH92] HUMPHREYS, RONALDA et Jan HERRMANN. « Sodium-layer synthetic beacons for adaptive optics ». In : *The Lincoln Laboratory Journal* 5.1 (1992), p. 45-66 (cf. p. 23).

[Jah+16] JAHN, HUGOT, FUSCO et al. « Laser guide star spot shrinkage for affordable wavefront sensors ». In : *Adaptive Optics Systems V*. T. 9909. International Society for Optics et Photonics. 2016, p. 99096L (cf. p. 66).

[Jan+19] Pierre JANIN-POTIRON, Vincent CHAMBOULEYRON, Lauren SCHATZ et al. « Adaptive optics with programmable Fourier-based wavefront sensors : a spatial light modulator approach to the LAM/ONERA on-sky pyramid sensor testbed ». In : *Journal of Astronomical Telescopes, Instruments, and Systems* 5.3 (2019), p. 039001 (cf. p. 191).

[Jey+92] TH JEYS, RM HEINRICHS, KF WALL et al. « Observation of optical pumping of mesospheric sodium ». In : *Optics letters* 17.16 (1992), p. 1143-1145 (cf. p. 46).

[Joh+12] JOHNS, MCCARTHY, RAYBOULD et al. « Giant magellan telescope : overview ». In : *Ground-based and Airborne Telescopes IV*. T. 8444. International Society for Optics et Photonics. 2012, 84441H (cf. p. 24).

[Ker+88] KERN, MERKLE, GAFFARD et al. « Prototype of an adaptive optical system for astronomical observation ». In : *Real-Time Image Processing : Concepts and Technologies*. T. 860. International Society for Optics et Photonics. 1988, p. 9-15 (cf. p. 24).

[Kol+17] KOLB, MADEC, ARSENAULT et al. « AOF – first on-sky performance of the GALACSI GLAO mode (or how to close 10 loops in less than 5 minutes) ». In : jan. 2017. DOI : 10.26698/AO4ELT5.0038 (cf. p. 58).

[Kol62] KOLMOGOROV. « A refinement of previous hypotheses concerning the local structure of turbulence in a viscous incompressible fluid at high Reynolds number ». In : *Journal of Fluid Mechanics* 13.1 (1962), p. 82-85 (cf. p. 25).

[Kol91] KOLMOGOROV. « The local structure of turbulence in incompressible viscous fluid for very large Reynolds numbers ». In : *Proceedings of the Royal Society of London. Series A : Mathematical and Physical Sciences* 434.1890 (1991), p. 9-13 (cf. p. 26).

[Mad12] MADEC. « Overview of deformable mirror technologies for adaptive optics and astronomy ». In : *Adaptive Optics Systems III*. T. 8447. International Society for Optics et Photonics. 2012, p. 844705 (cf. p. 35).

[MP16] Alexandre JTS MELLO et Daniel R PIPA. « Improving centroiding by super-resolution reconstruction of sodium layer density in Shack–Hartmann wavefront sensors ». In : *Applied optics* 55.14 (2016), p. 3701-3710 (cf. p. 69).

[Mer+90] MERKLE, ROUSSET, KERN et al. « First diffraction-limited astronomical images with adaptive optics ». In : *Advanced Technology Optical Telescopes IV*. T. 1236. International Society for Optics et Photonics. 1990, p. 193-202 (cf. p. 24).

[Mic+01] MICHAILLE, CLIFFORD, DAINTY et al. « Characterization of the mesospheric sodium layer at La Palma ». In : *Monthly Notices of the Royal Astronomical Society* 328.4 (2001), p. 993-1000 (cf. p. 47).

[MFT98] Peter W MILONNI, Robert Q FUGATE et John M TELLE. « Analysis of measured photon returns from sodium beacons ». In : *JOSA A* 15.1 (1998), p. 217-233 (cf. p. 47).

[Mou+10] MOUSSAOUI, CLEMESHA, HOLZLÖHNER et al. « Statistics of the sodium layer parameters at low geographic latitude and its impact on adaptive-optics sodium laser guide star characteristics ». In : *Astronomy & Astrophysics* 511 (2010), A31 (cf. p. 47, 48).

[Nea+02] NEAL, DANIEL, COPLAND et al. « Shack-Hartmann wavefront sensor precision and accuracy ». In : *Advanced Characterization Techniques for Optical, Semiconductor, and Data Storage Components*. T. 4779. International Society for Optics et Photonics. 2002, p. 148-160 (cf. p. 33).

[Nei+13] NEICHEL, D'ORGEVILLE, CALLINGHAM et al. « Characterization of the sodium layer at Cerro Pachón, and impact on laser guide star performance ». In : *Monthly Notices of the Royal Astronomical Society* 429.4 (2013), p. 3522-3532 (cf. p. 47).

[NFC09] NEICHEL, FUSCO et CONAN. « Tomographic reconstruction for wide-field adaptive optics systems : Fourier domain analysis and fundamental limitations ». In : *JOSA A* 26.1 (2009), p. 219-235 (cf. p. 111).

[Nei+16] NEICHEL, FUSCO, SAUVAGE et al. « The adaptive optics modes for HARMONI : from Classical to Laser Assisted Tomographic AO ». In : *Adaptive Optics Systems V*. T. 9909. International Society for Optics et Photonics. 2016, p. 990909 (cf. p. 103).

[Nei+14] NEICHEL, RIGAUT, VIDAL et al. « Gemini multiconjugate adaptive optics system review–II. Commissioning, operation and overall performance ». In : *Monthly Notices of the Royal Astronomical Society* 440.2 (2014), p. 1002-1019 (cf. p. 58, 69, 145).

[Nol76] Robert J NOLL. « Zernike polynomials and atmospheric turbulence ». In : *JOsA* 66.3 (1976), p. 207-211 (cf. p. 31).

[OSu+00] Créidhe O'SULLIVAN, RM REDFERN, N AGEORGES et al. « Short timescale variability of the mesospheric sodium layer ». In : *Experimental Astronomy* 10.1 (2000), p. 147-156 (cf. p. 47).

[PH14] PFROMMER et HICKSON. « High resolution mesospheric sodium properties for adaptive optics applications ». In : *Astronomy & Astrophysics* 565 (2014), A102 (cf. p. 47).

[PF76] CA PRIMMERMAN et DG FOUCHE. « Thermal-blooming compensation : experimental observations using a deformable-mirror system ». In : *Applied Optics* 15.4 (1976), p. 990-995 (cf. p. 23).

[Pri03] Jérome PRIMOT. « Theoretical description of Shack–Hartmann wave-front sensor ». In : *Optics Communications* 222.1-6 (2003), p. 81-92 (cf. p. 33).

[Qui+13] Fernando QUIRÓS-PACHECO, Enrico PINNA, Alfio PUGLISI et al. « Pyramid wavefront sensor performance with laser guide stars ». In : *Third Adaptive Optics for Extremely Large Telescopes (AO4ELT) Conference*. 2013 (cf. p. 64).

[Rab+10] RABIEN, AGEORGES, BARL et al. « ARGOS : the laser guide star system for the LBT ». In : *Adaptive Optics Systems II*. T. 7736. International Society for Optics et Photonics. 2010, 77360E (cf. p. 58).

[Rag+18] RAGAZZONI, PORTALURI, VIOTTO et al. « Ingot laser guide stars wavefront sensing ». In : *arXiv preprint arXiv :1808.03685* (2018) (cf. p. 65).

[Rag96] Roberto RAGAZZONI. « Pupil plane wavefront sensing with an oscillating prism ». In : *Journal of modern optics* 43.2 (1996), p. 289-293 (cf. p. 34).

[RF99] Roberto RAGAZZONI et J FARINATO. « Sensitivity of a pyramidic wave front sensor in closed loop adaptive optics ». In : *Astronomy and Astrophysics* 350 (1999), p. L23-L26 (cf. p. 34).

[Rag+20] RAGAZZONI, VIOTTO, PORTALURI et al. « Pupil plane wavefront sensing for extended and 3d sources ». In : *arXiv preprint arXiv :2012.07560* (2020) (cf. p. 65).

[Ree+14] REEVE, MYERS, MORRIS et al. « DRAGON, the Durham real-time, tomographic adaptive optics test bench : progress and results ». In : *Adaptive Optics Systems IV*. T. 9148. SPIE. 2014, p. 1903-1912 (cf. p. 169).

[Rig+92] RIGAUT, FRANCOIS, GENDRON et al. « Laser guide star in adaptive optics-The tilt determination problem ». In : *Astronomy and Astrophysics* 261 (1992), p. 677-684 (cf. p. 52).

[Rig+98] RIGAUT, FRANCOIS, Jean-Pierre VÉRAN et al. « Analytical model for Shack-Hartmann-based adaptive optics systems ». In : *Adaptive Optical System Technologies*. T. 3353. International Society for Optics et Photonics. 1998, p. 1038-1048 (cf. p. 193).

[RN18] RIGAUT et NEICHEL. « Multiconjugate adaptive optics for astronomy ». In : *Annual Review of Astronomy and Astrophysics* 56 (2018), p. 277-314 (cf. p. 58).

[Rig+14] RIGAUT, NEICHEL, BOCCAS et al. « Gemini multiconjugate adaptive optics system review–I. Design, trade-offs and integration ». In : *Monthly Notices of the Royal Astronomical Society* 437.3 (2014), p. 2361-2375 (cf. p. 58).

[Rod88] RODDIER. « Curvature sensing and compensation : a new concept in adaptive optics ». In : *Applied Optics* 27.7 (1988), p. 1223-1225 (cf. p. 24).

[RS09] ROSS et SEAN. « Limitations and applicability of the Maréchal approximation ». In : *Applied optics* 48.10 (2009), p. 1812-1818 (cf. p. 38).

[Sax+17] SAXENHUBER, AUZINGER, LOUARN et al. « Comparison of methods for the reduction of reconstructed layers in atmospheric tomography ». In : *Applied optics* 56.10 (2017), p. 2621-2629 (cf. p. 111).

[Sch+14] SCHREIBER, LIEM, FREIER et al. « Analysis of stimulated Raman scattering in cw kW fiber oscillators ». In : *Fiber Lasers XI : Technology, Systems, and Applications*. T. 8961. International Society for Optics et Photonics. 2014, 89611T (cf. p. 62).

[STO05] SEIFERT, TIZIANI et OSTEN. « Wavefront reconstruction with the adaptive Shack–Hartmann sensor ». In : *Optics communications* 245.1-6 (2005), p. 255-269 (cf. p. 36).

[Siv+18] SIVO, MARIN, RIGAUT et al. « An infusion of new blood using the Toptica laser with GeMS : results of the commissioning and science performance ». In : *Adaptive Optics Systems VI*. T. 10703. International Society for Optics et Photonics. 2018, 107030P (cf. p. 58, 113).

[Ste03] Daniel A STECK. « Sodium D Line Data (2001) ». In : *URL http ://steck. us/alkalidata/sodiumnumbers. pdf* (2003) (cf. p. 44).

[TCB95] H TAKAHASHI, BR CLEMESHA et PP BATISTA. « Predominant semi-annual oscillation of the upper mesospheric airglow intensities and temperatures in the equatorial region ». In : *Journal of Atmospheric and Terrestrial Physics* 57.4 (1995), p. 407-414 (cf. p. 47).

[Tal+08] M TALLON, I TALLON-BOSC, C BÉCHET et al. « Wavefront reconstruction with elongated sodium laser guide stars ». In : *SF2A-2008* (2008), p. 77 (cf. p. 68).

[Tal+10] Michel TALLON, Isabelle TALLON-BOSC, Clémentine BÉCHET et al. « Fractal iterative method for fast atmospheric tomography on extremely large telescopes ». In : *Adaptive Optics Systems II*. T. 7736. International Society for Optics et Photonics. 2010, p. 77360X (cf. p. 110).

[Tat16] TATARSKI. *Wave propagation in a turbulent medium*. Courier Dover Publications, 2016 (cf. p. 27).

[Tat71] Valerian Ilitch TATARSKII. « The effects of the turbulent atmosphere on wave propagation ». In : *Jerusalem : Israel Program for Scientific Translations, 1971* (1971) (cf. p. 28).

[TER13] TATULLI, ERIC et AN RAMAPRAKASH. « Laser tomography adaptive optics : a performance study ». In : *JOSA A* 30.12 (2013), p. 2482-2501 (cf. p. 58).

[Tho+08] SJ THOMAS, S ADKINS, D GAVEL et al. « Study of optimal wavefront sensing with elongated laser guide stars ». In : *Monthly Notices of the Royal Astronomical Society* 387.1 (2008), p. 173-187 (cf. p. 54, 71).

[Tih63] Andrei Nikolajevits TIHONOV. « Solution of incorrectly formulated problems and the regularization method ». In : *Soviet Math.* 4 (1963), p. 1035-1038 (cf. p. 57).

[VH00] Jean-Pierre VÉRAN et Glen HERRIOT. « Centroid gain compensation in Shack–Hartmann adaptive optics systems with natural or laser guide star ». In : *JOSA A* 17.8 (2000), p. 1430-1439 (cf. p. 69).

[Vér+05] VÉRINAUD, LOUARN, KORKIAKOSKI et al. « Adaptive optics for high-contrast imaging : pyramid sensor versus spatially filtered shack—hartmann sensor ». In : *Monthly Notices of the Royal Astronomical Society : Letters* 357.1 (2005), p. L26-L30 (cf. p. 34).

[Ver+99] Elise VERNET-VIARD, Francoise DELPLANCKE, Norbert N HUBIN et al. « LGS Na spot elongation and Rayleigh scattering effects on Shack-Hartmann wavefront sensor performances ». In : *Adaptive Optics Systems and Technology*. T. 3762. International Society for Optics et Photonics. 1999, p. 8-19 (cf. p. 53).

[Ver+11] VERNIN, MUÑOZ-TUÑÓN, SARAZIN et al. « European extremely large telescope site characterization i : Overview ». In : *Publications of the Astronomical Society of the Pacific* 123.909 (2011), p. 1334 (cf. p. 24).

[Vio+18] VIOTTO, PORTALURI, ARCIDIACONO et al. « Dealing with the cigar : preliminary performance estimation of an INGOT WFS ». In : *Adaptive Optics Systems VI*. T. 10703. International Society for Optics et Photonics. 2018, p. 107030V (cf. p. 65).

[WM78] JY WANG et JK MARKEY. « Modal compensation of atmospheric turbulence phase distortion ». In : *JOSA* 68.1 (1978), p. 78-87 (cf. p. 32).

[WS80] JY WANG et D Es SILVA. « Wave-front interpretation with Zernike polynomials ». In : *Applied optics* 19.9 (1980), p. 1510-1518 (cf. p. 31).

[WK08] B WIDROW et I KOLLAR. « Roundoff Error in Digital Computation, Signal Processing, Control, and Communications ». In : *Cambridge University Press* (2008), p. 61-108 (cf. p. 99).

[Wiz+06] Peter L WIZINOWICH, David LE MIGNANT, Antonin H BOUCHEZ et al. « The WM Keck Observatory laser guide star adaptive optics system : overview ». In : *Publications of the Astronomical Society of the Pacific* 118.840 (2006), p. 297 (cf. p. 44).

ANNEXES

A. Overview of PAPYRUS

During my 3 years at LAM, I actively participated in the development of the PAPYRUS project. PAPYRUS is a project led by the students of the R&D group of LAM. I report here on the description of the project and current status. A paper to SPIE has been published, which is added in an Annexe.

A.1. Project Description

The Provence Adaptive-optics PYramid RUn System (PAPYRUS) is an adaptive optics system to be installed at the Coude focus of the T152 telescope (diameter of 1.52 m) at Observatoire de Haute Provence (OHP). The main specificity of Papyrus is to use a pyramid wavefront sensor, which shows better SNR performance than the usual Shack-Hartmann wavefront sensor. The pyramid wavefront sensor has widely been described theoretically (FAUVARQUE, NEICHEL, FUSCO et al. 2017,O. FAUVARQUE, JANIN-POTIRON, C. CORREIA et al. 2019) and tested on bench (JANIN-POTIRON, V. CHAMBOULEYRON, SCHATZ et al. 2019), but only a few on-sky experiments using pyramids are available.

Toward this goal, PAPYRUS is aimed at gaining experience with pyramids on-sky. It materializes the missing step between the current tests performed at LAM and the future generation of pyramid wavefront sensors such as ELT/HARMONI.

The specificity of PAPYRUS is to be a low cost and student-led project. As such, PAPYRUS uses components already available at LAM and ONERA to drastically reduce hardware costs. It is fully led by a group of 15 students, including PhD and post-docs.

A.2. Project objectives

There are 4 main objectives to the PAPYRUS project that can be summarized by :

— Technological : As stated above, PAPYRUS is a demonstrator allowing access to a pyramid wavefront sensor on sky. As such, it allows to test new components, concepts, calibration procedures, and control laws... As an example, PAPYRUS will be used to validate a newly proposed concept of “gain scheduling camera” (CHAMBOULEYRON, FAUVARQUE, SAUVAGE et al. 2021), in order to compensate in real-time for the pyramid optical gains.

— Astronomical : Even though the telescope size is limited, we anticipate to use the science data produced by PAPYRUS, for instance, to validate PSF-Reconstruction concepts, or postprocessing newly developed methods (FÉTICK, MUGNIER, T. FUSCO et al. 2020). We also expect to accommodate space for visiting instruments, like newly developed spectrographs such as VIPA from IPAG.

— Pedagogical : PAPYRUS will be a pedagogical on-sky AO bench located near Marseille, available to teach AO techniques to students coming from different laboratories or summer schools at OHP.

— Managerial : by being a project led by students, it allows the team to understand and follow all the project steps. As such, the team has been organized in a project-oriented approach, with defined roles (PI, PM etc...), regular meetings, and a PDR / FDR / PAE phase approach. As such, the project will follow the steps : System specification and requirements, Optical and Mechanical Design, Assembly and testing at LAM, Installation and testing at OHP, Maintenance and eventual upgrades at OHP.

A.3. Introduction of the T152

The site of OHP has been chosen for accessibility reasons. It is the closest observatory to LAM. It is also interesting to note that this is this same telescope that was used by Come-On for the first AO demonstration back in 1992.
Moreover, the OHP T152 telescope provides space for installing an AO bench and the telescope is available almost 80% of the year. The telescope observation time will have to be shared with the AURELIE instrument, the latter being used only 50 (clear) nights per year approximately. OHP gets from approximately 60-80 cloudy nights per year (Fig. .1), and it remains around **220-240 available clear nights per year for PAPYRUS** .

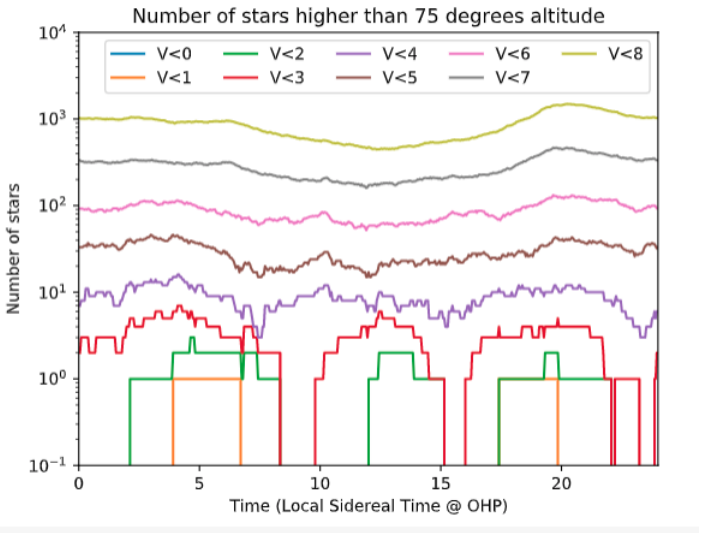

FIGURE .1. – Number of stars higher than 75° of altitude vs local sideral time at OHP (ASCC-2.5 catalog data).

The T152 telescope is made of four mirrors of 85% reflectivity each (data given 26 years ago, in 1995), providing a **total transmission of 52%**. The main drawback is the **T152 important pointing error of** ± 2 **arcmins**. Once the star has been located in the T152 within this error range, a manual search would have to be performed to make it appear on the PAPYRUS camera. This manual searching phase will slightly reduce

the effective AO lock time of PAPYRUS but is perfectly manageable according to OHP astronomers.

B. Adaptive Optics Design and error budget

The main components of PAPYRUS are recycled from other AO experiments and then are fixed. This is the case of the deformable mirror (ALPAO 17x17), the glass pyramid, the wavefront sensor camera (OCAM – First Light Imaging), and the science camera (ORCA – Hamamatsu). These components are fixed, the AO design and AO error budget are also fixed. The goal of the error budget below is not to define a design but to show the expected performance. The wavefront sensing is centered at 635 nm (that is the calibration laser wavelength), with a 20 nm bandwidth. The ORCA scientific camera wavelength ranges from 400 nm to 1000 nm. The flux is separated using a 50% - 50% beam splitter.

In the current design, the number of phase measurements allowed by the pyramid and the camera is approximately $n_{LL,camera} = 60$, which is much higher than the linear number of actuators $n_{act} = 17$. Aliasing will not be the dominant term in the error budget. A high number of measurements would be an issue in the presence of Read-out noise, but this is not the case with the OCAM. This oversampling also allows for relaxed specifications in terms of optical alignment, which is good. Note that the pyramid pixels could always be binned to reduce the oversampling if needed for specific tests. However, this also allows to consider future upgrades, with a DM allowing more actuators.

The performance of the system may be stated in terms of Strehl ratio between the AO corrected long exposure and the T152 diffraction limit. Using the Marechal approximation, this Strehl ratio is related to the residual electromagnetic phase variance over the pupil as :

$$S_R = exp(-\sigma^2), \tag{.1}$$

The usual way of balancing an AO error budget(RIGAUT, FRANCOIS, VÉRAN et al. 1998) is to write the phase variance σ^2 as the quadratic sum of different contributions

$$\sigma^2 = \sigma^2_{fitting} + \sigma^2_{aliasing} + \sigma^2_{noise} + \sigma^2_{temporal} + \sigma^2_{others} \tag{.2}$$

B.1. Fitting Error

The ALPAO 17x17 deformable mirror on a 1.52 m pupil gives a pitch of $d = 9.5$ cm. The r_0 at OHP is of the order of 5 cm at 550 nm (see Figure 32), corresponding to 5.94 cm at the WFS wavelength of 635 nm. The residual variance is then

$$\sigma^2_{fitting} = 0.27\left(\frac{d}{r_0}\right)^{5/3} = 0.6rad^2. \tag{.3}$$

This gives a Strehl ratio not exceeding 55% at 635nm, due to the fitting error only.

B.2. Aliasing Error

The aliasing error for a Shack-Hartmann is around 40% of the fitting error. Regarding the pyramid, the aliasing error is much smaller. Moreover, the PAPYRUS pyramid sensing will be oversampled by a factor of two with respect to the DM number of actuators, reducing again the aliasing effect. Thus, aliasing will not be dominant for PAPYRUS. It is neglected. Therefore, the aliasing error is :

$$\sigma^2_{aliasing} = 0 rad^2. \tag{.4}$$

B.3. Wavefront Noise Error

The photon noise and detector noise both produce intensity fluctuations on the wavefront sensor and consequently in the estimated wavefront. The advantage of our AO design is to use a low-noise OCAM2K detector for wavefront sensing. Detector noise is thus neglected. Since PAPYRUS will be targeting bright stars in its early design, photon noise will be mitigated. In order to achieve a correct SNR = 10 for each measurement, one needs 100 photons per point of measure per frame. This flux on the detector translates into the flux of the AO guiding target

$$N_{ph/m^2/s} = N_{ph/meas/frame} \frac{f}{\eta} \left(\frac{n_{meas}}{D} \right)^2. \tag{.5}$$

where $N_{ph/m^2/s}$ is the flux of the guiding target in photons per m^2 per second, $N_{ph/meas/frame}$ = 100 is the desired flux on the detector in photons per point of measurement per frame, f = 300 Hz is the frame frequency, η = 10% is the global photon efficiency from telescope to the WFS detector, n_{meas} = 16 is the number of measurements in the diameter, D = 1.52 m is the telescope diameter. One finds $N_{ph/m^2/s} = 33 \times 10^6$, For a wavelength of 700 nm and a filter width of 20 nm, this flux is obtained for stars of magnitude $V4$. With this condition on the star magnitude, the noise error propagated in the loop is neglected, therefore

$$\sigma^2_{noise} = 0 rad^2. \tag{.6}$$

B.4. Temporal Error

The temporal error comes from the delay between the actual phase present on the pupil and its correction by the deformable mirror. The temporal error writes :

$$\sigma^2_{temporal} = 0.04 \left(\frac{V}{D \cdot B_w} \right) \left(\frac{D}{r_0} \right) \sum_{n=1}^{N_r} (n+1)^{-2/3}, \tag{.7}$$

Where V is the equivalent windspeed, N_r is the number of radial orders corrected, B_w is the AO bandwidth. For a simple integrator at frequency f , delay τ and gain g, the bandwidth is :

$$B_w = \frac{f}{2\pi}\sqrt{\frac{g}{1+2\tau f}}, \tag{.8}$$

And a reasonable choice of g ensuring robustness and speed would be :

$$g \approx \frac{1}{1+\tau f}, \tag{.9}$$

We can recognize τf as the number of frames delay. For a system with 2 frames delay, $g = 0.33$ and $B_w = 0.041 f$. For a windspeed of $V = 7$ m/s, $f = 300$ Hz and wavelength $\lambda = 653$nm, we can computes :

$$\sigma^2_{temporal} = 5.9 rad^2, \tag{.10}$$

Here we see that the dominant error (by a large factor) is the temporal error. This is because the current AO system can only run at about 300Hz. This limitations comes from 2 parts. First, because at this stage of the project we use an home-made RTC developed in MATLAB. This RTC is extremely convenient for the development, as it is very flexible. We can also plug it directly into our simulation tools (OOMAO), which makes it a very powerful tool to debug the bench. However, all the interfaces with the camera and the DM are not optimized. We are then currently working with ALPAO to upgrade this RTC to their ACE RTC, and reduce significantly all the delays. The second reason why the loop rate is limited comes from the DM itself. Indeed, the 17x17 ALPAO DM that we use here has been the first one developed (10 years ago). It suffers from some latency in the actuator raising time, and limits the overall bandwidth of PAPYRUS. Here again we are working closely with ALPAO to propose an upgrade of the DM for a faster (and maybe higher actuator density) one.

B.5. Others Error

Other sources of error include, but are not limited to, scintillation on the pupil, non-common path errors, and calibration errors. These errors are not taken into account, especially in front of the important temporal error.

B.6. Overall Performance

From the error budget presented above, the expected PAPYRUS performance is shown in Fig. .2. It ranges from a SR of 3% with the first configuration, to a SR of 50% once the RTC upgrade will be implemented.

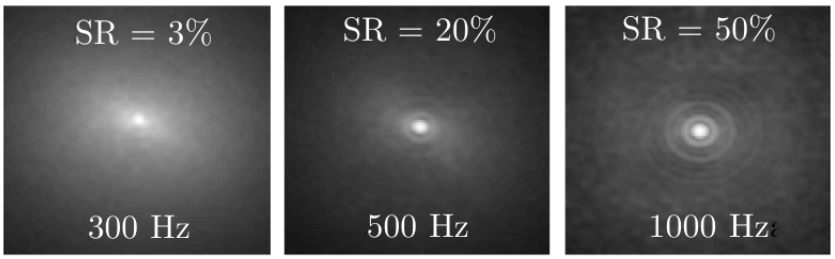

FIGURE .2. – Expected performance of PAPYRUS vs. the AO loop rate. The first design runs at 300Hz, but a future upgrade to 500Hz and 1kHz will come soon

C. Optical and Mechanical Design

C.1. Initial data and design challenges

The PAPYRUS optical design is built to work together with the T152 telescope at OHP. The T152 is a F/28.56 Cassegrain with a focal length of 43.4 m and a maximum field of view (FoV) of ±3°. The telescope plate scale is such as the Airy disk radius is 13.95 µm. As explained above, the other constraints for the optical design come from the cameras, which are already available. Their parameters were also driving the design. The initial data for the optical design development are :

1. Diameter of off-the-shelf mirror used for slow tip/tilt =25.4 mm;
2. Diameter of the existing DM = 37.5 mm;
3. Max diameter of the existing fast tip/tilt mirror = 12mm;
4. Format of ORCA science camera = 13.312×13.312 mm^2 with 2048×2048 pixels;
5. Format of OCAM WFS camera= 5.76×5.7 mm^2 with 240×240 pixels;
6. The measured pyramid parameters : facet angle =8.9°, material LF5, leading to deflection angle of ±5.44°;
7. Science camera ±1';
8. WFS FoV = ±0 :25';
9. Working wavebands = 400-1000 nm (Science camera) and 630-690 nm (WFS with filter).

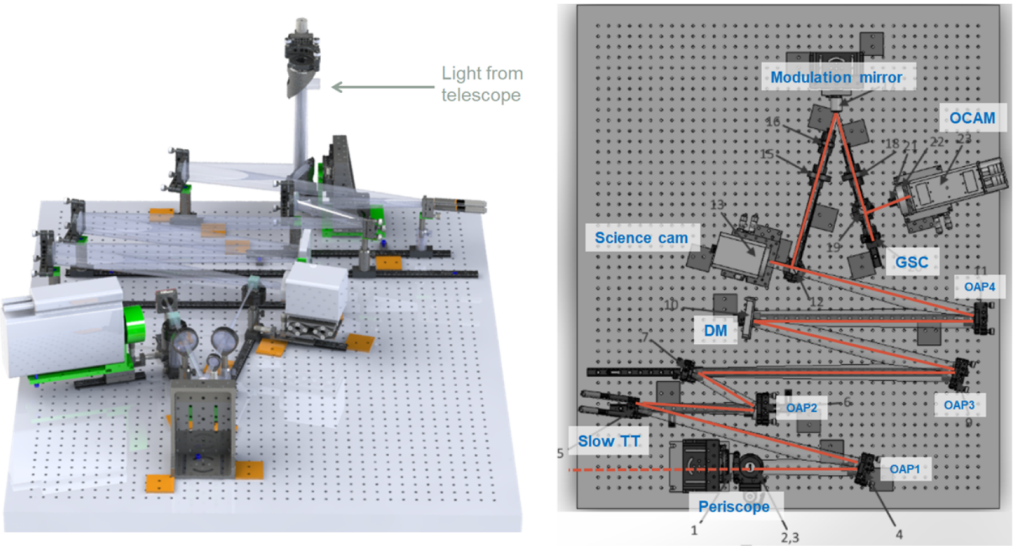

FIGURE .3. – (left) : Opto-mechanical model of PAPYRUS in 3D view (right) : top view. GSC : gain scheduling camera. DM : deformable mirror. OAP : off-axis parabola. Slow TT : slow tip-tilt mirror.

The optical design is shown in Fig. .3 the analysis of its performance is presented in the SPIE paper that is attached in the ANNEXE.

D. CURRENT STATUS

Here I present some of the tests in which I participated, and that have been carried at LAM, regarding the pyramid component and the Deformable Mirror.

D.1. Test of the pyramid

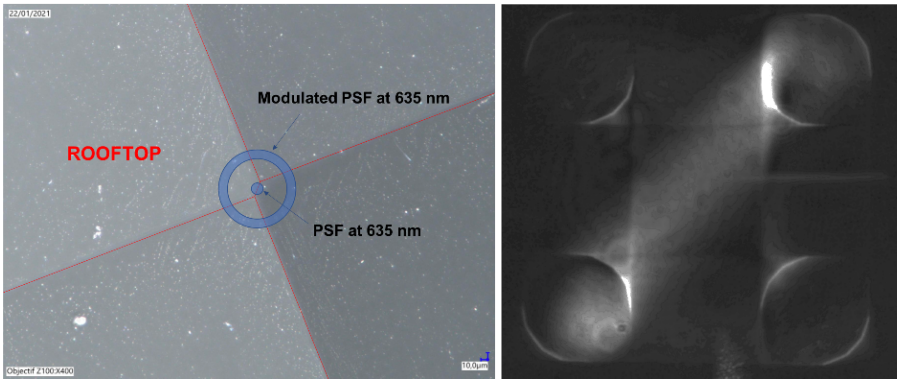

FIGURE .4. – (left) : Picture of the PAPYRUS pyramid tip, showing a "rooftop" configuration (right) : Impact of the rooftop pattern on the WFS measurements.

The critical components of PAPYRUS have been tested individually. The glass pyramid is obviously one of these critical components. Pictures of the pyramid tip Fig. .4 show a "rooftop" configuration due to manufacture precision. The rooftop size is approximately the diffraction size that would prevent WFS sensing in one direction if non-modulated. However, the modulation of the PSF around the pyramid tip solves this issue.

D.2. Characterization of the deformable mirror

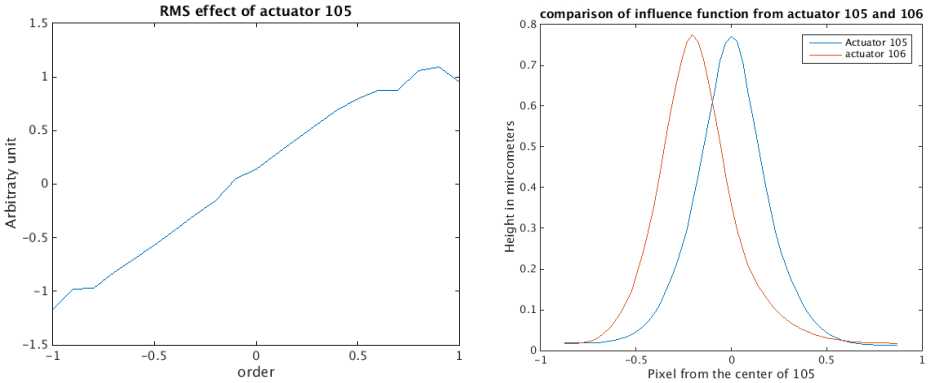

FIGURE .5. – (left) : The linearity range of actuator 105 (right) : Comparison of influence function for actuator crosstalk.

The measurements about DM are the linearity range of a single actuator and the crosstalk caused by adjacent acturators. The DM is a 17 × 17 actuator ALPAO mirror. It was previously used by ONERA on the BOA bench. The actuators are commanded with Matlab through the ALPAO controller. In practice, each actuator has a range from -1 to 1 that we can ask, and the controller adds the voltage. The controller then applies the tension on each actuator. The actuators have a linearity range out of which their answer changes shape and intensity.

From the (Fig. .5 left), the actuator shape can change drastically when out of its linearity range. Here shows the RMS displacement caused by an actuator in function of the order. We begin for this actuator to see the nonlinearity effect under -0.8 and over 0.7, and from (right), since the actuators are positioned pretty close on the DM, here we can see the same influence functions for the next actuator. This allows us to compute the mechanical coupling as the remaining height of actuator 105 at the centre of actuator 106 : 46% (example for this pair of actuators).

D.3. Testing the WFS branch

The WFS branch has been aligned and tested at LAM as shown by Fig. .6. It includes the pyramid, the WFS camera, the DM and the modulation mirror. We processed the raw intensities and were able to compute the calibration matrix of the system by

sending push-pull commands on the DM. This is almost the first demonstration of the closed-loop system.

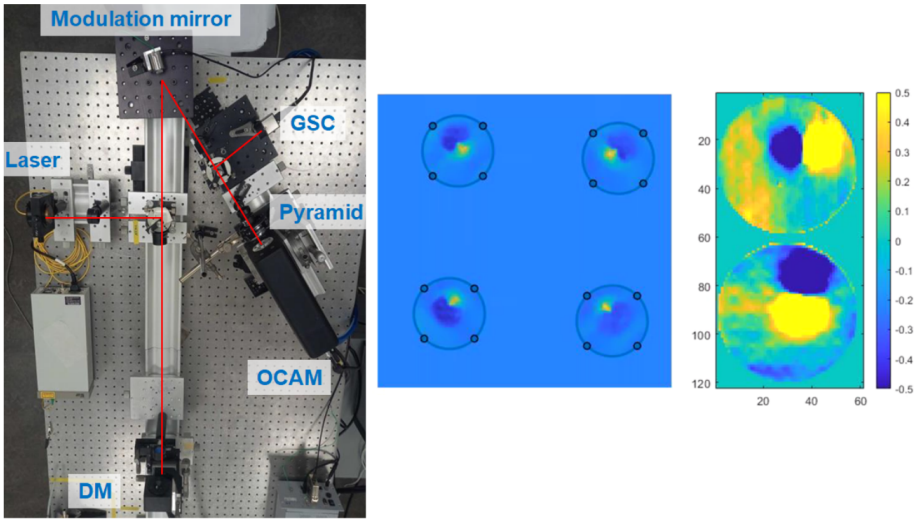

FIGURE .6. – Tests of the WFS branch at LAM. (Left) : picture of the WFS branch. (Middle) : image seen on the WFS camera when a poke is sent to the DM. (Right) : computed slopes maps.

D.4. On-sky measurements at OHP

Measurements at the Coude focus of the T152 telescope have been performed on July 20th and 21st, 2021. The objectives of these measurements were to characterise the telescope pupil plane and focal plane. The possible high-amplitude movement of these planes is problematic for the AO system. However, the pupil plane has shown stability better than 1% of the diameter during a long-exposure observation. The movement of the pupil is consequently less than a fraction of the point of measurement of the phase (equivalent to a subaperture of a Shack-Hartmann WFS). In Fig. .7 we show some the images acquired during this first test campaign.

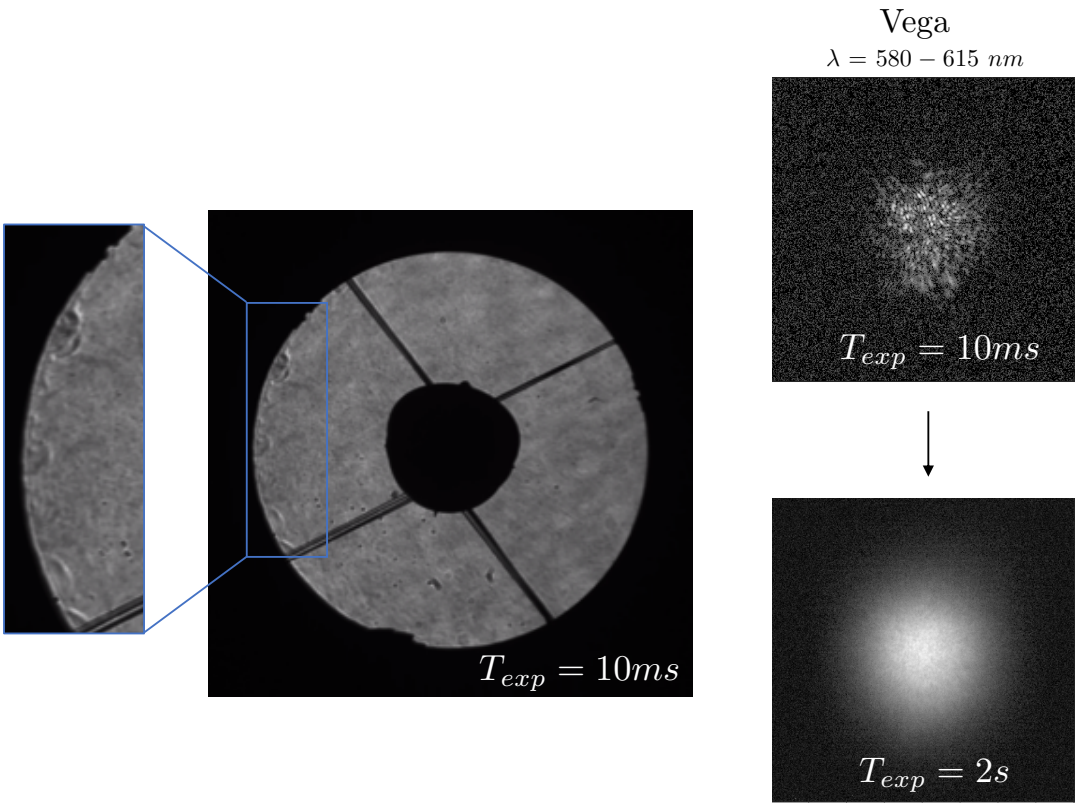

FIGURE .7. – Measurement at the T152, with the pupil image where we see scintillation, and associated short exposure and long exposure PSFs.

E. conclusion

As it was presented here, PAPYRUS will soon allow LAM to improve its operational expertise on pyramids and deliver an AO corrected image at OHP. The system has been designed, the components have been characterized, and the first integration is underway with preparations for arrival at OHP also well advanced.

From my perspective, it was very instructive to participate to this project, as I could understand all the required step of building an AO system from scratch. I participated to many of the tests of the DM, the Pyramid and the optical alignment. I learned a lot on practical aspects, and could work with the team. This was a very exciting experience, and I am looking forward the 1st light of the papyrus system.

F. PAPYRUS SPIE PAPER

Current status of PAPYRUS : the pyramid based adaptive optics system at LAM/OHP

Muslimov E.[c], Levraud N.[a,b], Chambouleyron V.[a,b], Boudjema I.[a], Lau A.[a], Caillat A.[a], Pedreros F.[a], Otten G.[a], El Hadi K.[a], Joaquina K.[a], Maxime M.[a], EL Morsy M.[a], Beltramo Martin O.[a], Fétick R.[a,b], Ke Z.[a], Sauvage J-F.[a,b], Neichel B.[a], Fusco T.[a,b], Schmitt J.[d], Le Van Suu A.[d], Charton J.[e], Schimpf A.[e], Martin B.[e], Dintrono F.[e], Esposito S.[f], and Pina E.[f]

[a]Laboratoire d'Astrophysique de Marseille, France
[b]DOTA,ONERA, Université Paris Saclay, F-91123 Palaiseau, France
[c]NOVA Optical IR Instrumentation Group, Dwingeloo, Netherlands
[d]Observatoire de Haute Provence, Saint-Michel-L'observatoire, France
[e]ALPAO, Montbonnot-Saint-Martin, France
[f]Osservatorio Astrofisico di Arcetri, INAF, Italie

ABSTRACT

The Provence Adaptive optics Pyramid Run System (PAPYRUS) is a pyramid-based Adaptive Optics (AO) system that will be installed at the Coude focus of the 1.52m telescope (T152) at the Observatoire de Haute Provence (OHP). The project is being developed by PhD students and Postdocs across France with support from staff members consolidating the existing expertise and hardware into an R&D testbed. This testbed allows us to run various pyramid wavefront sensing (WFS) control algorithms on-sky and experiment on new concepts for wavefront control with additional benefit from the high number of available nights at this telescope. It will also function as a teaching tool for students during the planned AO summer school at OHP. To our knowledge, this is one of the first pedagogic pyramid-based AO systems on-sky. The key components of PAPYRUS are a 17x17 actuators Alpao deformable mirror with a Alpao RTC, a very low noise camera OCAM2k, and a 4-faces glass pyramid. PAPYRUS is designed in order to be a simple and modular system to explore wavefront control with a pyramid WFS on sky. We present an overview of PAPYRUS, a description of the opto-mechanical design and the current status of the project.

Keywords: Adaptive Optics, Pyramid sensor

1. INTRODUCTION

1.1 Presentation of the project

The Provence Adaptive-optics PYramid RUn System (PAPYRUS) is an adaptive optics system to be installed at the Coude focus of the T152 telescope (diameter of 1.52 m) at Observatoire de Haute Provence (OHP). The main specificity of Papyrus is to use a pyramid wavefront sensor, which shows better SNR performances than the usual Shack-Hartmann wavefront sensor. The pyramid wavefront sensor has widely been described theoretically[1,2] and tested on bench.[3] PAPYRUS is a demonstrator of feasibility on sky and a TRL maturation step in between the current tests performed at LAM and the future generation of pyramid wavefront sensors such as ELT/HARMONI.

The specificity of PAPYRUS is to be a low cost and student led project. Indeed PAPYRUS will use components already available at LAM and ONERA in order to drastically reduce hardware costs. The PAPYRUS project encompasses all the following steps:

Further author information::
Muslimov E. : E-mail: eduard.muslimov@lam.fr
Levraud N.: E-mail: nicolas.levraud@lam.fr
Fétick R.: E-mail: romain.fetick@lam.fr

- System specification and requirements
- System optical and mechanical design
- Assembly and testing at LAM
- Installation and testing at OHP
- Maintenance and eventual upgrades at OHP

1.2 PAPYRUS project objectives

As stated above, PAPYRUS is a demonstrator of capability to place a pyramid wavefront sensor on sky. The LAM/GRD and ONERA teams will gain a valuable knowledge on the pyramid behaviour, especially regarding the development of specific control laws. The impact of the PSF modulation on the pyramid will be a major topic of study thanks to a dedicated modulation mirror and to a dedicated pyramid focal plane camera[4] ("gain scheduling camera"). Management of the pyramid optical gains and non-linearities is still a subject under active research. PAPYRUS might be upgraded in the future to test new techniques or components for astronomy with AO.

Moreover, PAPYRUS data will be used to check image post-processing possibilities from pyramid AO systems. PSF analysis, PSF estimation[5] or deconvolution[6] is envisaged.

Finally, PAPYRUS will be a pedagogical on-sky AO bench located near Marseille (France) to teach on AO techniques students coming from different laboratories or summer schools at OHP. Observing proposals may be issued by astronomers once the system performances and sky coverage have been validated on sky.

1.3 The Observatoire de Haute Provence (OHP) site

The astronomical site of OHP, located inthe South-East of France, has been chosen for accessibility reasons. It is the closest observatory to the development laboratory at LAM, the OHP T152 telescope has available space for installing an AO bench and available observation time. The telescope observation time will have to be shared with the AURELIE instrument, the latter being used only 50 (clear) nights per year approximately. The OHP suffers from approximately 60-80 cloudy nights per year (figure 3), it remains around 220-240 available clear nights per year for PAPYRUS.

The OHP is supporting the PAPYRUS effort. OHP will allow installation of the AO bench on the telescope and teaching some PAPYRUS people to use the telescope in autonomy. The T152 telescope is made of four mirrors of 88% reflectivity each, providing a total transmission of 52%. Recent coating on the primary mirror might slightly improve this transmission factor. The main drawback is the T152 important pointing error of ± 2 arcmin. Once the star has been located in the T152 within this error range, a manual search would have to be performed to make it appear on the PAPYRUS camera. This manual searching phase will reduce slightly the effective AO lock time of PAPYRUS but is perfectly manageable according to OHP astronomers and our own usage of the telescope.

2. ADAPTIVE OPTICS DESIGN

2.1 Atmospheric conditions at OHP

The adaptive optics design and performances depends on the atmospheric conditions at the observing site. Data from OHP[7] in Fig.1 show ~ 60 nights of good seeing $s < 2$". The median of the data is in between $s = 2$" and $s = 4$", representing approximately 200 nights per year. These values give a typical Fried parameter $4 < r_0 < 6$ cm at a wavelength of 600 nm.

The median wind speed at OHP is about 5 m/s, with bursts up to 7 m/s.

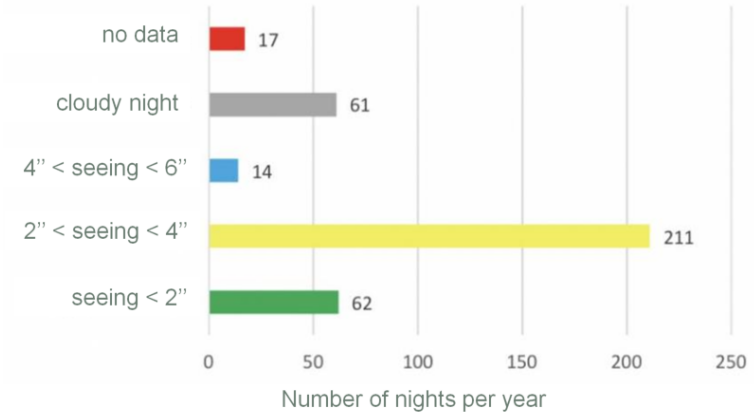

Figure 1. Statistics of seeing at OHP in 2018. Image taken and adpted from OHP website.

2.2 Adaptive optics error budget

The performances of the system may be stated in term of Strehl ratio between the AO corrected long exposure and the T152 diffraction limit. Using the Marechal approximation, this Strehl ratio is related to the residual electromagnetic phase variance over the pupil as

$$S_r = e^{-\sigma^2} \tag{1}$$

The usual way of balancing an AO error budget[8] is to write the phase variance σ^2 as the quadratic sum of different contributions

$$\sigma^2 = \sigma^2_{\text{fitting}} + \sigma^2_{\text{aliasing}} + \sigma^2_{\text{noise}} + \sigma^2_{\text{temporal}} + \sigma^2_{\text{others}} \tag{2}$$

The definition and computations of these terms is given below. These expressions being chromatic, we choose to give all values in the visible, at a wavelength of 635 nm.

2.2.1 Fitting error

The so-called fitting error is due to the limited number of actuators of the deformable mirror. Thus the high spatial frequencies of the turbulent phase cannot be corrected by the AO system and are present in the residuals. The expression of this error is

$$\sigma^2_{\text{fitting}} = 0.27 \left(\frac{d}{r_0} \right)^{5/3} \tag{3}$$

with d the pitch between two actuators and r_0 the Fried parameter of the turbulence. For our 17×17 deformable mirror on a $D = 1.52$ m pupil, the pitch is 9.5 cm, giving an error of

$$\sigma^2_{\text{fitting}} = 0.6 \text{ rad}^2 \tag{4}$$

2.2.2 Aliasing error

The wavefront measurement is sampled for detection, producing aliasing of the high frequencies onto the low frequencies. This information from the high frequencies enters in the AO loop and generates a deformable mirror response. However the aliasing is smaller on a pyramid wavefront sensor than ona Shack-Hartmann wavefront sensor. It is then neglected in our AO budget

$$\sigma^2_{\text{aliasing}} = 0 \text{ rad}^2 \tag{5}$$

2.2.3 Noise error

The photon noise and detector noise both produce intensity fluctuations on the wavefront sensor and consequently in the estimated wavefront. The advantage of our AO design is to use a low-noise OCAM^{2}K detector for wavefront sensing. Detector noise is thus neglected.

Since PAPYRUS will be targeting bright stars in its early design, photon noise will be mitigated. In order to achieve a correct SNR = 10 on each measurement, one needs 100 photons per point of measure per frame. This flux on the detector translates into flux of the AO guiding target as

$$N_{\mathrm{ph/m2/s}} = N_{\mathrm{ph/meas/frame}} \frac{F}{\eta} \left(\frac{n_{meas}}{D} \right)^2 \tag{6}$$

where $N_{\mathrm{ph/m2/s}}$ is the flux of the guiding target in photons per m^2 per second, $N_{\mathrm{ph/meas/frame}} = 100$ is the desired flux on the detector in photons per point of measurement per frame, $F = 300$ Hz is the frame frequency, $\eta \simeq 10\%$ is the global photon efficiency from telescope to the WFS detector, $n_{meas} = 16$ is the number of measurements in the diameter, $D = 1.52$ m is the telescope diameter. One finds

$$N_{\mathrm{ph/m2/s}} = 33 \times 10^6 \tag{7}$$

For a wavelength of 700 nm and a filter width of 20 nm, this flux is obtained for stars of magnitude $V \leq 4$. With this condition on the star magnitude the noise error propagated in the loop is neglected

$$\sigma^2_{\mathrm{noise}} = 0 \text{ rad}^2 \tag{8}$$

2.2.4 Temporal error

The temporal error comes from the delay between the actual phase present on the pupil and its correction by the deformable mirror. The temporal error writes

$$\sigma^2_{\mathrm{temporal}} = 0.04 \left(\frac{V}{DB} \right)^2 \left(\frac{D}{r_0} \right)^{5/3} \sum_{n=1}^{N_r} (n+1)^{-2/3} \tag{9}$$

with V the turbulence equivalent wind speed (Taylor frozen flow hypothesis), B the AO loop bandwidth and N_r the number of radial modes corrected. For a control law including an integrator, the equivalent bandwidth writes

$$B = \frac{F}{2\pi} \sqrt{\frac{g}{1 + 2\tau F}} \tag{10}$$

with g the integrator gain and τ the loop delay. A reasonable choice of gain ensuring both performances and robustness is

$$g = \frac{1}{1 + \tau F} \tag{11}$$

Considering $\tau F = 2$ frames delay for PAPYRUS and a wind speed $V = 7$ m/s, we deduce the bandwidth and then the temporal error

$$\sigma^2_{\mathrm{temporal}} = 5.9 \text{ rad}^2 \tag{12}$$

2.2.5 Other sources of error

Other sources of error include, but are not limited to, scintillation on the pupil, non-common path errors, and calibration errors. These errors are not taken into account, especially in front of the important temporal error.

2.3 Conclusions on the budget

The error budget above is highly dominated by the temporal error. This error is established with the highest wind speed at OHP, and thus corresponds to a worst case of PAPYRUS usage. It is planned to mitigate this error by implementing more complex control laws to increase the bandwidth, and using a better RTC. Indeed we plan to replace our current computer (run on Matlab) by a dedicated ALPAO high-speed RTC.

Adaptive-optics corrected PSF are simulated using OOMAO[9] end-to-end simulations with the PAPYRUS system parameters, see Fig. 2. The temporal error being the dominant one, we use three different AO loop frequencies for the simulations. It shows that the current $F = 300$ Hz is quite limitating and incline us to go for a better RTC at $F = 500$ Hz at least.

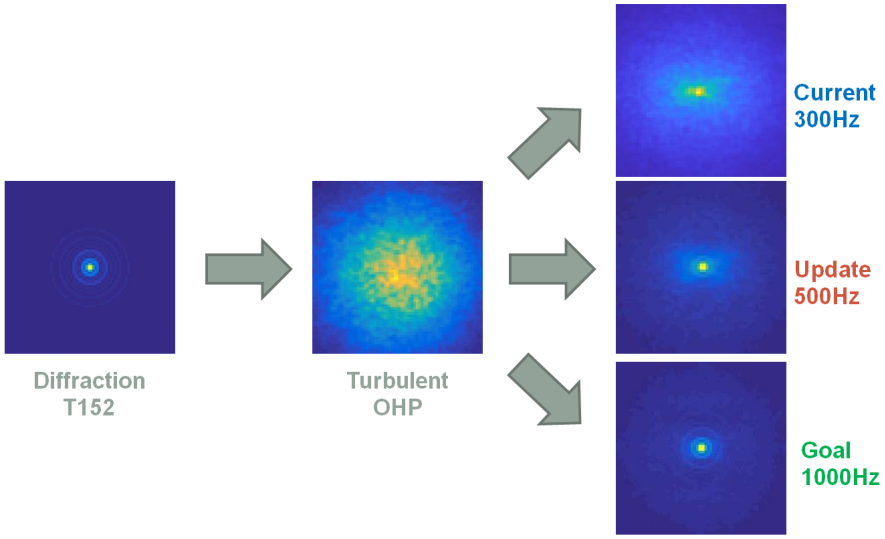

Figure 2. PSF from end-to-end simulations. Three cases of loop frequency are considered to simulate the PAPYRUS PSF.

3. OPTICAL DESIGN

3.1 Initial data and design challenges

The optical design is built to work together with the T152 telescope at OHP. It represents an *F/28.56* Cassegrain system with the focal length of 43.4 m and the maximum field of view (FoV) of $\pm 3°$. The telescope has residual aberrations, which don't exceed $16.8\mu m$,while the Airy disk radius is $13.95\mu m$.

Also, we had certain cameras available for the scientific and wavefront sensing branches as well as the commercial deformable and tip-tilt mirrors. Their parameters were also driving the design.

Thus, except of the telescope parameters the initial data for the optical design development included:

1. Diameter of off-the-shelf mirror used for slow tip/tilt =25.4 mm;
2. Diameter of the existing DM = 37.5 mm;
3. Max diameter of the existing fast tip/tilt mirror = 12 mm;
4. Format of ORCA science camera = $13.312 \times 13.312 mm^2$ with 2048×2048 pixels;
5. Format of OCAM WFS camera= $5.76 \times 5.7 mm^2$ with 240×240 pixels;
6. The measured parameters of existing glass pyramid: facet angle = 8.9°, material LF5, leading to deflection angle of $\pm 5.44°$;

7. Science camera FoV = ±1";
8. WFS FoV = ±0.25 :;
9. Working wavebands = 400-1000 nm (Science camera) and 630-690 nm (WFS with filter).

In addition to these initial data there were some limitations, which made the development challenging. First, the project budget and the development time were limited. Therefore we had to rely only on off-the-shelf components and iteratively repeat the design to find compromise solutions. Second, since our demonstrator is targeting multiple tasks, its' design should be flexible with a possibility to replace some components, to connect testing and alignment modules or to feed other instruments through optical ports, to get an access to any par of it for educational purposes. Third, the optical design of the bench should provide a high image quality to minimise the instrumental WFE and the difference between the science and WFS branches. Finally, there were limitations in overall dimension and optical interfaces because the bench will be installed on a telescope among the existing instruments.

3.2 Optical design overview and analysis

With all of the above-listed initial values and limitations we developed the following optical design (see Figure 3). In order to provide flexible connection with the telescope and compensate the height difference the movable periscope unit 2, 3 is used to pick up the beam from the telescope focal plane 1. Hereafter we use two optical relays to form intermediate focal and pupil planes and place key components there. The relays are built on the basis of off-axis parabolic (OAP) mirrors. use of OAP allows to exclude chrmatic aberrations and significantly reduce the overall dimensions, although makes the alignment more difficult. The beam is collimated (4) and the pupil is imaged on the slow tip-tilt mirror 5. Further the beam is focused again (6) with -0.5^x magnification and the pupil is re-imaged to the infinity. Folding mirror 7 represents an optical port, which can be used to couple the telescope simulator optical to the intermediate focus 8. The beam is collimated again (9) and the pupil is imaged onto DM 10. Then it is focused (11) in the same way with -1^x magnification and the pupil projection to the infinity. The image formed in focal plane is detected by science camera 13. Before the science camera a beamsplitter 12 is mounted to feed the WFS branch. Note, that the WFS branch uses lens optics, because the components there should have short focal lenghts and work with relatively large angular fields. The WFS 1^{st} intermediate focus 14 can be used to set a diaphragm. The beam is re-collimated (15) and the pupil is projected to the modulation mirror 17. In the formed parallel beam after 15 a filter 16 can be mounted to minimize the WFS chromatism. It should be noted that some chromatic aberration is inherent to the pyramid itself regardless of the auxiliary optics properties. The beam is focused (18), while the pupil is projected to the infinity. The focused beam is split (19) to form two identical images at the tracking camera 20 and the tip of pyramid 21. The pyramid splits the beam in quadrants with 5.44° deflection. The resultant beams are collimated (22) and the pupil is projected to the WFS camera 23.

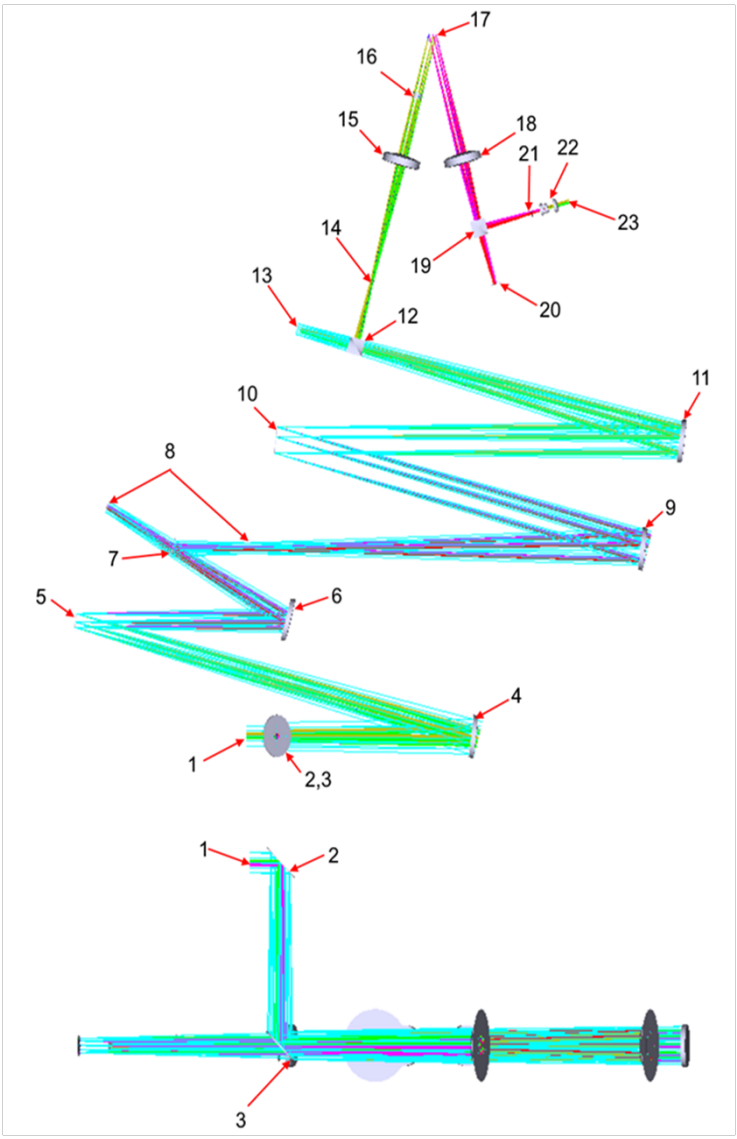

Figure 3. General view of the PAPYRUS optical design (see the text for the elements notation).

Thus, the optical design consists of a series of functional elements, each served with a collimating and focusing relay. Since each focusing component should project the pupil to the infinity, the pupils coincide with the focusing components focal planes. For the same reason, the collimating components form the pupil images in their back focal planes. The actual focal lengths and magnifications in the system were choosen to fit the initial design conditions and to obtain the focal lengths, $F/\#$ and field values close to those of available commercial components.

The Figure 4 shows the image quality in the field of view of science camera. The spot diagram root mean square (RMS) radii vary between 5.3 and 14.9 μm, while the Airy disk radius is 10.1μm. So, the image quality is diffraction limited on-axis and slightly degrades towards the field edge. The WFE RMS value is 0.048λ with the maximum of 0.16λ at 700 nm. The on sky quality will however be dominated by AO residuals and anisoplanatism, so this design is completely accepted for PAPYRUS.

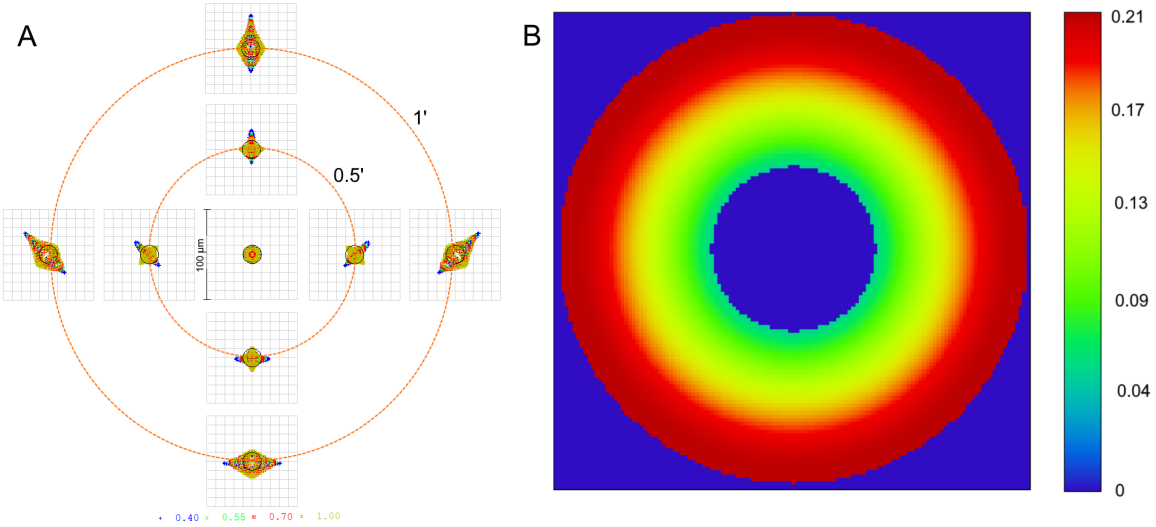

Figure 4. Image quality at the scientific camera: A – spot diagrams over the FoV (the colors correspond to wavelengths in μm); B – wavefront error in waves @0.7μm referred to the exit pupil plane.

The image quality assessment for the WFS branch is shown in Figure 5. The geometrical spot size remains stable across the field, since the nominal pyramid FoV is only ±14.4". It has the RMS radius of 5.1-6.0 μm , while the Airy radius is 12.1 μm. The WFE for a single pyramid facet is 0.046λ RMS at 700 nm. It becomes possible to reach the diffraction limit only with use of a red band filter. Otherwise the chromatic aberrations inherent to this system would blur the spot images by factor of 4.

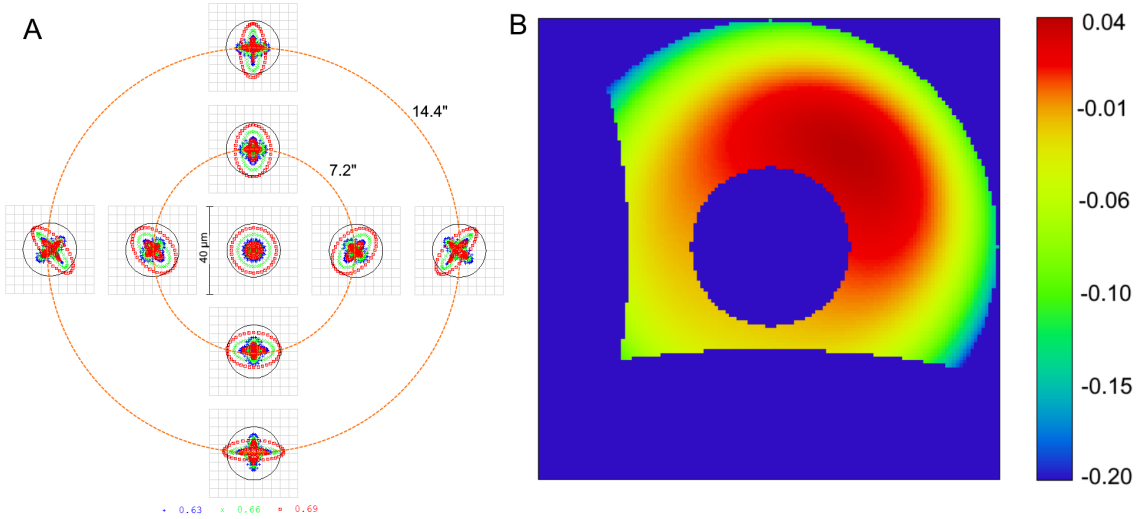

Figure 5. WFS branch image quality at the tracking camera: A – spot diagrams over the FoV (the colors correspond to wavelengths in μm with filter); B – wavefront error in waves @0.7μm referred to the exit pupil plane.

We would like to note separately the design issue related to the last WFS lens, which forms the image on the camera after the pyramid. It should work with a relatively low $F/\#$ and extended field of view, but also in an unordinary setup, where the pupil is shifted and doesn't coincide with the nominal aperture stop or its' images. In the meantime this lens should be an off-the-shelf component and provide a high image quality. A $Canon^{TM}$ EF-S 24mm F/2.8 STM pancake photographic lens was chosen, since it is has small total length and provide

high image quality. However, to account for possible vignetting and aberrations growth is this setup we had to reconstruct an approximate optical design of the lens. An approximate algorithm of this reverse-engineering is given below. We hope that it can be useful for those, who are going to use commercial lenses in non-standard laboratory setups.

1. The general data about the lens like the number of lenses and groups as well as the composition of positive and negative components were taken from the manufacturer.[10]
2. The closest patent was found.[11] The lens composition is similar to the known one and the publication date is the closest ot the lens commercial release.
3. The patent lens was scaled to fit the focal length and the first lens diameter of the commercial lens.
4. The lens was optimized to fit such criteria as the MTF values and vignetting known from open sources. The radii of curvature and thicknesses were used as free variables. In addition to standard boundary conditions defining the edge and center thicknesses, the overall system length and diameters and optical powers of individual components were restricted. The lens design after optimization is shown in Figure 6,

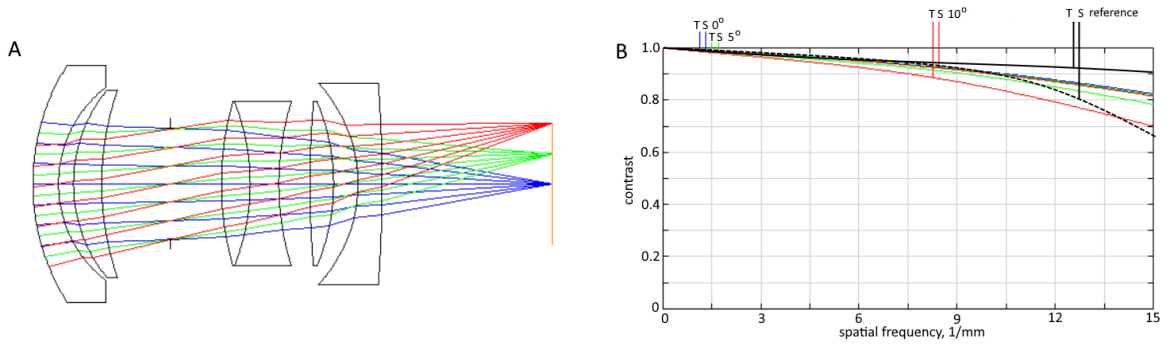

Figure 6. Reconstructed design of the WFS lens: A – general view, B – MTF in comparison with the reference curve from open sources.

The figure 7 shows the opto-mechanical implementation of PAPYRUS with the different elements already presented before. The optomechanical design uses off-the-shelf parts for all the adjustments and holding the components and has as less as possible custom parts only as mechanical interface adapters. The mechnaical mounts provide the necessary number of degrees of freedom for every unit. The entire bench is assembled on a single breadboard. The optical path is divided into straight segments and all the components of such a segment are mounted on a single optical rail. Position of each of the optical rails is given by a couple (line+corner) flat templates. The periscope assembly and the cameras are mounted via custom adapters, which can be 3d-printed or milled in aluminium. All the OAP mirrors have adapters to compensate the vertex lateral shift. Finally, the WFS camera together with the pyramid are mounted in a custom housing with adjustment rings and attached directly to the WFS camera C-mount. This optomechanical implementation allows some room for future upgades of the AO bench, and visiting scientific instrument to be adapted to the bench.

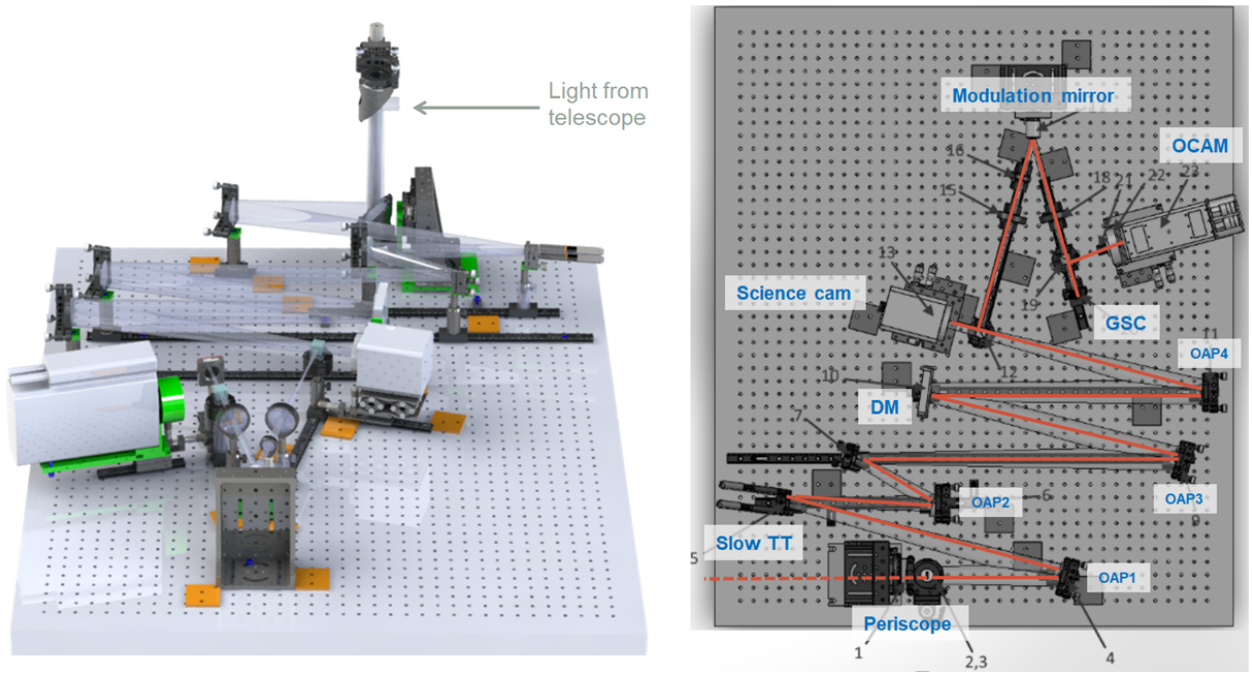

Figure 7. Opto-mechanical model of PAPYRUS in 3D view (left) and top view (right). GSC: gain scheduling camera. DM: deformable mirror. OAP: off-axis parabola. Slow TT: slow tip-tilt mirror.

4. CURRENT STATUS OF PAPYRUS

4.1 Assembly Integration and Tests

The AIT of PAPYRUS will be organized following this strategy:

- component validation at LAM
- global bench alignement and validation at LAM
- final coupling and commissioning at T152 OHP.

4.1.1 Test of the pyramid

The critical components of PAPYRUS have been tested individually. The glass pyramid is obviously one of these critical components. Pictures of the pyramid tip (Fig. 8) show a "rooftop" configuration due to manufacture precision. The rooftop size is approximately the diffraction size that would prevent WFS sensing in one direction if non modulated. However the modulation of the PSF around the pyramid tip solves this issue.

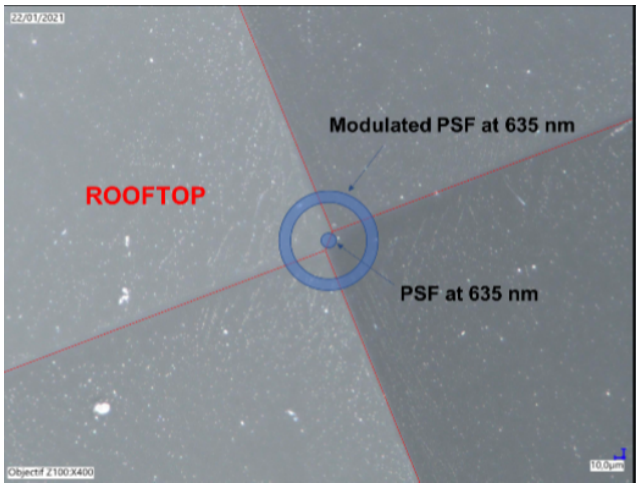

Figure 8. Picture of the PAPYRUS pyramid tip, showing a "rooftop" configuration.

4.2 Testing the WFS branch

The WFS branch is the core of the AO instrument. This branch has already been aligned at LAM (Fig. 9) to test the critical components to work together: the pyramid, the WFS camera, the DM and the modulation mirror. We processed the raw intensities and were able to compute the calibration matrix of the system by sending push-pull commands on the DM.

Once the tests performed, the WFS branch has been unmounted. The alignment of the full bench is currently under process at LAM.

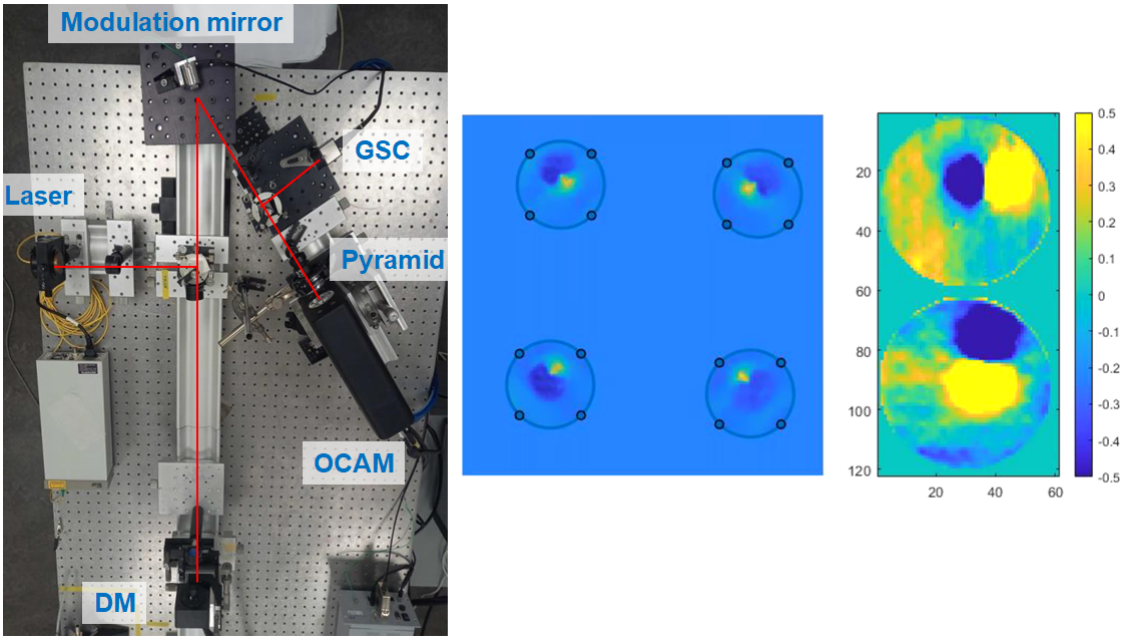

Figure 9. Tests of the WFS branch at LAM. Left: picture of the WFS branch. Middle: image seen on the WFS camera when a poke is sent to the DM. Right: computed slopes maps.

4.3 On-sky measurements at OHP

Measurements at the Coude focus of the T152 telescope have been performed on July 20th and 21st, 2021. The objective of these measurements is to characterise the telescope pupil plane and focal plane. The possible high-amplitude movements of these planes is problematic for the AO system. However the pupil plane has shown stability better than 1% of the diameter during a long-exposure observation. The movement of the pupil is consequently less than a fraction of point of measurement of the phase (equivalent to a sub-aperture for a Shack-Hartmann WFS).

The star position is targeted within a ± 2 arcmin uncertainty diameter in the sky due to the telescope pointing lack of accuracy. However once the star is found it can be correctly centred manually. Then the PSF suffers a small drift of ~ 20 arcsec/hour. This drift is supposed to come from the telescope weight unbalance that might accelerate or slow down the Earth rotation compensation. However this drift is small and will be managed by the PAPYRUS slow tip-tilt mirror.

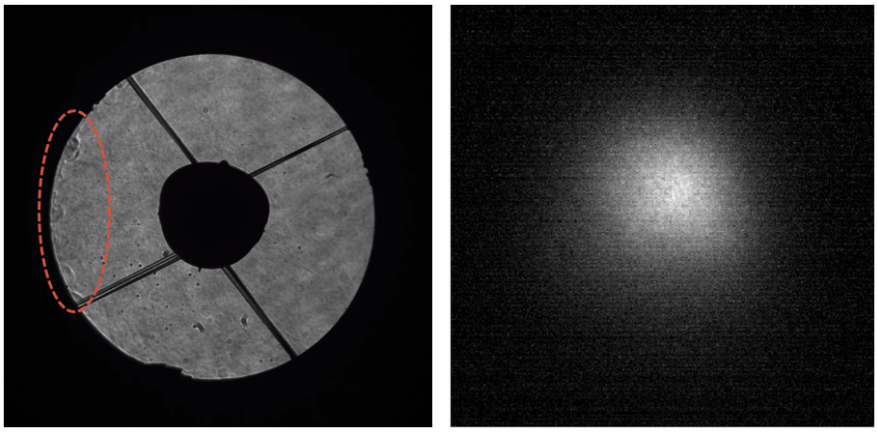

Figure 10. Characterisation of the OHP/T152 telescope. Left: image of the pupil. The dashed red ellipse shows presence of localised amplitude fluctuations at the edge of the pupil. Right: long-exposure PSF obtained on Vega.

4.4 Schedule

The schedule of the PAPYRUS project is given on Fig. 11. Integration at OHP is planned for end 2021, and PAPYRUS will be available for the astronomical community beginning or mid 2022.

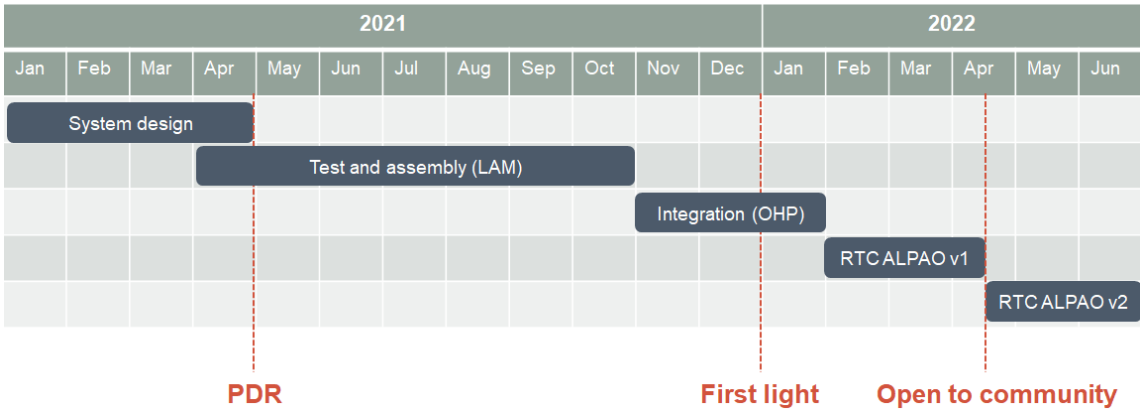

Figure 11. Schedule of the PAPYRUS project.

5. CONCLUSION

As it was presented here PAPYRUS will soon allow LAM to improved its operational expertise on Pyramids and deliver an AO corrected image at OHP. The system has been designed, the components have been characterised, and the first integration is underway with preparations for arrival at OHP also well advanced. The project will soon be opened to the community and we will welcome any new idea and collaboration to add new capabilities to the bench.

6. ACKNOWLEDGEMENT

This project has been supported by ONERA, LAM and ALPAO in particular the WOLF ANR. We also thanks First Light and the OHP for their contribution this project.

REFERENCES

[1] O. Fauvarque, B. Neichel, T. Fusco, J.-F. Sauvage, and O. Girault, "General formalism for fourier-based wave front sensing: application to the pyramid wave front sensors," *Journal of Astronomical Telescopes, Instruments, and Systems* **3**(1), p. 019001, 2017.

[2] O. Fauvarque, P. Janin-Potiron, C. Correia, Y. Brûlé, B. Neichel, V. Chambouleyron, J.-F. Sauvage, and T. Fusco, "Kernel formalism applied to fourier-based wave-front sensing in presence of residual phases," *JOSA A* **36**(7), pp. 1241–1251, 2019.

[3] P. Janin-Potiron, V. Chambouleyron, L. Schatz, O. Fauvarque, C. Z. Bond, Y. Abautret, E. R. Muslimov, K. El Hadi, J.-F. Sauvage, K. Dohlen, *et al.*, "Adaptive optics with programmable fourier-based wavefront sensors: a spatial light modulator approach to the lam/onera on-sky pyramid sensor testbed," *Journal of Astronomical Telescopes, Instruments, and Systems* **5**(3), p. 039001, 2019.

[4] V. Chambouleyron, O. Fauvarque, J.-F. Sauvage, B. Neichel, and T. Fusco, "The focal-plane assisted pyramid wavefront sensor: enabling frame-by-frame optical gains tracking," *arXiv preprint arXiv:2103.02297* , 2021.

[5] R. J. Fétick, L. Mugnier, T. Fusco, and B. Neichel, "Blind deconvolution in astronomy with adaptive optics: the parametric marginal approach," *Monthly Notices of the Royal Astronomical Society* **496**(4), pp. 4209–4220, 2020.

[6] L. M. Mugnier, T. Fusco, and J.-M. Conan, "Mistral: a myopic edge-preserving image restoration method, with application to astronomical adaptive-optics-corrected long-exposure images," *JOSA A* **21**(10), pp. 1841–1854, 2004.

[7] OHP, "meteorological data." http://www.obs-hp.fr/climatologie.shtml.

[8] F. J. Rigaut, J.-P. Véran, and O. Lai, "Analytical model for shack-hartmann-based adaptive optics systems," in *Adaptive Optical System Technologies*, **3353**, pp. 1038–1048, International Society for Optics and Photonics, 1998.

[9] R. Conan and C. Correia, "Object-oriented matlab adaptive optics toolbox," in *Adaptive optics systems IV*, **9148**, p. 91486C, International Society for Optics and Photonics, 2014.

[10] C. Inc., "Canon camera museum." https://global.canon/en/c-museum/product/ef434.html.

[11] M. Ohtake and M. Mori, "Compact wide-angle objective lens," Sept. 16 1997. US Patent 5,668,669A.